D5.6

BEACON

Bentonite Mechanical Evolution

SPECIFICATIONS FOR BEACON WP5: TESTING, VERIFICATION AND VALIDATION OF MODELS

STEP 3- predictive test cases

Deliverable D5.6
Report

Authors: R. Charlier (ULiege), B. Darde (ULiege) & J. Talandier (Andra)
with contributions from G. Scaringi, D. Mašín, P. Poskas, A. Narkuniene, D. Justinavicius, O. Kristensson, D. Malmberg, R. K. Newson, K. E. Thatcher, L. Zdravkovic, G. Pedone, D. Potts, A. Tsiampousi, J. A. Bosch, A. Ferrari, L. Laloui, S.s Beese, V. Kumar, L. Gramegna, M. V. Villar

Date of issue of this report: **30/04/2021**

Start date of project: **01/06/17** Duration: 60 Months

This project receives funding from the Euratom research and training programme 2014-2018 under grant agreement No 745 942		
Dissemination Level		
PU	Public	

REVIEW

Name	Internal/Project/External	Comments
All Beacon partners	Project internal	

DISTRIBUTION LIST

Name	Number of copies	Comments
Seifallah BEN HADJ HASSINE (EC) Beacon partners	Digital Digital	

Content

1 Introduction

The overall objective of the Beacon project is to evaluate the performance of an inhomogeneous bentonite barrier. Inhomogeneities mainly result, among others, from the initial distribution of dry density, the simultaneous use of several forms of bentonite materials (such as blocks and pellets), and external solicitations during operation, such as a non-uniform water flow.

Understanding the properties and fundamental processes leading to the homogenisation of bentonite, as well as improving the capabilities for numerical modelling, are essential for assessing the hydromechanical evolution and the resulting performances of the engineered barriers.

The purpose of WP5 is to contribute to the improvement of numerical models. In this work package, several experiments are proposed to test numerical models, from small-size tests (centimetres) to field-scale experiments (several meters). The idea is to start with simple tests and progressively increase the complexity in terms of scale, coupled processes, and initial/boundary conditions.

This report summarizes the results obtained by the partners involved in WP5 on complex lab tests. Three tests, performed by Ciemat within task WP4, have been proposed. The specifications of the tests are defined in detail in report D5.3.1. and summarised in section 2 of this report. In each test, the sample is composed of two layers of bentonite materials: one layer is a compacted bloc, the other layer is made of bentonite pellets and powder. These two layers have different initial densities and water content. The hydration proceeds differently for each test, with respectively a constant flux in the pellets basis, a constant pressure in the pellets basis and a constant pressure at the block basis. These 3 lab tests contain a number of features that can be found in bentonite based EBS.

8 partners have done the numerical simulations: ULg, BGR, CU-CTU, LEI, Clay Technology, ICL, EPFL and Quintessa. In section 3, details about the model and numerical results of the partners are presented.

In section 4, the results obtained by all the partners are compared with the measurements. An analysis is proposed in several steps:

- the material parameters and initial value,
- the water intake and the water content evolution,
- the density and water content evolution and final value,
- the stresses evolution.

A general conclusion is proposed at the end of section 4.

2 Main feature of the tests – why it is relevant for Beacon

2.1 Introduction

CIEMAT carried out a series of hydration tests in isochoric cells to evaluate the evolution of bentonite during hydration, initially put in place in a heterogeneous way (Table 2-1). The half of the cell is filled with bentonite pellets with an average dry density close to 1.30 g/cm³ and the other part with a bentonite block with a dry density of 1.60 g/cm³. Hydration with deionised water takes place through the bottom.

Table 2-1 List of constant volume tests performed by CIEMAT

Test	Hydration	Duration (days)	*T* (°C)
MGR21	Constant pressure: 15 kPa	34	23.1±0.6
MGR22	Constant flow: 0.05 cm³/h	266	22.4±1.3
MGR23	Constant pressure: 15 kPa	210	22.6±1.5
MGR24	Constant pressure: 15 kPa	14	22.5±0.6
MGR25	Constant pressure: 15 kPa	76	22.7±1.1
MGR26	Constant flow: 0.05 cm³/h	132	23.6±1.2
MGR27	Constant pressure: 15 kPa	-	

Among a set of seven experiments, two of them have been selected to compare the experimental results with the models (MGR22 and MGR23). The main interest is that the tests are performed with the same conditions except the boundary conditions concerning the water supply. In one case, a constant pressure is imposed (MGR23) and in the other a constant flow is imposed (MGR22). In these two tests, pellets layer is placed in the lower part of the cell and the block in the upper part.

One test have been selected for predictive modelling (MGR27). The conditions of the test are similar to the previous one except that pellets layer is located in the upper part of the cell and block on the lower part.

2.2 Description of the tests

2.2.1 Equipment

Tests have been performed at constant volume in oedometer. It consists of a cylindrical body with base and an upper piston that may move in the cylinder (Figure 2-1, Figure 2-2). The body has an inner diameter of 10 cm and the length of the sample inside was 10 cm. The top and bottom of the sample were in contact with filter papers and ceramic porous discs connected to outlets. The cell was placed in a rigid frame that guaranteed the constant volume of the sample by hindering the displacement

of the piston. An external LVDT measured the potential axial displacements, whereas a 10-t load cell in the upper part of the frame measured the force developed by the specimen.
Water is supplied through the bottom of the sample via a porous disc.

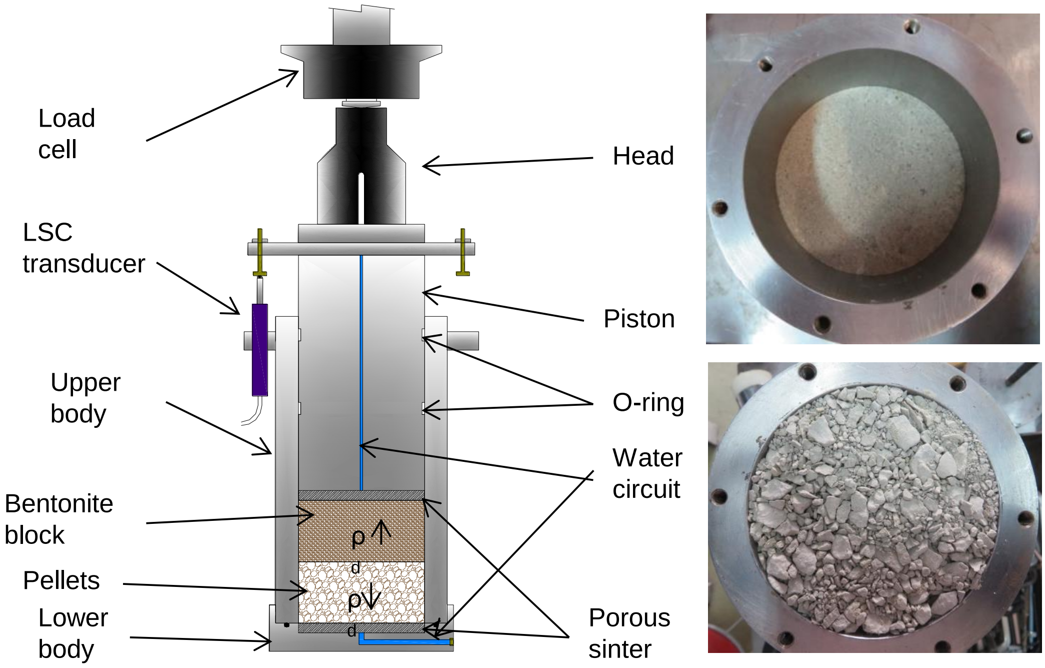

Figure 2-1: *Schematic representation of the MGR cell – MGR22 and MGR23 (left) and images of the block (upper right) and pellets (lower right)*

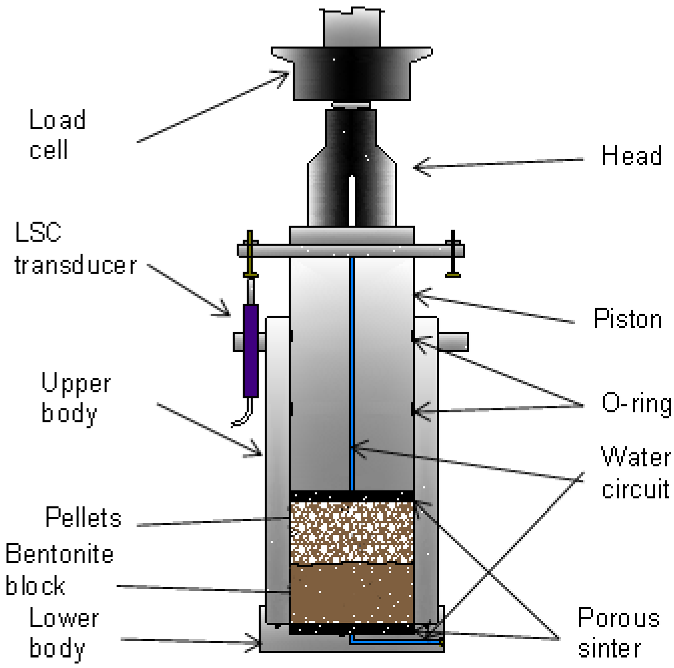

Figure 2-2: *Schematic representation of the MGR27 cell*

2.2.2 Preparation of specimens

The material used in all the tests was the FEBEX bentonite. The block part of the sample was compacted from the granulate material with its hygroscopic water content, which is 14%. The pellets were prepared in a factory for the EB project (ENRESA 2005). The bentonite was dried and milled in a three-step process to produce a fine grade powder with a water content of 3.3%. Later, a commercial plant with an in-line highly automated briquetting process produced coarse (>7 mm) and fine (0.4-2 mm) grained materials with dry densities of 2.11 and 2.13 g/cm3, respectively. These two grain size fractions were subsequently combined to fit a Fuller shape curve with a maximum diameter of 12.7 mm and a minimum diameter of 0.425 mm, in order to reduce segregation.

The bentonite block was directly compacted inside the cell and the pellets were poured on it and carefully shaken as necessary to get the target density. Depending of the case, the cell was overturned (MGR22, 23) or not (MGR27). Initial characteristics of the two layers are given in Table 2-2 for tests MGR22 and MGR23.

Table 2-2 **Initial characteristics of MGR22 and MGR23 tests**

	***w* (%)**	**h (cm)**	**ρ_d (g/cm^3)**	**S_r (%)**	***w* (%)**	**h (cm)**	**ρ_d (g/cm^3)**	**S_r (%)**
Test	***MGR22***				***MGR23***			
Pellets	9.9	5.04	1.28	25	3.5	5.00	1.30	9
Block	13.6	4.94	1.61	55	14.2	4.98	1.60	56
Total[b]	11.9	9.98	1.45	37	9.4	9.98	1.45	29

Initial characteristics of the two layers are given in Table 3-3 for tests MGR27.

Table 2-3 **Initial characteristics of MGR27 tests**

	***w* (%)**	**h (cm)**	**ρ_d (g/cm^3)**	**S_r (%)**
Test	**MGR27**			
Pellets	3.5	5.00	1.30	9
Block	14.2	4.98	1.60	56
Total	9.4	9.98	1.45	29

2.2.3 Test procedure

The water intake took place through the bottom surface. For MGR22 test, a low constant flow is imposed simulating a continuous contribution of water representative of Grimsel granite conditions. For MGR23 test, a constant pressure is imposed simulating reduced water intake conditions representative of Opalinus clay in Mont Terri (see Table 2-4).

Table 2-4 Conditions of hydration for each test

Test	Hydration	*T* (°C)
MGR22	Constant flow: 0.05 cm³/h	22.4±1.3
MGR23	Constant pressure: 14 kPa	22.6±1.5
MGR27	Constant pressure: 14 kPa	

In the first case (MGR22), the water intake was measured with an automatic volume change apparatus and in other cases (MGR23, MGR27) with a pressure/volume controller. During hydration the top outlet remained open to atmosphere and the pressure exerted by the material, the sample deformation and the water intake were measured and automatically recorded. The tests were performed at laboratory temperature.

At the end of the tests, the bentonite was subsampled to determine water content, dry density and pore size distribution. The blocks from MGR tests were sliced in 6 horizontal levels (3 for pellets and 3 for block).

2.2.4 Parameters

All parameters for this test can be found in D5.2.1 report from task 5.2 and in Hoffman et al, 2007.

2.2.5 Results for test MGR22 and MGR23

3 types of results are available for the two tests:

- the water intake by the sample function of time
- the swelling pressure measured on the top of the sample.
- The water content and dry density measured in subsamples as a function of the distance to the hydration surface.

Final characteristics of the samples are given in Table 2-5.

Table 2-5 **Final characteristics of MGR tests**

	w (%)	ρ_d (g/cm³)	h (cm)	S_r (%)	*w* (%)	ρ_d (g/cm³)	h (cm)	S_r (%)
Test	***MGR22***				***MGR23***			
Pellets	35.3	1.35	4.79	95	35.7	1.34	4.84	95
Block	30.7	1.51	5.27	106	31.1	1.51	5.29	107
Total	32.7	1.43	10.06	100	32.7	1.43	10.12	100

2.2.6 Results for test MGR27

No results have been given in the specifications for this test. It was expected some blind predictions from the partners. Details concerning MGR27 test will be available in the final deliverable from WP4 (D4.3) and in the paper from Villar et al., 2021. In the present document, the evolution of axial swelling pressure and water intake (Figure 2-3) as well as the final characteristics of the materials are given as basis for comparison (Table 2-6).

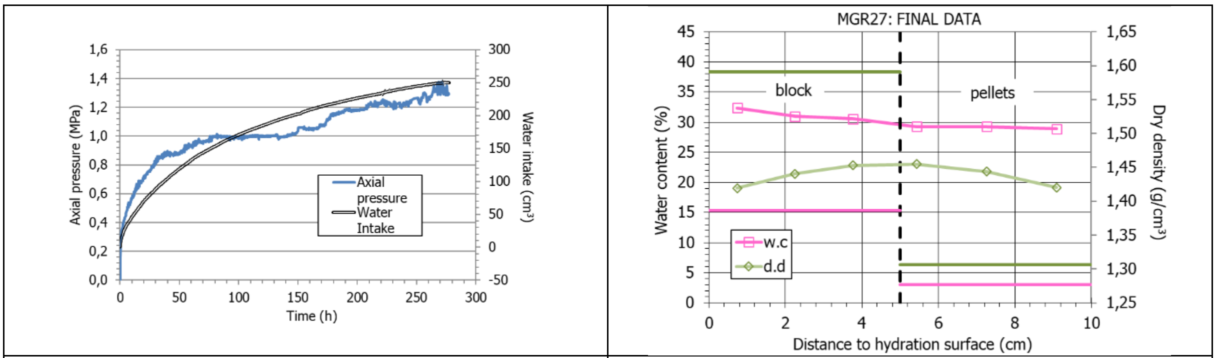

a b

Figure 2-3 *(a) swelling pressure and water intake, (b) initial and final water content and dry density for MGR27 test*

Table 2-6 Final characteristics of MGR27 test

	w (%)	**ρ_d (g/cm³)**	**h (cm)**	**S_r (%)**
Test	**MGR27**			
Pellets	32.3	1.434	4.563	98.7
Block	30.0	1.454	5.47	94.4
Total	31.01	1.44	10.02	96.4

3 Results

3.1 ULg

3.1.1 Description of the models

The constitutive model used by ULg to describe the behaviour of the FEBEX bentonite is presented in the Beacon deliverable D3.2 developed within the WP3 of the BEACON project.

Its development has been mostly based on the BBM model and on its improvements (Dieudonné). The model is formulated in the framework of the net stress, that is linked to the mechanical strains.

The water retention and transfer model has been developed during the Dieudonné thesis and are based on a double porosity partition.

The complete description is planned to be reported in the deliverable D3.3 of the WP3, including its implementation in the Finite Element code Lagamine (Charlier 1987, Collin 2003), which allows the numerical analysis of non-isothermal multiphase flow in deformable media.

3.1.2 Geometry and discretization

The MGR tests consist in a series of hydration tests in isochoric oedometer cell. Quantitative information is provided in order to evaluate possible bentonite heterogeneities sources. The considered oedometer cell is 10 cm high with 10 cm diameter. Each experimental test considers the combination of pellets and compacted block of Febex bentonite. The oedometer cell are filled with Febex bentonite pellets presenting dry density equal to ρ_d~1.30 Mg/m^3 and Febex compacted block with dry density equal to ρ_d~1.60 Mg/m^3, whose initial dry densities and structures noticeably differ. (Figure 3-1).

The numerical bentonite samples consist in 800 eight-noded isoparametric elements representing the bentonite (400 for the pellets and 400 for the compacted block). The problem is assumed bidimensional and oedometer conditions are considered [Figure 3-2].
The strong heterogeneity of the pellets-mixture material is well-recognized, but for sake of simplicity, in this modelling strategy, the pellets layer is considered homogeneous, presenting the same hydro-mechanical properties and state in the entire domain, as well as bentonite block layer.
An interface element is modelled with 40 3-noded isoparametric elements in order to reproduce the interaction between the bentonite materials and wall of the cell (green line Figure 3-2). For further details, refer to (Cerfontaine, et al., 2015).

For tests MGR21, 22, 23 and 24 the pellet layer is placed on the bottom part of the sample in contact with the wetting surface and the block part in the upper part of the sample. Test MGR27 considers the block part on the bottom of the sample in contact with the wetting surface and the pellet part on the top (the conditions are inverted with respect to the other tests).

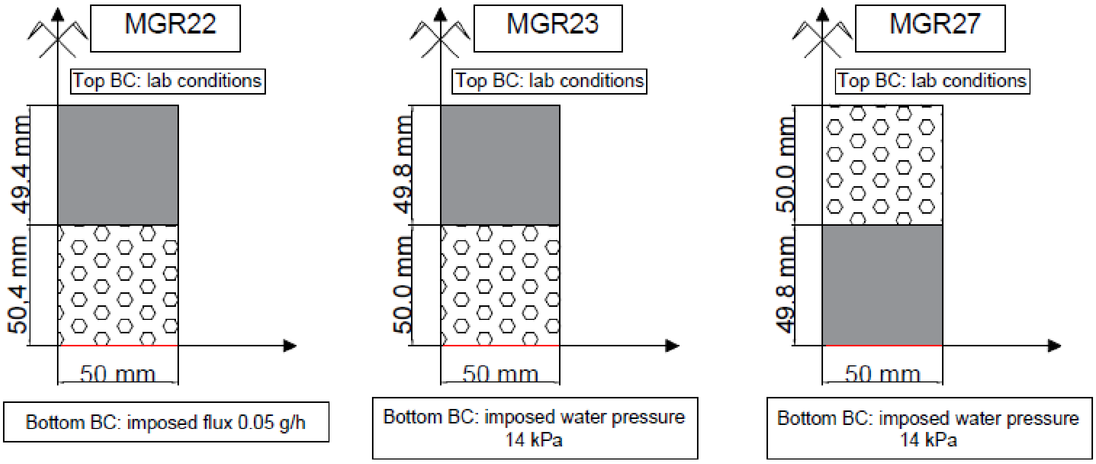

Figure 3-1: *Characteristics of the samples*

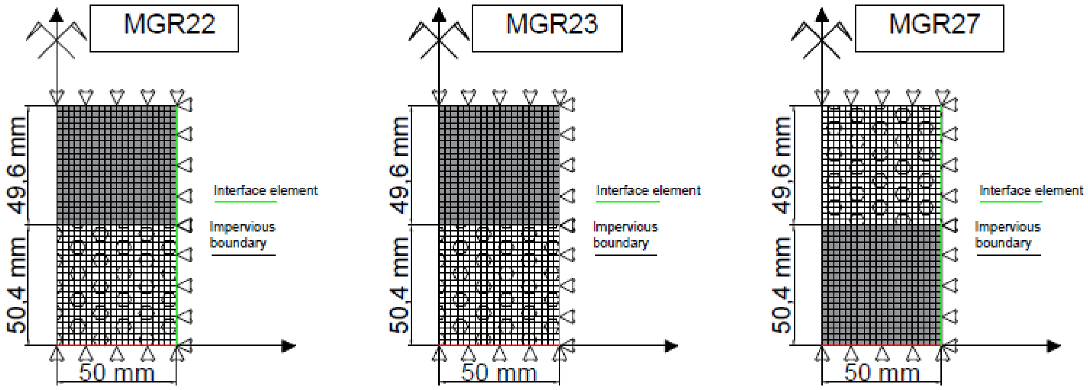

Figure 3-2: *Boundary conditions of the model*

3.1.3 Input parameters

BBM mechanical model

The Barcelona Basic Model (Alonso, et al., 1990) is adopted to model the mechanical behaviour of the bentonite Febex blocks and pellet mixture. The mechanical parameters for the Febex blocks compacted to a dry density ρ_d=1.7 Mg/m^3 (Table 3-1) are calibrated in (Dieudonne, 2016) (Figure 3-3) in order to reproduce the experimental results obtained by (Lloret, et al., 2002) (Figure 3-4 and Figure 3-5).

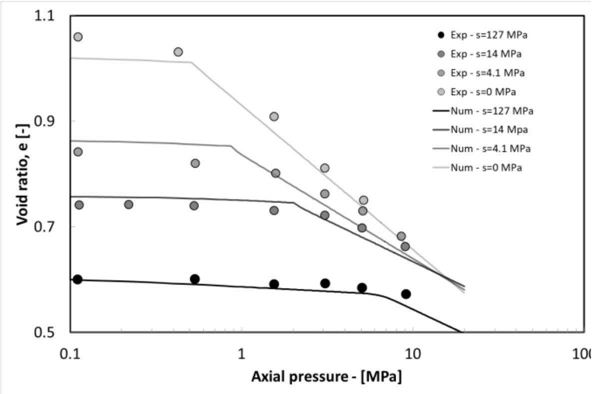

Figure 3-3: *Controlled-suction oedometer tests on Febex bentonite. Comparison between experimental data* ***(Lloret, et al., 2002)*** *and model responses on loading paths*

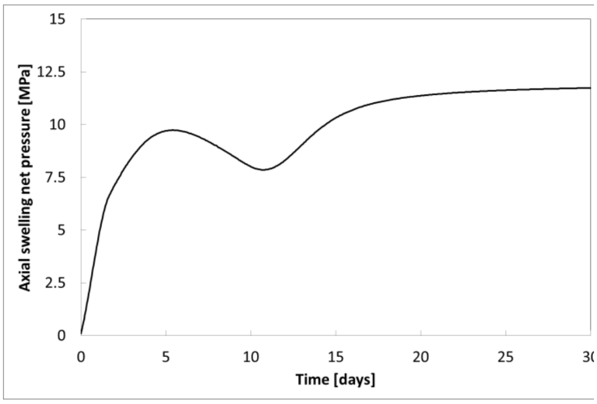

Figure 3-4: *Numerical results for the modelling of the experimental campaign presented in* ***(Villar, et al., 2009)***

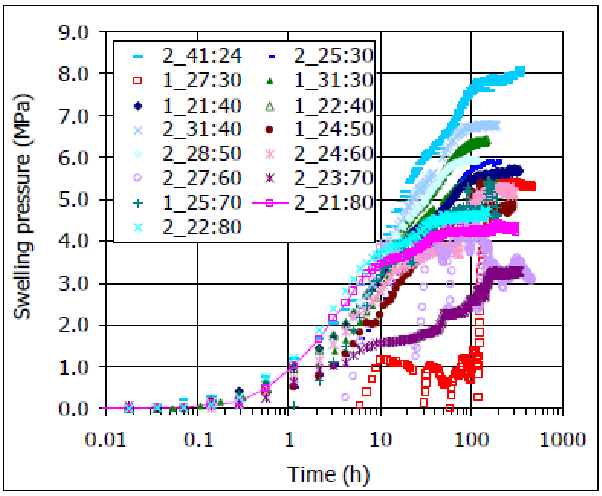

Figure 3-5: *Evolution of swelling pressure in infiltration tests performed at different temperatures (indicated in °C after the test reference) in FEBEX samples compacted at nominal dry density 1.7 g/cm³ obtained in* ***(Villar, et al., 2009)***

Since the Barcelona Basic Model overestimates the swelling pressure when low level of suction is reached, the elastic suction swelling modulus κ_s is depending on the average stress in order to overcome this limitation and is calibrated in order to reproduce the experimental data (Figure 3-5).

The numerical results concerning the compacted blocks material (Figure 3-4) reproduce quite well the maximum value of swelling pressure.

The mechanical parameters for the Febex pellet mixture of ρ_d=1.35 Mg/m³ are selected in agreement with (Hoffman, et al., 2007). The calibrated values are reported in Table 3-1.

The dry density bentonite initial values of the following tests are not exactly the same as the ones calibrated in these experimental campaigns, nevertheless they are very similar (ρ_d=1.60 Mg/m³ instead of ρ_d=1.70 Mg/m³ *for the block and* ρ_d=1.28 Mg/m³ instead of ρ_d=1.35 Mg/m³ *for the pellets).*

Table 3-1 Mechanical parameters selected for the bentonite Febex blocks and pellets mixture

			Blocks	Pellets mixture
ρ_d	[Mg/m^3]	Dry density	1.60	1.28
κ	[-]	Elastic compressibility coefficient for changes in mean net stress	0.012	0.074
κ_s	[-]	Elastic compressibility coefficient for changes in suction	0.12	0.075
α_p	[-]	Parameter controlling the stress dependency of the swelling strain for change in suction	4.4×10^{-8}	3×10^{-6}
p_0*	[MPa]	Preconsolidation pressure for saturated state	1.6	0.65
p_c	[MPa]	Reference pressure controlling the shape of the LC curve	0.395	0.325
$\lambda(0)$	[-]	Slope of the saturated virgin consolidation line	0.12	0.20
r	[-]	Parameter defining the minimum soil compressibility	0.55	0.70
ω	[MPa^{-1}]	Parameter controlling the soil stiffness	0.25	0.008
c(0)	[MPa]	Cohesion in saturated conditions	0	0
k	[-]	Parameter controlling the increase of cohesion for increase in suction	0.0046	0.0046
φ	[°]	Friction angle	20	26
ν	[-]	Poisson ratio	0.25	0.35

Double porosity hydraulic model

For the hydraulic behaviour of both materials, the double porosity formulation with microstructure evolution and dry density dependence proposed and calibrated by (Dieudonne, 2016) is selected. The hydraulic parameters and the obtained water retention curve in constant volume conditions are presented respectively in Table 3-2 and Figure 3-6.

Table 3-2 Parameters of the water retention curve model

e_{m0}	[-]	Microstructural void ratio for the dry material	0.35
β_0	[-]	Parameters quantifying the swelling potential of the aggregates	0.15
β_1	[-]		0.35
C_{ads}	[MPa^{-1}]	Parameter associated to the desaturation rate of the soil	0.0028
n_{ads}	[-]	Parameter controlling the WRC curvature in the high suction range	0.78
n	[-]	Material parameters	3
m	[-]		0.15
A	[MPa]	Parameter controlling the dependence of the air-entry pressure on the macrostructural void ratio	0.24

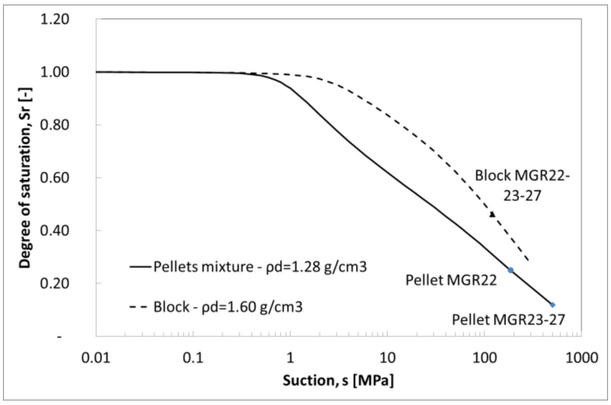

Figure 3-6: *Water retention curves for constant volume conditions predicted by* ***(Dieudonne, 2016)*** *for Febex bentonite of ρ_d=1.6 cm/g^3 and ρ_d=1.28 g/cm^3 and initial simulations states*

The parameters for the water permeability evolution (Table 3-3) were calibrated by best-fitting the responses of the water intake time evolution for the 2 different assembly types on test MGR23. Consequentially, the model is validated by comparing the swelling pressure kinetics and final dry density and water content distributions with all the other tests.

Table 3-3 Parameters of the permeability evolution model

		Test	Pellets	Block
C_k	[m^2]	Reference permeability	1.8 ×10-20	1.8 ×10-20
expm	[-]	Model parameters	1.5	0.4
expn	[-]		0.2	0.4
γ	[-]	Parameter controlling the evolution of relative permeability	3	3.4

Interface element

An interface element is modelled in order to reproduce a displacement constraint for the bentonite in the normal direction at the place of the cell wall and its interaction with it. For further details concerning the interface element, refer to (Cerfontaine, et al., 2015).
The longitudinal and transversal transmissivity is set equal to 1×10^{-99} (i.e. there is no water exchange between the interface and the bentonite).
In this modelling strategy, the total stress formulation is selected for the mechanical constitutive model of the interface element. The reason of the use of the total stress formulation instead of the effective stress one is explained.
A typical effective stress formulation reads:

$$\sigma = \sigma' - p \qquad \textbf{3-1}$$

Where p can represent the suction or the pore water pressure. Therefore, when there is negative pore water pressure (i.e. suction), the "effective" stress is higher with respect to the total one. The Mohr Coulomb criterion implemented for the interface element reads:

$$\tau \leq p_N tan\phi + c \qquad \textbf{3-2}$$

Consequentially, when the effective stress formulation is used in an un-saturated state, the interface presents a certain resistance, which is proportional to the suction value in the corresponding element.
Therefore, the suction in the interface would be high and would cause a high resistance to the sliding. For instance, considering a suction equal to 66 MPa multiplied by the friction coefficient 0.05, it could give a resistance equal to 3.3 MPa (still higher than the developed swelling pressure in the simulation).

Table 3-4 Interface mechanical properties

Friction angle	$\boldsymbol{\varphi}$	[°]	20
Friction coefficient	$\boldsymbol{\mu}$	[-]	0.360
Cohesion	$\boldsymbol{c'}$	[MPa]	0

3.1.4 Initial and boundary conditions

Constant volume conditions are assumed imposing vertical zero-displacement condition on the top and bottom ends of the sample and horizontal zero displacement conditions on the vertical boundary representing the cell wall (Figure 3-2). On the interface, which is defined on the lateral boundary of the domain, the bentonite can slide during the deformation (green line Figure 3-2).
In test MGR22, the pellets mixture presents an initial suction equal s=185 MPa and a corresponding initial saturation Sr=25% (water content w=10%), whereas the blocks report an initial suction value equal to s=80 MPa and an initial saturation Sr=55% (water content w=13.6%)

In test 24, 23 and MGR27, the pellets mixture presents an initial suction equal s=500 MPa (according to the selected water retention model) and a corresponding initial saturation Sr=12% (water content w=4.9%), whereas the blocks report an initial suction value equal to s=80 MPa and an initial saturation Sr=55% (water content w=13.6%).
In test MGR21, the pellets mixture presents an initial suction equal s=200 MPa (according to the selected water retention model) and a corresponding initial saturation Sr=22% (water content w=9.8%), whereas the blocks report an initial suction value equal to s=80 MPa and an initial saturation Sr=55% (water content w=13.6%).
The hydration of the samples is provided from the bottom end in different methods [red line Figure 3-2]. MGR22 considers constant water injection equal to 0.049 g/h occurring between the 10th and the 220th days of the simulation time. Tests MGR21, 24, 23 and MGR27 consider pressure evolution from -500 MPa for test MGR23 and 24, -200 MPa for test MGR21 and -80MPa for MGR27 to 0.014 MPa (0.014 MPa pore water pressure) occurring in 1000 seconds.
All the samples are subjected to an initial confining stress values of 0.10 MPa axially (vertically) and 0.10 MPa radially (horizontally).

3.1.5 Results MGR24, MGR21 and MGR23

This series of tests considers constant volume hydration tests, in which the hydraulic load is applied from the bottom face imposing constant water pressure equal to 14 kPa. The numerical samples are composed on the bottom part of a pellet layer 50.4 mm high presenting dry density equal to ρ_d=1.28 Mg/m^3 in direct contact with the hydration face and on the top of a bentonite compacted block layer 49.6 mm high presenting dry density equal to ρ_d=1.60 Mg/m^3.
These three tests present the same boundary conditions and initial dry density. They differ for the granulometry curve for the pelletized material of test MGR21 and in water content distributions because of the pellet layer water content of test MGR21. In this latter case, the pellet material presents an initial water content equal to w=10%, whereas tests MGR23 and MGR24 have water content in the pellet layer equal to w=4.9%. The tests also differ because they are stopped at different saturation stages allowing the analysis of transient hydro-mechanical states.
Figure 3-7 shows the total swelling pressure evolution comparison between the experimental results and numerical predictions for tests MGR21, 23 and 24. The experimental swelling pressure results refer to the top axial pressure measurement. For sake of completeness, the numerical predictions report axial total swelling pressure on the top and bottom faces and radial measurements at z=25 mm from the wetting face (i.e. at the centre of the pellet layer) and at z=75 mm (i.e. at the centre of the block layer).
The swelling pressure numerical results refer to the configuration of MGR23 test (pellet layer suction equal to s=500 MPa, differently from MGR21, in which pellet layer suction is equal to s=200 MPa). The swelling pressure results of test MGR21 are in general 5% lower with respect to all the measurements of tests MGR23 and 24 confirming that the block material initial state is the main responsible for the development of the swelling capacity of the sample and that the initial state of the pellets layer plays a minor role.
Firstly, it can be observed that the top and bottom numerical axial swelling pressures differ of about 1 MPa consistently with the hypothesis of friction development at the cell wall. The top axial numerical swelling pressure reproduces remarkably well the experimental initial pressure development for all the analysed cases. As well as the

initial linear pressure development, the transient phase, with the abrupt swelling pressure development rate change and final stabilisation, is very nicely reproduced for test MGR23.

The permeability law evolution for pellets mixtures and block layer has been calibrated on water intake evolution for test MGR23 (Figure 3-8). Due to this, apart from the experimental plateau occurring between the 5th and 25th days, the water intake evolution is nicely reproduced as well as the final state. Good results are obtained also for test MGR24, which presents the same initial state. Less good correspondence is found for the comparison between the experimental and numerical outcomes of test MGR21 (different initial state in the pellet layer). Figure 3-9 presents the comparisons between the experimental and numerical top axial swelling pressure as function of water intake. As already observed, the experimental plateau of test MGR23 is not reproduces numerically. Consequentially, the swelling pressure increase at zero water intake is not captured. Nevertheless, the numerical results are in good agreement for all the other phases. Discrepancies are also found for test MGR21 between the numerical and experimental results.

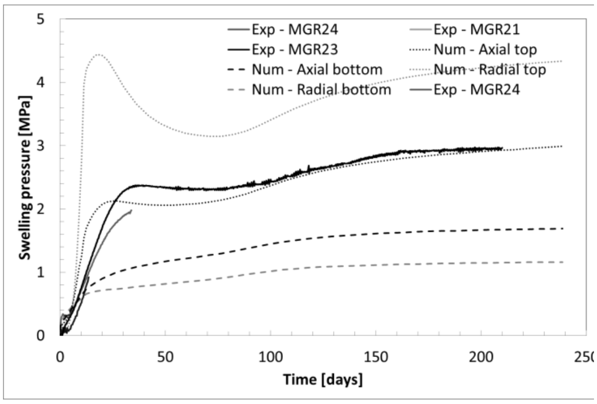

Figure 3-7: Total swelling pressure evolution for test MGR23, MGR21 and MGR24. Comparison between experimental results on the top axial measurement of the samples and numerical predictions at the axial top and bottom faces of the sample and radial measurement at the cell wall at z=25 mm and z=75 mm from the wetting surface

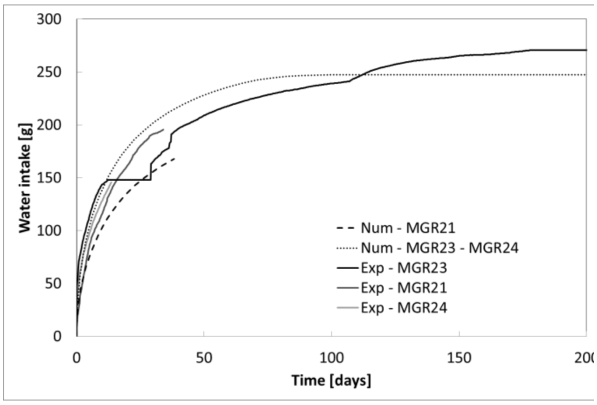

Figure 3-8: Water intake evolution for test MGR23, MGR21 and MGR24. Comparison between experimental results and numerical predictions

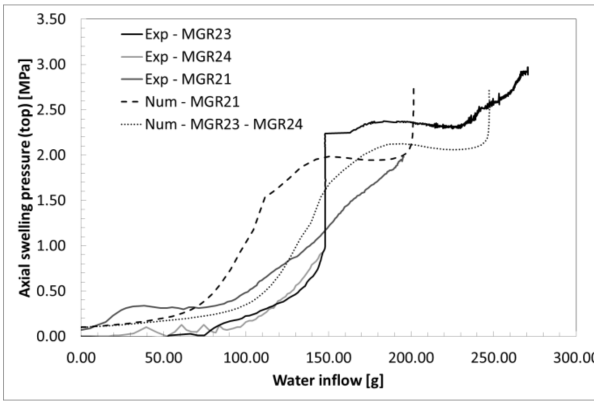

Figure 3-9: Top axial pressure function of water intake for tests MGR23, MGR21 and MGR23. Comparison between experimental results and numerical predictions

3.1.6 Day 14 – test MGR24

Intermediate results are presented in the following for test MGR24 (stopped at day 14). The numerical results are in perfect agreement for the water content, saturation and dry density experimental distributions (Figure 3-10, Figure 3-11 and Figure 3-12). Numerical results refer to the central part of the sample and to the border. Since very small differences are observed it can be concluded that at this stage the role of friction with the cell wall is negligible. The dry density profiles show that as the hydration begins the first wetted pellet material starts to swell compacting the pellet portion in contact with the block part. This pellet portion is also compacted due to the block swelling. The pellet and block dry densities at this stage are still very well noticeably far. Moreover, the two different layers due to the different initial dry density present different swelling capacity. Namely, the block presents a swelling capacity, which is higher than the pellet one. Experimental and numerical results both reproduce this phenomenon.

Figure 3-13 shows the permeability evolution through the sample. The pellet layer permeability decreases remarkably in the hydration direction due to the supposed micro-structure evolution. The permeability of the block layer does not change that evidently as assumed for the pellets.

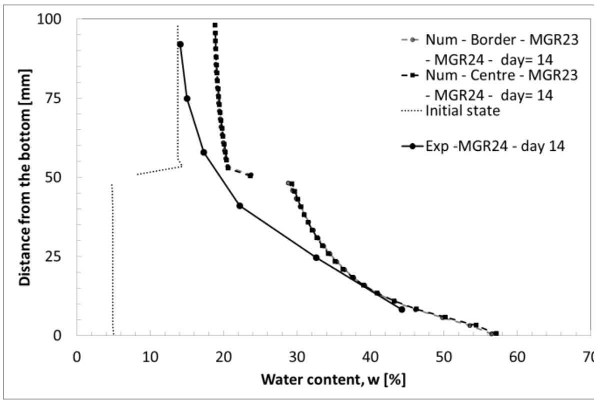

Figure 3-10: *Initial and* final water content along the samples of MGR24 test. Comparison between experimental results and numerical predictions.

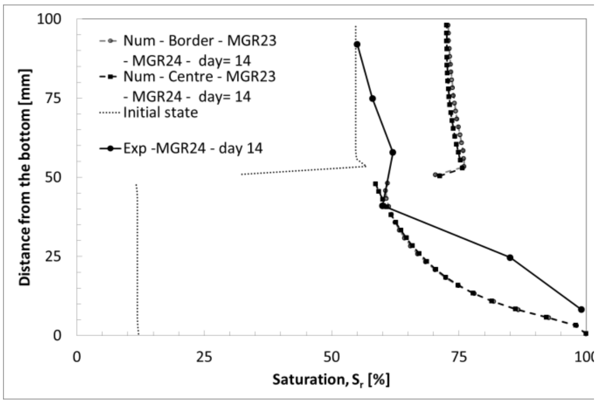

Figure 3-11: *Initial and* final saturation along the samples of MGR24 test. Comparison between experimental results and numerical predictions.

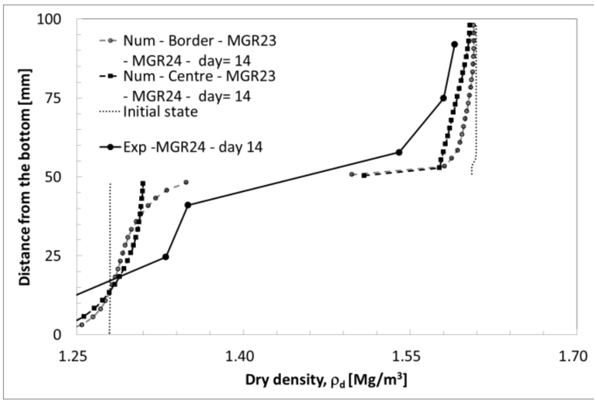

Figure 3-12: *Initial and* final dry density along the samples of MGR24 test. Comparison between experimental results and numerical predictions.

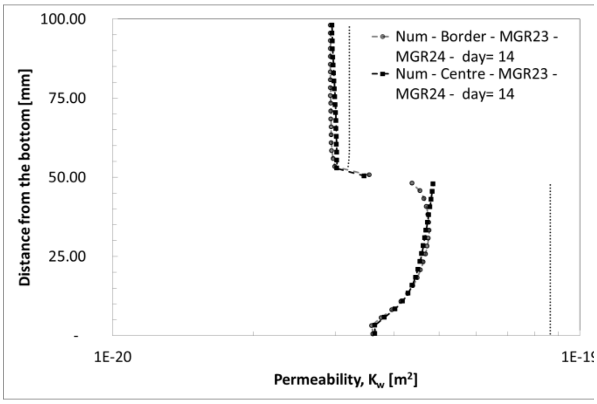

Figure 3-13: *Initial and final permeability* along the samples of MGR24 test. Numerical predictions.

3.1.7 Day 34 – test MGR21

Intermediate results are presented in the following for test MGR21 (stopped at day 34). The numerical results are in perfect agreement for the water content, saturation and dry density experimental distributions (Figure 3-14, Figure 3-15 and Figure 3-16). The pellet layer part presents a general compaction consistently with the general expansion of the compacted block swelling deformation. At this stage, the transition between the pellet and block layers is less abrupt with respect to the previous stage. Numerical results refer to the central part of the sample and to the border and differences are observed between numerical dry densities. It can be concluded that at this stage the role of friction with the cell wall is not negligible as in the previous phase. Figure 3-17 shows the permeability evolution through the sample. The pellet layer permeability continues to decrease in the hydration direction due to the supposed micro-structure evolution and compaction. The permeability of the block layer does not change that evidently as assumed for the pellets. The role of friction can be observed also in the permeability profiles.

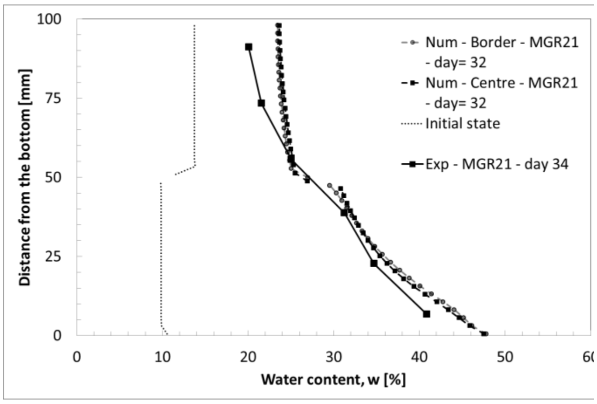

Figure 3-14: *Initial and* final water content along the samples of MGR21 test. Comparison between experimental results and numerical predictions.

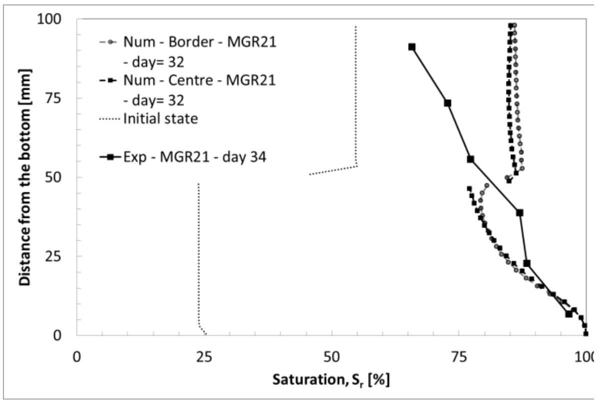

Figure 3-15: *Initial and* final saturation along the samples of MGR21 test. Comparison between experimental results and numerical predictions.

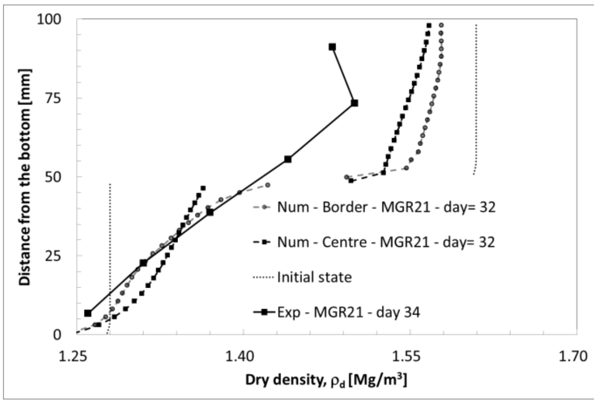

Figure 3-16: *Initial and* final dry density along the samples of MGR21 test. Comparison between experimental results and numerical predictions.

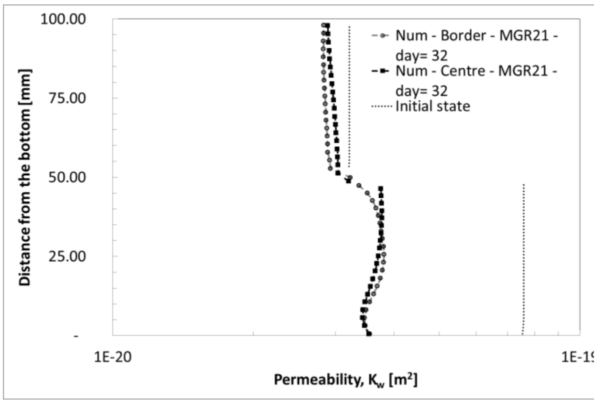

Figure 3-17: *Initial and final permeability* along the samples of MGR21 test. Numerical predictions.

3.1.8 Day 210 – test MGR23

Final results are presented in the following for test MGR23 (stopped at day 210). The numerical results are in good agreement for the water content, saturation and dry density experimental distributions (Figure 3-18, Figure 3-19 and Figure 3-20). The numerical results for water content distribution are higher in the pellets layer with respect to the experimental ones. This is related to the saturation distribution, which is 100% for the numerical simulation and lower for the experimental test. The pellet layer part presents a general compaction consistently with the general expansion of the compacted block swelling deformation, in good agreement with the experimental results. At this stage, the transition between the pellet and block layers is smooth (Figure 3-20). Numerical results refer to the central part of the sample and to the border and differences are observed between numerical dry densities. It can be concluded that at this stage the role of friction with the cell wall is remarkable. Figure 3-21 shows the permeability evolution through the sample. The pellet layer permeability is similar to the block part one, inversely related to the dry density distribution, this presenting a certain vertical gradient. Indeed, the lowest permeability is found for the highest corresponding dry density.

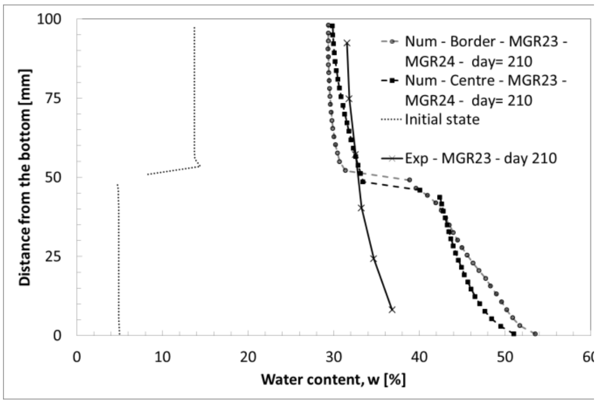

Figure 3-18: *Initial and* final water content along the samples of MGR23 test. Comparison between experimental results and numerical predictions.

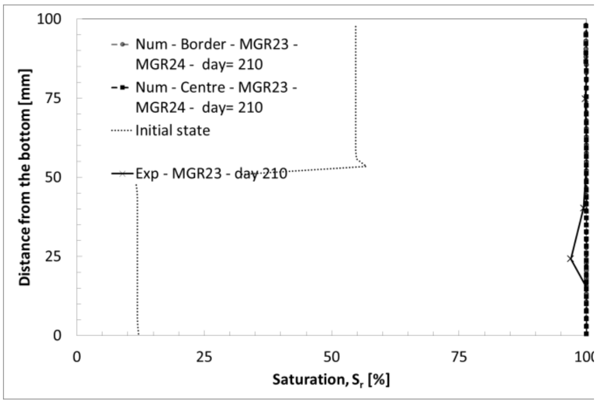

Figure 3-19: *Initial and* final saturation along the samples of MGR23 test. Comparison between experimental results and numerical predictions.

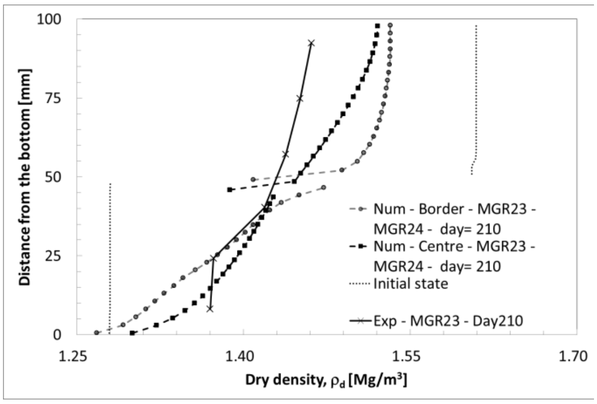

Figure 3-20: *Initial and* final dry density along the samples of MGR23 test. Comparison between experimental results and numerical predictions.

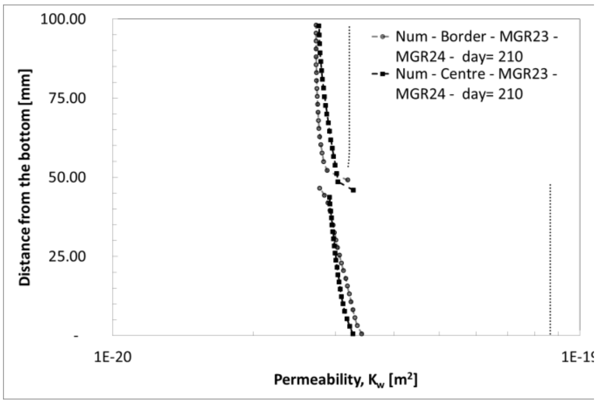

Figure 3-21: *Initial and final permeability* along the samples of MGR23 test. Numerical predictions.

3.1.9 Results MGR22

This test considers constant volume hydration tests, in which the hydraulic load is applied from the bottom face imposing constant water inflow equal to 0.05 g/h. The numerical sample is composed on the bottom part of a pellet layer 50.4 mm high presenting dry density equal to ρ_d=1.28 Mg/m³ in direct contact with the hydration face and on the top of a bentonite compacted block layer 49.6 mm high presenting dry density equal to ρ_d=1.60 Mg/m³, as for the previous cases.
This test differs from MGR23 and 24 for the granulometry curve of the pelletized material and in water content distributions because of the pellet layer water content

(which are equal to the ones of test MGR21). In this latter case, as for case MGR21, the pellet material presents an initial water content equal to w=10%, whereas tests MGR23 and MGR24 have water content in the pellet layer equal to w=4.9%.
Figure 3-22 shows the total swelling pressure evolution comparison between the experimental results and numerical predictions for test MGR22. The experimental swelling pressure results refer to the top axial pressure measurement. For sake of completeness, the numerical predictions report axial total swelling pressure on the top and bottom faces and radial measurements at z=25 mm from the wetting face (i.e. at the centre of the pellet layer) and at z=75 mm (i.e. at the centre of the block layer).
Firstly, it can be observed that the top and bottom numerical axial swelling pressures differ of about 1 MPa consistently with the hypothesis of friction development at the cell wall (as for tests MGR21, 23 and 24). The top axial numerical swelling pressure does not reproduce the experimental initial pressure development for the analysed case.
The transient phase, with the abrupt swelling pressure development rate change is reproduced
A very small pressure peak is observed in the pellet layer and partially transmitted to the block one. This is basically related to the establishment of water overpressure (Figure 3-24 and Figure 3-25, considering p_w=-s) due to the boundary conditions. The effective stress formulation adopted for the full saturated state causes this peak. The pressure peak is partially transmitted to the block part. As the pore overpressure is dissipated thanks to water transfer from the pellet to the block, the pressure decreases again. The top axial numerical swelling pressure at stabilisation is not as high as the experimental one because the block is not fully saturated, therefore further swelling capacity can be developed.
The axial swelling pressures as water inflow function do not correspond in the initial phase but they agree in the transient one.

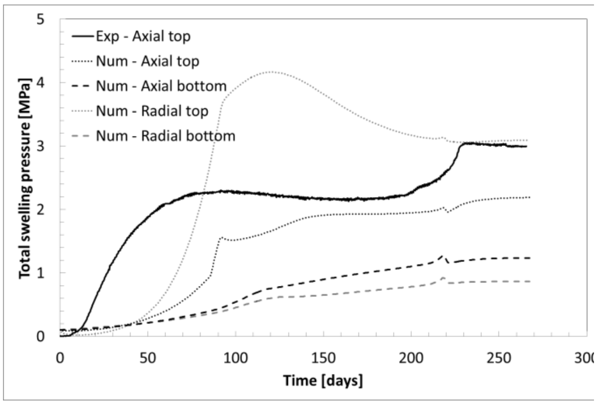

Figure 3-22: *Total swelling pressure evolution for test MGR22. Comparison between experimental results on the top axial measurement of the sample and numerical predictions at the axial top and bottom faces of the sample and radial at the cell wall at z=25 mm and z=75 mm from the wetting surface.*

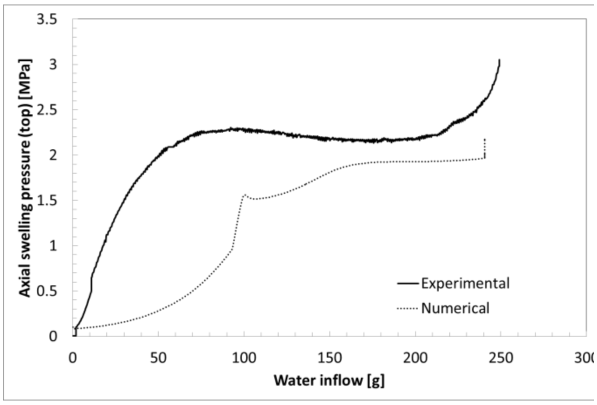

Figure 3-23: *Top axial pressure function of water intake for test MGR22. Comparison between experimental results and numerical predictions.*

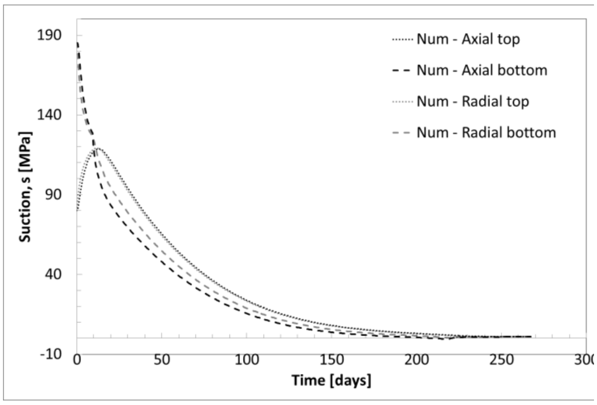

Figure 3-24: *Suction evolution for test MGR22. Comparison between numerical predictions at the axial top and bottom face of the sample and radial at the cell wall at z=25 mm (pellets) and z=75 mm (block) from the wetting surface.*

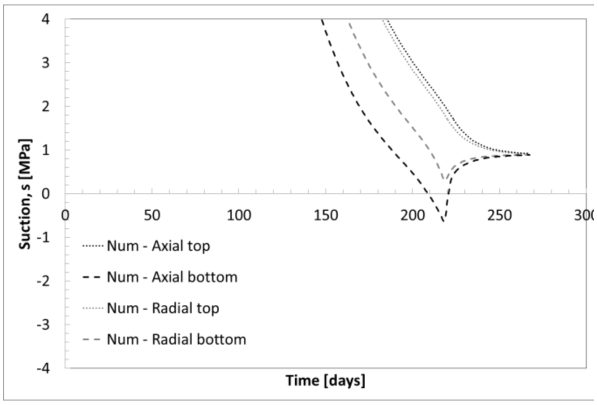

Figure 3-25: *Suction evolution for test MGR22. Comparison between numerical predictions at the axial top and bottom face of the sample and radial at the cell wall at z=25 mm (pellets) and z=75 mm (block) from the wetting surface (detail).*

Final results are presented in the following for test MGR22 (stopped at day 260). The numerical results are in good agreement for the water content, saturation and dry density experimental distributions (Figure 3-26, Figure 3-27 and Figure 3-28). The numerical results for water content distribution are higher in the pellets layer with respect to the experimental ones. This is related to the dry density distribution of the pellets, which is lower for the numerical results than in the experimental ones. The pellet layer part presents a general compaction consistently with the general expansion of the compacted block swelling deformation in good agreement with the experimental results. At this stage, the transition between the pellet and block layers is less smooth in the numerical results with respect to the experimental ones (Figure 3-28). Namely, it means that in the numerical simulations, the block has swollen less than expected.

Numerical results refer to the central part of the sample and to the border and evident differences are observed between numerical dry densities also in this case. It can be concluded that at this stage the role of friction with the cell wall is remarkable. Figure 3-29 shows the permeability evolution through the sample. The pellet layer permeability is similar to the block part one, inversely related to the dry density distribution, thus presenting a certain vertical gradient (less smooth than the one of test MGR23). Nevertheless, also in this case, the lowest permeability is found for the highest corresponding dry density.

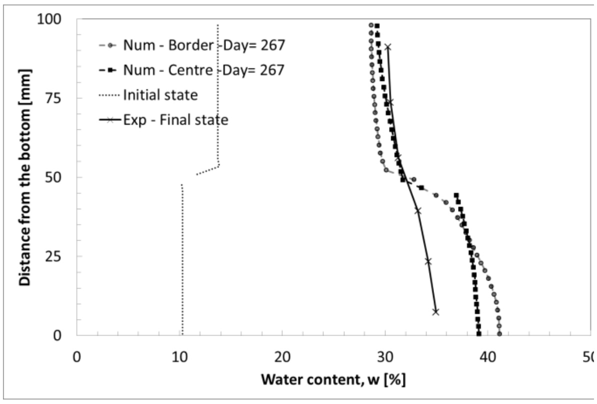

Figure 3-26: *Initial and* final water content along the samples of MGR22 test. Comparison between experimental results and numerical predictions.

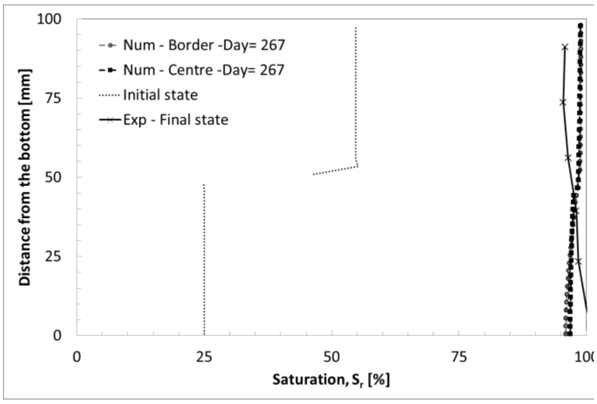

Figure 3-27: *Initial and* final saturation along the samples of MGR22 test. Comparison between experimental results and numerical predictions.

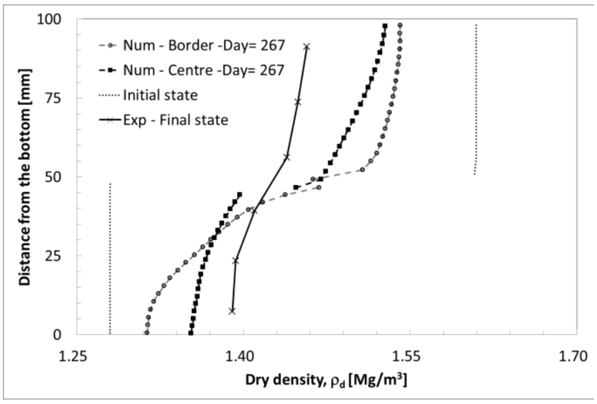

Figure 3-28: *Initial and* final dry density along the samples of MGR22 test. Comparison between experimental results and numerical predictions.

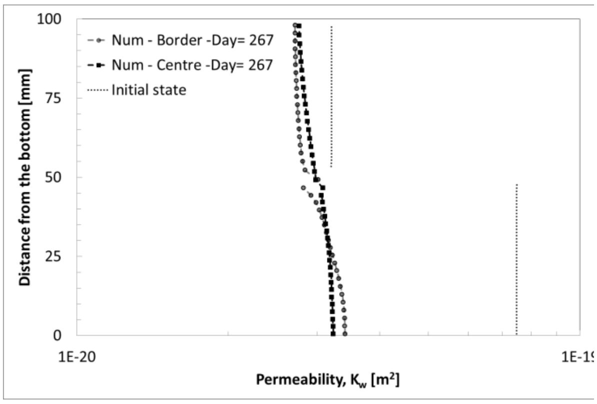

Figure 3-29: *Initial and* final permeability along the samples of MGR22 test. Numerical predictions.

3.1.10 Results MGR27

This test simulation considers constant volume hydration tests, in which the hydraulic load is applied from the bottom face imposing constant water pressure equal to 14 kPa. The numerical sample is composed on the bottom part of a bentonite compacted block layer 50.4 mm high presenting dry density equal to ρ_d=1.60 Mg/m^3 in direct contact with the hydration face and on the top part of a pellet layer 49.6 mm high presenting dry density equal to ρ_d=1.28 Mg/m^3 (the contrary with respect to tests MGR21, 22, 23 and 24).

Figure 3-30 shows the total swelling pressure evolution comparison between the experimental results of test MGR23 and numerical predictions for tests MGR27. The experimental swelling pressure results refer to the top axial pressure measurement. For sake of completeness, the numerical predictions report axial total swelling pressure on the top and bottom faces and radial measurements at z=25 mm from the wetting face (i.e. at the centre of the block layer) and at z=75 mm (i.e. at the centre of the pellet layer).

Firstly, it can be observed that the top and bottom numerical axial swelling pressures differ of about 1 MPa consistently with the hypothesis of friction development at the cell wall. The top axial numerical swelling pressure is much lower with respect to the bottom one (the contrary with respect to test MGR23).

In this simulation, the abrupt swelling pressure development rate change and final stabilisation already found in MGR23 top measurement is reported in the numerical bottom measurement with a slightly lower value. The numerical top axial swelling pressure is about 1.5 MPa.

The permeability law evolution for pellets mixtures and block layer has been calibrated on water intake evolution for test MGR23 (Figure 3-32). In this case, the Febex compacted block, which presents an initial lower permeability with respect to the pellet part, is in direct contact with the hydration source. Due to this, the water intake is slightly slower at the beginning. Nevertheless, the stabilisation time and the final water quantity are similar with respect to the one of case MGR23.

Figure 3-31 presents the comparisons between the experimental and numerical top axial swelling pressure as function of water intake. The numerical prediction of test MGR27 is completely different with respect to the other analysed case due to the material configuration. The swelling pressure increase with water is slower and the final value is smaller.

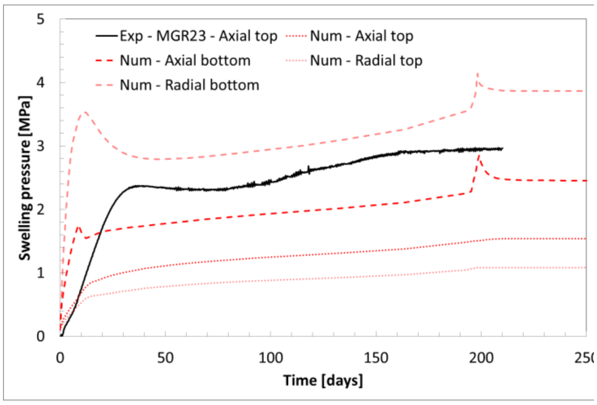

Figure 3-30: *Total swelling pressure evolution Comparison between experimental results on the top axial measurement of the sample of test MGR23 and numerical predictions at the axial top and bottom faces of the sample and radial measurement at the cell wall at z=25 mm and z=75 mm from the wetting surface for test MGR27.*

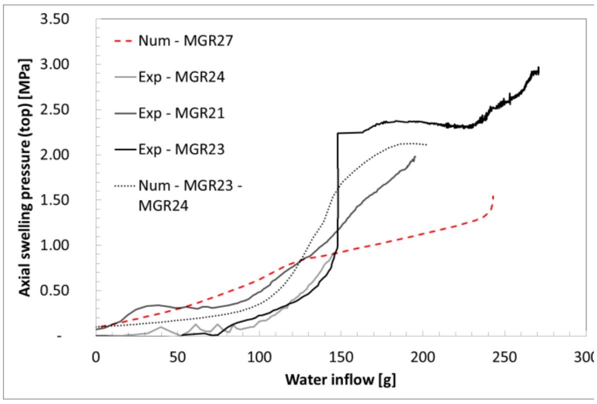

Figure 3-31: *Top axial pressure function of water intake for tests MGR23, MGR21 and MGR23. Comparison between experimental results and numerical predictions for tests MGR23, 24 and 27.*

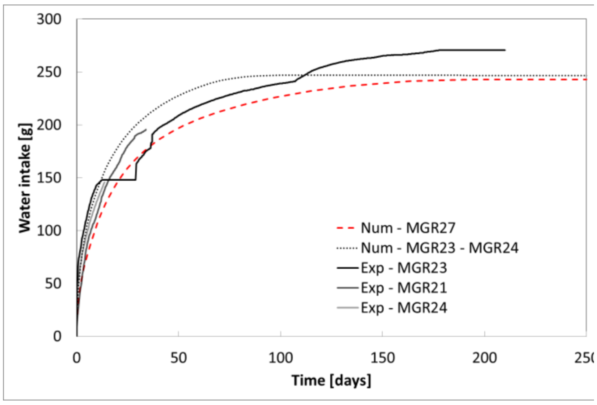

Figure 3-32: *Water intake evolution. Comparison between experimental results of tests MGR21, 22 and 23 and numerical predictions for tests MGR23, 24 and 27.*

Final results are presented in the following for test MGR23 and test MGR27 (analysed at day 210). The numerical prediction of MGR27 are described and compared to MGR23 ones.

MGR27 final water content distribution (Figure 3-33) is higher in the top pellet layer and lower in the bottom compacted block part (in contrast with numerical and experimental results of test MGR23) and directly correlated to the full saturated state and dry density distribution.

MGR27 dry density distribution (Figure 3-35) shows that in the bottom compacted block part the material placed closest to the wetting surface has swollen the most, whereas the following block material presents homogeneous dry density with almost no gradient.

The axial central part of the pellet layer seems like it has been uniformly compacted with a much higher dry density with respect to the initial state, similar to the

compacted block one. A possible dry density gradient is recorded on the border where the role of friction is particularly relevant.
Nevertheless, it is predicted that the densest material is found close to the central part of the sample.
Figure 3-36 shows the permeability evolution through the sample. The pellet layer permeability is similar to the block part one, inversely related to the dry density distribution. Also in this case, the lowest permeability is found for the highest corresponding dry density.

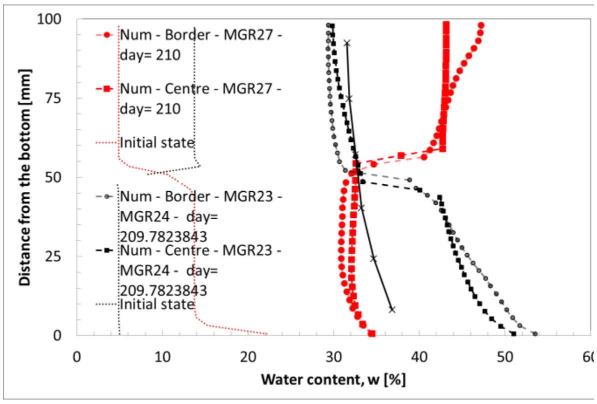

Figure 3-33: *Initial and* final water content along the samples. Comparison between experimental results of MGR23 test and numerical predictions of MGR23 and 27 tests.

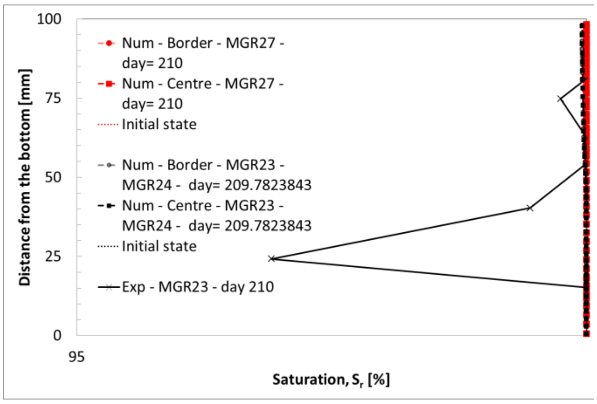

Figure 3-34: *Initial and* final saturation along the samples. Comparison between experimental results of MGR23 test and numerical predictions of MGR23 and 27 tests.

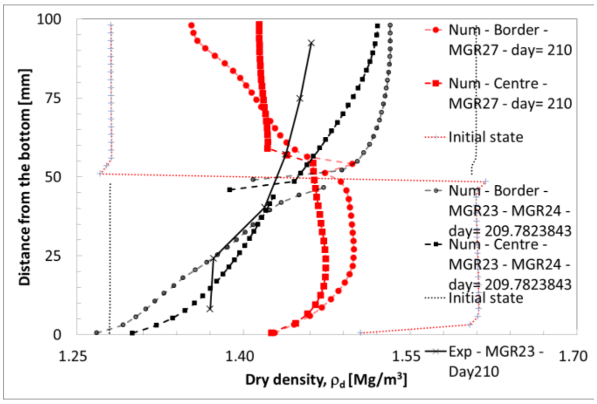

Figure 3-35: *Initial and final dry density along the samples Comparison between experimental results of MGR23 test and numerical predictions of MGR23 and 27 tests.*

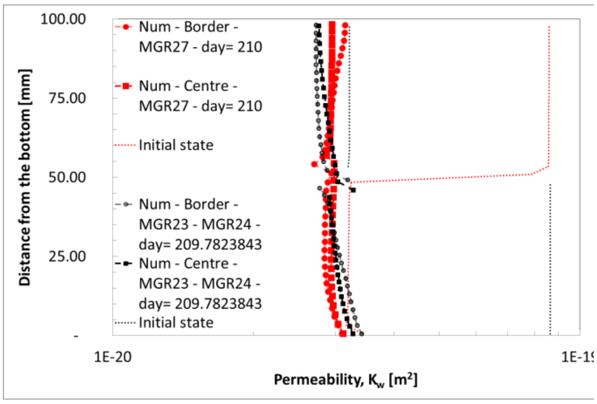

Figure 3-36: *initial and final permeability* along the samples of MGR23 and 27 tests. Numerical predictions.

3.1.11 Discussion

In this work, experimental tests performed by CIEMAT in the context of Beacon project have been numerically reproduced.
In addition, a blind prediction of constant volume hydration test of MGR27 configuration has been presented.
This work involved a preliminary calibration procedure with respect to the mechanical and hydraulic parameters.

The real initial state of the components has been taken in consideration for the analysis and the development of friction with the cell wall has been also considered.
The predictions of the numerical modelling of tests MGR21, 22, 23 and 24 provided remarkable correspondences with experimental results with respect to water intake and swelling pressure evolution, to intermediate states of water content, saturation and dry density and final ones, despite the different initial states, materials and boundary conditions.

3.2 CU/CTU

The tests were performed using the current version of the THM double-structure hypoplastic model for expansive clays, which has been updated in BEACON described in Deliverable 3.2. No special further adaptations/features were incorporated.

3.2.1 Geometry and discretization

The finite-element simulations were performed in SIFEL finite element code in axisymmetric condition. The domain was 50 mm wide and 100 mm high, approximately equal to the specifications. It was realised with 200 square elements, with a side of 0.5 mm; that is, 10x10 elements in each (block/pellet) subdomain. The thickness of the block and pellet layers was taken equal to half the height, that is 50 mm each.

3.2.2 Input parameters

The hypoplastic parameters were calibrated from experimental results on FEBEX bentonite, available in the BEACON deliverables and in the literature. In particular, we adopted swelling pressure results for different dry densities, constant volume water retention tests for different dry densities and oedometric swelling/compression tests at various values of total suction. All the experiments have been reported by Lloret et al. (2005). Experimental results along with model predictions are shown in Figure 3-37.

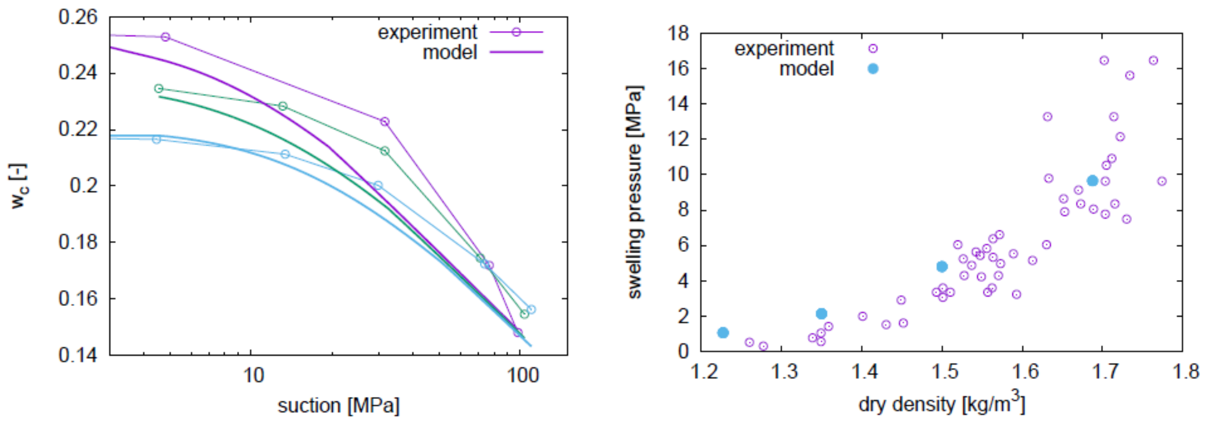

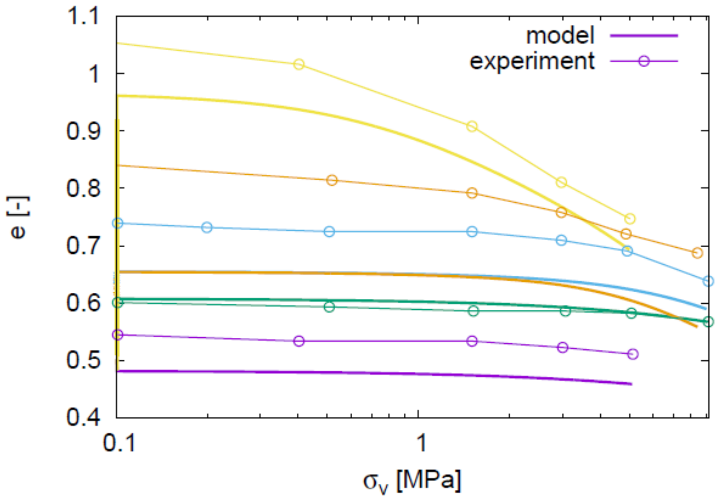

Figure 3-37 *Experimental results on FEBEX bentonite (Lloret et al., 2005)compared with model predictions adopted to calibrate model parameters used in this deliverable*

Model parameters which have been used in the analyses are indicated in Table 3-5.

Table 3-5 ***Model parameters used in simulations, calibrated using FEBEX experimental data by Lloret et al. (2005)***

Parameter	Unit	Value
φ_c	°	25
λ^*	–	0.14
κ^*	–	0.025
N	–	1.80
υ	–	0.25
n_s	–	0.012
l_s	–	-0.005
n_T	–	-0.07
l_T	–	0
m	–	0.3
α_s	$1/K$	0.00015
κ_m	–	0.075
s_r	kPa	-1000
e_{r0}^m	–	0.95
c_{sh}	–	0.100
s_{e0}	kPa	-2000
e_0^M	–	0.10
T_r	K	294
a	N/m	0.118
b	$N/(mK)$	-0.000154
a_e	–	0.75
λ_{p0}	–	0.55

Furthermore, values of permeabilities indicated in Table 3-6 were used. Note that we differentiated the values for the two sub-domains (block and pellets). The permeabilities have been specified by using back-analysis of the swelling pressure time-evolution curves, which lead to a lower permeability to the pellets in consideration of their higher internal dry density (despite the overall lower dry density of the assembly). In our models, we did not consider triple-structure of the pellet zone and we must note that the selected permeability is relevant for representation of swelling pressure evolution (which is controlled by pellet swelling), rather than to representation of water flow through the pellet zone (which is controlled by macropores between the pellets). In the simulations, we used constant value of permeability independent of total suction.

Table 3-6 Permeabilities of block and pellet zones used in simulations

$k_{pellets}$	m^2	$5 \cdot 10^{-21}$
k_{blocks}	m^2	$2 \cdot 10^{-20}$

3.2.3 Initial and boundary conditions

The initial suction values were chosen based on the initial water contents so as to be reasonable in the light of published experiments on the FEBEX bentonite (Figure 3-38).

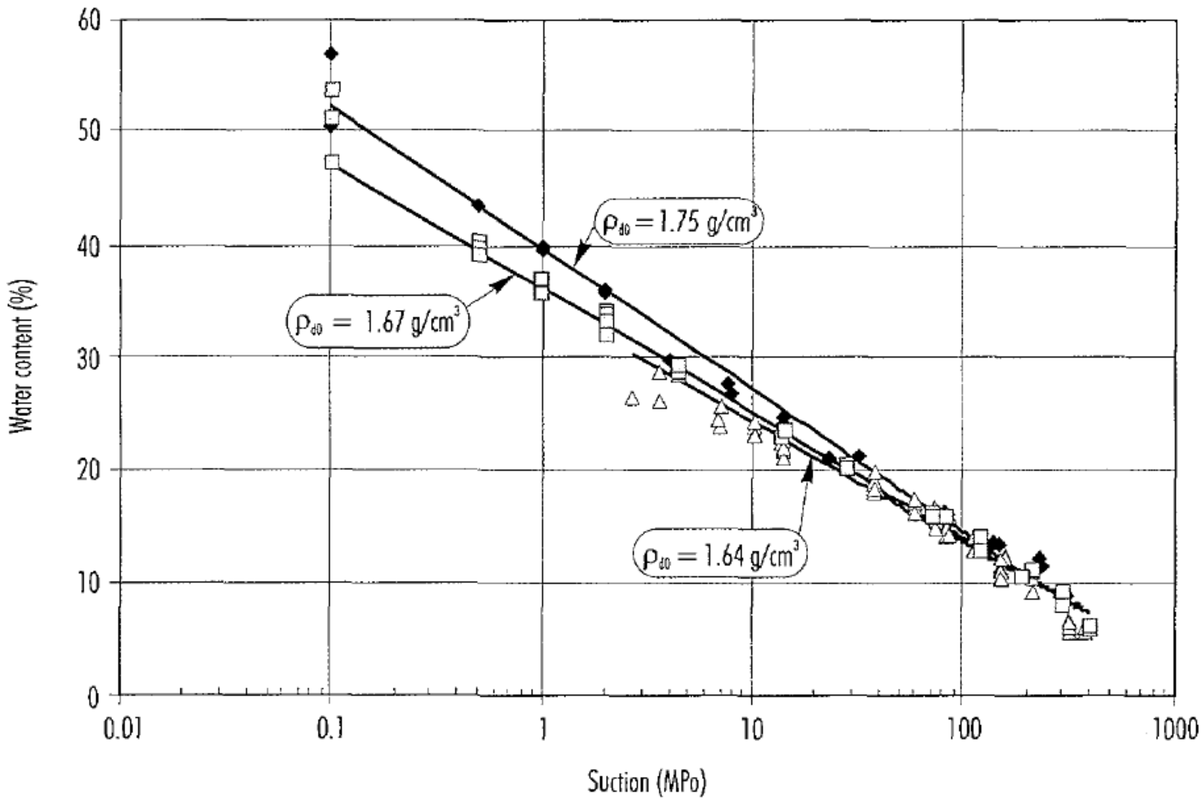

Figure 3-38: *Unconfined WRCs on FEBEX bentonite used for initial suction estimation (Fig. 2.8 from ENRESA, 2000)*

In fact, our calculations which were bound to experimental water retention curves (Figure 3-37) led either to an overestimation of the suction with unreasonable values (in the order of several GPa) or to an overestimation of the initial water content. In our simulations, we were considering initial suction as the initial condition and thus the initial water content has been somewhat over predicted (Table 3-7). Consequently, we also need a smaller water intake to reach saturation, which is reflected in smaller water flows.

Table 3-7 Initial conditions (suction and water content) used in simulations

		used value	*actual value*
$w_{0,pellets,MGR22}$	$-$	0.151	*0.100*
$w_{0,blocks,MGR22}$	$-$	0.178	*0.136*
$w_{0,pellets,MGR23}$	$-$	0.106	*0.034*
$w_{0,blocks,MGR23}$	$-$	0.178	*0.142*
$w_{0,pellets,MGR27}$	$-$	0.106	*0.034*
$w_{0,blocks,MGR27}$	$-$	0.178	*0.142*
$s_{0,pellets,MGR22}$	MPa	-100	
$s_{0,blocks,MGR22}$	MPa	-50	
$s_{0,pellets,MGR23}$	MPa	-300	
$s_{0,blocks,MGR23}$	MPa	-50	
$s_{0,pellets,MGR27}$	MPa	-300	
$s_{0,blocks,MGR27}$	MPa	-50	

As for the hydraulic boundary condition, we could not impose a constant water flow from the bottom of the domain as this option has not been available in SIFEL finite element package used in simulations. For that reason, we have specified a constant pressure at the bottom boundary, which was taken equal to 15 kPa in all tests. This value has been set such that the water flow has been well approximated over the experiment duration. However, by this procedure we have over predicted water flow at the beginning of the experiments.

3.2.4 Results MGR22

The Figure 3-39 shows the results of the simulation in terms of axial and radial stresses, evolution of dry density, and evolution of water content for MGR22.

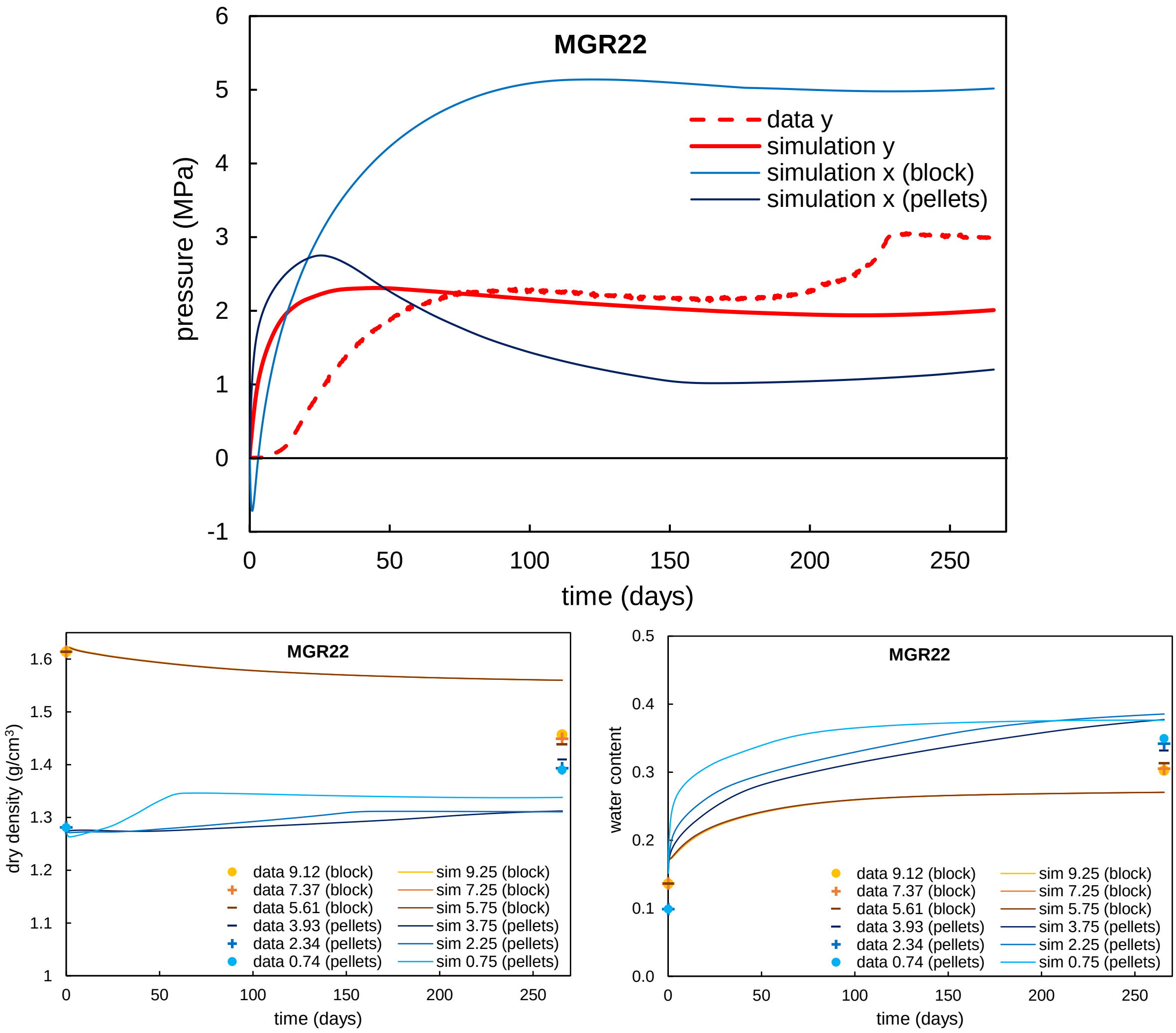

Figure 3-39: *Simulated results of test MGR22 compared with experimental results*

3.2.5 Results MGR23

The Figure 3-40 shows the results of the simulation in terms of axial and radial stresses, evolution of dry density, and evolution of water content for MGR23.

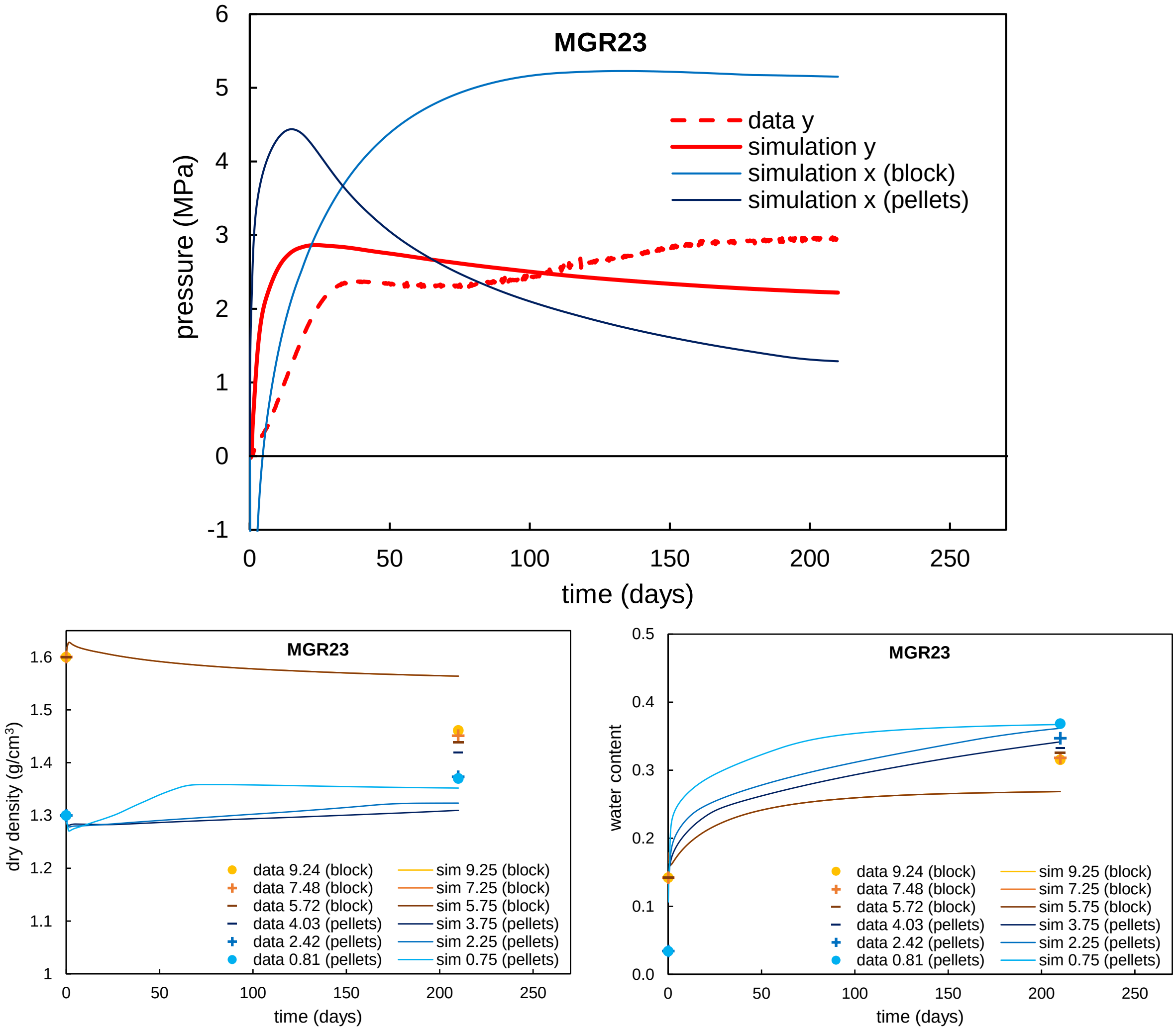

Figure 3-40: Simulated results of test MGR23 compared with experimental results

3.2.6 Results MGR27

The Figure 3-41 shows the results of the simulation in terms of axial and radial stresses, dry density, water content, void ratio, and degree of saturation for MGR27.

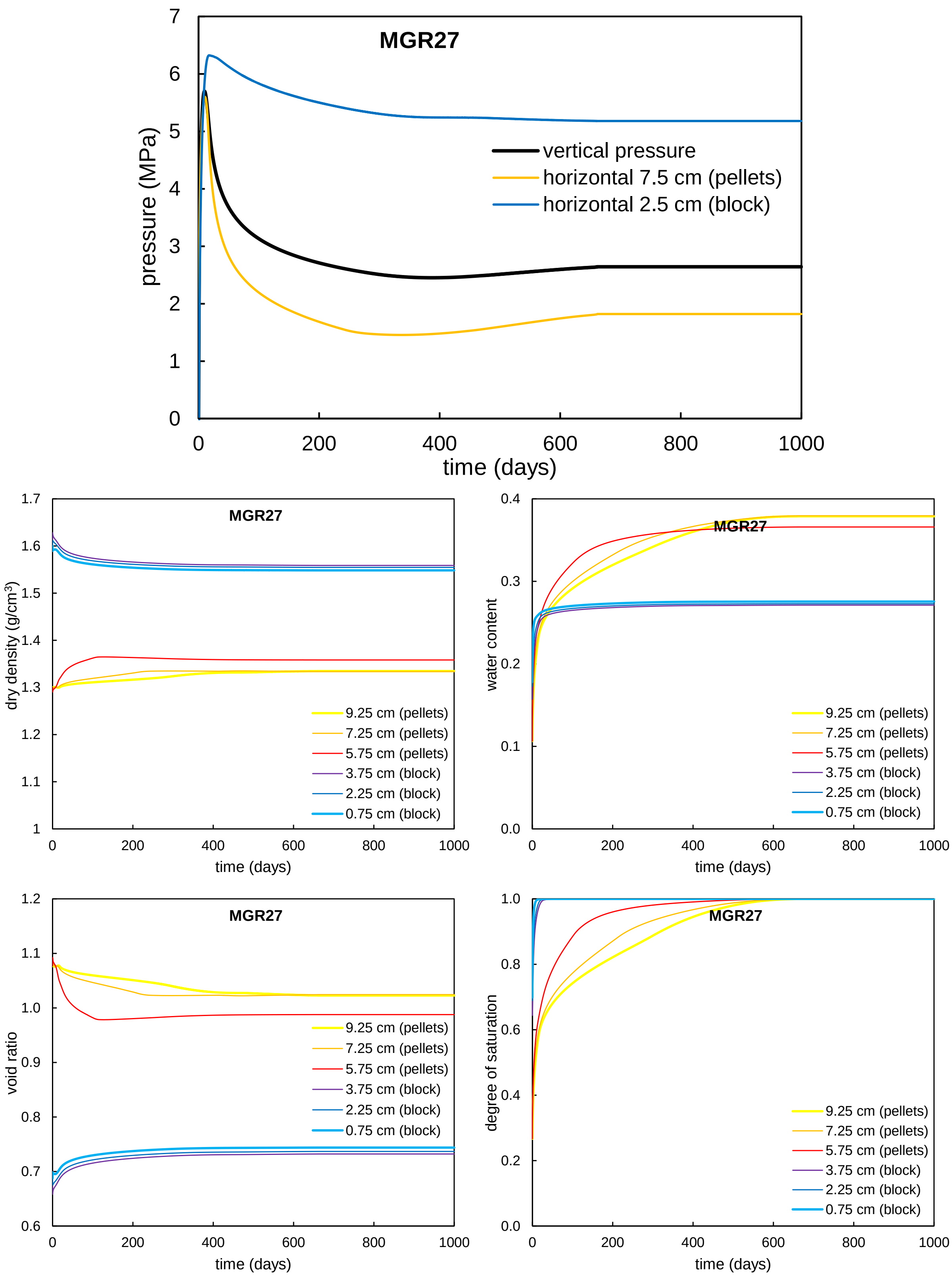

Figure 3-41: *Simulated results of test MGR27*

3.2.7 Discussion

Overall, we judge the simulation results for MGR22 and MGR23 satisfactory as we can capture the magnitude and, partly, also the trends of swelling pressures. However, we recognise a number of shortcomings:

- We were unable to fit, at the same time, the initial suction and initial water content on the basis of our calibration on FEBEX experimental data (Figure 3-37). We chose to keep reasonable values for suction, but this came with an overestimation of the initial water contents and underestimation of the fluxes.

- It was not possible to assign a constant water flow condition for MGR22 due to software limitation and we had to assign a constant pressure condition as in the other tests. Consequently, we could not reproduce the experimental pattern of constant water flow and we had to accept an initially higher water flow, which reduced over time. This may in part explain the faster rise in swelling pressures that we observed.

- Similarly to past simulations, we were able to get a trend in homogenisation, but the final homogenisation was less pronounced than in the experiment. The more porous domain does not shrink enough under the swelling pressure of the less porous one, and the less porous one does not swell enough due to the constraints by the more porous one. Some improvement could be obtained by adjusting the model parameters, but it came at the expenses of the overall fit to the experimental values during calibration (Figure 3-37), thus it was discarded.

- Finally, we note that the simulation results are quite sensitive to the permeability of the bottom layer (the pellets in MGR22 and MGR23) while they are much less sensitive to the permeability of the top layer (the block in MGR22 and MGR23). Consequently, we could well back-analyse permeability of the block layer but not of the pellet layer, which is critical in MGR27 simulations where the order of layers is switched. This might influence our accuracy of time-evolution of variables in MGR27 test.

3.3 Clay Tech

3.3.1 Introduction

The approach taken by Clay Technology for analyzing these tests has been to continue to apply and develop the Hysteresis Based Material (HBM) model (Börgesson et al. 2018; Dueck et al. 2018). HBM has been implemented in Comsol Multiphysics, a general numerical tool where both built in "physics modules" and equation-based user input facilities have been used.

A description of the model setup is given in chapter 3.3.2. The three following chapters, 3.3.4, 3.3.5 and 3.3.6, contain graphs and descriptions of selected results obtained from simulations of test MGR22, MGR23, and MGR27, respectively. For MGR22 and MGR23 experimental data are also given. Chapter 3.3.7 starts with a description of the overall strategy applied for the models and then follows a discussion of the behavior/performance of the models.

3.3.2 Model description

The models consist of three different components, block, granular filling, and an "interface". The interface component was introduced to avoid numerical difficulties due to the large difference in initial conditions between the granular filling and block. All balance equations are solved for in the block and pellet filling components whereas only the force balance is activated in the interface component. Water may however flow "through" (or pass) the interface by introducing flow conditions on either side of the interface governed by the pressure difference over the interface material.

Different representations have been used for the clay in block-form and granular filling regarding the function describing the relative load bearing area and the permeability.

Geometry and discretization

The experiments were represented using an axisymmetric geometry with three different sections axially, an upper (approx. 50 mm), an interface (0.1 mm) and a lower section (approx. 50 mm). The exact heights of the upper and lower sections vary slightly between the experiments, exact values are given in Table 3-8. Dependent on the test setup the upper and lower section are identified as granular filling or block material. Radial homogeneity has been assumed and wall friction is not accounted for, which results in a one-dimensional model. Therefore, the radial dimension has been dictated by numerical efficiency only.

Table 3-8 Geometry

Modelled experiment	Height of lower section [mm]	Height of upper section [mm]	Radius [mm]
MGR22	50.4	49.4	1
MGR23	50.0	49.8	1
MGR27	49.8	50.0	1

The upper and lower sections were discretized with 50 × 1 elements and the interface with 1 × 1 elements in the axial × radial direction, respectively. The shape functions type and order are given in Table 3-9.

Table 3-9 Shape functions

Variable	Shape function type and order
Stress, path variable	Discontinuous Lagrange, Quadratic
Displacements	Lagrange, Cubic
Liquid pressure, void ratio, micro void ratio	Lagrange, Quadratic

Initial conditions

Water content w_0 and dry density ρ_d were given from the tests. Using a solid density of ρ_s = 2735 kg/m³ and adopting $\boldsymbol{\sigma}_0 = \mathbf{0}$ MPa and $\boldsymbol{f}_0 = \mathbf{0}$ a complete initial state could be computed for the models. The initial void ratio e_0 was directly given by dry and solid density. To obtain the pair of initial suction and initial micro void ratio $\{s_0, e_\mu{}^0\}$ an iterative scheme as outlined in Table 3-10 below was used. The initial conditions used in the models are given in Table 3-11 and Table 3-12.

Table 3-10 Scheme for calculating the initial suction and micro void ratio

Guess initial suction	${}^{i}s_0$
Micro void ratio*	${}^{i}e_\mu{}^0 = \dfrac{\rho_s}{{}^{\mu}\tilde{\rho}_l\left({}^{i}s_0\right)} w_0$
Update initial suction	$-\boldsymbol{\sigma}_0 = \tilde{\alpha}\left(e_0, {}^{i}e_\mu{}^0\right)\left(\tilde{\Psi}_M\left({}^{i}e_\mu{}^0\right)\mathbf{1} + \tilde{\Psi}_\Delta\left({}^{i}e_\mu{}^0\right)\boldsymbol{f}_0 - {}^{i+1}s_0\mathbf{1}\right)$
Reiterate (go to *)	if $\left\|{}^{i+1}s_0 - {}^{i}s_0\right\| > tol \Longrightarrow {}^{i}s_0 = {}^{i+1}s_0$
Accept solution	if $\left\|{}^{i+1}s_0 - {}^{i}s_0\right\| \le tol \Longrightarrow \{s_0, e_\mu{}^0\} = \{{}^{i}s_0, {}^{i}e_\mu{}^0\}$

Table 3-11 Initial conditions: Test MGR22

Parameter	Block	Granular filling	Interface
w_0	0.136	0.099	-
$f_0 : \boldsymbol{f}_0 = f_0\mathbf{1}$	0	0	-
$\sigma_0 : \boldsymbol{\sigma}_0 = \sigma_0\mathbf{1}$ [MPa]	0	0	0
e_0	0.69876 (1610 kg/m³)	1.1367 (1280 kg/m³)	-
$e_\mu{}^0$	0.38798	0.29254	-
s_0 [MPa]	97.6	189.7	-

Table 3-12 Initial conditions: Test MGR23&27

Parameter	Block	Granular filling	Interface
w_0	0.142	0.035	-
$f_0 : \boldsymbol{f}_0 = f_0 \mathbf{1}$	0	0	-
$\sigma_0 : \boldsymbol{\sigma}_0 = \sigma_0 \mathbf{1}$ [MPa]	0	0	0
e_0	0.70938 (1600 kg/m³)	1.1038 (1300 kg/m³)	-
$e_\mu{}^0$	0.40352	0.12018	-
s_0 [MPa]	87.7	565.4	-

Boundary/source conditions

Table 3-13 Boundary conditions

BC	MGR22	MGR23&27
Hydraulic at lower horizontal boundary	influx = 0.05 cm³/h if s > 0.05 MPa influx = 1E-3·s kg/(m²s) otherwise	p = 114 kPa
Hydraulic at all other boundaries	No flow	
Mechanical at all boundaries	Rollers (zero displacements in normal direction, zero traction in tangential direction)	

The source/internal boundary flux applied at the interface material boundaries were formulated by using the Comsol flux/source option. The flux/source option is given on the format: $-\boldsymbol{n} \cdot \boldsymbol{\Gamma} = g$, where $\boldsymbol{n}$ is the normal vector to the surface, $\boldsymbol{\Gamma}$ the flux vector, and g the source term to be prescribed. The formulation of g is described below in Figure 3-42. K = 10^{-12} kg/(m²·s·Pa) was used in the models.

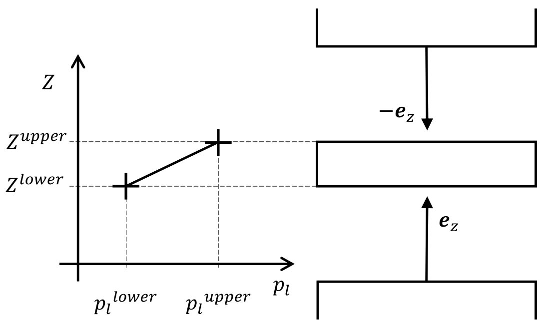

$$\boldsymbol{n} = \boldsymbol{e}_z \ at\ lower\ boundary$$
$$\boldsymbol{n} = -\boldsymbol{e}_z \ at\ upper\ boundary$$
$$\boldsymbol{\Gamma} = {}^{\mu}\rho_l \boldsymbol{q}_l$$
$$\boldsymbol{e}_z \cdot \boldsymbol{q}_l = -k\frac{\Delta p_l}{\Delta z} = -k\frac{p_l{}^{upper} - p_l{}^{lower}}{z^{upper} - z^{lower}}$$
$$g = {}^{\mu}\rho_l \frac{k}{\Delta z}\Delta p_l = K\Delta p_l \ at\ lower\ boundary$$
$$g = -{}^{\mu}\rho_l \frac{k}{\Delta z}\Delta p_l = -K\Delta p_l \ at\ upper\ boundary$$

Figure 3-42: *Description of the formulation used at the internal interface boundaries*

3.3.3 Balance equations

Solid mass balance solved for in the clay components:

$$\dot{\phi} = (1-\phi)\dot{\boldsymbol{\varepsilon}}_v\,.$$

Water mass balance solved for in the clay components:

$$\frac{1}{1+e}\overline{{}^{\mu}\rho_l e_{\mu}}^{\,\cdot} + \operatorname{div}\left({}^{\mu}\rho_l \boldsymbol{q}_l\right) + \frac{1}{1+e}\overline{{}^{m}\theta_g{}^{w}\left(e-e_{\mu}\right)}^{\,\cdot} + \operatorname{div}\left(\boldsymbol{i}_g{}^{w}\right) = {}^{\mu}f_l{}^{w} + {}^{m}f_g{}^{w}\,.$$

Force balance solved for in all components:

$$\operatorname{div}\boldsymbol{\sigma} + \boldsymbol{b} = \boldsymbol{0}\,.$$

Hydraulic constitutive relations (clay components only)

Suction: $s = p_g - p_l$ where $p_g = 0.1\ \mathrm{MPa}$
Liquid (water) density: ${}^{\mu}\tilde{\rho}_l(\mathrm{s}) = \rho_l{}^{0}\exp(-\alpha_l s)$
Liquid (water) flux: $\tilde{\boldsymbol{q}}_l\left(e, e_{\mu}, s\right) = -\frac{\tilde{\kappa}(e,e_{\mu})}{\mu}\operatorname{grad}(-s)$
Permeability: $\tilde{\kappa}\left(e, e_{\mu}\right) = \kappa_{ref}\left(\frac{e}{e_{ref}}\right)^{\beta}\left(\frac{e_{\mu}}{e}\right)^{\lambda}$

The gas phase is assumed to be a mixture of two ideal gases, vapor and dry air ($p_g = p_g{}^{w} + p_g{}^{a}$). To define the gas phase the following have been used,

$$\tilde{\rho}_g(s,T) = {}^{m}\tilde{\theta}_g{}^{w}(s,T) + {}^{m}\tilde{\theta}_g{}^{a}(s,T)\,,$$

$${}^{m}\tilde{\theta}_g{}^{w}(s,T) = \frac{M_w}{RT}\,\tilde{p}_g{}^{w}{}_{sat}(T)\widetilde{RH}(s,T),$$

$${}^{m}\tilde{\theta}_g{}^{a}(s,T) = \frac{M_a}{RT}\left(p_g - \tilde{p}_g{}^{w}{}_{sat}(T)\widetilde{RH}(s,T)\right),$$

$$\tilde{p}_g{}^{w}{}_{sat}(T) = 136075\cdot 10^{6}\exp\left(\frac{-5239.7}{T}\right),$$

$$\widetilde{RH}(s,T) = \exp\left(\frac{-sM_w}{RT\,{}^{\mu}\tilde{\rho}_l(\mathrm{s})}\right).$$

The vapor flux $\boldsymbol{i}_g{}^{w}$ is driven by a gradient in vapor mass concentration c which can be rewritten as a gradient in liquid pore pressure (or suction) and temperature,

$$\boldsymbol{i}_g{}^{w} = -\widetilde{\boldsymbol{D}}\left(e, e_{\mu}, s, T\right)\left[\frac{\partial\tilde{c}(s,T)}{\partial s}\nabla s + \frac{\partial\tilde{c}(s,T)}{\partial T}\nabla T\right],$$

$$\tilde{c}(s,T) = \left[\frac{{}^{m}\theta_g{}^{w}(s,T)}{\rho_g(s,T)}\right],$$

$$\widetilde{\boldsymbol{D}}\left(e, e_{\mu}, s, T\right) = \tau\phi\tilde{\rho}_g(s,T)\left(1-\frac{e_{\mu}}{e}\right)D\,\frac{T^{n}}{p_g}\boldsymbol{1}\,.$$

Table 3-14 Hydraulic parameters

Parameter	Value	Source
$\rho_l{}^0$	998 kg/m³	Beacon D5.1.2 (Test 1B)
α_l	$4.5 \cdot 10^{-11}$ 1/Pa	Set one order lower than usual in order to avoid a low liquid water density at high suction.
μ	$1 \cdot 10^{-3}$ Pa·s	Handbook value
e_{ref}	0.7	Åkesson et. al. (2010)
β	6	Åkesson et. al. (2010)
Block k_{ref}	$0.45 \cdot 10^{-20}$ m²	Åkesson et. al. (2010)
Granular filling k_{ref}	4 × k_{ref} (Block)	Fitted against water uptake data
λ	3	Åkesson et. al. (2010)
τ	0.8	Beacon D5.2.2 (Clay Technology modelling of FEBEX)
D	$5.9 \cdot 10^{-6}$ m²Pa/s/K^n	Åkesson et. al. (2010)
n	2.3	Åkesson et. al. (2010)
M_w	0.018 mol/kg	Handbook value
M_a	0.029 mol/kg	Handbook value
R	8.314472 J/mol/K	Handbook value

Mechanical constitutive relations

The interface component is linear elastic with E = 1000 MPa and ν = 0.2.

Below follows a short summation of the clay components mechanical material model. The total stress is given by,

$$\boldsymbol{\sigma} = \alpha\boldsymbol{\sigma}' ,$$

where $\alpha = \tilde{\alpha}(e, e_\mu)$ is a function used for translating the stresses present in the saturated clay phase at the lower structural level $\boldsymbol{\sigma}'$ to total stresses present in the unsaturated clay $\boldsymbol{\sigma}$. Different representations of the function describing the relative load bearing area have been used for the clay in block-form and granular filling.

- Block: $\alpha = \tilde{\alpha}_b(e, e_\mu) = \left(\frac{1+e_\mu}{1+e}\right)^\gamma$
- Granular filling: $\alpha = \tilde{\alpha}_g(e, e_\mu) = \left(\frac{1+e_\mu}{1+e}\right)^\gamma \left(1 - \left(\frac{1}{1+e_{ref}}\right)^{\gamma_{ref}}\right) + \left(\frac{1}{1+e_{ref}}\right)^{\gamma_{ref}}$

The change made to this function for the granular filling can be thought of as the granular filling material being less efficient in transferring load as compared to the block material.

The stress in the saturated grain phase is related to a clay potential function and suction according to, $-\boldsymbol{\sigma}' = \boldsymbol{\Psi} - s\mathbf{1}$, where the clay potential function $\boldsymbol{\Psi} = \Psi_M\mathbf{1} + \Psi_\Delta\boldsymbol{f}$ has contributions,

$$\Psi_M = \frac{p_{sw}^{high} + p_{sw}^{low}}{2} \quad \text{and} \quad \Psi_\Delta = \frac{p_{sw}^{high} - p_{sw}^{low}}{2},$$

where the high and low swelling pressure/retention curves have the format,

$$\tilde{p}_{sw}^{\beta}(e_\mu) = \left(p_{sw}^{\beta}\right)_0 \exp(c_0^\beta + c_1^\beta e_\mu{}^{0.5} + c_2^\beta e_\mu + c_3^\beta e_\mu{}^2 + c_4^\beta e_\mu{}^3) \text{ where } \beta = high, low.$$

The micro void ratio e_μ is governed by the differential,

$$de_\mu = \frac{\partial e_\mu}{\partial e} de + \frac{\partial e_\mu}{\partial s} ds\,,$$

where,

$$\frac{\partial e_\mu}{\partial e} = \tilde{\alpha}(e, e_\mu)$$

$$\frac{\partial e_\mu}{\partial s} = \text{smooth\_step}(s) \left(\frac{\partial e_\mu}{\partial s}\right)^*$$

$$\left(\frac{\partial e_\mu}{\partial s}\right)^* = \begin{cases} \dfrac{(e - e_\mu)\Psi_M(e_\mu)}{\max(s, s_{min})} \dfrac{1}{(e - e_\mu)\dfrac{\partial \Psi_M}{\partial e_\mu} - \Psi_M(e_\mu)} & \text{if } \dot{s} < 0 \\ \dfrac{-e_{step}}{\left|s - \Psi_M(e_\mu - e_{step})\right|} & \text{otherwise} \end{cases}.$$

The function named $\text{smooth\_step}(s)$, smoothly cuts the term below a set suction value, and s_{min}, limits the minimum suction value in the denominator. Both were introduced for numerical reasons.

The path dependent variable $\boldsymbol{f}$ is given by,

$$d\boldsymbol{f} = \frac{\partial \boldsymbol{f}}{\partial \boldsymbol{\varepsilon}} d\boldsymbol{\varepsilon}\,,$$

where the differentials are given by,

$$\frac{\partial f_{\alpha\beta}}{\partial \varepsilon_{\alpha\beta}} = -K_{\alpha\beta}\left[\sqrt{\left(\frac{\varphi_{\alpha\beta}}{2}\right)^2 - \omega_{\alpha\beta}} + \text{sgn}(\,\dot{\varepsilon}_{\alpha\beta})\left(\frac{\varphi_{\alpha\beta}}{2} + f_{\alpha\beta}\right)\right].$$

The sgn-function is given by,

$$\text{sgn}(x) = \begin{cases} -1 & \text{if} \quad x < 0 \\ 0 & \text{if} \quad x = 0 \\ 1 & \text{if} \quad x > 0 \end{cases}.$$

In the present formulation $K_{\alpha\beta}$ has two possible values, one for $\alpha = \beta$ and another for $\alpha \neq \beta$, respectively. The expressions for $\varphi_{\alpha\beta}$ and $\omega_{\alpha\beta}$ are given below.

Table 3-15 Terms present in the HBM path dependent variable evolution law.

α,β	$\varphi_{\alpha\beta}$	$\omega_{\alpha\beta}$
1,1	$-0.7(f_{22}+f_{33})$	$f_{22}{}^2+f_{33}{}^2-0.7f_{22}f_{33}+2.7\left(f_{13}{}^2+f_{23}{}^2+f_{12}{}^2\right)-0.9R^2$
2,2	$-0.7(f_{11}+f_{33})$	$f_{11}{}^2+f_{33}{}^2-0.7f_{11}f_{33}+2.7\left(f_{13}{}^2+f_{23}{}^2+f_{12}{}^2\right)-0.9R^2$
3,3	$-0.7(f_{11}+f_{22})$	$f_{11}{}^2+f_{22}{}^2-0.7f_{11}f_{22}+2.7\left(f_{13}{}^2+f_{23}{}^2+f_{12}{}^2\right)-0.9R^2$
2,3	0	$\frac{10}{27}\left(f_{11}{}^2+f_{22}{}^2+f_{33}{}^2\right)-\frac{7}{27}(f_{11}f_{22}+f_{22}f_{33}+f_{11}f_{33})+\left(f_{13}{}^2+f_{12}{}^2\right)-\frac{R^2}{3}$
1,3	0	$\frac{10}{27}\left(f_{11}{}^2+f_{22}{}^2+f_{33}{}^2\right)-\frac{7}{27}(f_{11}f_{22}+f_{22}f_{33}+f_{11}f_{33})+\left(f_{23}{}^2+f_{12}{}^2\right)-\frac{R^2}{3}$
1,2	0	$\frac{10}{27}\left(f_{11}{}^2+f_{22}{}^2+f_{33}{}^2\right)-\frac{7}{27}(f_{11}f_{22}+f_{22}f_{33}+f_{11}f_{33})+\left(f_{13}{}^2+f_{23}{}^2\right)-\frac{R^2}{3}$

Table 3-16 HBM parameters

Parameter	Value	Source
c_0^{low}	6.2595	Fitted against data (Tab. A-18) in Villar et al. (2018)
c_1^{low}	3.0793	Fitted against data (Tab. A-18) in Villar et al. (2018)
c_2^{low}	-10.9511	Fitted against data (Tab. A-18) in Villar et al. (2018)
c_3^{low}	2.2654	Fitted against data (Tab. A-18) in Villar et al. (2018)
c_4^{low}	-0.1214	Fitted against data (Tab. A-18) in Villar et al. (2018)
c_0^{high}	6.4195	Fitted against data (Tab. A-18) in Villar et al. (2018)
c_1^{high}	3.7863	Fitted against data (Tab. A-18) in Villar et al. (2018)
c_2^{high}	-11.7552	Fitted against data (Tab. A-18) in Villar et al. (2018)
c_3^{high}	3.1794	Fitted against data (Tab. A-18) in Villar et al. (2018)
c_4^{high}	-0.3182	Fitted against data (Tab. A-18) in Villar et al. (2018)
$\left(p_{sw}^{low\,\&\,high}\right)_0$	10^6 Pa	Fitted against data (Tab. A-18) in Villar et al. (2018)
Block γ	7	Beacon D3.1
Granular filling γ	17	New, fitted against dry density profiles
Granular filling γ_{ref}	Block γ	New, fitted against dry density profiles
Granular filling e_{ref}	Block e_0	New, fitted against dry density profiles
K_{aa}	40	Beacon D5.1.2 (Test 1B)
K_{ab}	40	$K_{ab} = K_{aa}$ (has no effect in the present case)
R	0.9	Beacon D5.2.2 (obtained from studying small example problems)
e_{step}	0.05	Beacon D5.2.2 (obtained from studying small example problems)

3.3.4 Results MGR22

To describe and study the behavior/performance of the models, cumulative water inflow, axial compressive stress, water content profile and dry density profile have been chosen, mainly since experimental data exist. For MGR22 the experimental and model data are given in Figure 3-43 for cumulative water inflow, Figure 3-44 for axial compressive stress, Figure 3-45 for dry density profile and Figure 3-46 for water content profile.

In Figure 3-43 the simulated cumulative water inflow can be seen to agree reasonably with the experimental data. There are some discrepancies:

- There is a "latency" in the experimental data which could indicate an initial tube/filter filling not included in the simulation.
- The use of a smooth boundary condition when suction ≤ 0.05 MPa gives a more gradual final saturation process in the model.
- The measured final water uptake is greater in the experiment.

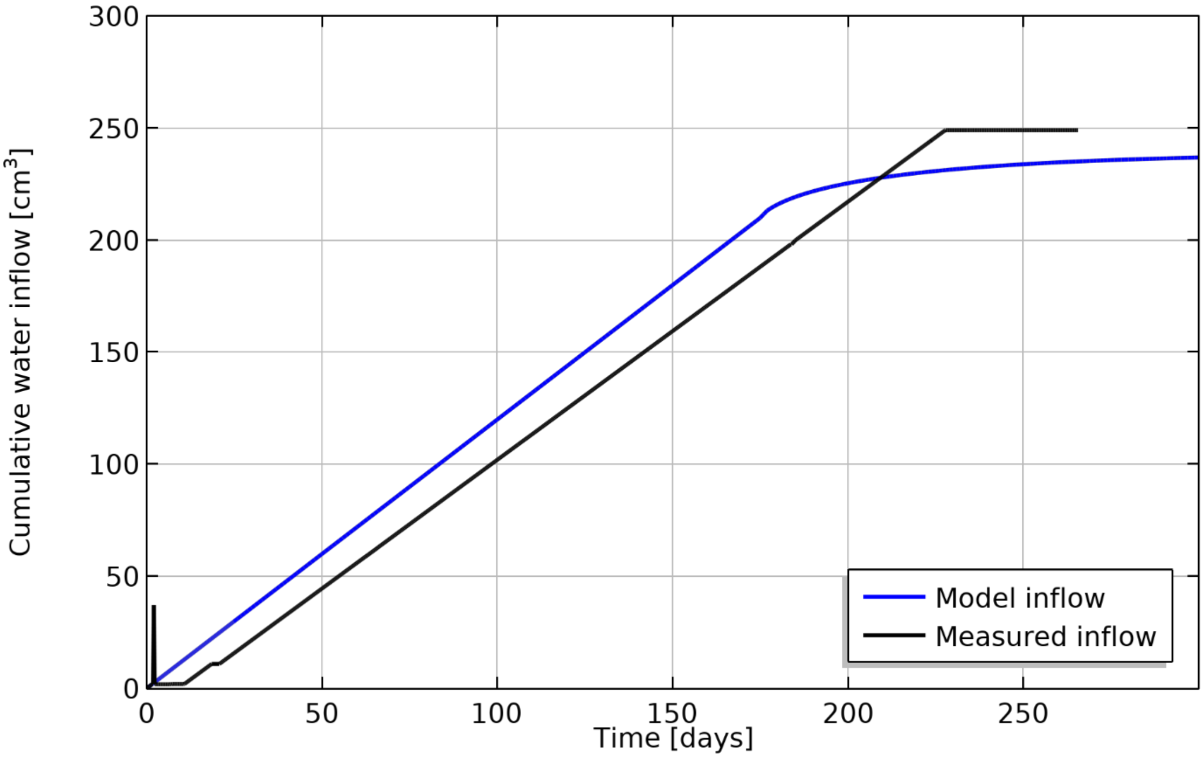

Figure 3-43: *Water intake data MGR22, experiment and simulation*

The simulated and measured evolution of axial compressive stress in Figure 3-44 have common overall features. There is a sequence of a first rapid increase – first plateau – second rapid increase – second plateau. The timing and levels between the features for the two data sets are, however, not similar.

- Again, there is a "latency" in the experimental data. This most probably come from the observed latency in water uptake.
- The use of a smooth hydraulic boundary condition when suction ≤ 0.05 MPa also results in a more gradual final axial compressive stress evolution in the model.
- The difference in final stress magnitude could come from not including wall friction and using an unrepresentative clay potential function parametrization.

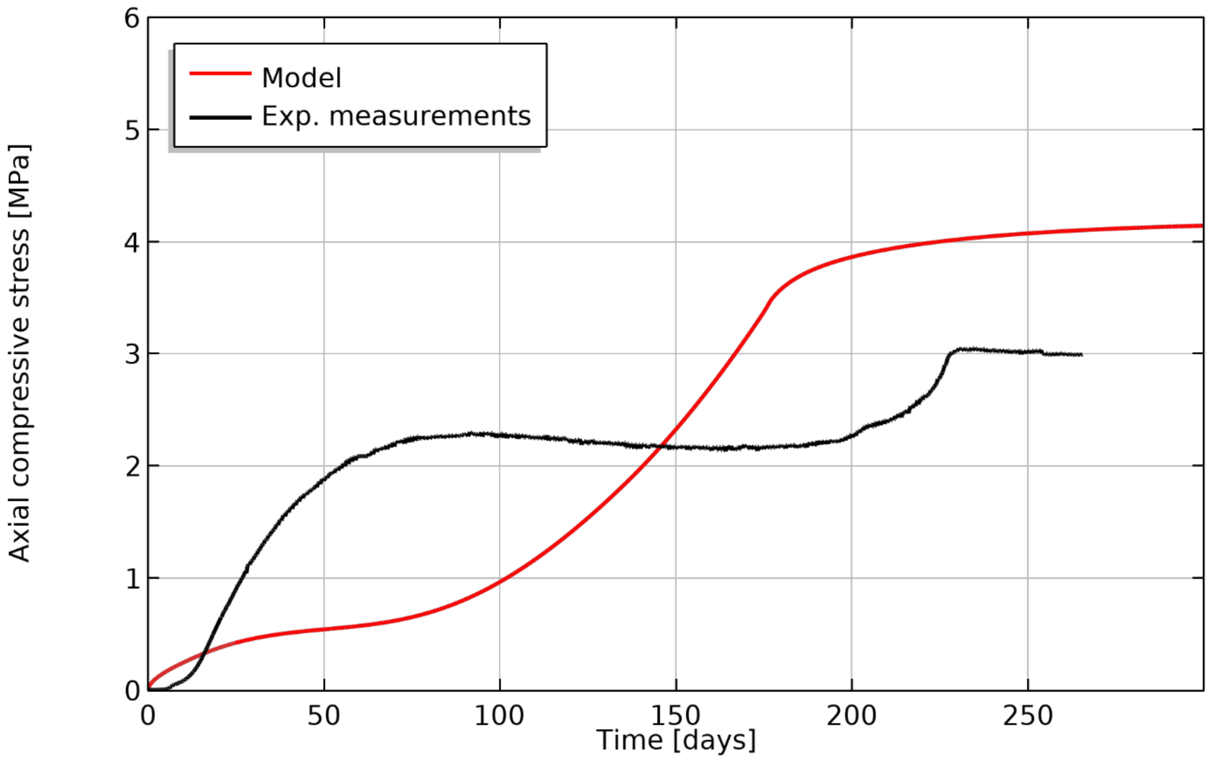

Figure 3-44: *Axial compressive stress data MGR22, experiment and simulation*

The simulated axial profile of dry density, given in Figure 3-45, agrees well with the measurements. Also here, the effect from using the interface material, allowing for a discontinuous void ratio field and thereby producing a discontinuous dry density field, can be seen in the graph. The initial dry density distribution is indicated by the dashed line.

The homogenized initial dry density is 1.44 g/cm^3. Since all measurements are situated below the obtained model profile there is a mismatch between the given initial condition and the measurements.

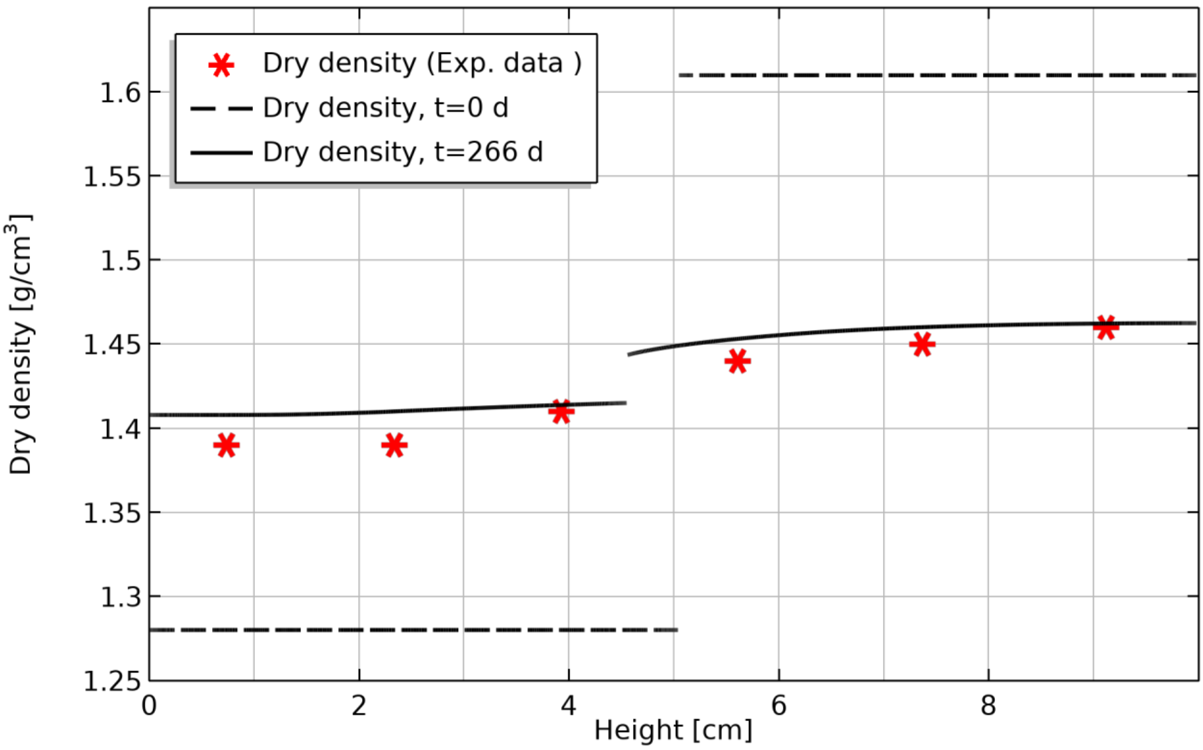

Figure 3-45: *Dry density profile data MGR22, experiment sample data and simulation data*

The simulated axial profile of water content, given in Figure 3-46, agrees very well with the measurements. The effect from using the interface material, allowing for a discontinuous void ratio field, and thereby producing a discontinuous water content field, can be seen in the graph. In Figure 3-46 the initial water content distribution is indicated by the dashed line.

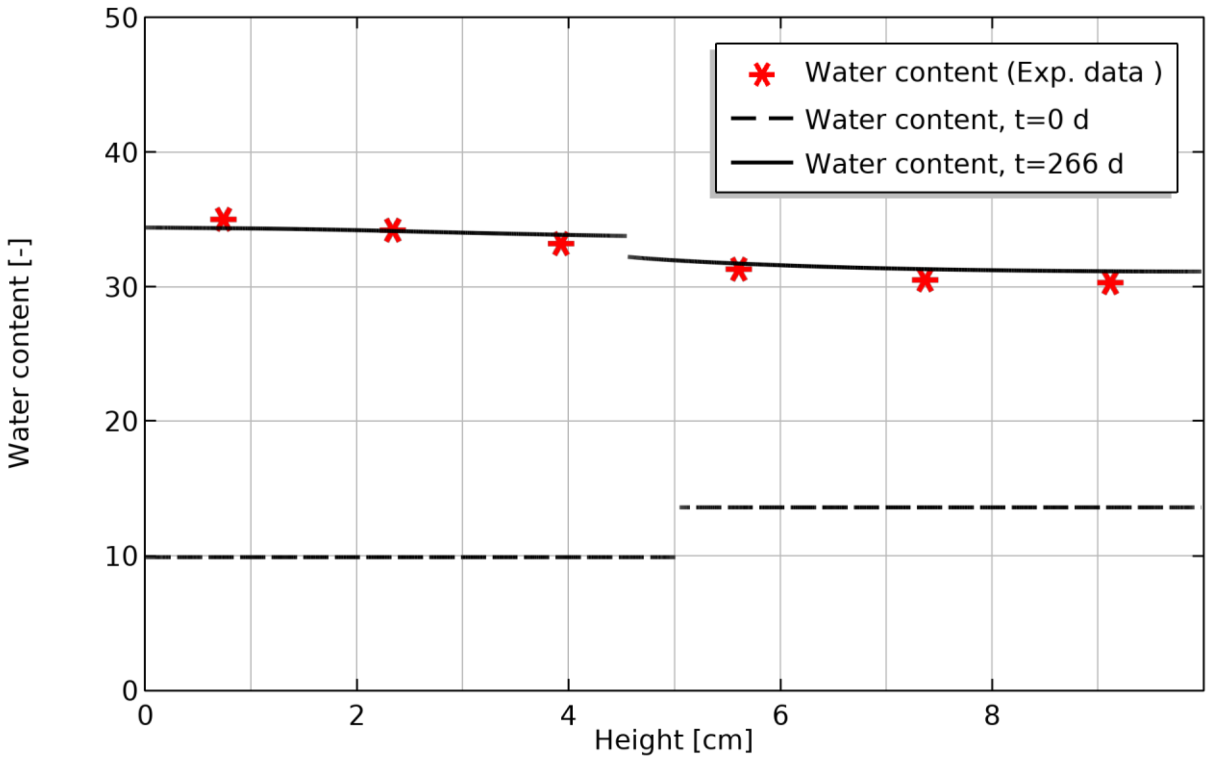

Figure 3-46: *Water content profile data MGR22, experiment sample data and simulation data*

3.3.5 Results MGR23

For MGR23 the experimental and model data are given in Figure 3-47 for cumulative water inflow, Figure 3-48 for axial compressive stress, Figure 3-49 for dry density profile and Figure 3-50 for water content profile.

In Figure 3-47 the simulated cumulative water inflow can be seen to agree well with the experimental data. The model data is smooth whereas the measurements have a plateau at 150 cm^3 and some kinks. The final water uptake in the model is less than what was measured in the experiment.

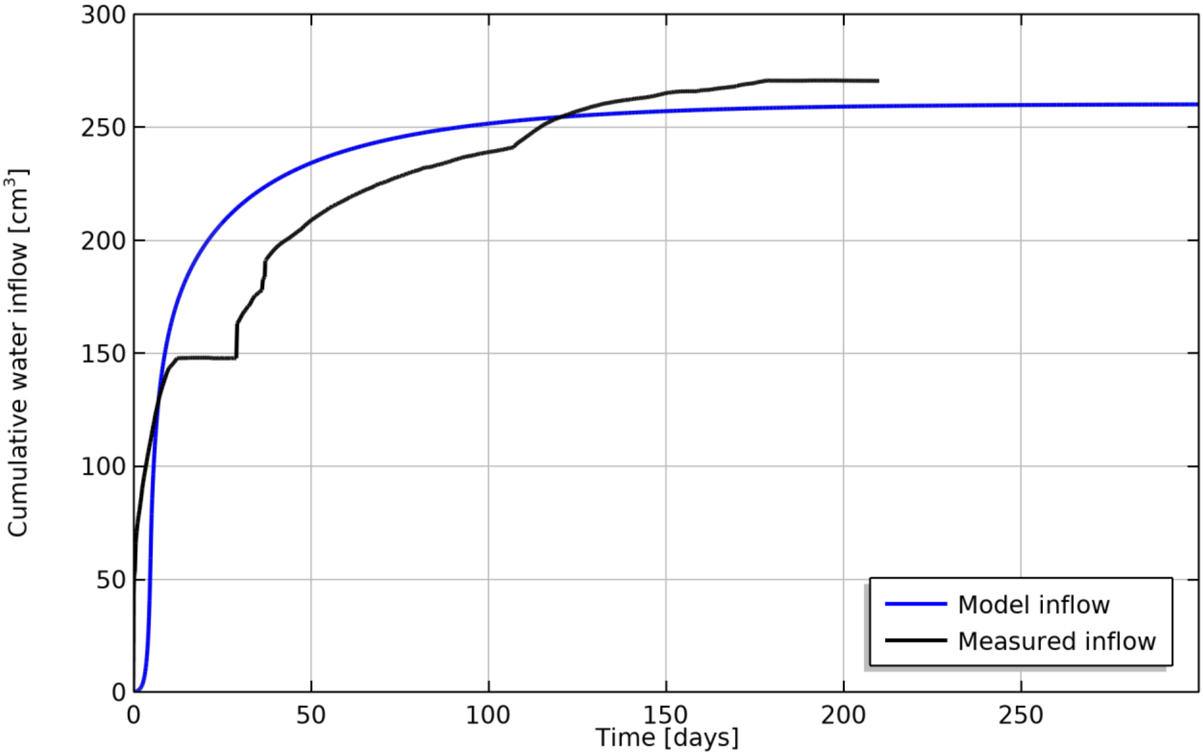

Figure 3-47: *Water intake data MGR23, experiment and simulation*

The simulated and measured evolution of axial compressive stress shown in Figure 3-48 have a clear difference in magnitude.

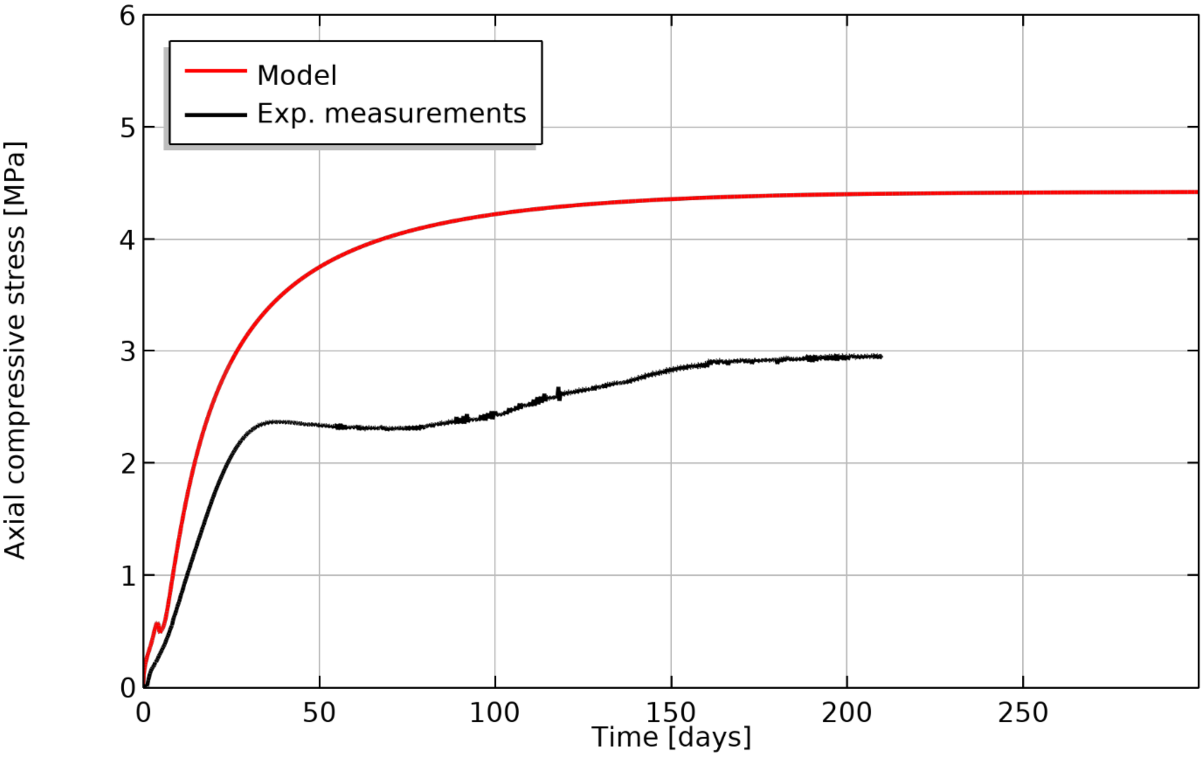

Figure 3-48: *Axial compressive stress data MGR23, experiment and simulation*

The simulated axial profile of dry density, given in Figure 3-49, agrees reasonably well with the measurements. The effect from using the interface material, allowing for a discontinuous void ratio field, and thereby producing a discontinuous dry density field, can be seen in the graph. The initial dry density distribution is indicated by the dashed line.

For this case, the homogenized initial dry density is 1.45 g/cm³. Since all but one of the measurements are situated well below the obtained model profile there is also here a mismatch between the given initial condition and the measurements.

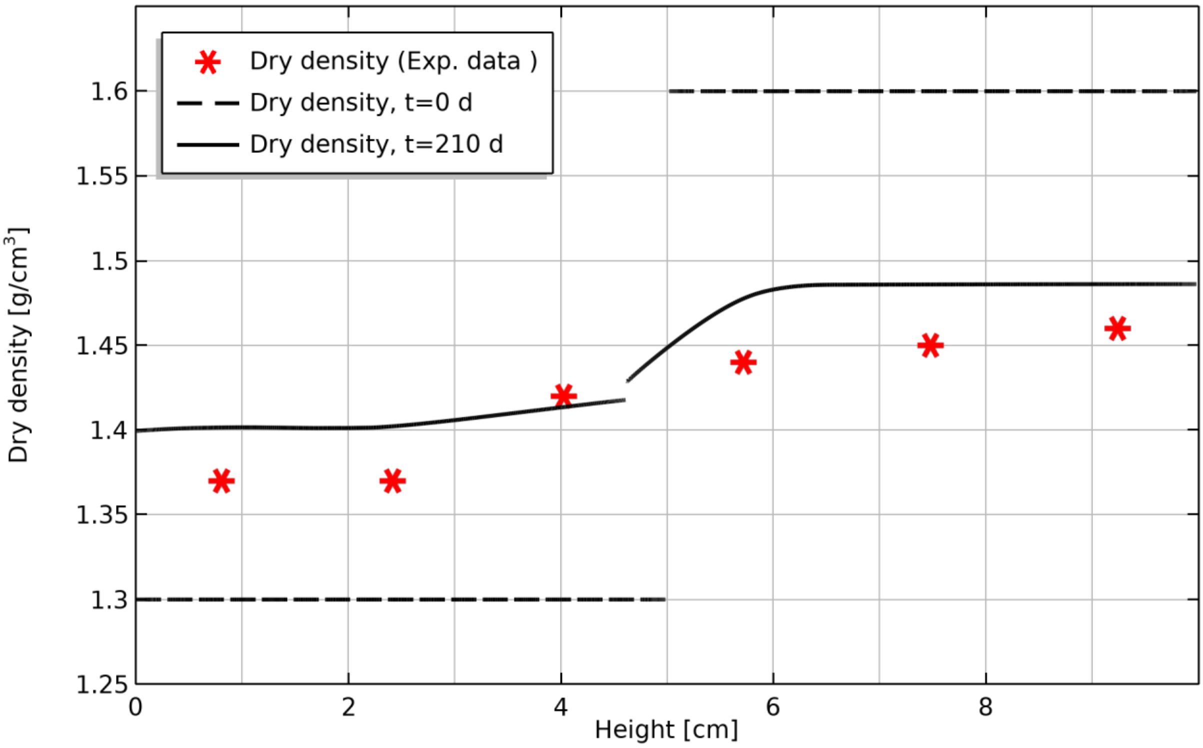

Figure 3-49: *Dry density profile data MGR23, experiment sample data and simulation data*

The simulated axial profile of water content, given in Figure 3-50, agrees rather well with the measurements. The effect from using the interface material, allowing for a discontinuous void ratio field, and thereby producing a discontinuous water content field, can be seen in the graph. The initial water content distribution is indicated by the dashed line.

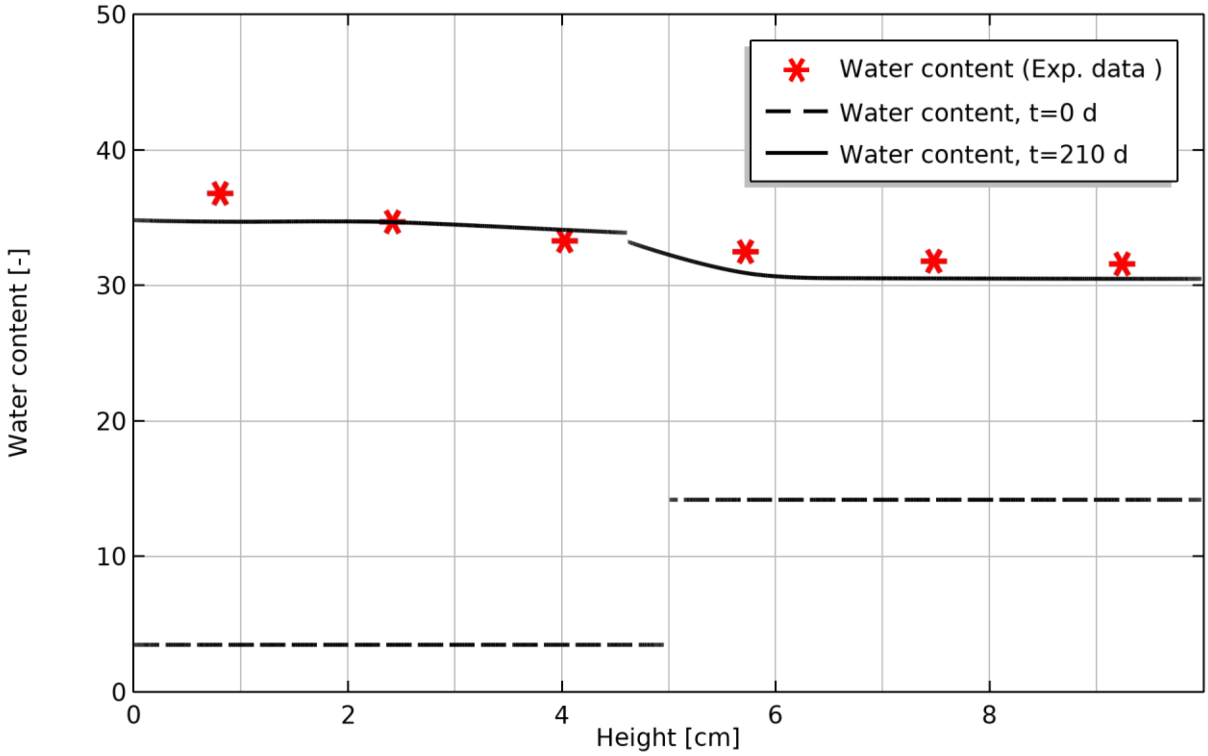

Figure 3-50: *Water content profile data MGR23, experiment sample data and simulation data*

3.3.6 Results MGR27

For MGR27 the model data are given in Figure 3-51 for cumulative water inflow, Figure 3-52 for axial compressive stress, Figure 3-53 for dry density profile and Figure 3-54 for water content profile.

As can be seen when comparing the water intake in Figure 3-51 the evolution is expected to be much slower in MGR27 as compared to MGR22/23. If the test is dismantled before steady state is reached it will this be difficult to directly compare experimental and measured dry densities/water contents without evaluating the models at either the same time or, more ideally, at the same level of water intake as the experiment.

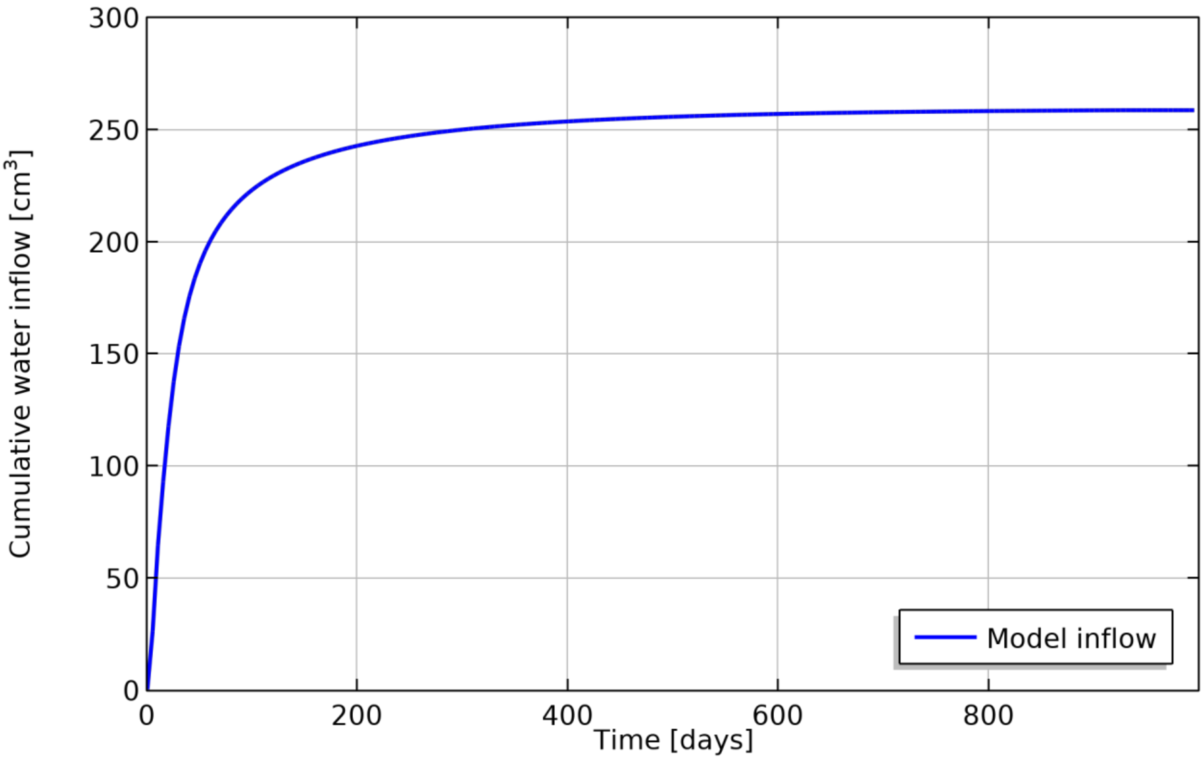

Figure 3-51: *Water intake data MGR27, simulation*

From Figure 3-52 it can be seen that a similar evolution in the axial compressive stress would be expected in MGR27 as that seen in MGR22/23, even though it is likely that we also here overestimate the magnitude. It should be note that wall friction may also be important here – this is discussed further in section 0.

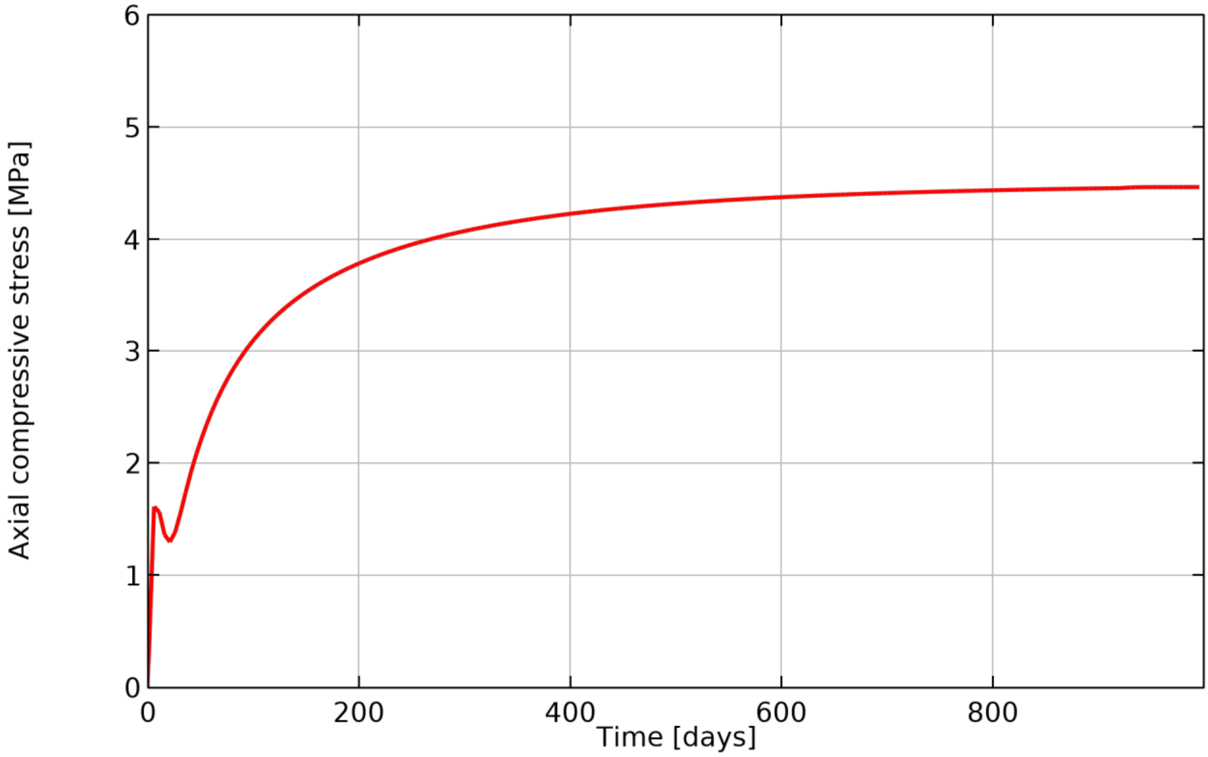

Figure 3-52: *Axial compressive stress data MGR27, simulation*

Figure 3-53 and Figure 3-54 shows that we predict a much more homogenized final state in MGR27 as compared to MGR22/23. This will, however, be somewhat dependent on the time of dismantling as can be seen in Figure 3-53, where the dry density profiles at several different times are shown.
Further comments on this and the MGR27 results in general are given in the discussion.

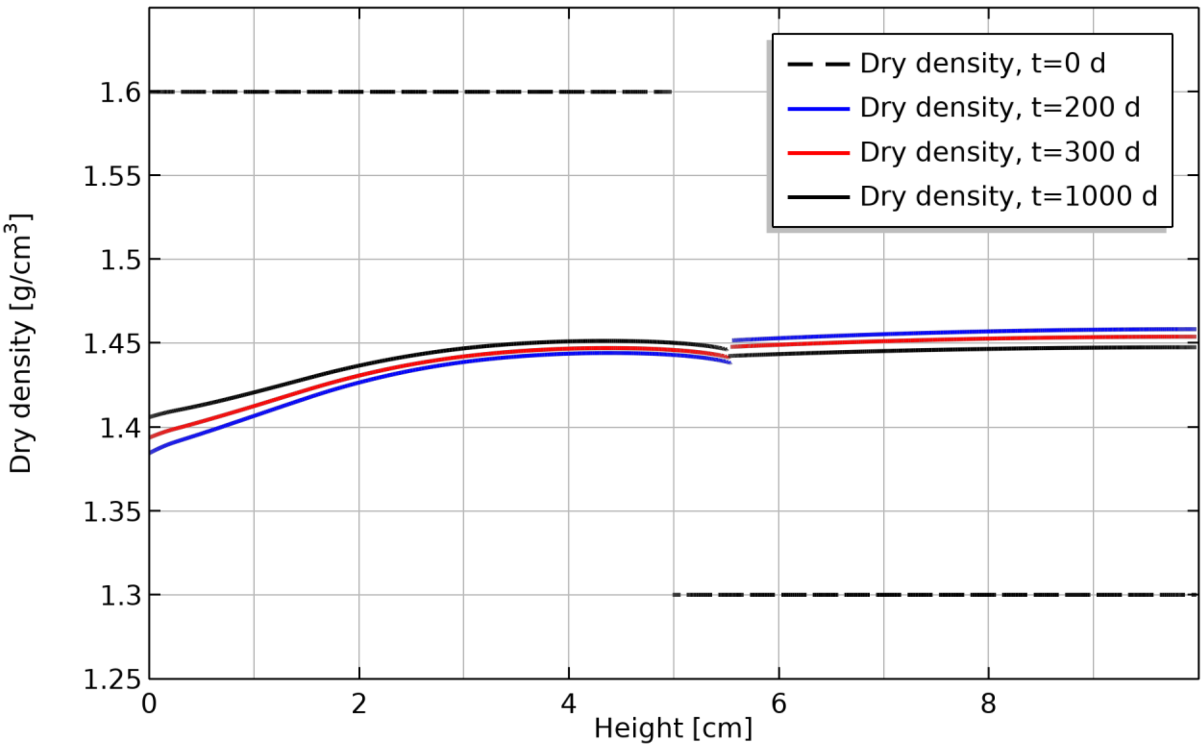

***Figure 3-53:** Dry density profiles at different times from the model of MGR27*

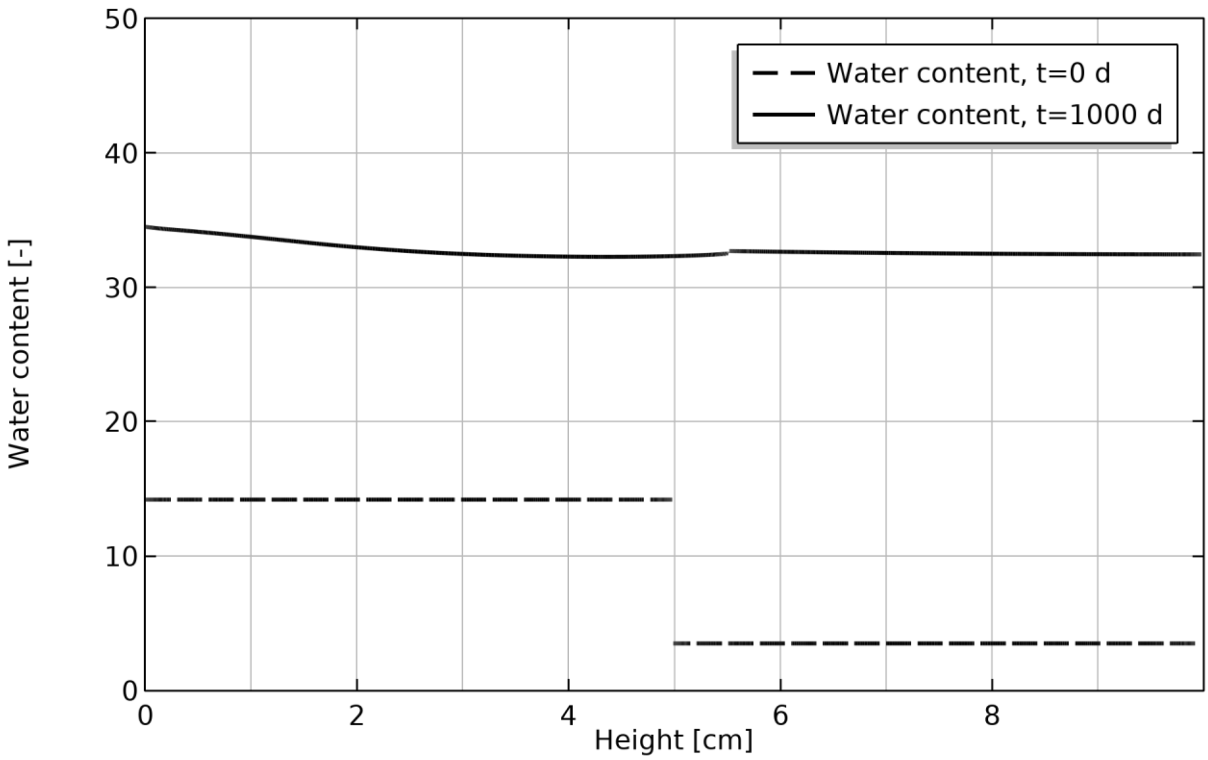

***Figure 3-54:** Water content profile data MGR27, simulation*

3.3.7 Discussion

In this chapter the strategy used when developing the models is first briefly outlined. In the following subchapters more detailed discussions of the model behavior/performance are given in connection to the results shown in chapter 3.3.4, 3.3.5 and 3.3.6.

As for the modelling strategy, the goal was to keep the unsaturated block representation as close to what was used in the previous Febex model as possible. The change from this was the clay potential, which was lowered at low void ratios to get rid of convergence issues early in the simulations. A new representation was developed for the granular filling by changing the block setup in two ways: the permeability, and the relative load bearing area function. The permeability of the granular filling was determined from performing a parameter sweep and adopting the value which gave the most representative solution in terms of water inflow evolution. The mechanical representation of the granular filling was changed as to obtain more reasonable final dry density profiles. More specifically, the relative load bearing area function was changed.

Due to properties of the implementation of the material model in Comsol, an interface material had to be introduced in order to avoid unwanted effects at the interface between the clay materials. The solid mass balance and water mass balance were formulated and solved for as one common equation system. In this equation system the liquid water pore pressure and void ratio were the unknowns to solve for and they were, due to being solved from a common equation system, approximated by the same type of shape function. For the present case, the liquid water pore pressure should be continuous over the interface between the two materials. The void ratio, however, should not be governed by such a constraint. This made it hard to reconcile the use of the common equation system with the wanted appearance of the two variables over the material interface. A non-porous linear elastic interface material with prescribed fluxes at its interfaces, governed by the liquid pore pressure difference over the interface material, were therefore introduced between the block and granular filling materials. This allowed for a continuous water flow over the interface, while allowing for a discontinuity in the void ratio profile.

Discussion related to the cumulative water inflow

In the models the water flux is handled using Darcy's flow model, with the liquid flux being proportional to the suction gradient in the clay multiplied with the permeability, k. The latter is dependent on both the porosity and the liquid saturation in the clay.

Initially the same permeability relation was used for both the granular filling and block. This, however, led to a significantly slower hydraulic evolution than what was seen in the experiments. This is unsurprising as we would expect the dry granular filling to be much more permeable than the block material, as it is essentially a double-porosity system, in which the water transport in the pore space between granules can be very high. Including a more realistic water-transport description in the granular filling was not possible here but will be considered in the future. To achieve a more realistic rate of hydration the permeability in the granular filling were here instead just multiplied by a factor, f_k. In Figure 3-55 a comparison of the water inflow rate for the model MGR23 with two different values (1 and 4) of f_k is shown. As can be seen the higher value (4) gives a much better agreement with experimental data than the lower value (1), and hence the latter was used in all models presented here.

In Figure 3-55 it can also be seen that the amount of water taken up by the bentonite in the models of MGR23 is 261 cm³. At this point the buffer is essentially fully water saturated. In the experiment, however, a higher value of 271 cm³ of water is taken up before full saturation is achieved. A theoretical calculation of the available water volume for the initial conditions specified gives an available pore volume of 261 cm³, indicating that more water enters the experiment than the initial available pore volume. The difference between experimental and theoretical vales can be partially understood from the measured vertical deformation in the experiment, which is about 0.26mm, corresponding to an increased pore volume of about 2 cm³. The remaining difference may, for example, be due to the experimental setup (e.g. filter volume etc.) which is not included in the model.

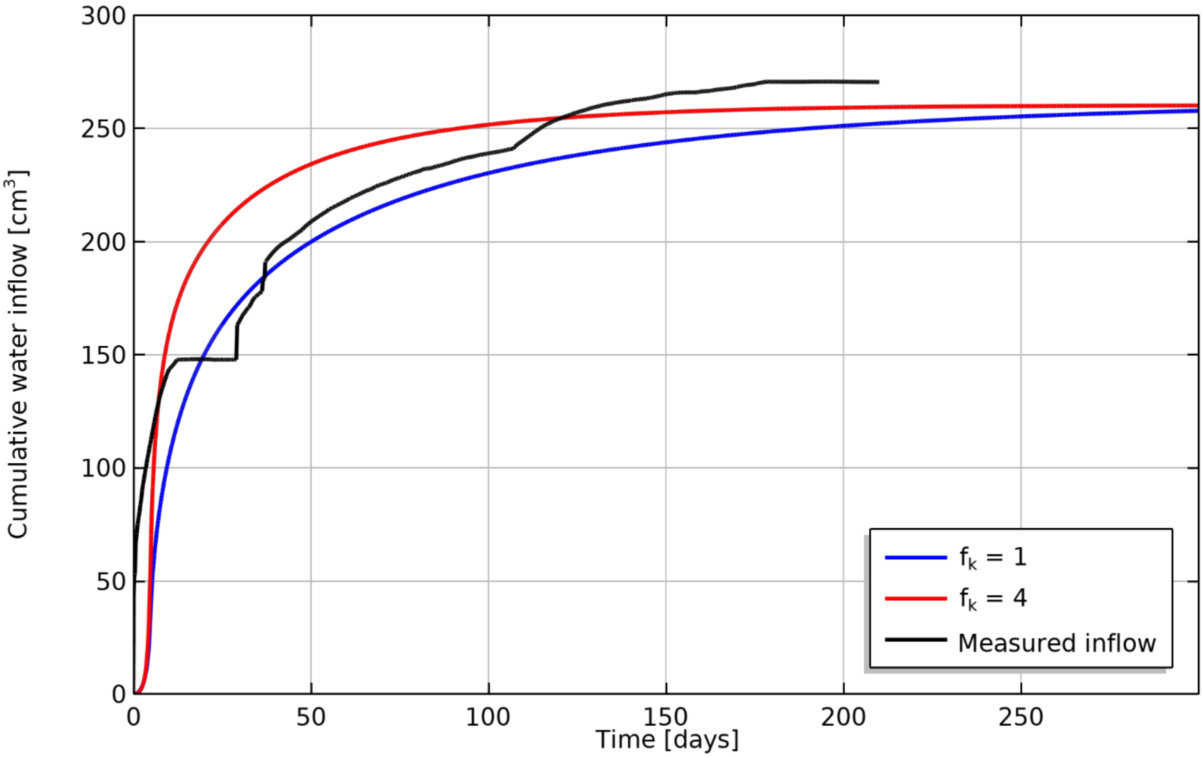

Figure 3-55: *Water inflow in the model of MGR23 with the same permeability in the block and pellets (blue line) and with a four times higher permeability in the pellets (red line) compared to the measured inflow (black line)*

The liquid density in the models is dependent on the capillary suction in the clay component. While this is appropriate when considering the compressive properties of water (which are small but existent) it can give rise to unphysical values of the liquid density at high values of suction. Originally the parameterization defined in Åkesson et al 2010 was used: $\rho_l = 998\exp(-4.5\times 10^{-10}s)$ kg/m³, where s denotes the capillary suction. However, with the high values of initial suction present in the models reported here (about 500 MPa) the liquid density reached values below 800 kg/m³ and the suction dependence was lessened by one order of magnitude to $\rho_l =$

$998\exp(-4.5\times10^{-11}s)$. In the future a different expression should be considered, which takes into account the compressibility of water, while avoiding low values of the liquid density in dry conditions.

Discussion related to the axial compressive stress

Comparing the results from MGR22 and MGR23 gives an opportunity to study the effect of using different hydraulic boundary conditions: constant flow and constant pressure, respectively. When comparing the axial compressive stress evolution in MGR22 and MGR23 (given in Figure 3-44 and Figure 3-48, respectively) the appearances are quite different. The main cause is the difference in water uptake evolution, where MGR23 has a significantly higher water uptake rate.

Comparing the results from MGR23 and MGR27 gives information about how different stacking sequence of materials, block on top of granular filling, granular filling on top of block, affects the behavior of the system. Due to the difference in the stacking sequence of the materials, MGR27, where water inflow is applied at the more impermeable block material, has a slower build-up of stress. In MGR27 there is also a more pronounced "kink" in the water uptake curve early in the process. Clearly, competing processes, such as water uptake from bottom which gives a swelling of the bottom material, and water redistribution towards the granular filling which gives a shrinkage of the block, become more pronounced in MGR27.

Both the model of MGR22 and that of MGR23 shows a higher axial compressive stress as compared to the measured values. For the final state of the MGR22 and MGR23 models, where the dry density is somewhere about 1.45 g/cm^3, the axial compressive stress is overestimated by about 1 MPa. Two possible reasons for this are discussed below: the effect of neglecting wall friction and the effect of using an unrepresentative clay potential.

Wall friction

If including wall friction in the models, the axial compressive stress would most likely be affected, and this could explain some of the difference between the measurements and model results in MGR22 and MGR23. If studying the deformation field evolution however, the displacement is directed downwards in all points. This indicates that the friction force would be oriented upwards which would not decrease the axial compressive stress at the top of the test cell. It is therefore not likely the reason for overestimating the axial compressive stress. For the MGR27 model, however, the displacements are directed upwards, indicating a downward orientation of the friction force. So, omitting the wall friction for this model, could have an effect when comparing the axial compressive stress at the top of the test cell.

Clay potential

As mentioned in the description of the modelling strategy, a new parameterization of the clay potential was developed to reduce convergence issues arising early on in the simulations, due to the large difference in initial conditions for the granular filling and block. The introduction of the interface material was in part also aimed at solving the same issue, and the models could possibly be solved without the new clay potential.

However, the new parameterization only lowered the values of the clay potential at low void ratios with no significant effect for the void ratios relevant at the final state of the system. The final state of the experiments shows dry densities somewhere about 1.4 - 1.45 g/cm³ which equals a void ratio of about 0.95 - 0.89. To attain an axial compressive stress that agrees with the measurements, the functions governing the clay potential could be refitted so as to reduce the value by about 1 MPa at the relevant void ratios.

In Figure 3-56 the evolution in clay potential – micro void ratio space is shown for two points from the model of MGR23. The solid blue line shows the evolution in the mid-point of the granular filling volume, while the solid green line shows the evolution in the mid-point of the block. The dashed and dashed dot black lines show the lower and upper limits of the clay potential. The model starts out at very high levels of the clay potential, due to the initial high suction and then moves, as the suction decrease to lower levels of the clay potential and thus to higher values of the micro void ratio. When looking at the large range of values in clay potential and micro void ratio it is clear that a small adjustment around a micro void ratio of about 0.9, with a reduction in the value of the clay potential limits in this region by about 1 MPa would not alter the general shape of the curves (Ψ_{low} and Ψ_{high}) significantly and would reduce the axial compressive stress seen in the models to the same level as experimental measurements.

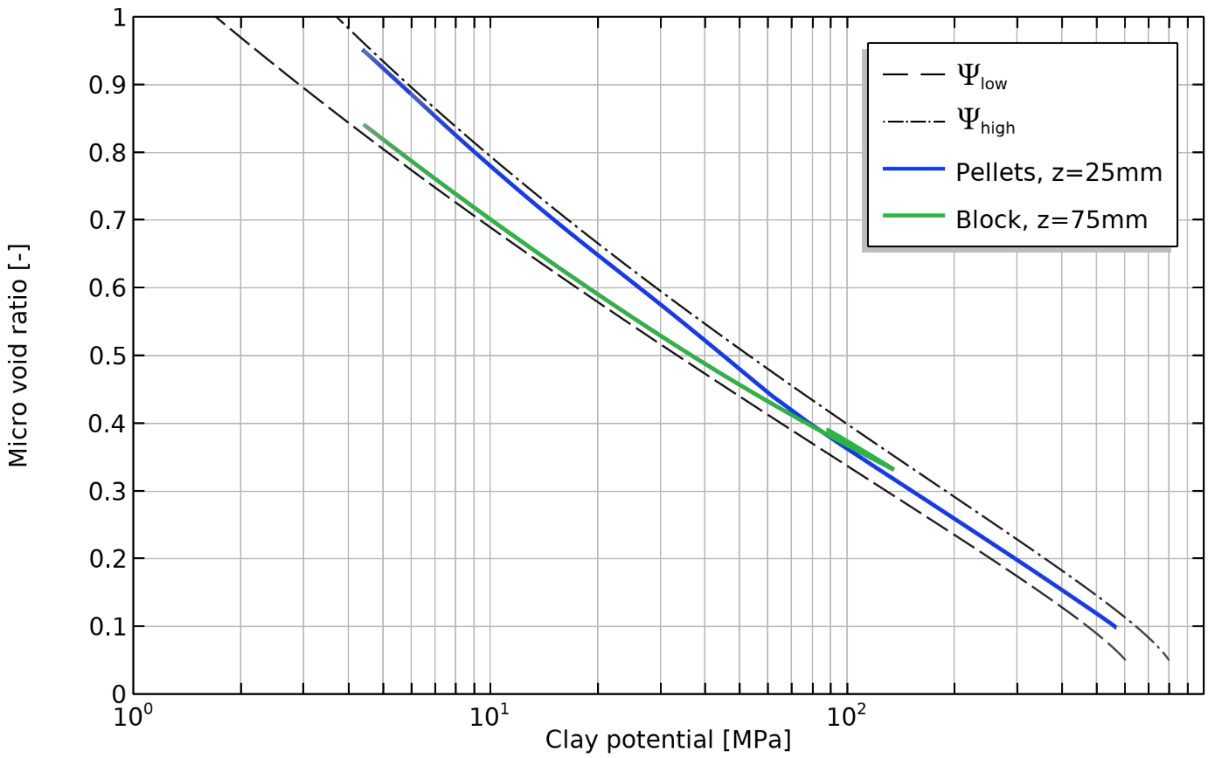

Figure 3-56: *Evolution of the clay potential in axial direction in two different points from the model of MGR23. One point in block and one in the granular filling*

The clay potential and thereby its parametrization is at the very heart of the HBM model. It is therefore essential for the performance of the model that the parametrization accurately represents the character of the material. To obtain a model which accurately can represent the material behavior over a wide range of states, the clay potential also must be parametrized accurately over a wide range of states. This in turn demands an experimental data set of sufficient resolution, range, and accuracy to confidently being able to design a reliable parametrization. More specifically the functions governing the clay potential should be fitted against data obtained from retention tests and swelling pressure tests.

As mentioned above, the functions governing the clay potential could be refitted as to attain an axial compressive stress that agrees with the measurements in the present task. It could indeed be that such a refitment would lead to a more representative clay potential and thereby a more representative model overall. The disagreement may, however, have other origins, such as sensor precision, boundary conditions (here no vertical displacement of the top boundary is allowed) and neglecting other processes (such as the above-mentioned wall friction). To determine if an incorrect parameterization of the clay potential is the actual cause of the mismatch between modelled and measured axial compressive stress the clay potential parameterization should be evaluated using more data for the Febex bentonite, which, to our knowledge is not currently available.

Discussion related to the dry density profiles

Comparison of MGR22 and MGR23 gives an opportunity to study the influence from using different hydraulic boundary conditions, constant flow or constant pressure, respectively. In MGR22 the water uptake is slower as compared to MGR23, and as Figure 3-45 and Figure 3-49 show, the difference in water uptake rate gives different levels of final homogenization.

To gain some insight in how the homogenization process evolves for MGR22 and MGR23, sequences of dry density profiles are plotted in Figure 3-57. It should be noted that, since the water uptake rate is different for the two models, the time at which the dry density profiles are plotted is different for obtaining a relevant set of profiles from which the homogenization can be studied. For MGR22 the evolution of the profiles is quite uncomplicated, but for MGR23 the homogenization process shows more complexity. In MGR22 there is time for water being distributed more homogeneously and thereby the swelling/pressure build-up/compression processes will also take place more homogeneously. In MGR23, on the other hand, where the water inflow rate is higher the processes will have a more localized and dynamic character.

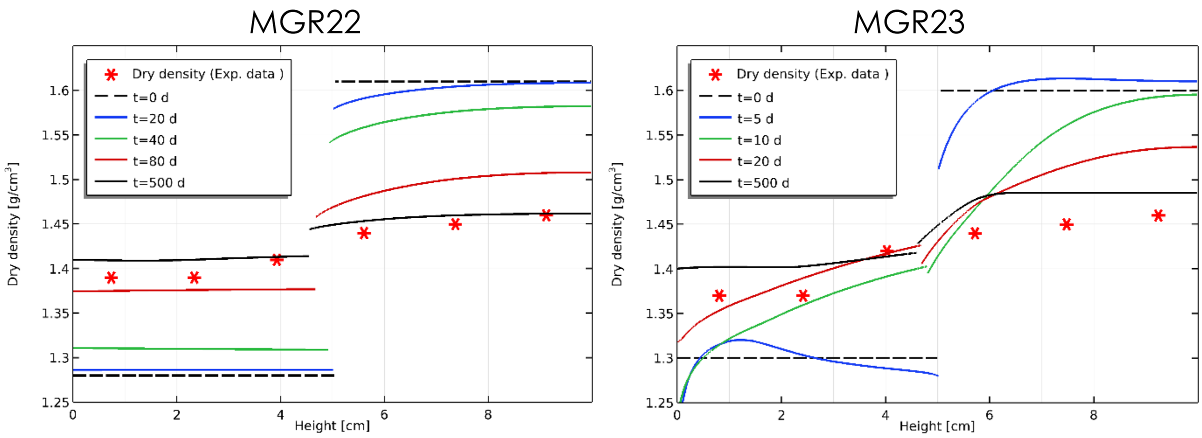

Figure 3-57: *Sequence of dry density profiles for MGR22 to the left and MGR23 to the right. Note that the times for plotting are not equal for the two models*

Comparing results from MGR23 and MGR27 gives information about how different stacking sequence of materials, block on top of granular filling, granular filling on top of block, affects the behavior of the system. Differences are obvious when looking at Figure 3-49 and Figure 3-53, the block has swollen more, and the granular filling has been compressed more in MGR27.

Sequences of dry density profiles for MGR23 and MGR27 are plotted in Figure 3-58. As above, the water uptake rate is different for the two models and therefore the time at which the dry density profiles are plotted is also different. When studying the homogenization process in the block for MGR23 and MGR27 the models show similar behavior. In the MGR27 model water is supplied to the block at its left boundary and in the MGR23 model the block interface towards the granular filling, the left boundary of the block, can be viewed as a point where water is supplied to the block. It is therefore not surprising that the block homogenization in MGR23 and MGR27 has similarities. In MGR23 the granular filling can be considered a filter through which the water has to pass and the dry density evolution in the block therefore becomes less dynamic as compared to what is seen in MGR27. The homogenization process in the granular filling is different for MGR23 and MGR27. There are, however, similarities in the granular filling homogenization process between MGR22, to the left in Figure 3-57, and MGR27, to the right in Figure 3-58. In MGR27 the block material acts as a filter for the granular filling which therefore experiences a slow inflow of water at the interface boundary, which has similarities to the conditions of the granular filling in MGR22.

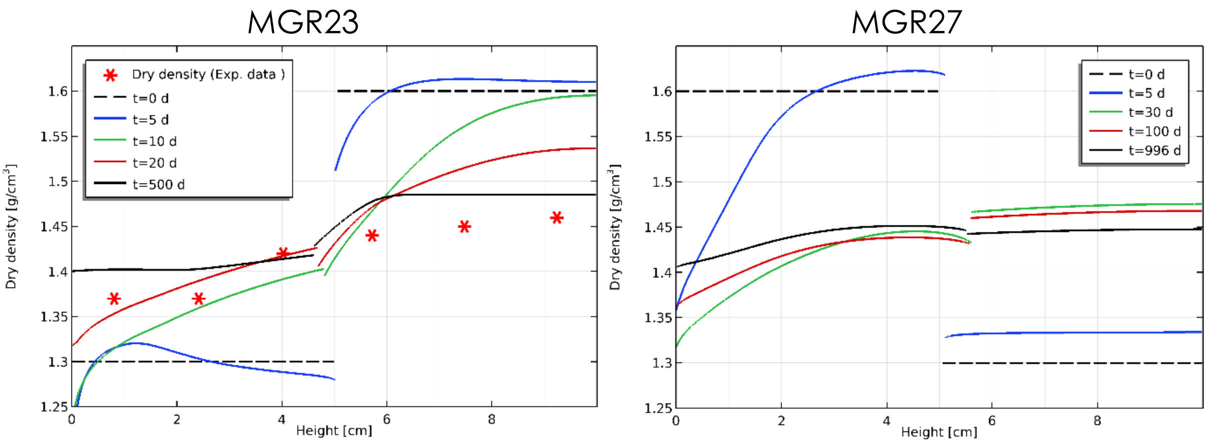

Figure 3-58: *Sequence of dry density profiles for MGR23 to the left and MGR27 to the right. Note that the times for plotting are not equal for the two models*

The new relative load bearing area function

Without any changes to the relative load bearing area function, $\tilde{\alpha}(e, e_\mu)$, for the granular filling the obtained dry density profile become much less gradual over the interface of the two materials. $\tilde{\alpha}(e, e_\mu)$ was therefore changed, lowered, for the granular filling material in such way as to obtain a more gradual change in the dry density profile. In Figure 3-59 dry density profiles are shown for two identical models except for the relative load bearing area function of the granular filling material. The profile indicated by $\gamma = 7$ is obtained from the model using the "original", block material, function and the profile indicated by $\gamma = 17$ is obtained from the model using the new, granular filling material, function.

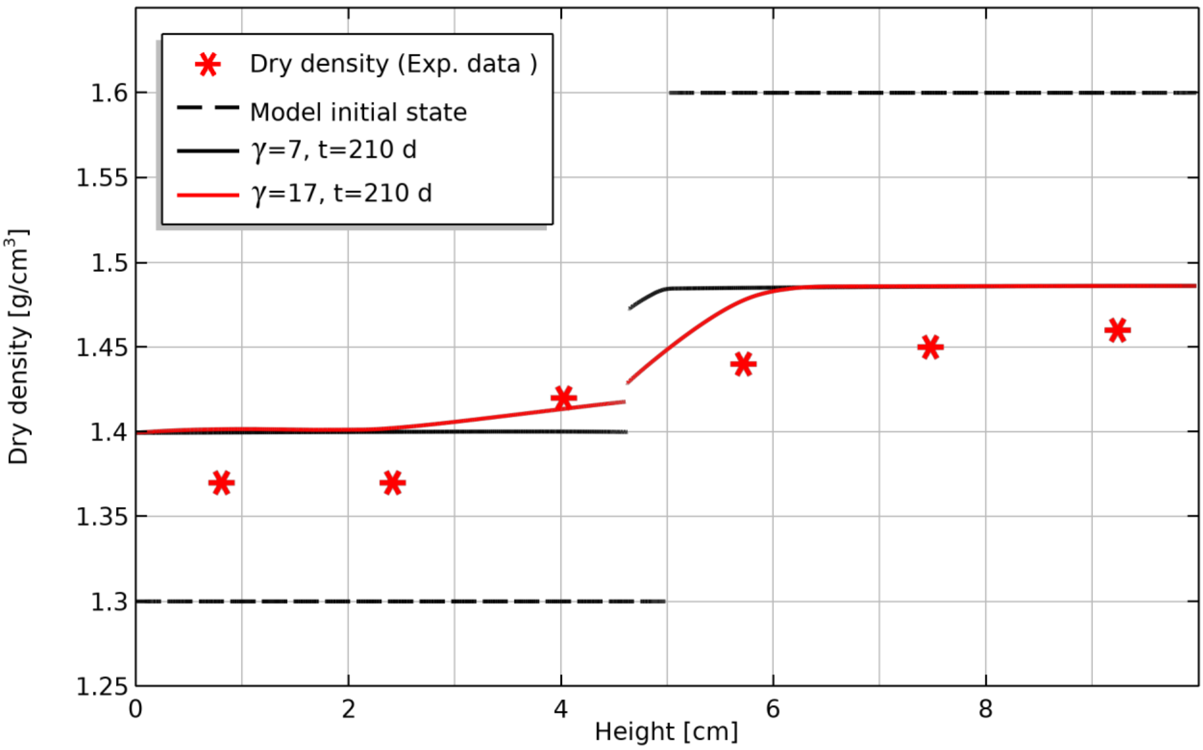

Figure 3-59: *Dry density profiles for MGR23 using different alpha-functions in the granular filling.* γ*= 7 indicates use of the "original" block function and* γ*= 17 indicates use of the newly developed function*

The decrease of the relative load bearing area function translates into a granular filling representation which becomes "less efficient "at transferring the load as compared to the block material. This can be thought of as if there is more stress-free material in the granular filling representation, e.g., if larger granules transfer load (are stressed) and smaller granules does not (are stress-free). This results in a material which is softer. To confirm that this adjustment of the model agrees with reality however, the stiffness of granular fillings at unsaturated states should be determined from experiments.

The expressions used are:

- Block: $\tilde{\alpha}_b(e, e_\mu) = \left(\frac{1+e_\mu}{1+e}\right)^\gamma$
- Granular filling: $\tilde{\alpha}_g(e, e_\mu) = \left(\frac{1+e_\mu}{1+e}\right)^\gamma \left(1 - \left(\frac{1}{1+e_{ref}}\right)^{\gamma_{ref}}\right) + \left(\frac{1}{1+e_{ref}}\right)^{\gamma_{ref}}$

The relative load bearing area functions can be expressed in terms of meso porosity ϕ_m using that,

$$\frac{1+e_\mu}{1+e} = \frac{Saturated\ clay\ volume}{Unsaturated\ clay\ volume} = 1 - \phi_m\,,$$

In Figure 3-60 the used relative load bearing area functions are plotted against $1 - \phi_m$.

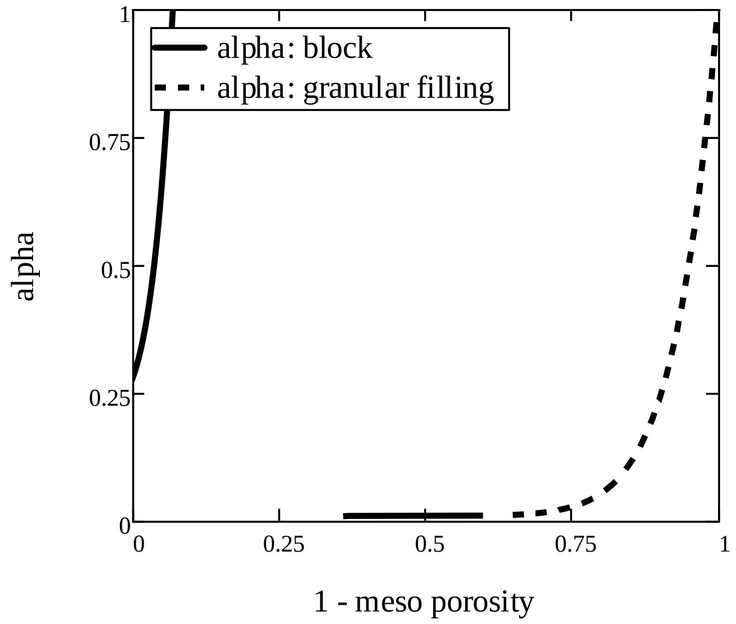

Figure 3-60: *Block and granular filling alpha-functions*

3.4 LEI

3.4.1 Description of the model

Modelling of CIEMAT tests MGR21-MGR24 and MGR27 was performed with LEI model developed in numerical tool COMSOL Multiphysics v5.6 (for more description see BEACON WP3 deliverable reports D3.2 and D3.3. COMSOL Multiphysics is general-purpose platform software for modelling engineering applications. It allows conventional physics-based user interfaces and coupled systems of partial differential equations for simulation with finite element method.
For the modelling of hydro-mechanical (HM) response of hydration of FEBEX bentonite (compacted block and pellets mixture) Richard 's equation was applied for the water flow modelling. It was assumed that bentonite mechanical response in terms of deformation or/and developed swelling pressure are mainly governed by bentonite saturation. At the current stage wetting induced swelling was modelled as linear elastic deformation and its impact on porosity change was assessed. Young's modulus dependency on saturation was considered in the model. HM model included couplings to consider impact of mechanical deformations on water balance, porosity change impact on specific moisture capacity, on storage coefficient and on permeability.
At this stage plastic deformations of bentonite have not been considered.

3.4.2 Geometry and discretization

CIEMAT tests MGR21-MGR24 and MGR27 were performed in a constant-volume oedometer with a 100 mm diameter and a height of approximately 100 mm (Villar & Talandier, 2020; Beacon D4.1, 2019). The initial heights of bentonite block layer varied between 49.4 mm and 50.1 mm and the initial heights of pellets mixture layer varied between 49.7 mm and 50.4 mm as it is indicated in Table 3-17:

Table 3-17 Initial heights of bentonite layers in analysed experiments (Villar & Talandier, 2020; Beacon D4.1, 2019)

	MGR21 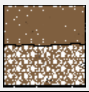	MGR22 	MGR23 	MGR24 	MGR27 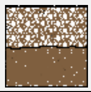
Height of block zone, mm	50.1	49.4	49.8	49.7	49.8
Height of pellets mixture zone, mm	49.7	50.4	50.0	50.2	50.0
Total height of sample, mm	99.8	99.8	99.8	99.9	99.8

The modelling has been performed under 2-D axisymmetric conditions and analysed domains were discretized into 1502 triangular grid elements as it could be seen in Figure 3-61. Contact surface between bentonite pellets and block layers was more discretized to reduce numerical errors and to have more accurate modelling results for the comparison with experimental data.

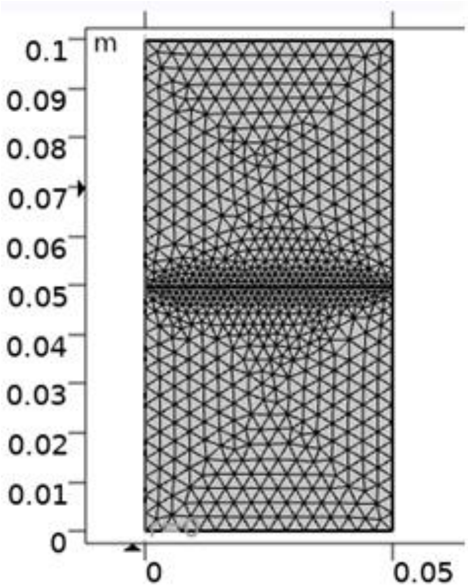

Figure 3-61: *Computational grid of COMSOL Multiphysics model*

Final measured and modelled heights of bentonite pellets and block layers are presented in Table 3-18.

Table 3-18 Final measured and modelled heights of bentonite layers in MGR tests

	MGR21 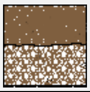	**MGR22** 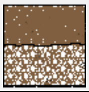	**MGR23** 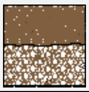	**MGR24** 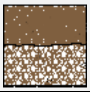	**MGR27** 
Height of block zone, mm (measured)	53.3	52.7	52.9	51.3	Data not provided
Height of pellets mixture zone, mm (measured)	48.0	47.9	48.4	49.3	Data not provided
Height of block zone, mm (modelled)	53.2	53.2	53.6	51.3	53.5
Height of pellets mixture zone, mm (modelled)	46.6	46.6	46.2	48.5	46.3

3.4.3 Input parameters

The initial values of HM processes related parameters for bentonite pellets and block zones for modelled tests MGR21-MGR24 and MGR27 are summarized in Table 3-19.

Table 3-19 Initial characteristics of bentonite materials for different modelled cases

Parameter	MGR21 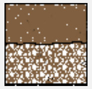		MGR22 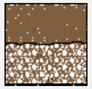		MGR23 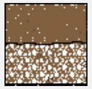		MGR24 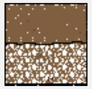		MGR27 	
	Pellets zone	Block zone	Pellets zone	Block zone	Pellets zone	Block zone	Pellets zone	Block zone	Pellets zone	Block zone
Solid density*, kg/m³	2700									
Initial dry density*, kg/m³	1260	1600	1280	1610	1300	1600	1280	1620	1300	1600
Initial porosity, -	0.5333	0.4074	0.5259	0.4037	0.5185	0.4074	0.5259	0.4	0.5185	0.4074
Saturated hydraulic conductivity, m/s	$\log k = \begin{cases} -6.00\rho_d - 4.09 & 1.30 \le \rho_d \le 1.47 \\ -2.96\rho_d - 8.57 & 1.47 \le \rho_d \le 1.84 \end{cases}$ (Talandier, 2018)									
Initial hydraulic conductivity, m/s	$1.3 \cdot 10^{-13}$	$7{,}0 \cdot 10^{-15}$	$1.14 \cdot 10^{-13}$	$7{,}47 \cdot 10^{-15}$	$1.2 \cdot 10^{-14}$	$8.7 \cdot 10^{-15}$	$3.9 \cdot 10^{-14}$	$7.2 \cdot 10^{-15}$	$1.2 \cdot 10^{-14}$	$9.4 \cdot 10^{-15}$
Relative permeability function	$K_{rel}=S_e^{1.9}$	$K_{rel}=S_e^{3}$	$K_{rel}=S_e^{1.9}$	$K_{rel}=S_e^{3}$	$K_{rel}=S_e^{1.9}$	$K_{rel}=S_e^{3}$	$K_{rel}=S_e^{1.9}$	$K_{rel}=S_e^{3}$	$K_{rel}=S_e^{1.9}$	$K_{rel}=S_e^{3}$
Water retention function	VG,	VG, P_0=4.5 MPa, λ=0.17	VG,	VG, P_0=4.5 MPa, λ=0.17	VG,	VG, P_0=4.5 MPa, λ=0.17	VG,	VG, P_0=4.5 MPa, λ=0.17	VG,	VG, P_0=4.5 MPa, λ=0.17

Parameter	MGR21 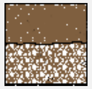		MGR22 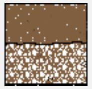		MGR23 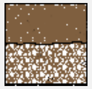		MGR24 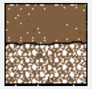		MGR27 	
	Pellets zone	Block zone	Pellets zone	Block zone	Pellets zone	Block zone	Pellets zone	Block zone	Pellets zone	Block zone
	P_0=0.95 MPa, λ=0.217		P_0=0.95 MPa, λ=0.217		P_0=0.95 MPa, λ=0.217		P_0=0.95 MPa, λ=0.217		P_0=0.95 MPa, λ=0.217	
Young modulus, MPa	$19 \cdot S_e$	$35/ S_e$	$19 \cdot S_e$	$35/ S_e$	$19 \cdot S_e$	$35/ S_e$	$19 \cdot S_e$	$35/ S_e$	$19 \cdot S_e$	$35/ S_e$
Poisson ration, -	0.41	0.3	0.41	0.3	0.41	0.3	0.41	0.3	0.41	0.3
Swelling coefficient, -	No swelling assumed	$0.165 \cdot S_e$	No swelling assumed	$0.165 \cdot S_e$	No swelling assumed	$0.165 \cdot S_e$	No swelling assumed	$0.165 \cdot S_e$	No swelling assumed	$0.165 \cdot S_e$

* - data from Villar & Talandier, 2020; Beacon D4.1, 2019.

Hydraulic conductivity of bentonite block and pellets was defined according to empirical relationship presented in Talandier, 2018 as a function of dry density (see in Table 3-19). Unsaturated hydraulic conductivity is highly dependent on the degree of saturation S_e and was expressed as the product of relative permeability k_r and the saturated hydraulic conductivity. The dependency of relative permeability on degree of saturation was expressed as a power law:

$$k_r = S_e^n \qquad [1]$$

For the pellet zone the exponent n=1.9 (Hoffman et al., 2007) and for the block zone the exponent n=3 (Talandier, 2018) were selected for LEI model.
Van Genuchten relation were used to describe water retention curves for both bentonite zones. Different shapes of curves were applied for LEI model as it could be seen Figure 3-62. Parameter values for both curves were obtained from (Hoffman et al., 2007) and (Talandier, 2018) taking into account dry densities of bentonite block and pellets.

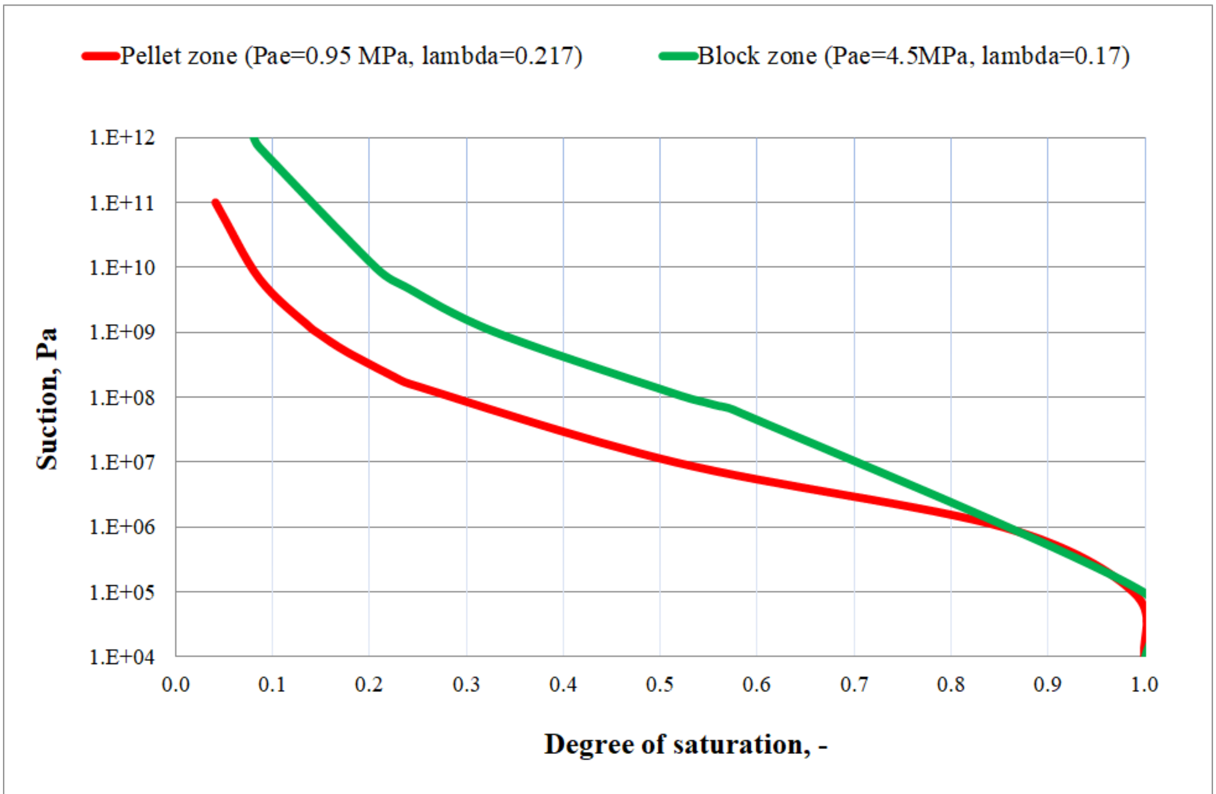

Figure 3-62: *Water retention curves for bentonite block and pellets zones applied for LEI model*

Mechanical parameters required to describe LEI linear swelling model are: swelling coefficient, Young's modulus and Poisson ratio. Considering the overall dry density of pellets zone, it was assumed that wetting pellets will swell into the void space around pellets, but there will be no overall swelling induced stress of a pellets zone as a whole. The pellets zone was assumed to be weaker from mechanical point of view as the interface of block and pellets zone was expected to be moved into the pellets zone (considering the final heights of zones). Swelling coefficient in block zone as well as

Young's modulus in both zones were assumed to be dependent on degree of saturation in LEI model. Three empirical expressions described in Table 3-19 were obtained as a result of model calibration with experimental data from tests MGR21-MGR24. Evolution of average Young's modulus in bentonite block and pellets zones for modelled cases are presented in Figure 3-63 and Figure 3-64, respectively. As it could be seen from Figure 3-63, despite the same expression of Young's modulus for bentonite block were used in each modelled case, but evolution of average Young's modulus was different due to different evolution of average degree of saturation in bentonite block in each case. The same phenomena were obtained in bentonite pellets as it could be seen in Figure 3-64.

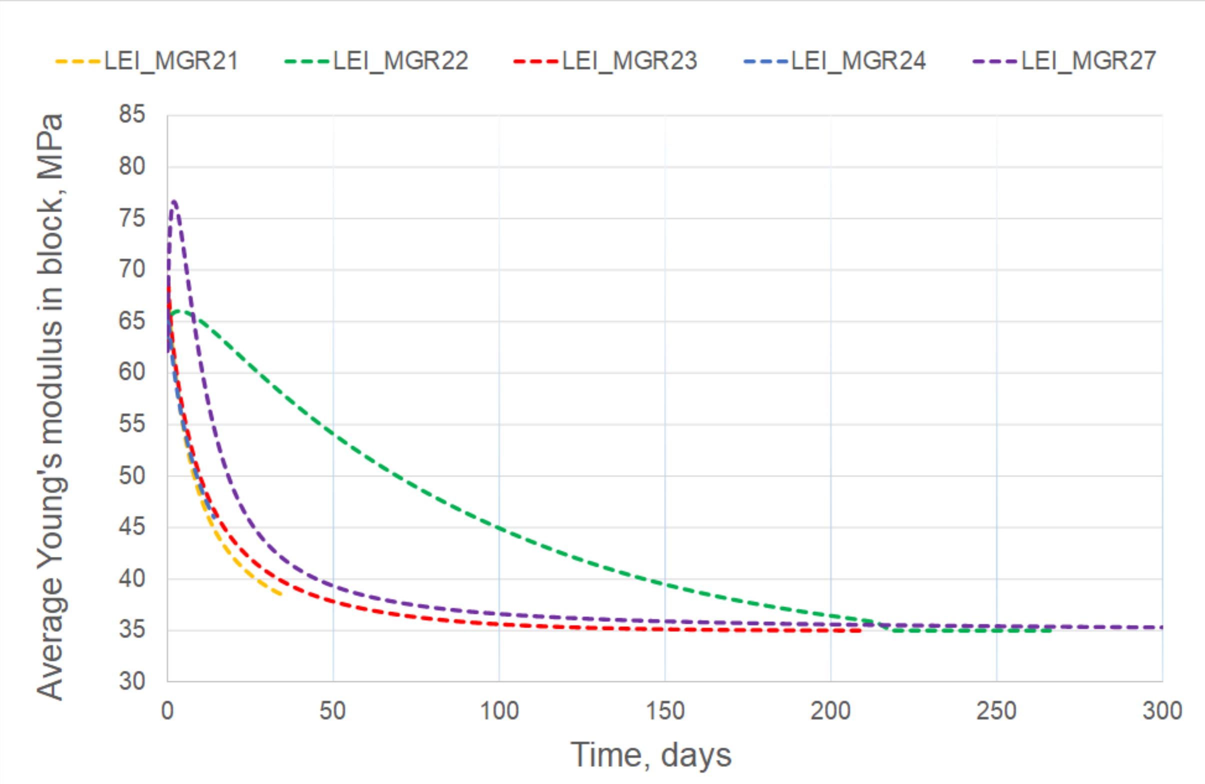

Figure 3-63: *Evolution of average Young's modulus in bentonite block for modelled test cases*

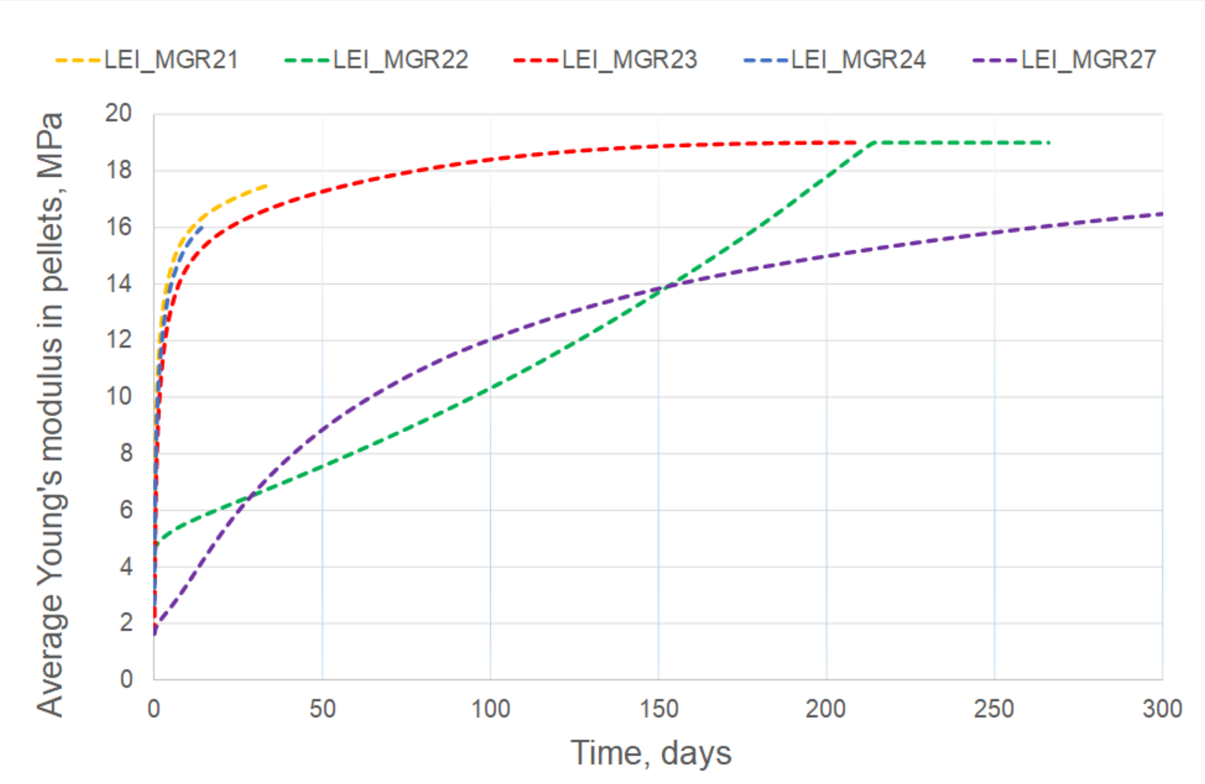

Figure 3-64: *Evolution of average Young's modulus in bentonite pellets for modelled test cases*

3.4.4 Initial and boundary conditions

Bentonite pellets layer was emplaced in the lower part of the cell and the bentonite block layer in the upper part in tests MGR21-MGR24. In the predictive test case MGR27 both layers located opposite - the pellets in the upper part of the cell and block on the lower part.

The initial conditions for modelled tests MGR21-MGR24 and MGR27 were slightly different as it could be seen in Table 3-20.

For the top, bottom and side boundaries of the model a zero-displacement condition in normal direction was set, i. e. wall friction was not taken into account in LEI model.

For the top and side boundaries no flow hydraulic conditions were set. For the bottom boundary a constant water pressure condition (p=15 kPa) for test cases MGR21, MGR23, MGR24, MGR27 or constant water inflow (0.05 cm^3/h) for test case MGR22 was imposed.

Figure 3-65 presents evolution of water intake of LEI model using different type of hydraulic conditions on bottom boundary as it was described above.

Table 3-20 Initial conditions for different modelled cases

Parameter	MGR21 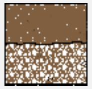		MGR22 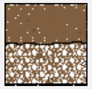		MGR23 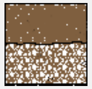		MGR24 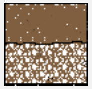		MGR27 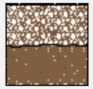	
	Pellets zone	Block zone	Pellets zone	Block zone	Pellets zone	Block zone	Pellets zone	Block zone	Pellets zone	Block zone
Initial gravimetric water content*, %	9.5	13.3	9.9	13.6	3.45	14.2	5.7	13.7	3.4	14.6
Initial degree of saturation*, -	22.6	52.1	24.1	54.6	8.6	56.0	13.8	55.2	8.6	57.5
Initial suction, Pa	$-2.03 \cdot 10^8$	$-1.07 \cdot 10^8$	$-1.61 \cdot 10^8$	$-8.43 \cdot 10^7$	$-6.65 \cdot 10^9$	$-7.42 \cdot 10^7$	$-1.21 \cdot 10^9$	$-7.98 \cdot 10^7$	$-6.65 \cdot 10^9$	$-6.49 \cdot 10^7$
Initial stress, MPa	0.01									
Temperature*, K	296.1		295.4		295.6		295.5		296.2	
Experiment duration*, days	34		266		210		14		Data not provided	

* - data from (Villar & &Talandier, 2020 ; Beacon D4.1, 2019).

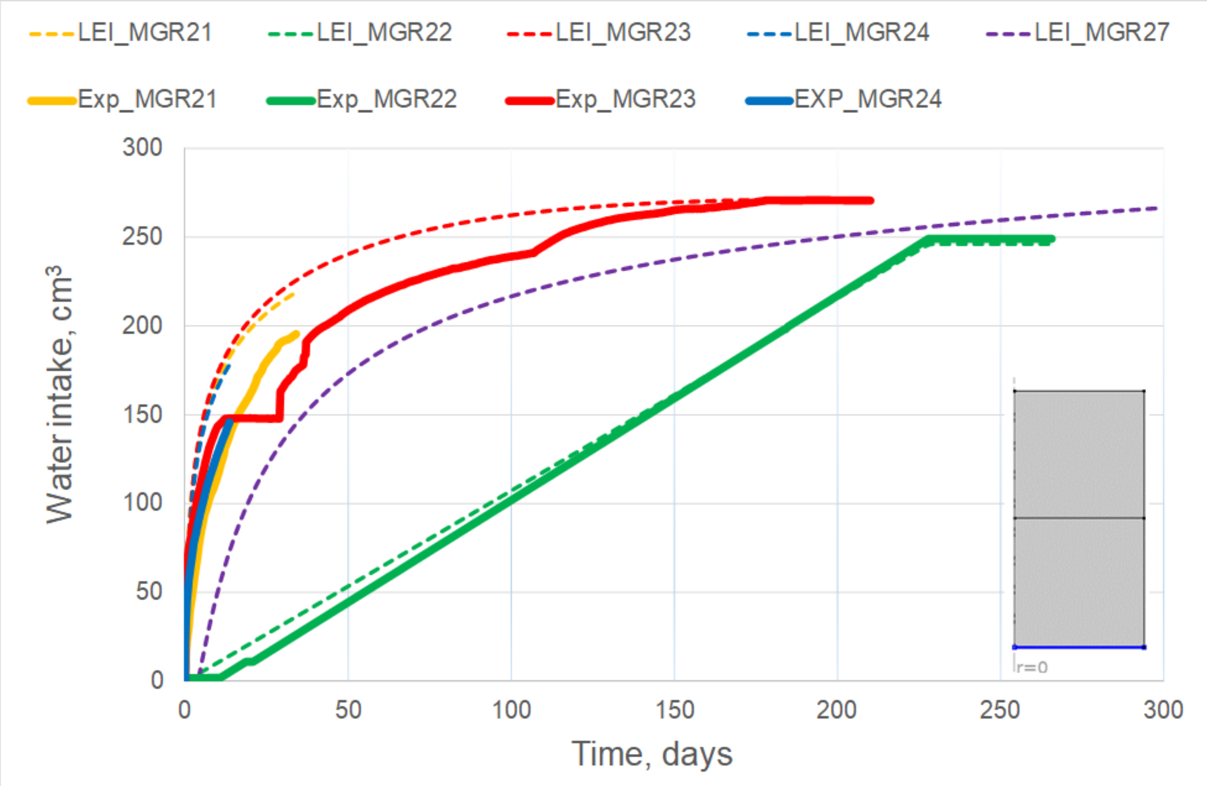

Figure 3-65: *Comparison of LEI modelling results (dashed lines) and the measurements (solid lines) of water intake to bentonite sample*

As it could be seen in Figure 3-65, different type of hydraulic conditions gave a different evolution of water intake – constant pressure gave much faster water intake than a constant inflow. As the experimental data of MGR22 and MGR23 showed, not only different evolution of water intake but also different volume of water necessary to saturate the whole samples were injected – 250 and 270 cm^3, respectively.
Very good agreement with experimental data was achieved using constant water inflow condition (test MGR22) in LEI model. Results of modelled cases using constant water pressure conditions (MGR21, MGR23-MGR24) were also in line with experimental data. Despite the fact that constant water pressure was applied for MGR27 test case as well, LEI modelling results showed that water intake was slower because the water was injected directly into bentonite block which has much lower permeability than bentonite pellets.

3.4.5 Results MGR22

In this section LEI modelling results of MGR22 test case using COMSOL Multiphysics are presented and compared to experimental data obtained by CIEMAT.
The comparison was made for several model outputs in two sub-sections: first time evolution of average degree of saturation of the whole sample and the axial stress on the top and the bottom of the sample are presented; later the analysis of gravimetric water content and dry density distribution along the sample after the dismantling of experiment (after 266 days) was performed and presented.

Time evolution of HM parameters

Average degree of saturation

In the test MGR22 a constant water inflow (0.05 cm³/h) boundary condition was applied to saturate the whole sample through the pellet zone. From water intake curves (see Figure 3-65) it could be seen that water inflow was much slower compared to other modelled cases. A half of the water volume necessary for full saturation (~125 cm³) was taken in about 120 days while it took only about 10 days in other cases (MGR21, MGR23 and MGR24). However, modelled average degree of saturation in the whole sample correlated quite well with experimental data as it could be seen in Figure 3-66. Minor differences were obtained during the first 100 days and after full saturation was reached. Within COMSOL Multiphysics model the degree of saturation is prescribed in such a way, that it could reach the maximum value of 1.0, while the experimental measurements reported it as 1.05. Time of full saturation was caught well – after about 226 days according to experimental data and after about 216 days in LEI model.

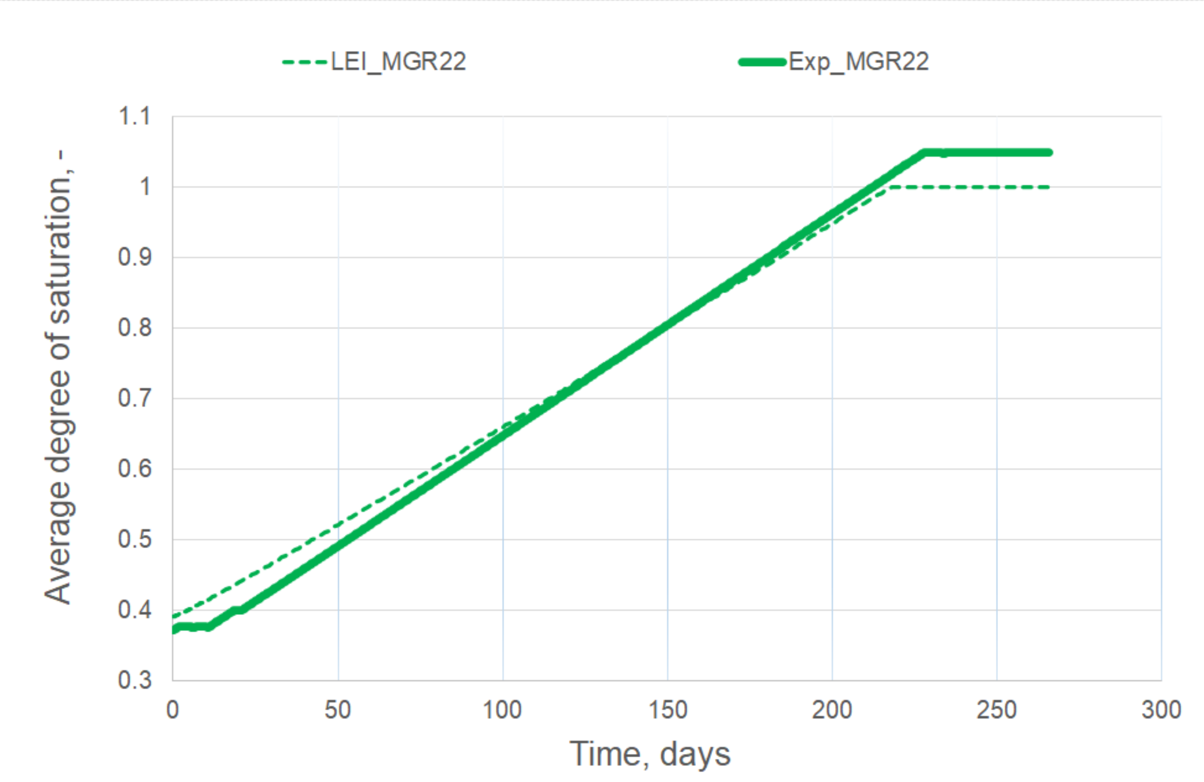

Figure 3-66: *Comparison of LEI modelling results (dashed line) and the measurements (solid line) of average degree of saturation in the whole sample*

Axial pressure

The measured axial pressure on the top (bentonite block) of the MGR22 sample and modelled axial pressure on the top (bentonite block) and the bottom (bentonite pellets) of the sample are presented in Figure 3-67. Experimental data showed that axial pressure development on the top of bentonite block could be segmented in four stages:

- Development of pressure and reaching of the first peak (about 2.2 MPa) during the first 80 days (in parallel - the average degree of saturation of the whole sample rose up to 0.58);
- Plateau of the pressure during the next 120 days (in parallel - the average degree of saturation of the whole sample rose up to 0.96);
- Steep increase of pressure and reaching of the second peak (about 3 MPa) during the next 27 days (in parallel – the whole sample becomes fully saturated);
- Plateau of the pressure till the end of experiment, while sample was fully saturated and no additional water was injected.

Despite of the peak value of axial pressure on the top of bentonite block was caught well in LEI model, but the overall shape of this curve was different. The modelled axial pressure on the bottom of the sample (in pellet zone) were the same as in the block zone, while wall friction was not taken into account in LEI model. CIEMAT did not measured axial pressure on the bottom of the sample, but according to measured data from similar POSIVA 1c experiment in BEACON (Talandier, 2018) it could be expected that axial pressure in pellet zone would be lower than in block zone. However, LEI model predicts well the peak pressure in the whole sample that is crucial for repository safety.

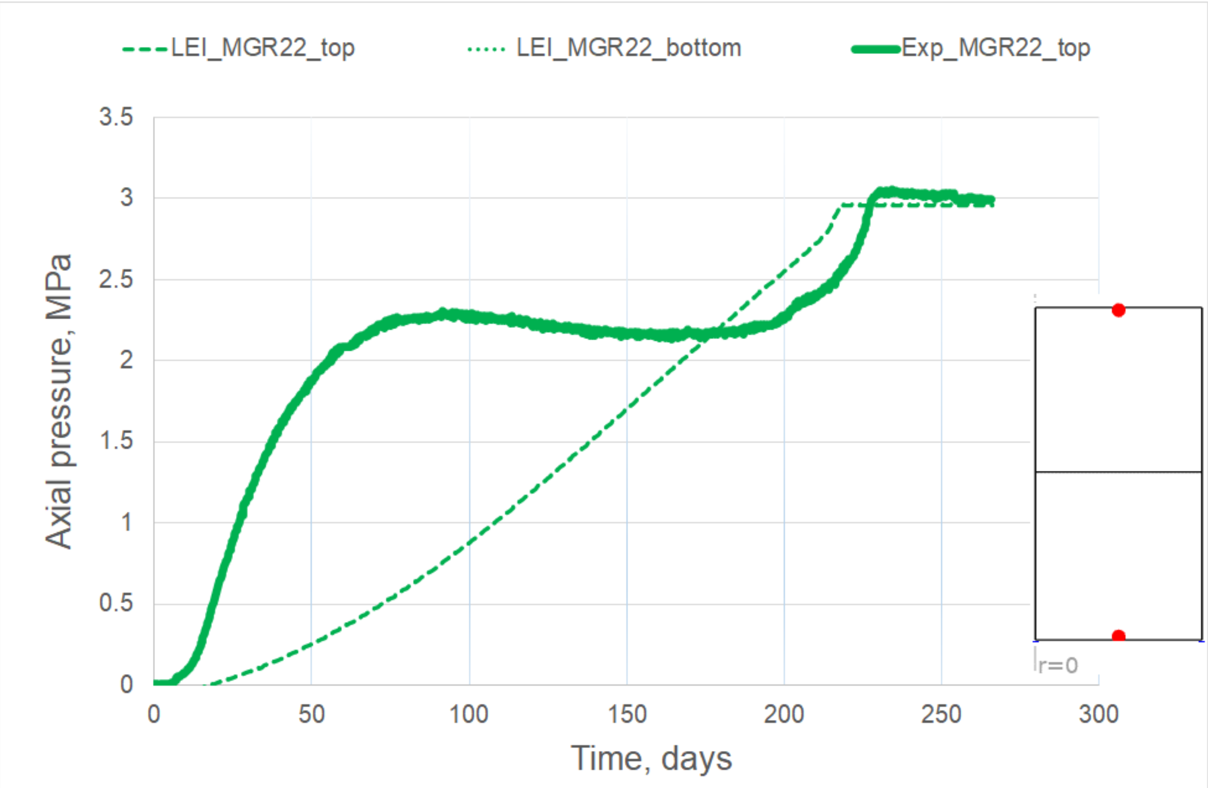

Figure 3-67: *Comparison of LEI modelling results (dashed/dotted lines) and the measurements (solid line) of axial pressure on the top and the bottom of the sample*

Distribution of parameter values along the distance from hydration surface

Vertical line at r=0.025 m was selected for the comparison of modelling results and measurements obtained after the final dismantling of experiment (after 266 days).

Gravimetric water content

Modelling results and measured data of the distribution of gravimetric water content in bentonite along the distance from hydration surface is presented in Figure 3-68. The initial values in each bentonite zone are indicated with black horizontal lines as well. As it could be seen LEI modelling results correlated quit well with experimental data. Slightly higher gravimeter water content was obtained in pellet zone compared to the experimental measurements.

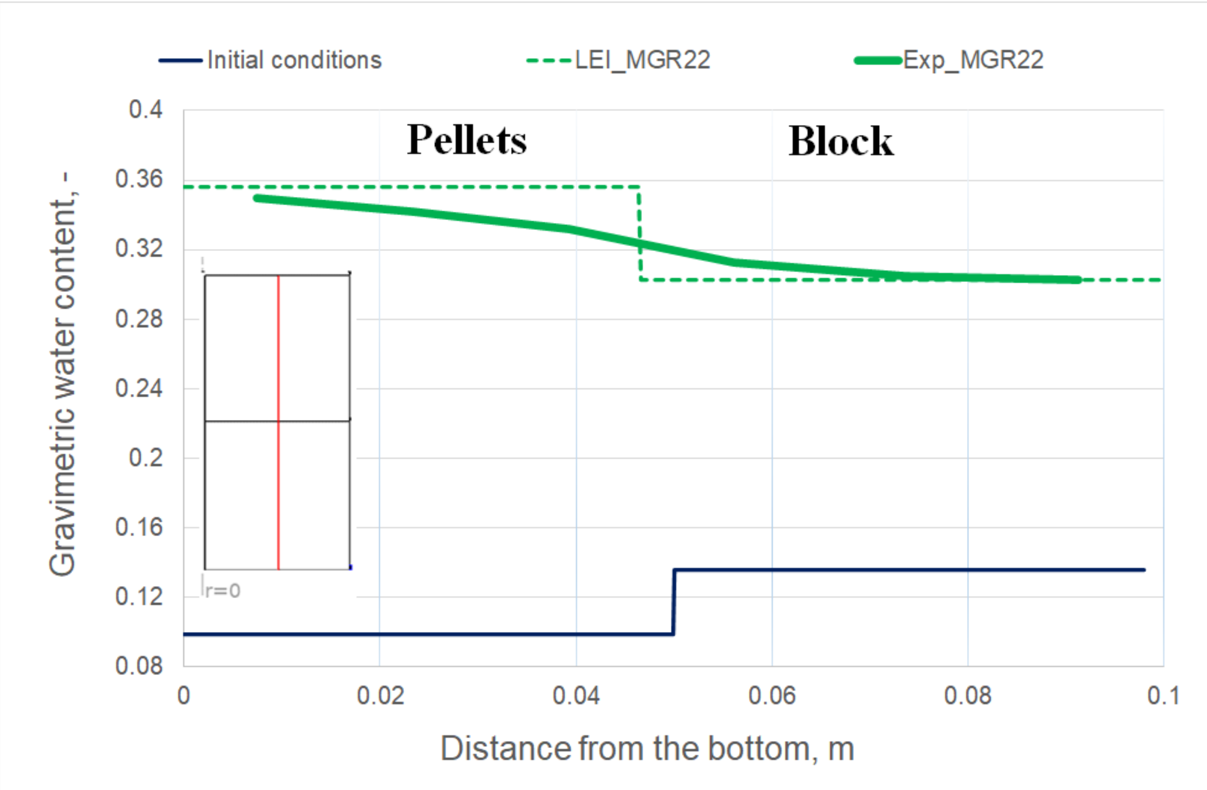

Figure 3-68: *Comparison of LEI modelling results (dashed lines) and the measurements (solid line) of gravimetric water content distribution along the sample*

Dry density

Modelling results and measured data of the distribution of dry density in bentonite along the distance from hydration surface is presented in Figure 3-69. The initial values in each bentonite zone are indicated with black horizontal lines as well. As it could be seen LEI distribution differed from the measured one. Two uniform distributions of dry density were obtained in both bentonite zones in LEI model, as experimental data showed gradual increase of dry density from pellet to block zones. However, the final values of dry density in LEI model were similar to experimental data, especially in pellets zone.

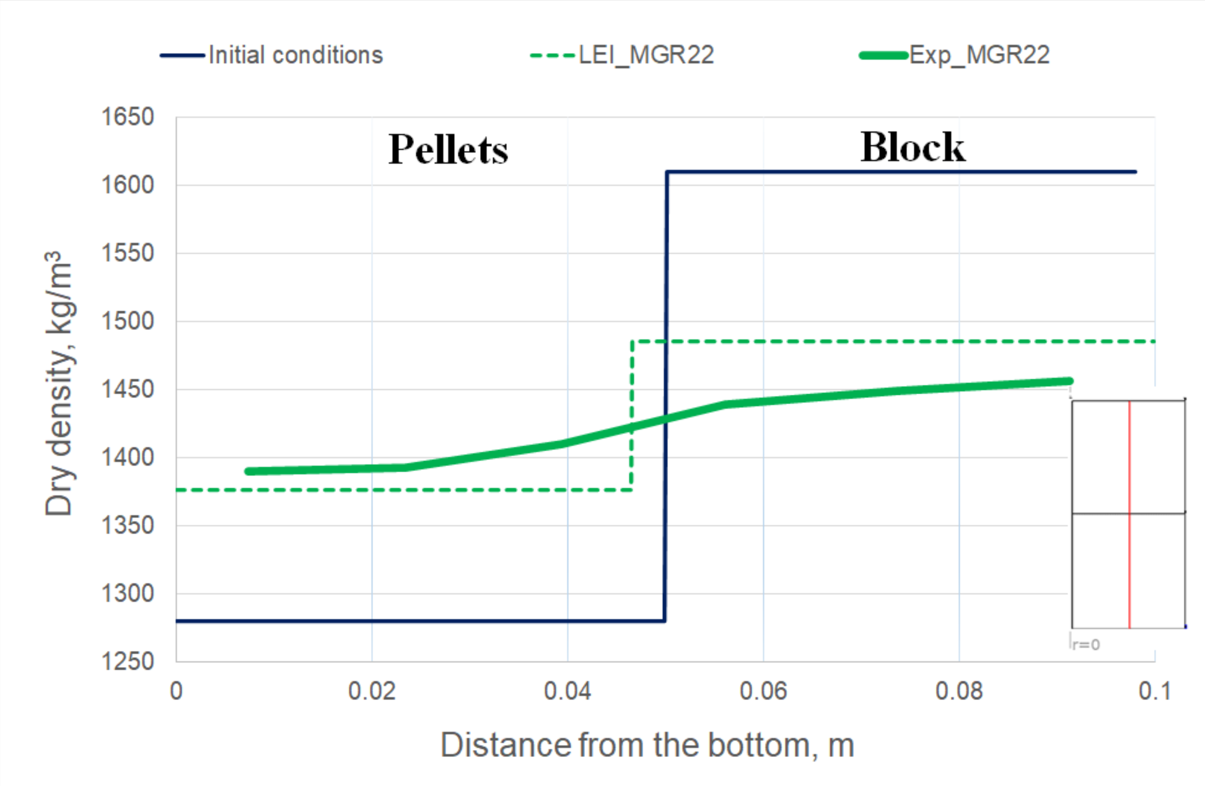

Figure 3-69: *Comparison of LEI modelling results (dashed lines) and the measurements (solid line) of dry density distribution along the sample*

3.4.6 Results MGR23

In this section LEI modelling results of MGR23 test case using COMSOL Multiphysics are presented and compared to experimental data obtained by CIEMAT. In addition, the results of MGR21 and MGR24 test cases are presented and analysed, while these cases are identical to MGR23 (it's the same test as MGR23 repeated twice with some minor differences of initial porosity and degree of saturation, see Table 3-19 and Table 3-20) but duration of these experiments was shorter – 34 and 17 days, respectively.
The comparison was made for several model outputs in two sub-sections: first time evolution of average degree of saturation of the whole sample and the axial stress on the top and bottom of the sample are presented; later the analysis of distribution of permeability, suction, gravimetric water content and dry density along the sample at selected times was performed and presented.

Time evolution of HM parameters

Average degree of saturation

A constant pressure (15 kPa) boundary condition was applied to saturate the whole sample through the pellet zone in all three tests (MGR21, MGR23 and MGR24). From water intake curves (see Figure 3-65) it could be seen that water inflow was faster compared to constant water inflow boundary condition (test case MGR22). The modelled time evolution of average degree of saturation in the whole samples are presented in Figure 3-70. As it could be seen the shapes of the modelled and experimental curves are similar, however slightly faster saturation was obtained in LEI model compared to experimental data in all three cases. The time of full saturation in

MGR23 test was estimated after about 175 days while in LEI model – after about 150 days. The modelled average degree of saturation at the end of MGR21 test (after 34 days) was 0.91, while experimental data showed 0.88 value. The corresponding saturation values at the end of MGR24 test (after 17 days) were 0.8 and 0.72, respectively.

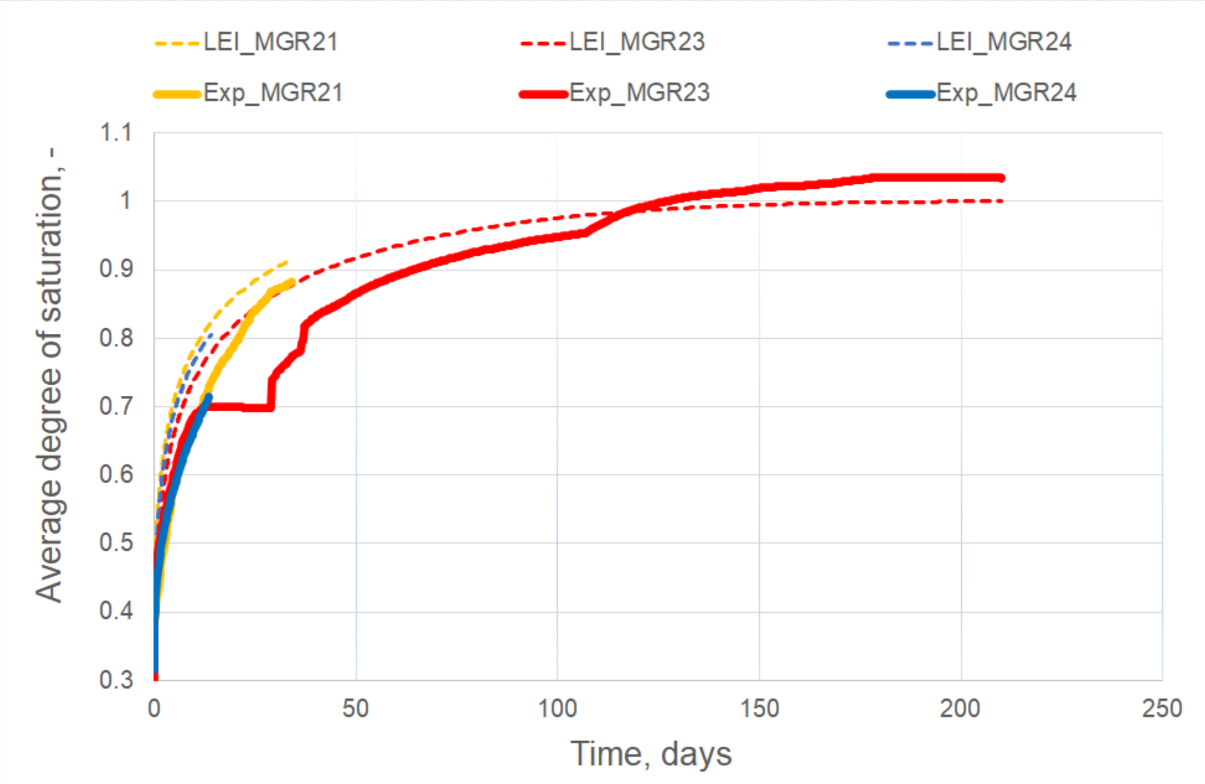

Figure 3-70: *Comparison of LEI modelling results (dashed coloured lines) and the measurements (solid-coloured lines) of average degree of saturation in the whole samples*

Swelling pressure

The measured and modelled axial pressure on the top (bentonite block) of the MGR21, MGR23 and MGR24 samples are presented in Figure 3-71. Experimental data of all three cases showed that the axial pressure on the top of bentonite block had sharp initial increase. In the longest test (MGR23) the peak was reached after 30-40 days and later steadily increased again until full saturation was reached, with a stable pressure value of about 3 MPa. Despite the peak value of axial pressure on the top of bentonite block was caught well in LEI model in MGR23 test case, but overall shape of this curve was slightly different - initial increase was not so sharp according to LEI modelling results.

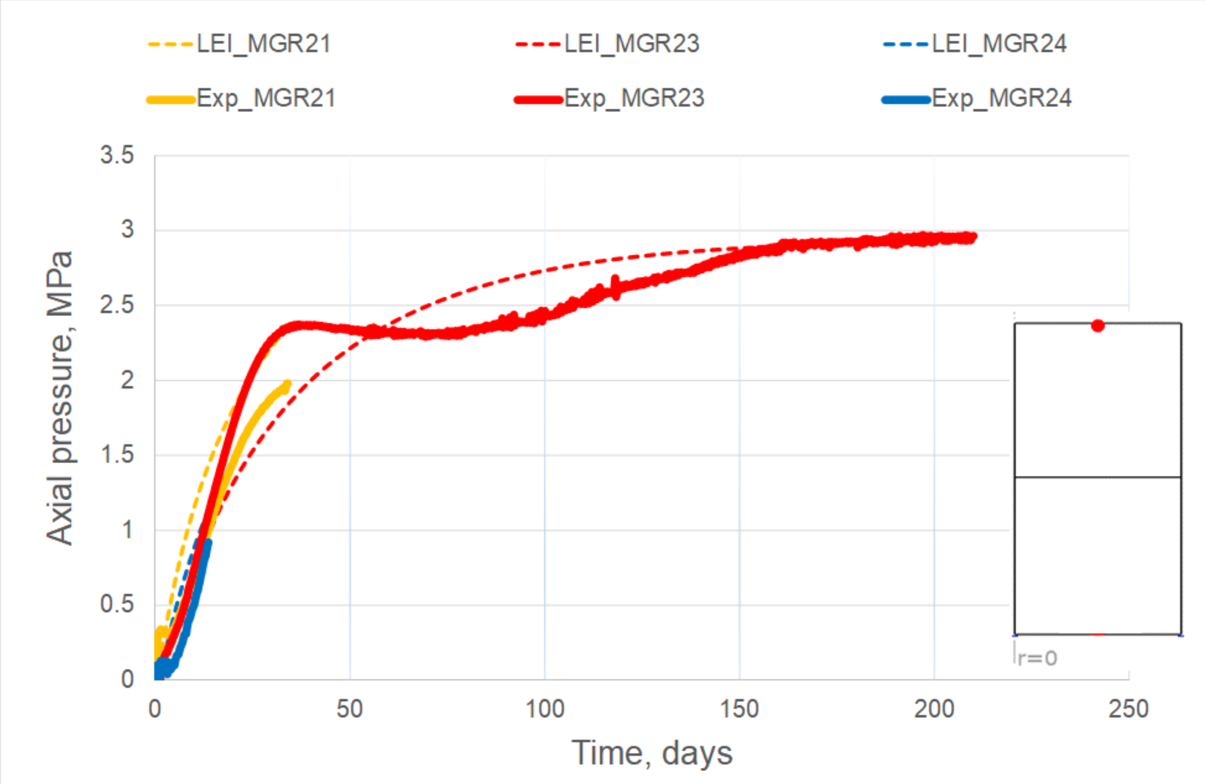

Figure 3-71: *Comparison of LEI modelling results (dashed coloured lines) and the measurements (solid-coloured lines) of axial pressure on the top of the samples*

Distribution of parameter values along the distance from hydration surface

Vertical line at r=0.025 m was selected for the comparison of modelling results and measurements obtained after the final dismantling of experiments MGR21, MGR23 and MGR24 (after 34, 14 and 210 days, respectively).

<u>Permeability and suction</u>

Permeability is a function of relative permeability function, degree of saturation and dry density in separate materials. Van Genuchten relationship relates the degree of saturation and the suction. Such a relationship differs for separate materials. Distributions of modelled permeability and suction in bentonite along the distance from hydration surface at different times are presented in Figure 3-72 and Figure 3-73.

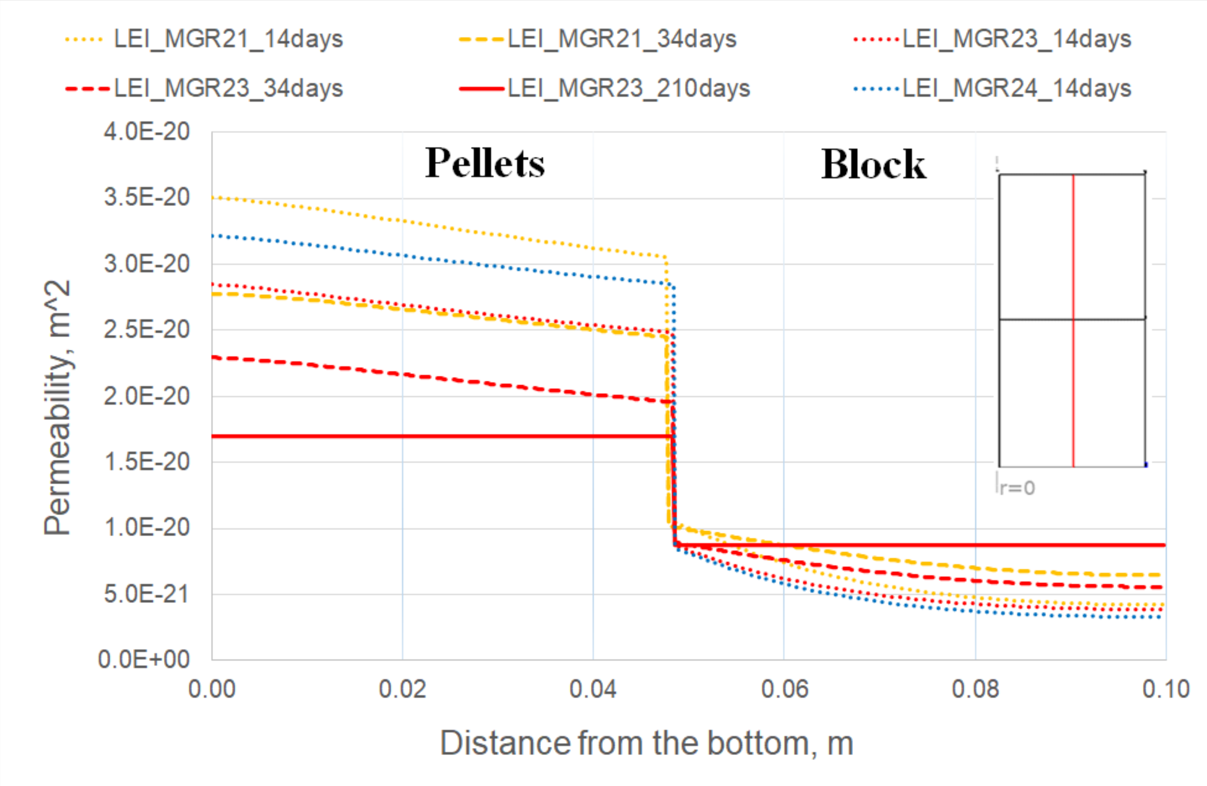

Figure 3-72: *Comparison of LEI modelling results of permeability distribution along the samples MGR21, MGR23 and MGR24 at different times*

As it could be seen from Figure 3-72, the distribution of permeability at each selected time strongly depends on material type and especially on dry density distribution (permeability (or hydraulic conductivity) in LEI model depends on dry density, see Table 3-19). It is clearly seen from MGR23 results after 210 days when sample was fully saturated and the shape of permeability distributions in both materials was horizontal lines, the same as the dry density distributions in Figure 3-75. Degree of saturation also influenced on the permeability values through relative permeability functions which were set different in both materials (see Table 3-19). Both dependencies influenced on different distributions of permeabilities in separate bentonite zones during all simulation time. In bentonite pellets the permeability varied between $3.5 \cdot 10^{-20}$ (MGR21, 14 days) and $1.7 \cdot 10^{-20}$ (MGR23, 210 days). In bentonite block the permeability varied between $9.0 \cdot 10^{-21}$ (MGR23, 210 days) and $3.3 \cdot 10^{-21}$ (MGR24, 14 days).

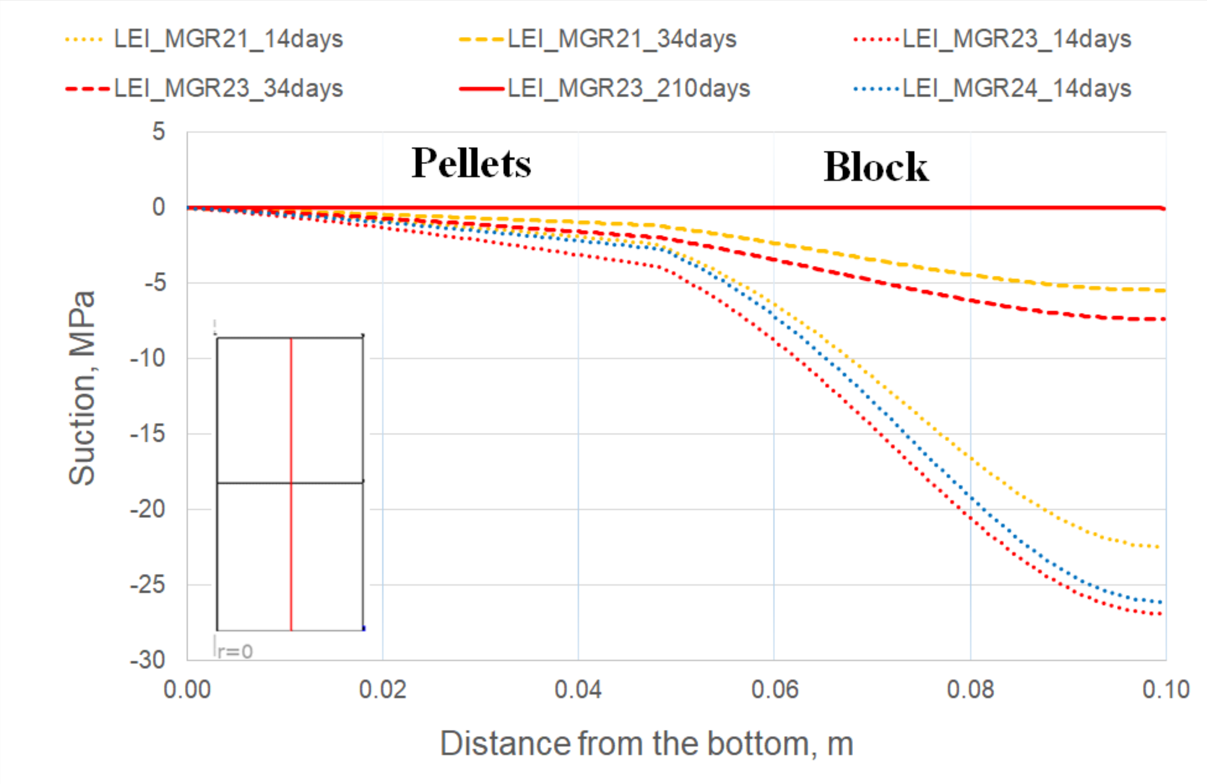

Figure 3-73: *Comparison of LEI modelling results of suction distribution along the samples MGR21, MGR23 and MGR24 at different times*

As it could be seen from Figure 3-73, the distribution of suction at each selected time strongly depends on material type as different values for Van Genuchten parameters were used to describe behaviour of bentonite block and pellets (see Figure 3-62). Degree of saturation also depend on suction values especially in the lower saturation zones – for example these values on the top of bentonite block after 14 days varied between -27 MPa (MGR23) and -22.4 MPa (MGR21) and after 34 days varied between -7.8 MPa (MGR23) and -5.5 MPa (MGR21). In parallel, the suction values varied around zero (fully saturated conditions) on the bottom of bentonite pellets in all three cases at analysed times. Comparing suction distributions at the same times between different modelled cases, only minor differences obtained while values of degree of saturation at particular times were very similar (see Figure 3-70).

<u>Gravimetric water content</u>

Modelling results and measured data of the distribution of gravimetric water content in bentonite along the distance from hydration surface in all three cases (after 34, 14 and 210 days) are presented in Figure 3-74. The initial values in each bentonite zone are indicated with black horizontal lines as well.

As it could be seen LEI modelling results of MGR23 case correlated quit well with experimental data. However, LEI model overestimated gravimetric water content in MGR21 and MGR24 test cases especially in bentonite block zone.

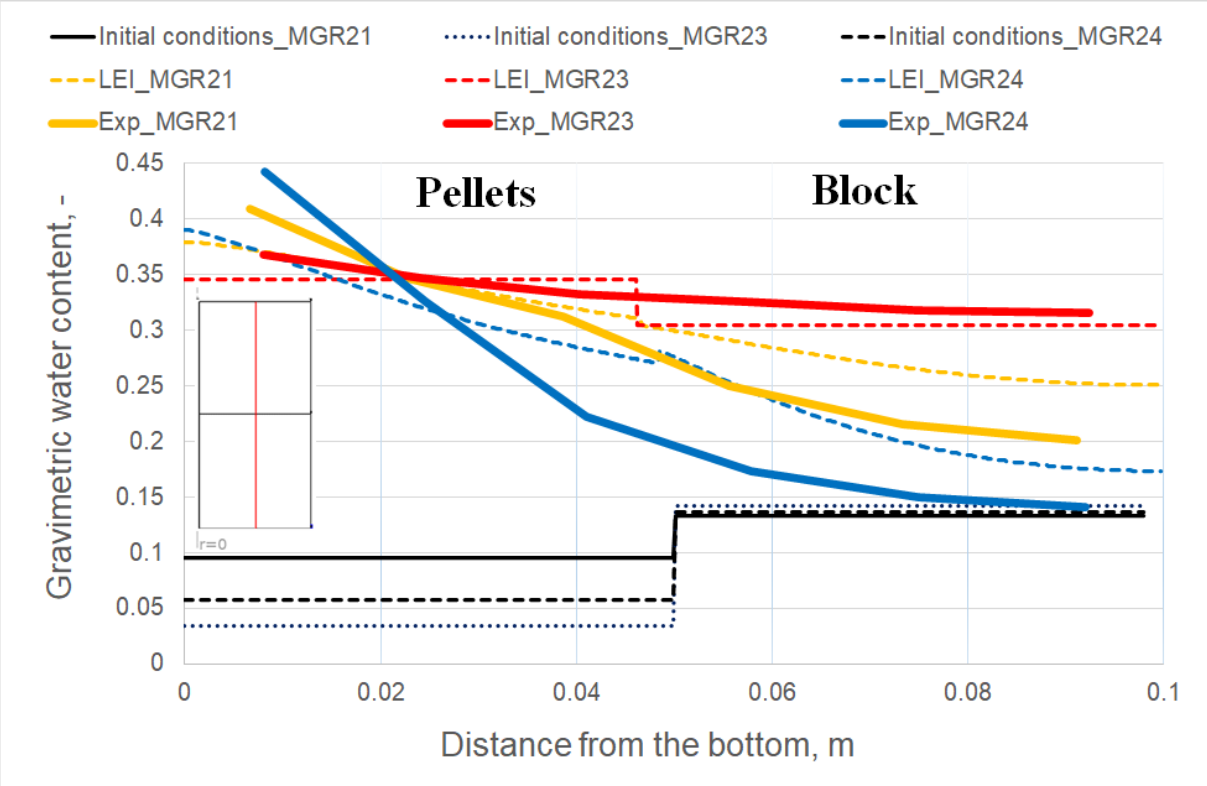

Figure 3-74: *Comparison of LEI modelling results (dashed coloured lines) and the measurements (solid-coloured lines) of gravimetric water content distribution along the samples*

<u>Dry density</u>

Modelling results and measured data of the distribution of dry density in bentonite along the distance from hydration surface in all three cases (after 34, 14 and 210 days) are presented in Figure 3-75. The initial values in each bentonite zone are indicated with black horizontal lines as well.

As it could be seen LEI modelled distributions differed from the measured ones, especially in MGR23 case where almost uniform distribution of dry density was obtained in both bentonite zones, while experimental data showed gradual increase of dry density from pellet to block zones. However, the final values of dry densities in LEI model were similar to experimental data, especially in pellets zone for all analysed cases.

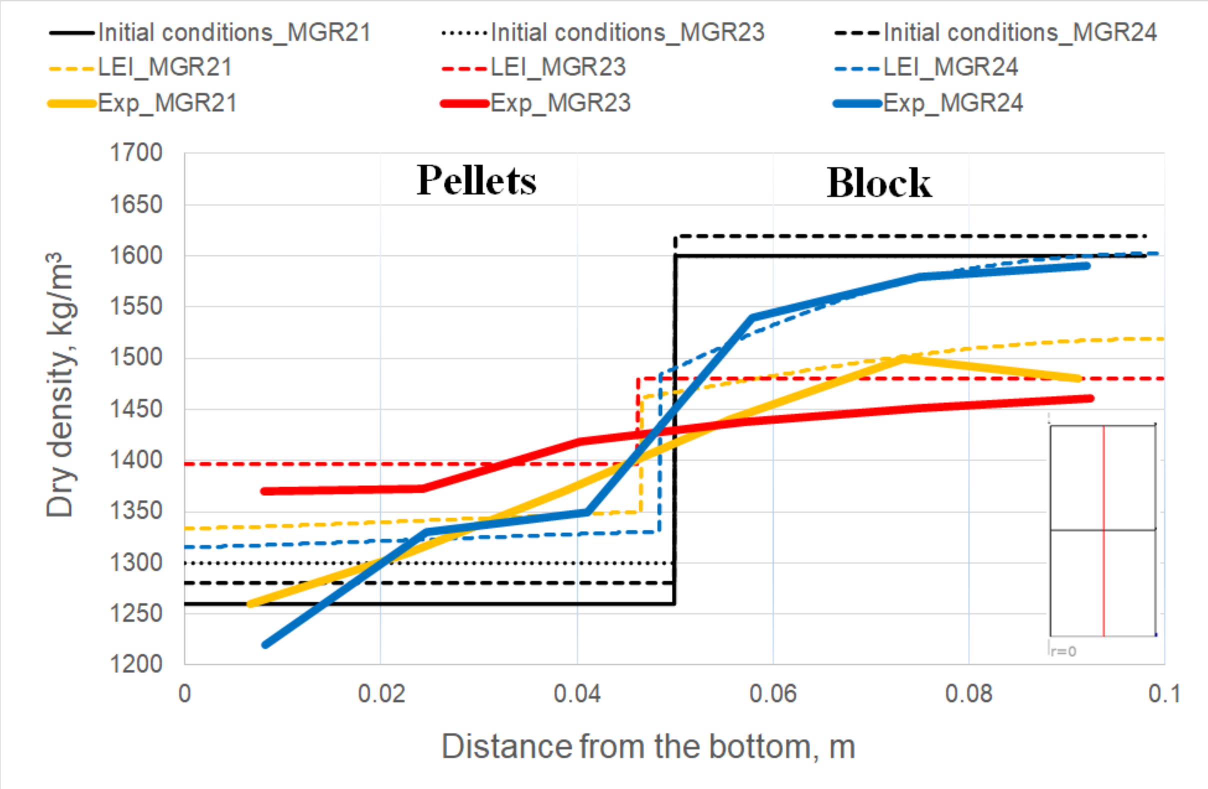

***Figure 3-75:** Comparison of LEI modelling results (dashed coloured lines) and the measurements (solid-coloured lines) of dry density distribution along the samples*

3.4.7 Results MGR27

In this section LEI modelling results of MGR27 test case using COMSOL Multiphysics are presented. Its predictive modelling of experiment with LEI model without providing experimental results in advance.
The comparison was made for several model outputs in two sub-sections: first time evolution of average degree of saturation of the whole sample and the axial stress on the top and the bottom of the sample are presented; later the analysis of gravimetric water content and dry density distribution along the sample after 300 days was performed and presented.

Time evolution of HM parameters

<u>Average degree of saturation</u>

A constant pressure (15 kPa) boundary condition was applied to saturate the whole sample through the bentonite block zone in MGR27 test case. From the water intake curves (see Figure 3-65) it could be seen that water inflow was slower compared to other cases where constant pressure boundary conditions were set (MGR21, MGR22-MGR23) while the water was injected direct to bentonite block having much lower permeability as bentonite pellets. The modelled evolutions of average degree of saturation in the whole sample and particular bentonite zones are presented in Figure 3-76. As it could be seen the whole sample was not fully saturated after 300 days and the average degree of saturation reached 0.93. The evolution of degree of saturation in particular bentonite zones was different – bentonite block was almost fully saturated after 200 days, while saturation of bentonite pellets reached 0.87 after 300 days.

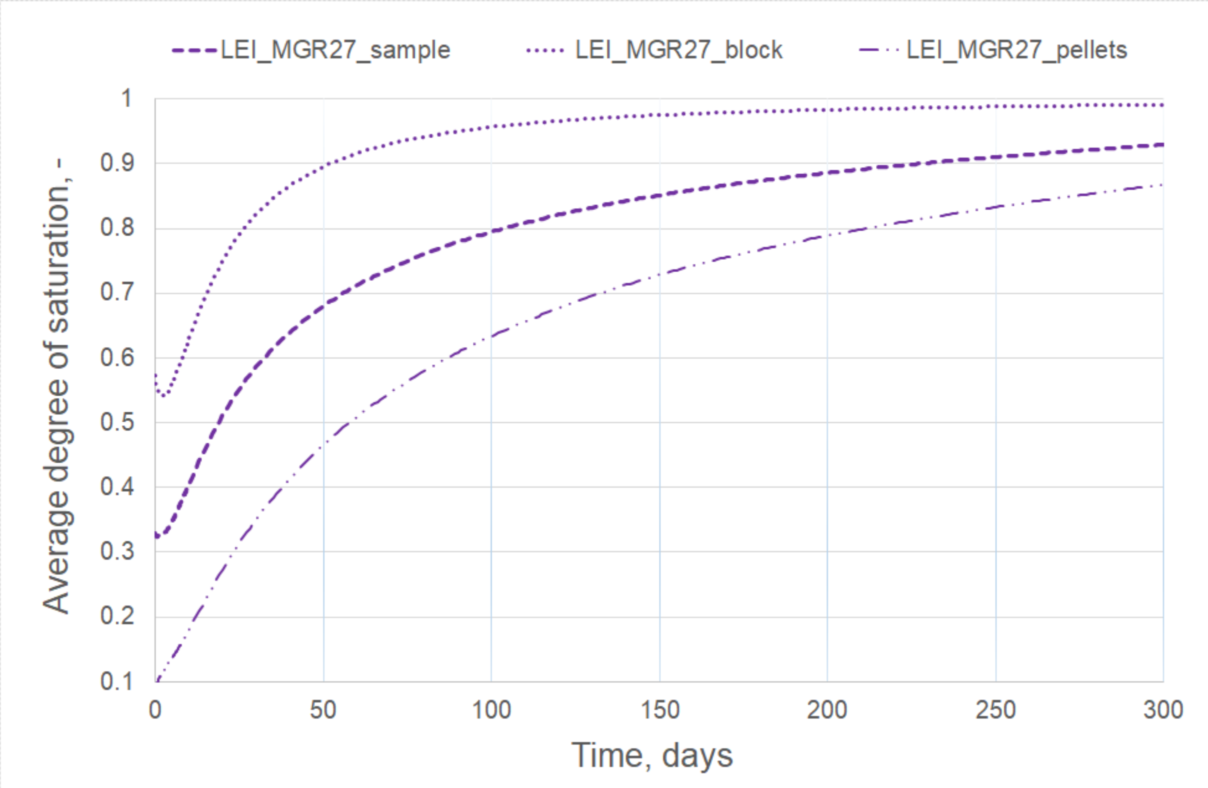

Figure 3-76: *LEI modelling results of average degree of saturation in the whole sample and particular bentonite zones*

<u>Swelling pressure</u>

The modelled axial pressure on the top (bentonite pellets) and the bottom (bentonite block) of the sample are presented in Figure 3-77. As it could be seen the evolution of axial pressure in both zones was the same while wall friction was not taken into account in LEI model. The profile of axial pressure could be divided in two steps – first sharp increase in the first 70 days (the pressure reached 1.5 MPa), later monotonic increase up to 2.5 MPa. Probably this value is final one, because bentonite block was almost fully saturated (see in Figure 3-76).

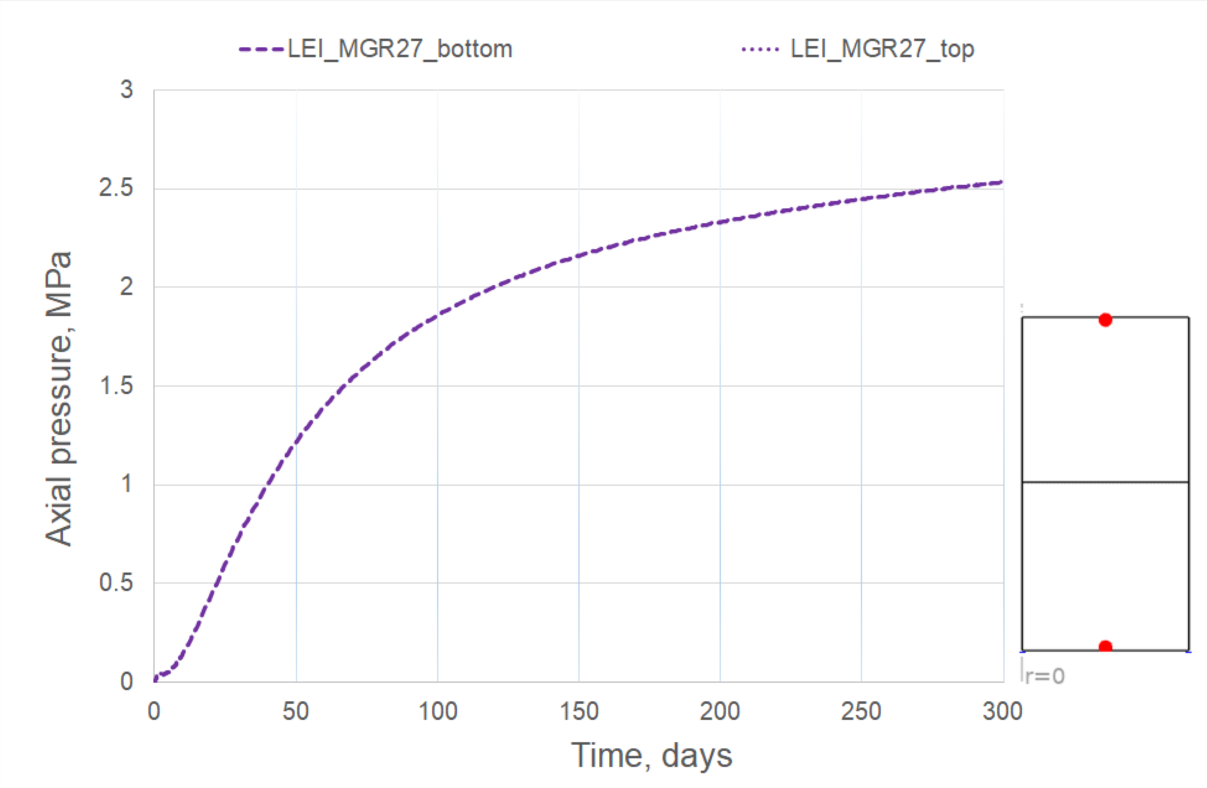

Figure 3-77: *LEI modelling results of axial pressure on the top and the bottom of the sample*

Distribution of parameter values along the distance from hydration surface

Vertical line at r=0.025 m was selected to present modelling results after 300 days.

<u>Gravimetric water content</u>

LEI modelling results of the distribution of gravimetric water content in bentonite along the distance from hydration surface is presented in Figure 3-78. The initial values in each bentonite zone are indicated with black horizontal lines as well. As it could be seen much higher gravimetric water content were obtained after 300 days in both bentonite zones compared to the initial values. Almost gradual distribution around 0.3 value was determined in both bentonite zones.

Figure 3-78: *LEI modelling results of gravimetric water content distribution along the sample*

<u>Dry density</u>

Modelling results of the distribution of dry density in bentonite along the distance from hydration surface is presented in Figure 3-79. The initial values in each bentonite zone are indicated with black horizontal lines as well. Two uniform distributions of dry density were obtained in both bentonite zones as in previous test cases. However, dry density in both zones changed significant:

- Increased from 1300 kg/m^3 up to about 1400 kg/m^3 in pellet zone;
- Decreased from 1600 kg/m^3 to about 1475 kg/m^3 in block zone.

As it could be seen from the figure bentonite block swelled toward the pellets zone of about 4 cm.

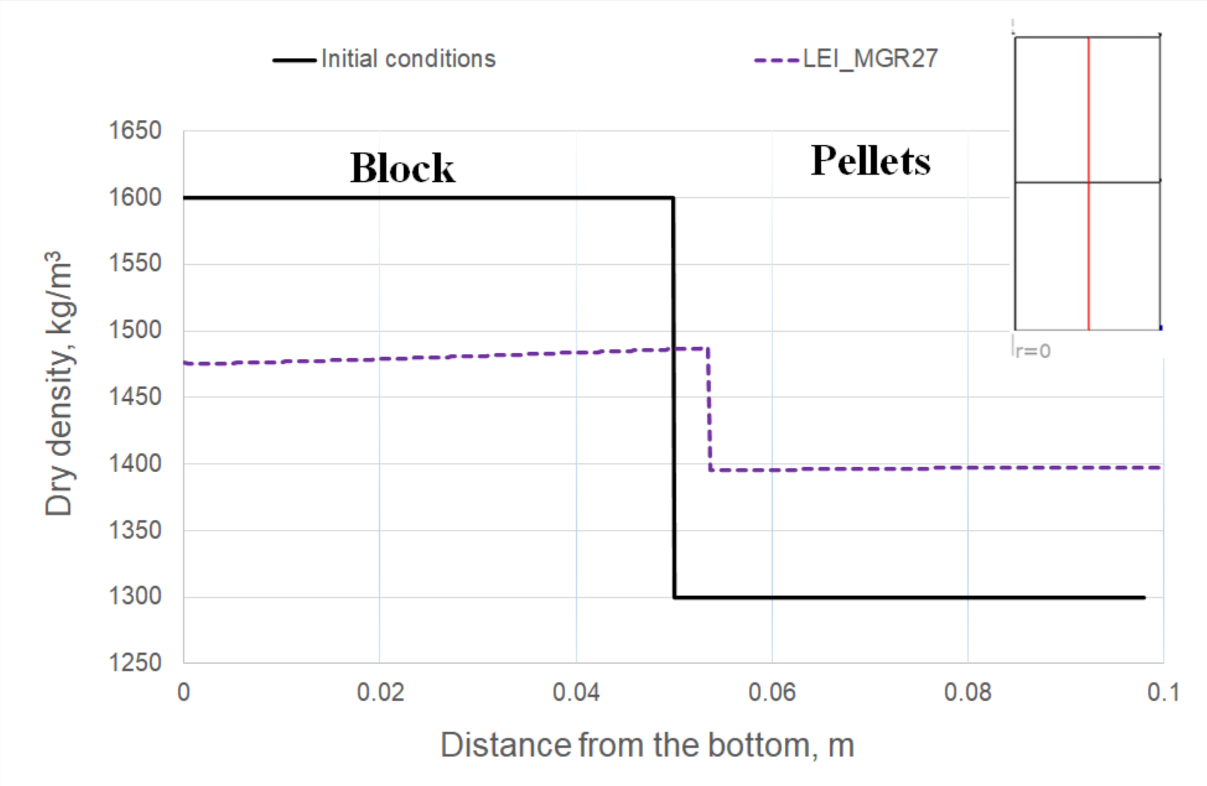

Figure 3-79: *LEI modelling results of dry density distribution along the sample*

3.4.8 Discussion

The five different bentonite hydration experiments have been successfully modelled by Lithuanian Energy Institute team applying model developed in BEACON WP3 in numerical tool COMSOL Multiphysics v5.6. For hydro-mechanical behaviour of FEBEX bentonite (compacted block and pellets mixture) Richard 's equation and linear elastic swelling model was coupled.

The selection of the values of HM parameters for bentonite block and pellets were based on available literature. However, few empirical expressions for mechanical parameters necessary for LEI model such as swelling coefficient in block zone and Young's modulus in both bentonite zones were obtained as a result of model calibration with experimental data from tests MGR21-MGR24.

In general, there is good agreement between LEI modelling results and experimental data, especially for water intake and average degree of saturation in all analysed MGR test cases. Despite the modelled evolution of axial pressure on the top of the bentonite block was different to experimental ones achieved in MGR22 and MGR23, but the peak value of about 3 MPa was represented well in LEI model. The same axial pressure profiles were obtained in the bottom and the top of the sample, as the wall friction was not taken into account in the model. However, the peak pressure in the whole sample was predicted well that is crucial for repository safety. Modelled distributions of gravimetric water contents and dry densities in bentonite along the distance from hydration surface differed from experimentally measured ones to some extent. However, the final values of these parameters are in line with experimental data.

Taking into account obtained results, it could be concluded that LEI model could be used for similar analysis in the future. However, for more precise modelling of dry density and gravimetric water content distributions, further investigations of behaviour of bentonite material in different forms and subsequent model development are needed.

3.5 Quintessa

3.5.1 Description of the models

The full description of Quintessa's coupled THM model can be found in Appendix F of Deliverable 3.1. In summary, the model uses an exponential curve parameterised by two constants (p_0 [MPa] and λ [-]) to represent the relationships between swelling pressure & dry density, suction & water content, and void ratio & vertical stress. This is of the form:

$$p = p_0 \cdot \exp\left(-\frac{e}{\lambda}\right)$$

where p is swelling pressure, stress or suction [MPa] and e is void ratio [-], which can also be expressed in terms of dry density or saturated water content.

The model is calibrated by fitting the parameters p_0 and λ to swelling pressure, water retention and oedometer data for the particular bentonite. This model has previously been applied to MX-80 and FEBEX bentonites.

The model uses a simple single-porosity formulation. No specific adaptations are used to model bentonite pellets; these are modelled in exactly the same way as block bentonite, with a reduced density used to represent the averaged bulk properties of the pellets and voids between them.

The model has been implemented in the multi-physics finite volume/mixed element code QPAC (Maul, 2013), together with a variety of boundary conditions to allow it to be applied to a range of bentonite experiments and tests. As described in D3.1, this includes the ability to model friction and swelling into void spaces.

3.5.2 Geometry and discretization

The geometry of the experiments is specified in the task specification (Deliverable 5.3.1). Each test is modelled as a cylinder with radius 50 mm. There is no radial or azimuthal discretisation; only the variation in the axial direction is of interest. Each test is discretised into 10 axial compartments: 5 corresponding to the bentonite block and 5 for the bentonite pellets (Figure 3-80).

For tests MGR22 and MGR23, the pellets are below the bentonite block. In MGR22, the initial height of the pellets is 5.039 cm and the initial height of the block is 4.939 cm, giving a total initial volume of 783.67 cm^3. In MGR23, the initial height of the pellets is 5.0 cm and the initial height of the block is 4.984 cm, giving a total initial volume of 784.14 cm^3. For test MGR27, the pellets are above the bentonite block. The initial heights of the pellets and block are 5 cm each, giving a total volume of 785.40 cm^3.

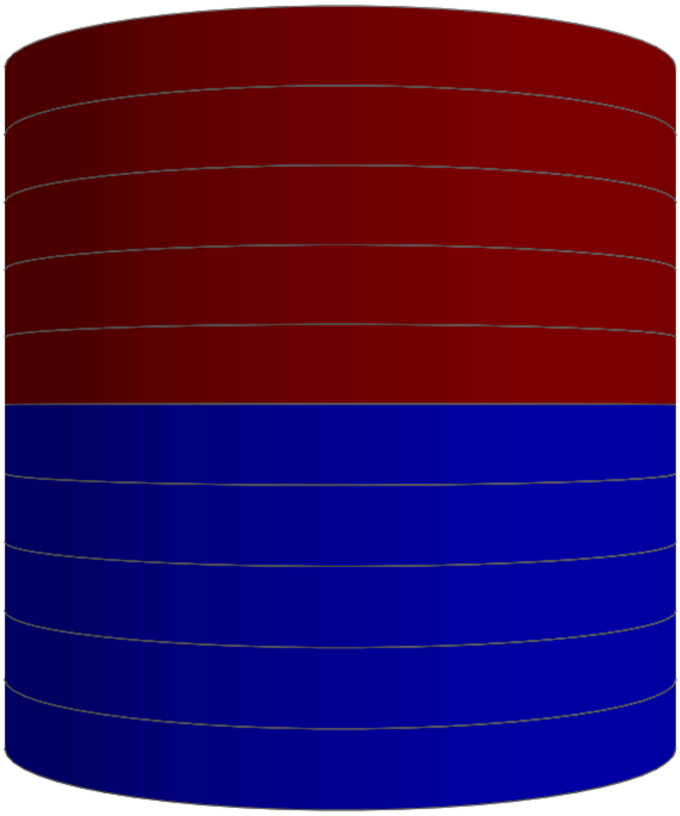

Figure 3-80: *Geometry and discretisation of the 1D QPAC model. In tests MGR22 and MGR23, the blue region represents pellets and the red region represents block bentonite. In test MGR27, the blue region represents block bentonite and the red region represents pellets.*

3.5.3 Input parameters

Apart from the initial conditions described in Section 3.5.4, the material parameters used to describe the FEBEX bentonite are entirely unchanged from the parameters used in the last task (5.2) to model the FEBEX experiment. These parameters were originally taken from the FEBEX experiment specification (ENRESA, 2000) where available, and the ILM parameters were calibrated to water retention, swelling and oedometer data for FEBEX bentonite (Thatcher, 2017). No further parameter calibration has been done for this specific set of tests. These tests are carried out at a fixed temperature so many of the thermal processes and parameters (e.g. vapour diffusivity) used in the FEBEX model are not needed to model these tests.

The parameters are repeated in Table 3-21 for convenience.

Table 3-21 Parameters used to describe FEBEX bentonite.

Parameter	Value	Units	Reference
Thermal Parameters			
Specific Heat Capacity, water [J kg^{-1} K^{-1}]	4183		Thatcher, 2017
Specific Heat Capacity, bentonite [J kg^{-1} K^{-1}]	1100		Thatcher, 2017
Specific Heat Capacity, vapour [J kg^{-1} K^{-1}]	1850		Thatcher, 2017
Thermal Conductivity [W m^{-1} K^{-1}]	$\frac{0.57-1.28}{1+\exp\left(\frac{S_w-0.65}{0.1}\right)}+1.28$		ENRESA, 2000
Mechanical Parameters			
Grain Density, bentonite [kg m^{-3}]	2700		ENRESA, 2000
Poisson's Ratio [-]	0.27		Thatcher, 2017
Initial Bulk Modulus [MPa]	100		Thatcher, 2017
Bulk Modulus Scaling Factor [-]	30		Thatcher, 2017
ILM p_0 [MPa]	$-7.895[\mathrm{MPa}\cdot\mathrm{C}^{-1}]\cdot T+1674[\mathrm{MPa}]$		Thatcher, 2017
ILM $1/\lambda$ [-]	-7		Thatcher, 2017
Hydraulic Parameters			
Tortuosity [-]	0.8		ENRESA, 2000
Hydraulic conductivity [m s^{-1}]	$\begin{cases}10^{-6\cdot\rho_d-4.09}, \rho_d\leq 1.47[g\cdot cm^{-3}]\\10^{-2.96\cdot\rho_d-8.57}, \rho_d> 1.47[g\cdot cm^{-3}]\end{cases}$		ENRESA, 2000

As a sensitivity test, friction was applied to the curved boundary of the cylinder in some of the models. In the absence of data, these sensitivity calculations used a friction coefficient of 0.3.

3.5.4 Initial and boundary conditions

The initial conditions (water content, dry density and temperature) are specified in D5.3.1 and summarised for each test in Table 3-22. The temperature is assumed to remain constant throughout each experiment.

Table 3-22 Initial conditions for each test

Test	Temperature (°C)	Dry Density (g/cm^3)		Water Content (%)	
		Pellets	Block	Pellets	Block
MGR21	*23.1*	*1.26*	*1.60*	9.5	*13.3*
MGR22	22.5	1.28	1.61	9.9	13.6
MGR23	22.5	1.30	1.60	3.4	14.2
MGR24	*22.5*	*1.28*	*1.62*	*5.7*	*13.7*
MGR27	23.2	1.30	1.60	3.4	14.6

In test MGR22, a constant flow rate is imposed on the bottom boundary. The water intake was measured throughout the experiment and this clearly shows a much lower flow rate for the first 10 days of the experiment, with flow stopping after 228 days when the bentonite is fully saturated (Figure 3-81). The inflow also appears to stop between 18.6 and 20.8 days. This was approximated in the QPAC model by imposing a flow rate of 0.0166 cm^3/h for the first 10 days, 0.048 cm^3/h from 10 to 18.6 days and 20.8 to 228 days, then 0 cm^3/h from 18.6 to 20.8 days and 228 to 270 days. There is a fixed 'no flow' boundary condition on all other boundaries. The specification suggests that there was an increase in injection pressure after 228 days when the bentonite is fully saturated, but this has not been specified in the model. In the experiment, a total measured 249.10 cm^3 of water was taken up by the bentonite during the test. Using the measured final dry density (1.43 g cm^{-3}) and volume (791 cm^3) of the sample, this suggests a final saturation of approximately 103%.

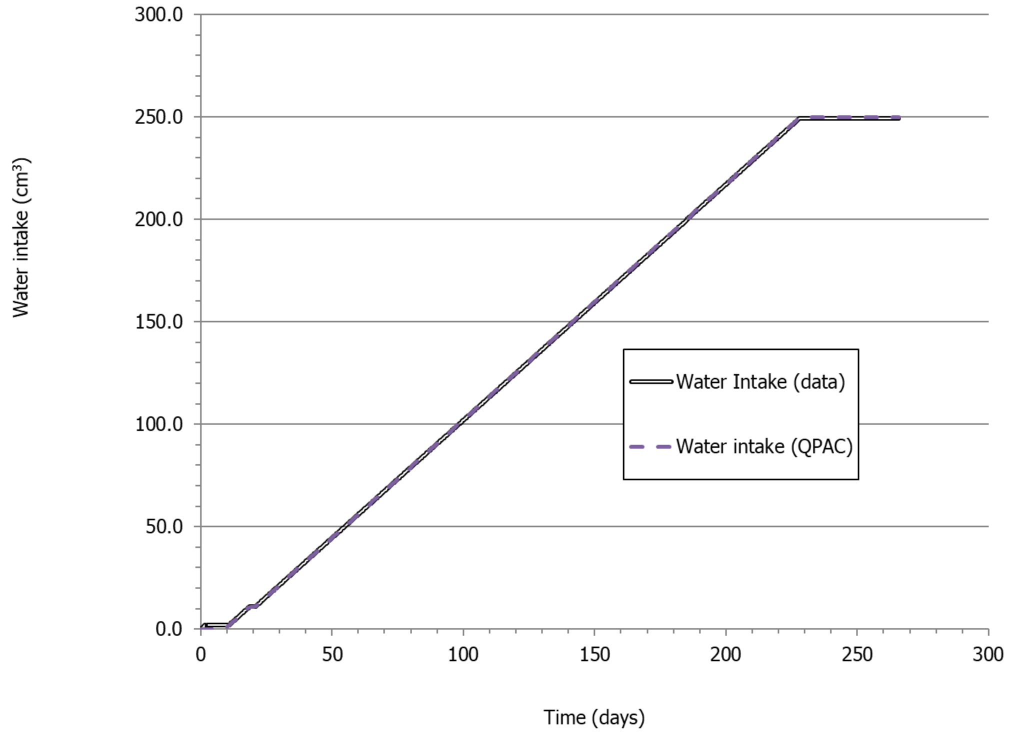

Figure 3-81: *Specified and measured water intake for test MGR22*

The results for test MGR22 suggest that there was a small increase in the volume of the sample, from an initial value of 783.67 cm^3 to a final value of 791 cm^3, corresponding to a height increase of approximately 0.9 mm. Therefore, a 0.9 mm gap is specified at the top of the sample as a boundary condition so the bentonite can swell freely into the gap. Initially, the other boundaries were modelled as simple roller boundaries, but friction was later added to the curved side boundary to oppose motion in the axial direction (see Section 3.5.5).

In tests MGR23 and MGR27, a constant water pressure of 15 kPa is imposed on the bottom boundary throughout the duration of the experiment (210 days). There is a fixed 'no flow' boundary condition on all other boundaries. Similar to test MGR22, the results for test MGR23 suggest that there was a small volume increase of the sample from an initial 784.14 cm^3 to a final 796 cm^3. This has again been represented as a boundary condition at the top of the sample allowing 1.5 mm of free axial expansion.

3.5.5 Results MGR22

The time evolution of axial stress calculated by the model with no friction is compared to the experimental data in Figure 3-82. The magnitude of the final stress (at the time of full saturation, 228 days) is well captured by the model, although there are differences in the transient behaviour. The maximum axial stress calculated by the model is 2.98 MPa, compared to a measured value of 3.05 MPa. The swelling pressure is very sensitive to the dry density of the sample because of the exponential curve used in the ILM; if the 0.9 mm increase in height and corresponding decrease in dry density of the sample were not accounted for in the model, the predicted maximum swelling pressure would be approximately 0.5 MPa higher (as shown in Figure 3-82).

In the model results, there is a 5-day delay between the start of hydration and the initial build-up of swelling pressure because of the time taken to swell into the void. This is consistent with the experimental data.

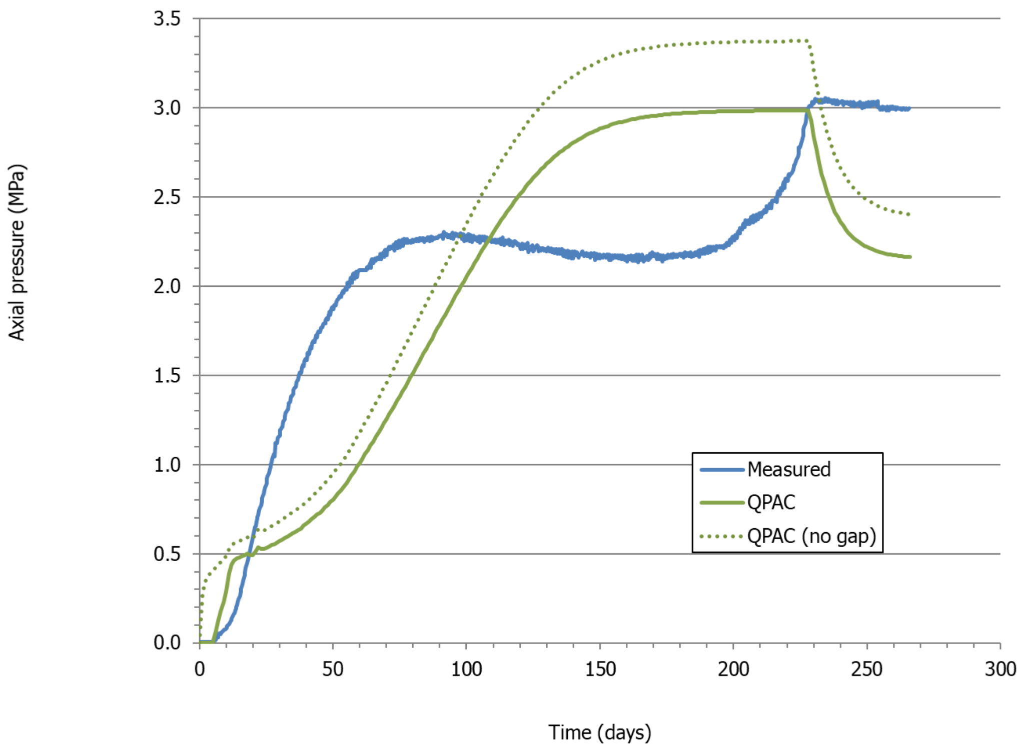

Figure 3-82: *Evolution of axial stress compared with measurements for test MGR22*

The initial and final axial profiles of water content and dry density are shown in Figure 3-83 and Figure 3-84 respectively. The measurements show a significant degree of homogenisation between the bentonite and pellets. There is a gradient of decreasing water content and increasing dry density with height.

The overall axial profile of water content is well predicted by the model. The average water content predicted by the model is 34.5%, slightly higher than the measured value, 32.7%. It is not clear why this is the case; calculating the final water content analytically from the known intake of water (249 cm^3), bentonite dry density and volume would suggest a final water content of 34% (or 33.5% if not accounting for the decrease in dry density).

The final dry density profile is less well predicted by the model, although the final average dry density is correct. The model predicts a higher dry density of the bentonite closest to the hydration surface and a lower dry density at the top of the bentonite. This is because of the boundary condition used which allows some swelling of the bentonite into a small void at the top of the experiment; without this boundary condition, the final dry density of the sample is predicted to be homogenous (with a higher average value). These results suggest that the void space may not be correctly represented in the model.

Introducing friction to the model improves the predicted profile of dry density in the bentonite pellets but not the bentonite block. It does not significantly change the predicted axial swelling pressure in the sample but does increase the axial stress in the top of the sample and decrease the stress in the bottom of the sample. Since there is no data to quantify the amount of friction between the sample and the container walls, results with and without friction are presented for each test.

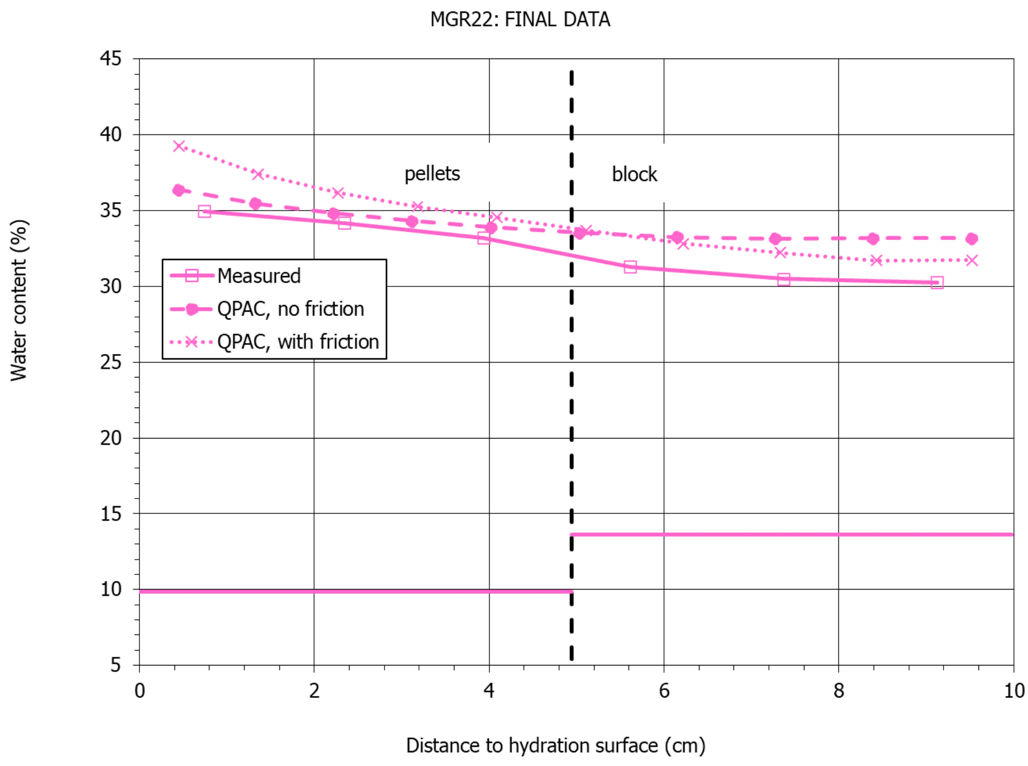

Figure 3-83: *Axial water content profile compared with measurements for test MGR22 (initial values shown as solid horizontal lines)*

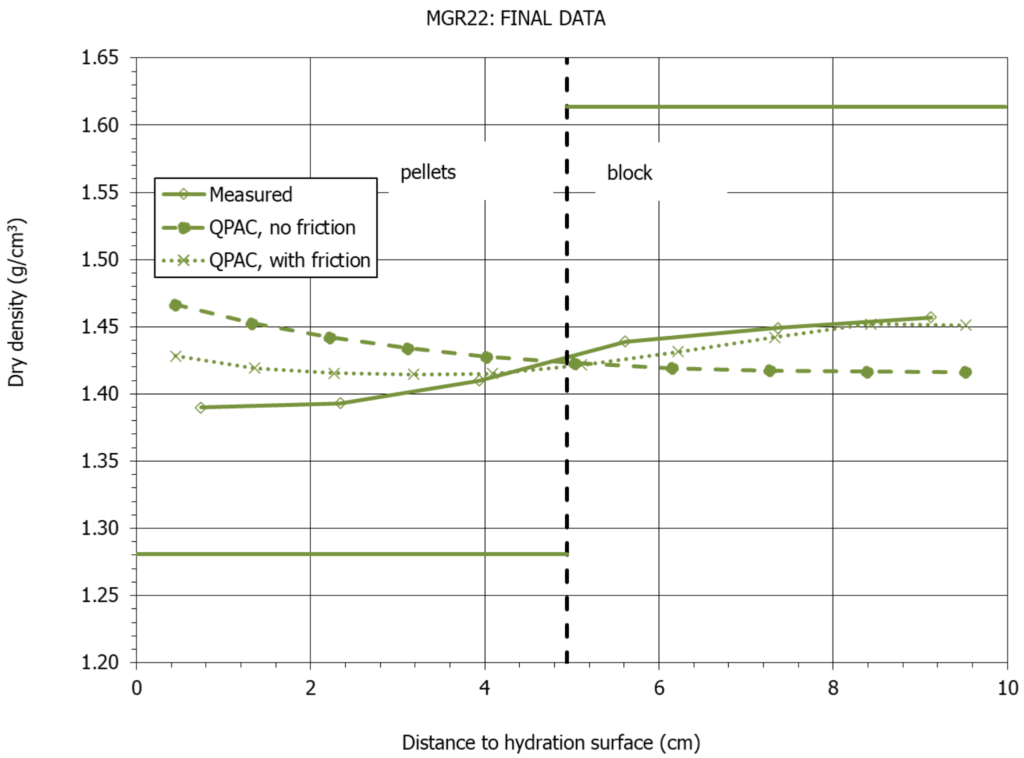

Figure 3-84: *Axial dry density profile compared with measurements for test MGR22 (initial values shown as solid horizontal lines)*

3.5.6 Results MGR23

Test MGR23 was repeated three times; test MGR23 ran for 210 days, test MGR21 ran for 34 days and test MGR24 ran for 14 days. These tests have approximately the same geometry of the bentonite pellets and block and use the same hydration boundary condition (a 15 kPa fixed pressure boundary). However, the tests are not completely identical, with some differences in the initial dry densities and water contents (see Table 3-22). The time evolution of water intake and axial stress for each test are compared against model predictions in Figure 3-85 and Figure 3-86 (for the model without friction).

Compared to test MGR22, the model and data both show a much faster initial rate of hydration. Unlike MGR22, axial stress begins to build up immediately after the start of hydration (in both the model and the measured data). The model predicts slightly faster rates of water intake and axial stress build-up than the data indicate, with the maximum axial pressure reached at an earlier time. Consequently, 55% of saturation is reached after 2 days (compared with 14 days in test MGR24) and 75% of saturation is reached after 12 days (compared with 34 days in test MGR21). However, the final values are well predicted by the model.

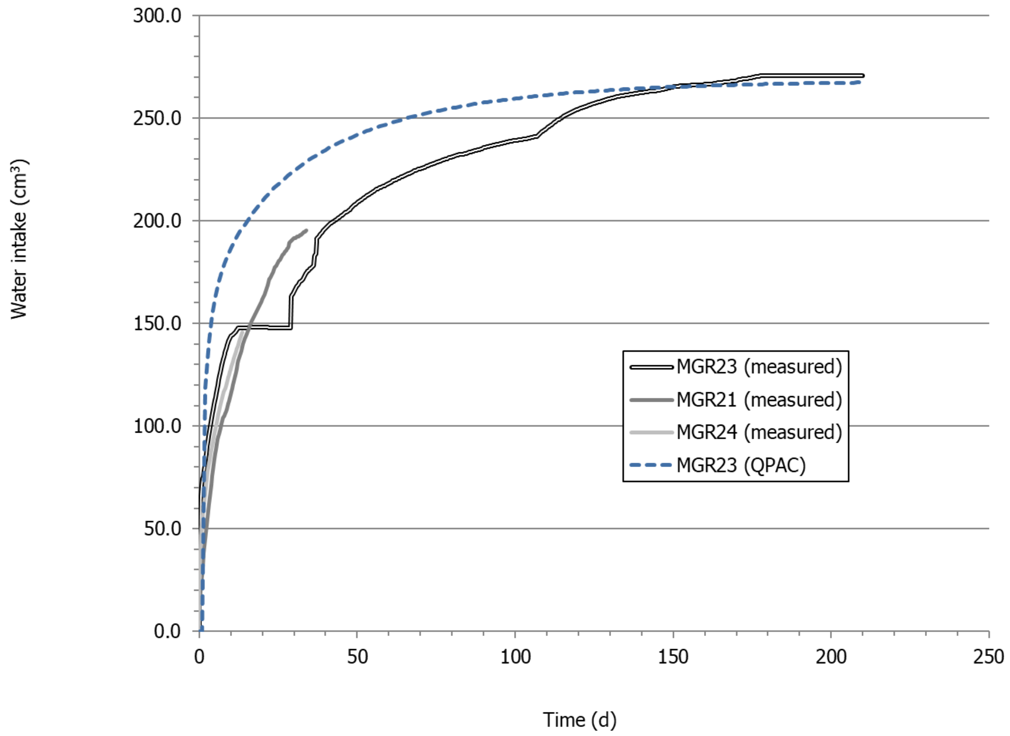

Figure 3-85: *Cumulative water intake compared with measurements for tests MGR23, MGR21 and MGR24*

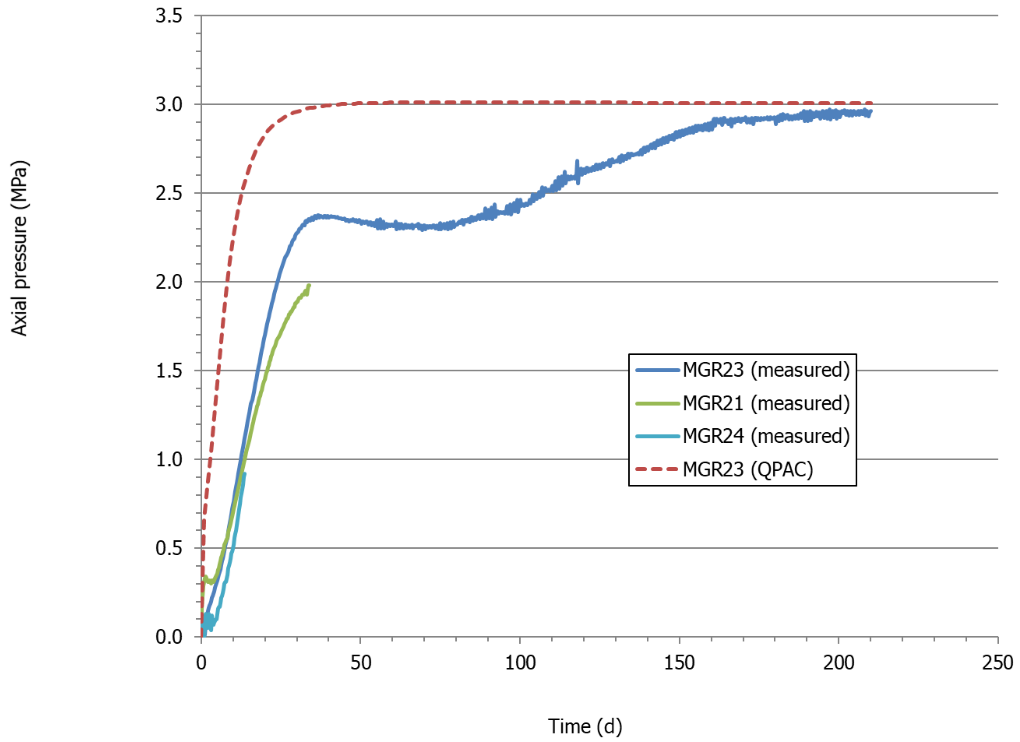

Figure 3-86: *Evolution of axial stress compared with measurements for tests MGR23, MGR21 and MGR24*

The initial and final axial profiles of water content and dry density are shown in Figure 3-87 and Figure 3-88 respectively. The data show a generally flat profile of water content with higher water content close to the hydration surface; the profile predicted by the model is similar. The model without friction predicts a more homogenous dry density distribution than seen in the data; the model with friction shows a better fit to the data.

Figure 3-89 and Figure 3-90 show the predicted water content and dry density distributions for test MGR24 (at 55% saturation) and test MGR21 (at 75% saturation) respectively, for the model without friction. These saturations are the final saturations at the end of the experiments but were reached earlier in the QPAC model. The tests illustrate the gradual homogenisation of the material as it saturates. In Figure 3-89, the gradient of water content is well-predicted by the model and the profile of dry density in the bentonite block is also similar to the data, but the profile of dry density in the pellets is flat (unchanged from its initial value). In test MGR21, a greater degree of homogeneity is predicted in the model than seen in the data; similar to test MGR23.

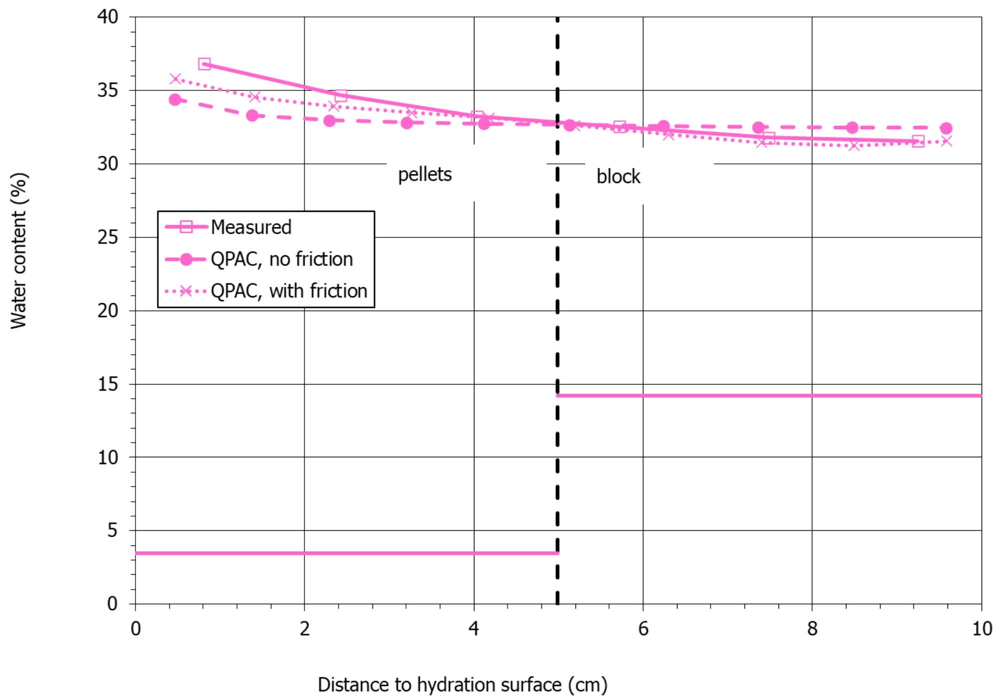

Figure 3-87: *Axial water content profile compared with measurements for test MGR23 (initial values shown as solid horizontal lines)*

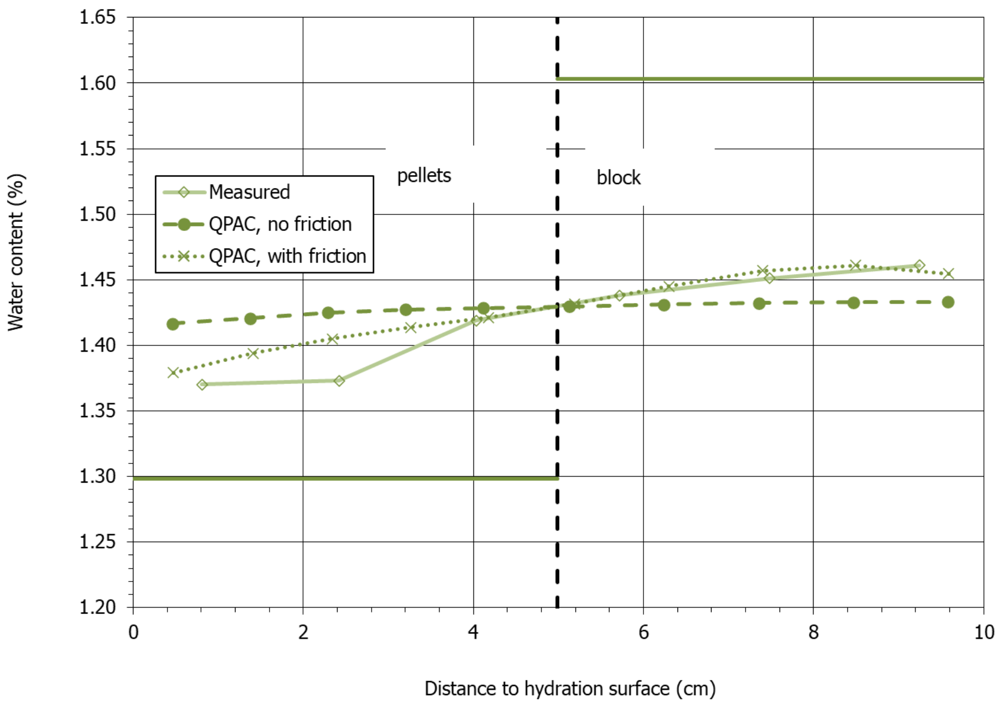

Figure 3-88: *Axial water content profile compared with measurements for test MGR23 (initial values shown as solid horizontal lines)*

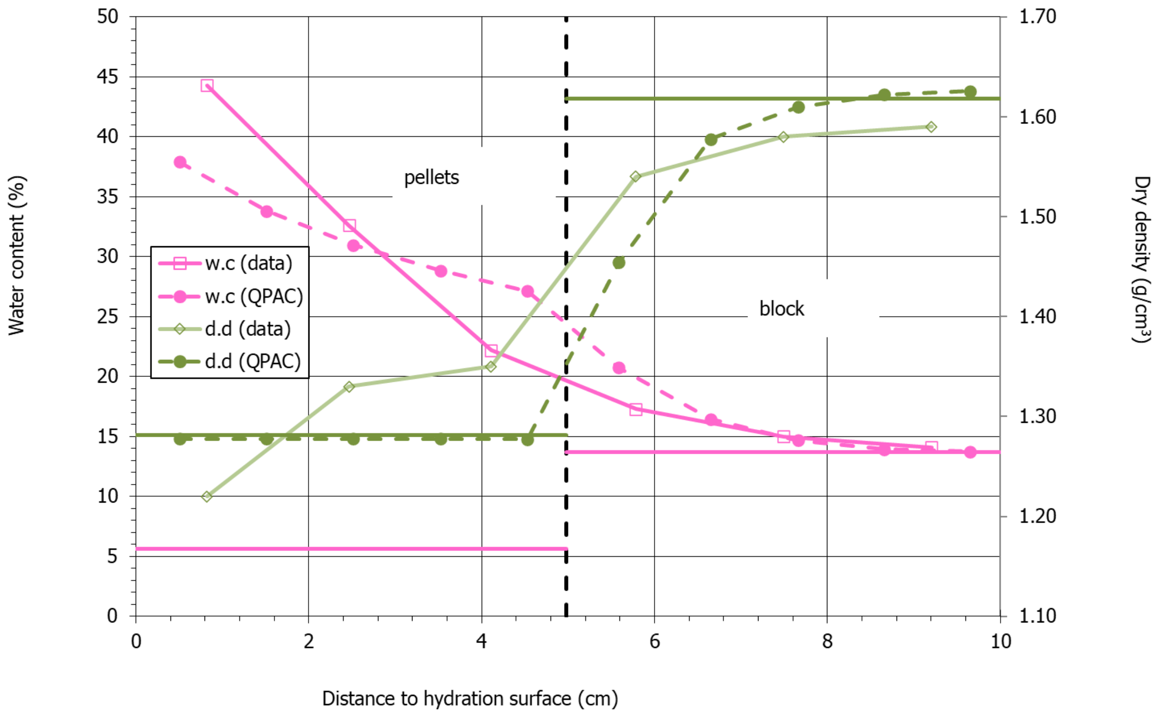

Figure 3-89: *Axial dry density and water content profiles compared with measurements for test MGR24 at 55% of total saturation (initial values shown as solid horizontal lines)*

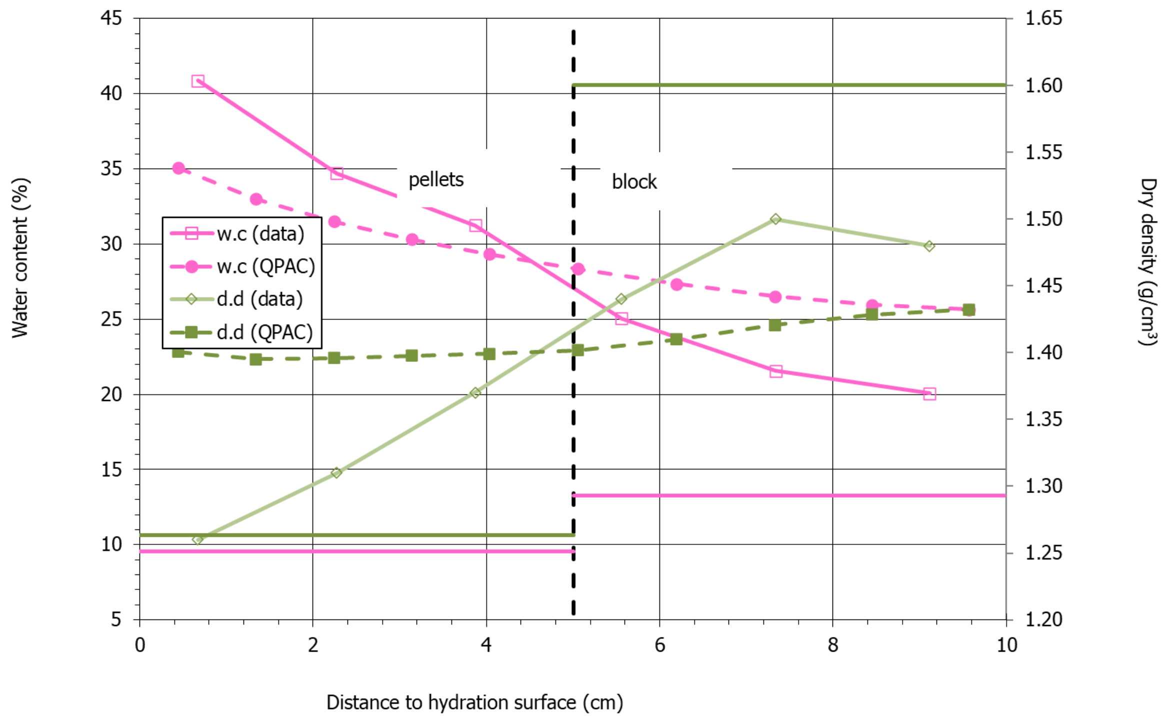

Figure 3-90: *Axial dry density and water content profiles compared with measurements for test MGR21 at 75% of total saturation (initial values shown as solid horizontal lines)*

3.5.7 Results MGR27

Blind predictions have been made for test MGR27. The predictions are compared with the predictions for test MGR23 in the following figures, since the two tests are similar apart from the relative positions of the bentonite block and pellets.

Figure 3-91 and Figure 3-92 show the predicted evolution of water intake and axial swelling pressure respectively. The key difference from test MGR23 is that the predicted uptake of water is slower, because of the lower initial suction in the block compared to the pellets. The final values for water intake and axial pressure are similar to test MGR23, as expected since the average properties of the sample are similar.

Since there was a small amount of expansion in tests MGR22 and MGR23 during the experiment, it is likely that there was also some void space in test MGR27, but this has not been included in the model since the final volume measurement is not available. The predicted time evolution of swelling pressure in MGR27 is similar to MGR23. As discussed above, the model predicts a faster equilibrium of axial stress than the MGR23 measurements, so it is likely that the axial stress predictions for MGR27 also reach equilibrium too soon.

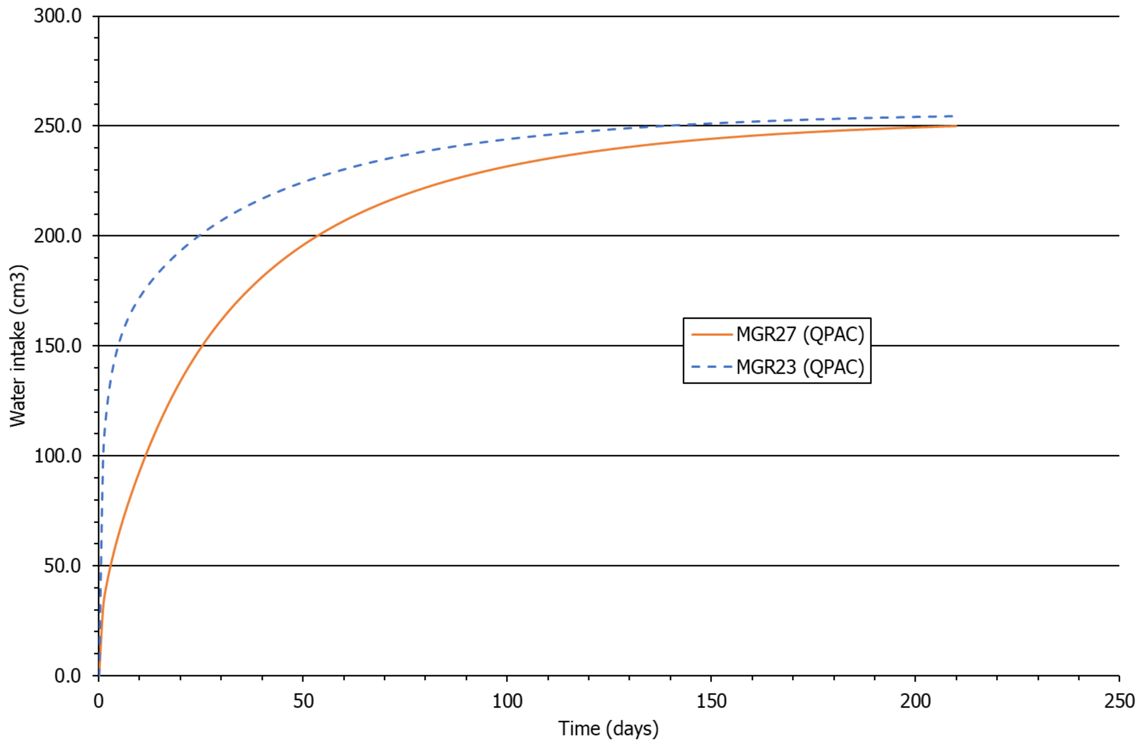

Figure 3-91: *Evolution of water intake compared with measurements for tests MGR27 and MGR23*

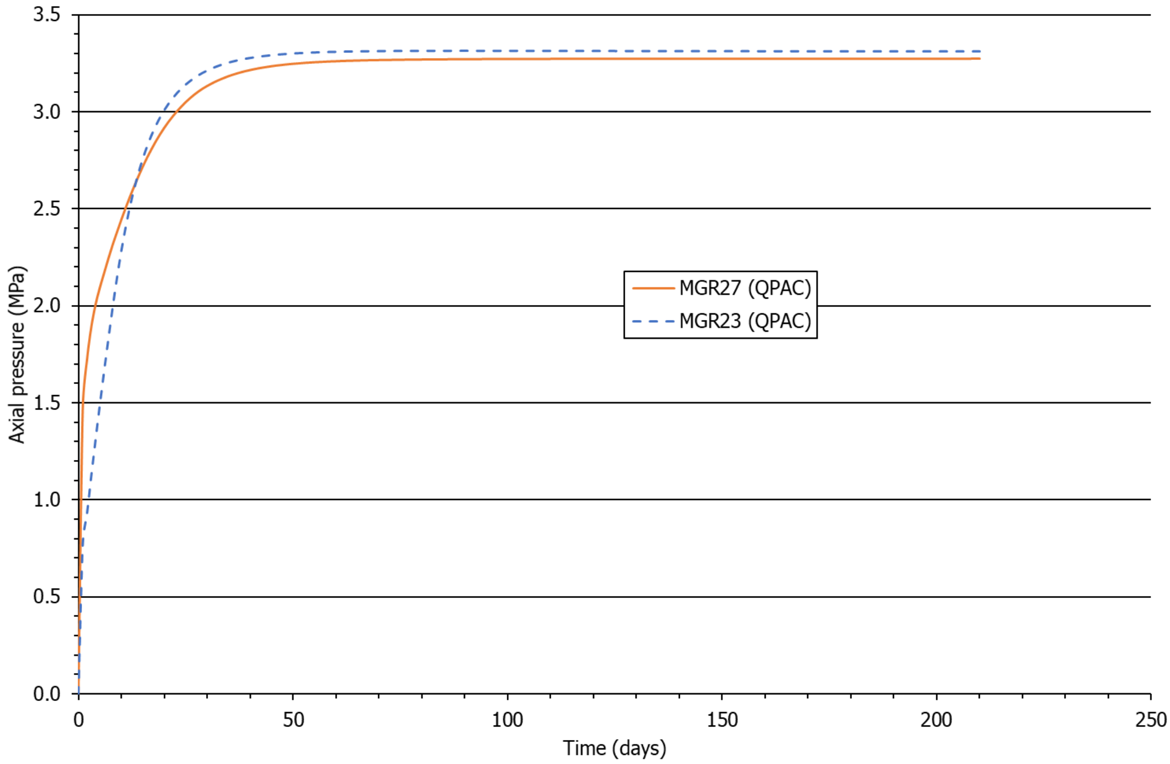

Figure 3-92: *Evolution of axial stress compared with measurements for tests MGR27 and MGR23*

Figure 3-93 shows the initial and predicted final axial profiles of dry density and water content. The predicted profiles without friction are very similar to test MGR23, with a significant amount of homogeneity throughout the sample, except close to the hydration surface. In test MGR23, the degree of homogeneity in the dry density profile was overestimated by the frictionless model so this is also likely to be true for test MGR27. The model with friction predicts a gradient of increasing dry density and decreasing water content with sample height.

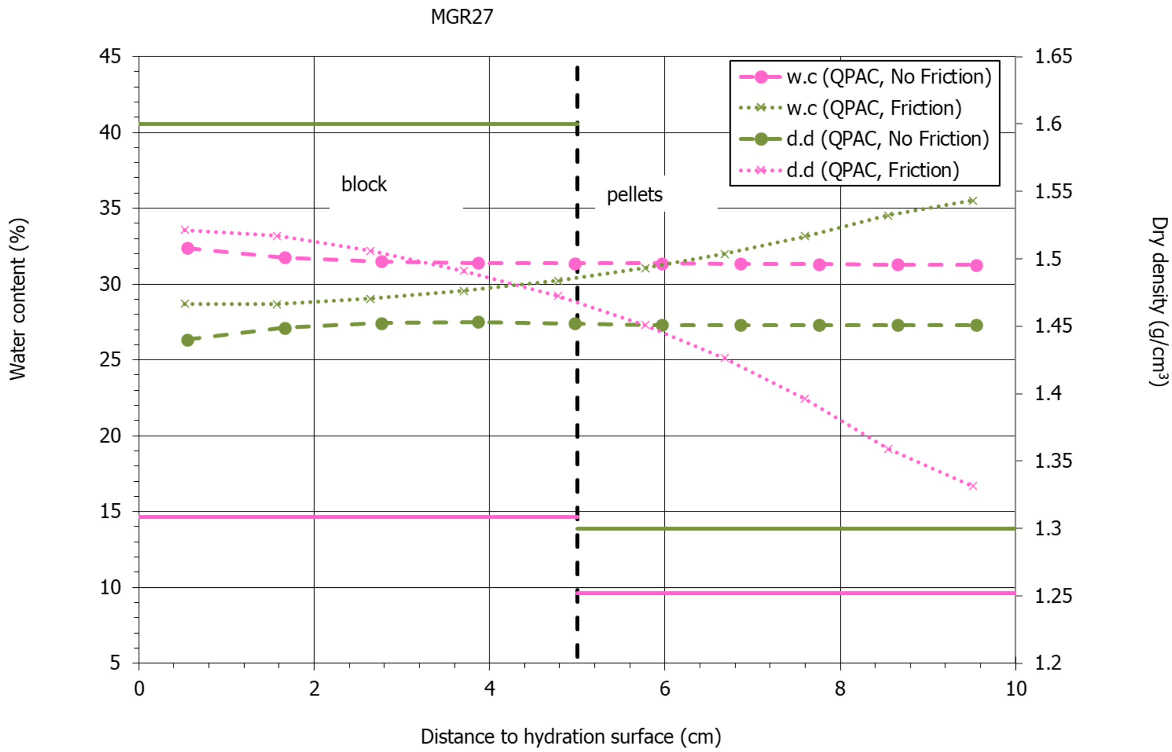

Figure 3-93: *Axial dry density and water content profiles predicted for MGR27*

3.5.8 Discussion

By using parameters for FEBEX bentonite without any calibration to this specific set of tests, our model has been able to produce good results for the evolution of axial swelling pressure, water intake, dry density and water content of the samples. As seen in previous tests, the model is more successful at reproducing final equilibrium values than transient behaviour.

The model is able to produce good results for the overall behaviour of the bentonite block-pellet mixture by simply representing the pellets as a bulk material with averaged properties. The dry density distributions in the pellets are not always well captured by the model; this may be due to the simplified pellet model, or possibly due to the choice of boundary conditions (in particular, assumptions about friction and void spaces). Both friction and void spaces have shown to be important to the model results; in particular, a small gap of the order of ~1 mm in a sample which is 10 cm high can have a significant impact on the predicted swelling pressure (of the order of ~0.5 MPa). There may therefore be a large degree of uncertainty in the results if the dimensions are not precisely measured.

3.6 EPFL

3.6.1 Description of the models

The constitutive model used by EPFL to describe the behaviour of the FEBEX bentonite is presented in the Beacon deliverable D3.2 developed within the WP3 of the BEACON project. Its development has been guided from previous experience of the application of ACMEG-TS (François and Laloui 2008) to modelling bentonite. The complete description is planned to be reported in the deliverable D3.3 of the WP3, including its implementation in the Finite Element code Lagamine (Charlier 1987, Collin 2003).

The model is formulated in the framework of a generalised effective stress, that is linked to the mechanical elastic strains, and the degree of saturation, which expresses the variation of compressibility under unsaturated conditions. A new water retention model, that takes explicitly into account the existence of adsorbed water, is used to predict the evolution of the degree of saturation with suction and deformation. The elastic domain is influenced by the stress history, the current temperature and the degree of saturation. The constitutive model has been implemented in the Finite Element code Lagamine (Charlier 1987, Collin et al. 2002), which allows the numerical analysis of non-isothermal multiphase flow in deformable media. For the simulations described in this report, water flow is considered in isothermal conditions.

3.6.2 Geometry and discretization

Figure 3-94 shows the Finite Element mesh used for the models, with the material distribution representative of the tests MGR22 and MGR23, that is he pellets are located on the lower side (water intake side). For the test MGR27, the block side corresponds to the lower part. 8-noded elements with 4 integration points (MWAT2) are used to discretise the domain. The domain is discretised into 10 elements for each material, that leads to a total of 20 elements. The problem is assumed to be axisymmetric and homogeneous in the radial direction, and accordingly a one-dimensional discretisation is used.

In the case of the MGR23 and MGR27, water pressure is imposed for the water intake, whereas water flow is imposed for the case of the MGR22. Zero lateral friction is assumed.

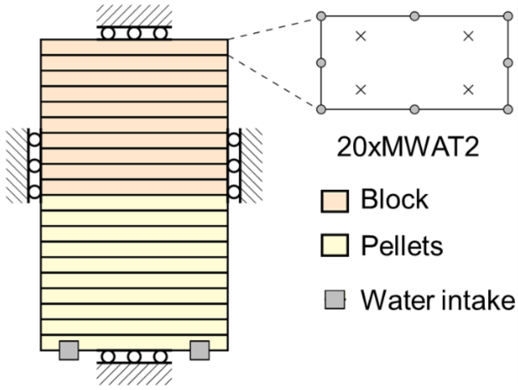

Figure 3-94 *Finite element mesh of the test MGR22 and MGR23. The same mesh is used for the test MGR27 but inverting the materials.*

3.6.3 Input parameters

In order to assess the predictive capabilities of the model, most input parameters are calibrated on the basis of complementary tests from the literature instead from the tests MGR22, MGR23. The water retention curve is calibrated as a first instance. Figure 3-95 shows the experimental data, which includes both results obtained from testing pellets (Hoffmann et al. 2007) and block form (Lloret et al. 2003) at dry densities representative of the tests MGR. The dependency of the water retention model on the dry density allows the use of the same parameters for both materials. The fit obtained with the model is quite satisfactory for both pellets and block, which do not show significant differences at high values of suction.

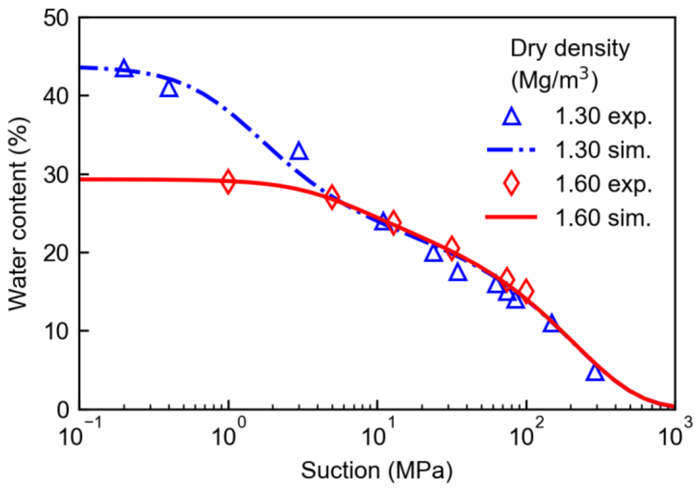

Figure 3-95 *Calibration of the water retention behaviour of FEBEX bentonite. Dry densities are representative of the initial state of the pellets (1.3 Mg/m³) and the blocks (1.6 Mg/m³). Experimental results reported in Hoffmann et al. (2007) for the pellets and Lloret et al. (2003) for the block.*

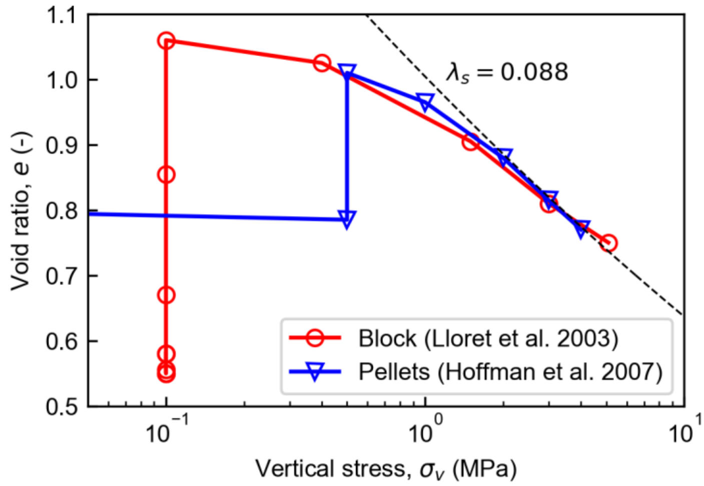

Figure 3-96 *Calibration of the slope and the position of the normal compression line at saturation for the FEBEX bentonite.*

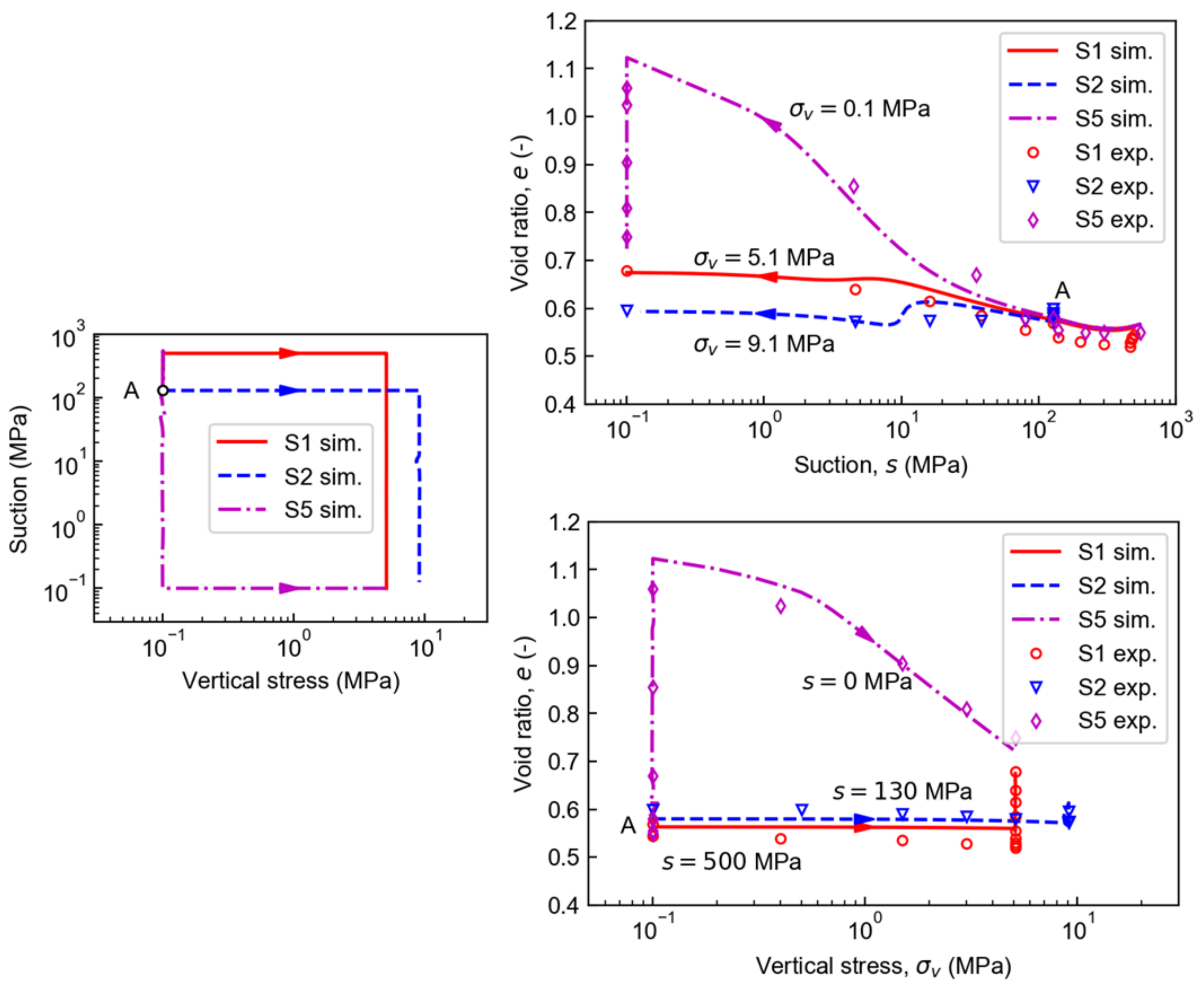

Figure 3-97 *Calibration of the mechanical parameters against suction controlled oedometer tests performed by Lloret et al. (2003)*

The position and slope of the normal compression line is calibrated against oedometric compression tests (Figure 3-96) also reported in Hoffmann et al. (2007) and Lloret et al. (2003) on pellets and blocks after saturation, assuming that at high stress the virgin compression line is representative of the normal compression line.

The remaining mechanical parameters at saturated states have been calibrated based on suction-controlled oedometric tests reported by Lloret et al. (2003) as shown in Figure 3-97. These results span several ranges of suction-stress values, following different stress paths. The parameters defining the saturated state behaviour κ, ν, ϕ' are set the same for blocks and pellets.

The parameters defining the unsaturated compressibility depend on the initial density of the material. Accordingly, different values of r, ζ and ξ are assigned for pellets and blocks. They have been calibrated on the basis of suction-controlled swelling pressure tests, as shown in Figure 3-98. The fit for the swelling pressure of the block is satisfactory, whereas the development of pressure of the pellets shows deviations at high suctions. Indeed, the model presents limitations to model bentonite at low densities. In both cases the swelling pressure at saturation (i.e. when suction tends to 0) is well captured.

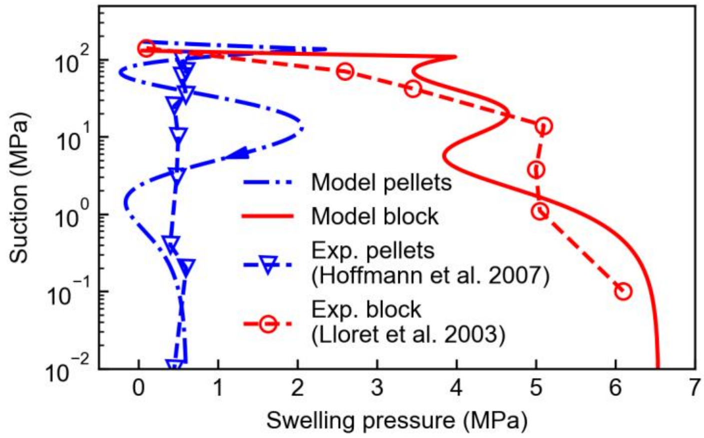

Figure 3-98 *Suction controlled swelling pressure tests. Model calibration against experimental results reported by Hoffmann et al. (2007) and Lloret et al. (2003).*

Figure 3-99 shows the adjustment of the hydraulic conductivity to the experimental data presented by Villar (2002) on block bentonite and of Hoffman et al. (2007) on saturated pellets. The adjustment for the block permeability is the same as in the previous analysis of the FEBEX test, whereas different permeability is used for the saturated pellets. The parameter α_k is modified with respect to the bentonite block in order to account for a higher water flow at low S_r due to the existence of macropores between the pellets. All the relevant input parameters for the analyses are summarised in Table 3.23.

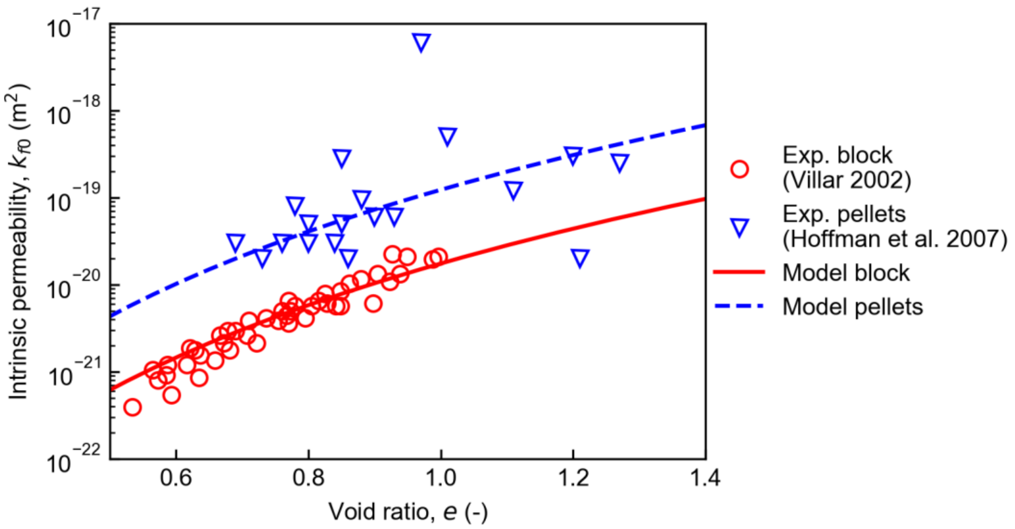

Figure 3-99 *Calibration of the intrinsic permeability to water for blocks and pellets. Experimental data from Villar (2002) and Hoffmann et al. (2007)*

Table 3.23 Material parameters for FEBEX bentonite in block and pellets form

Mechanical parameters		Hydraulic parameters	
Parameter	Value	Parameter	Value
κ	0.060	a	2 MPa^{-1}
ν	0.35	b	1.5
λ_s	0.088	n	1.8
$\phi_c' = \phi_e'$	16°	m	1.6
α	0.65	$e_{w,a}^C$	0.483
p_r'	10^{-7} MPa	$\rho_{w,a}$	1.2 Mg/m^3
r	0.37 (block) 0.70 (pellets)	$k_{f,0}$	$3\cdot10^{-21}$ m^2 (block) $2\cdot10^{-19}$ m^2 (pellets)
ζ	3.17 (block) 2.58 (pellets)	M	6
ξ	1.65 (block) 2.5 (pellets)	N	4
ρ_s	2720 g/m^3	α_k	2.9 (block) 1.2 (pellets)

3.6.4 Initial and boundary conditions

In all tests the initial state of the pellets and block are set the same. The pellets are assumed to start with a void ratio of 1.1 (dry density of 1.3 Mg/m^3) and a water content of 9.9% that according to the water retention in Figure 3-99 corresponds to an initial suction of 170 MPa. The initial void ratio of the block is 0.7 (dry density of 1.6 Mg/m^3) and the water content 13.8% that corresponds to an initial suction of 105 MPa.

Regarding the boundary conditions for the water intake, for the tests MGR23 and MGR27 a constant water pressure of 14 kPa is applied in the lower part. The case of the test MGR 22 involves more complexity. As noted from the specifications report of the experimental work, close to saturation the constant rate of water inflow was difficult to maintain without a significant water pressure build-up. From a modelling perspective the same issue is encountered due to the low pressure gradients when the sample is almost saturated, that require the application of positive pore water pressure in order to maintain the flow rate. The application of pore water pressure in an almost saturated sample influences the swelling pressure and therefore this stage has been avoided in the simulation. The strategy followed to simulate the test has been to apply the same water flow rate of the experiment up to the point at which positive water pressure starts to develop inside the bentonite.

3.6.5 Results MGR22

The swelling pressure development obtained for the test MGR22 can be compared to the experimental results in Figure 3-100. It can be noted that the model predicts a first increase of swelling pressure that is similar to the experimental observations before starting to deviate after around 100 days of hydration. The source of this decrease in pressure is the model limitation in modelling the swelling pressure of pellets at a low initial dry density, as observed in Figure 3-98. After around 220 days of water intake at constant water flow water pressure inside the pellets starts to develop significantly and therefore the water flow is stopped at this point. Afterwards the equilibration of internal water pressures results in a slight decrease in axial pressure and equilibrates at a value that is lower than the observed swelling pressure, although following a similar pattern. The sequence of flow applied is shown in Figure 3-101. As it can be seen the total water intake is very close to the experimental measurements.

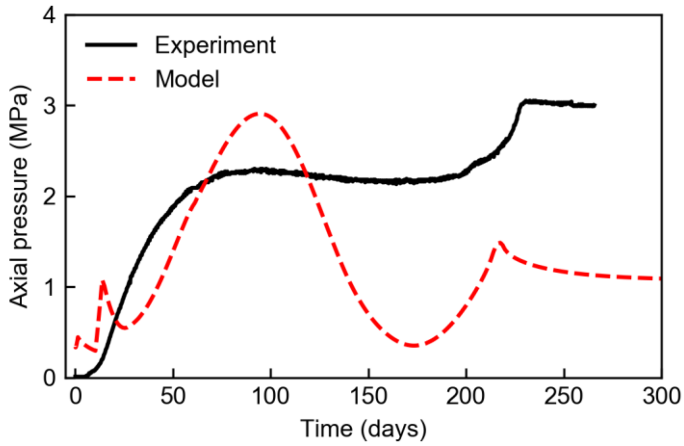

Figure 3-100 *Experimental and modelled axial pressure development in the test MGR22*

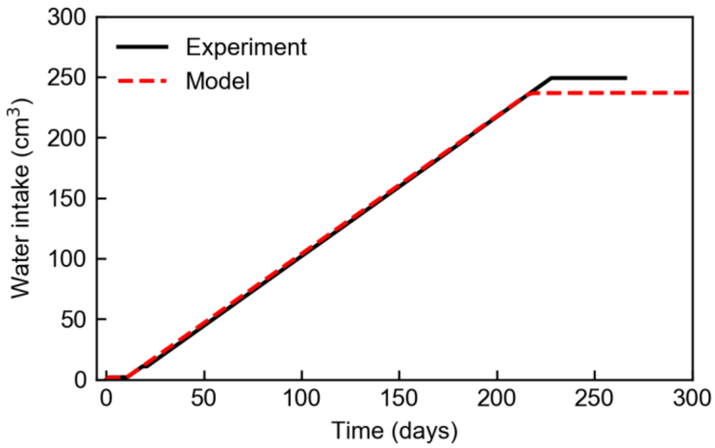

Figure 3-101 *Experimental and modelled water intake in the test MGR22*

The simulated profiles of dry density and water content are shown in Figure 3-102 in addition to the measurements after dismantling. Although no specific calibration for the test has been performed, the comparison shows a very good agreement of both profiles indicating that the volume change parameters are robust in spite of the discrepancy of the final swelling pressure.

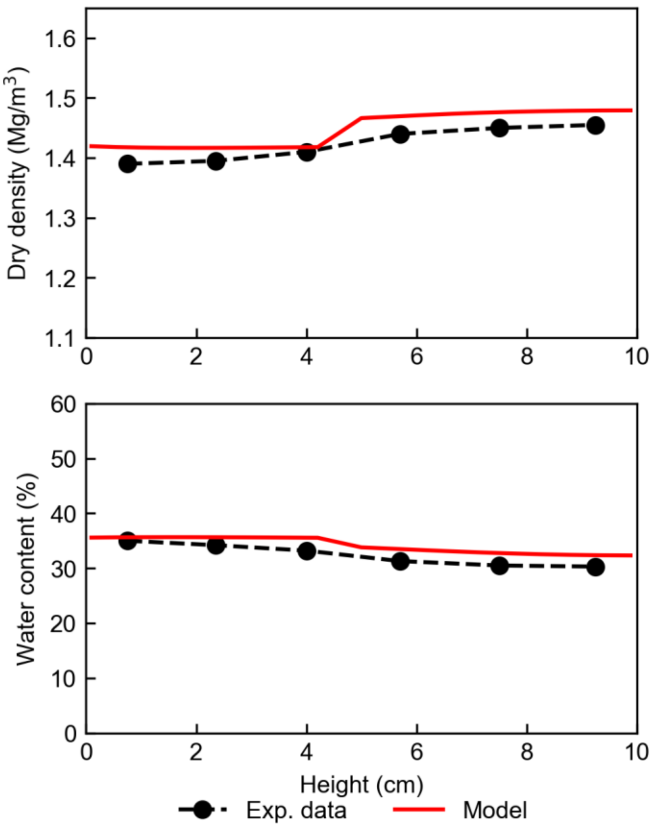

Figure 3-102 Comparison of the dry density and water content profiles measured after dismantling of the test MGR22 and the modelling results

3.6.6 Results MGR23

Figure 3-103 shows the simulated development of swelling pressure in the test MGR23 as well as the experimental results. It can be observed as in the case of the MGR22 that after a first increase, a collapse in terms of axial stress is simulated, that does not agree with the experimental results. Nevertheless, the subsequent pattern of swelling pressure up to equilibrium is similar to that measured, although it equilibrates at a lower swelling pressure. The predicted swelling pressure by the model lies in the range of expected swelling pressure in small-scale tests.

The water intake of the test is shown in Figure 3-104 for both the model and the experiment. In this case the model follows closely the trend of the experiment. Some deviations are observed after around 150 cm^3 of water intake. It is noted however that the deviation was not observed in the other two tests performed with constant water pressure (MGR21 and MGR24 form Beacon WP4 report).

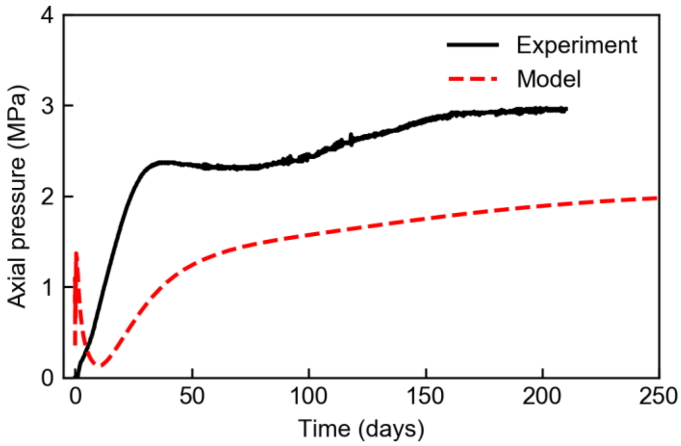

Figure 3-103 *Experimental and modelled axial pressure development in the test MGR23*

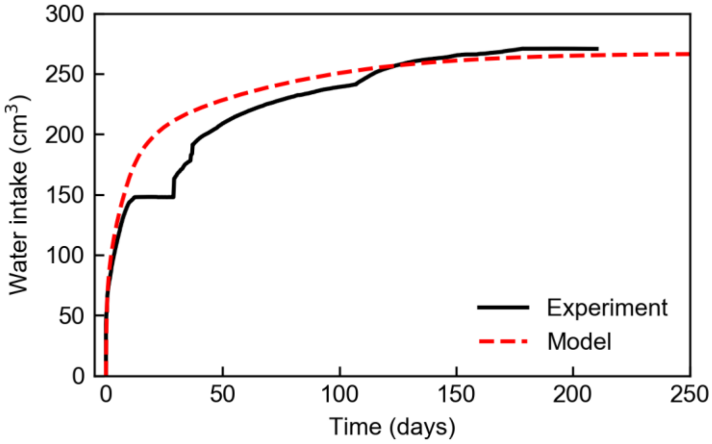

Figure 3-104 *Experimental and modelled water intake in the test MGR23*

The computed profiles of dry density, water content, water conductivity and suction at three times are shown in Figure 3-105. The three steps correspond to a water intake of 150, 250 and full saturation which correspond to the dismantling stages of the tests MGR21, MGR24 and MGR23 respectively. The measured profiles of dry density and water content are also represented in Figure 3-105. As in the case of the test MGR22, the modelling results show a good agreement in terms of both dry density and water content. The effects of the axial pressure collapse after 14 days (water intake of 150 cm^3) in the profile can be seen in the computed profile of dry density at the interface pellets-block. This suggests that the swelling pressure collapse is the effect of the model limitation for low density samples. The decrease in permeability of the pellets with increasing degree of saturation is in agreement with the experimental observations of Hoffmann et al. (2007).

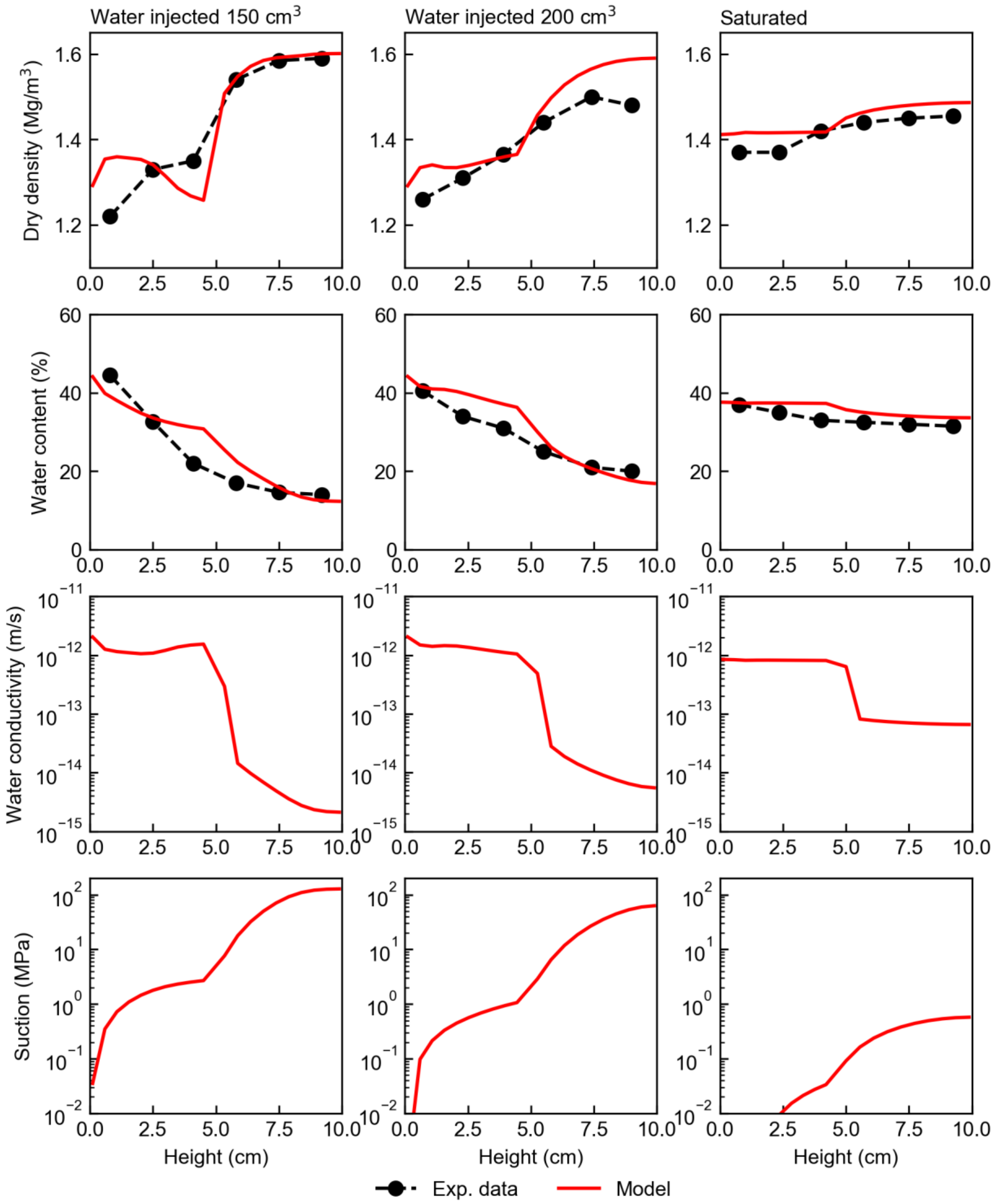

Figure 3-105 *Modelling results of the test MGR23 in terms of dry density, water content, water conductivity and suction at three different times corresponding to a water intake of 150 cm³, 200 cm³ and after saturation. The dismantling results in terms of dry density and water content from the tests MGR21 (final water intake of 150 cm³), MGR24 (final water intake of 150 cm³) and MGR23 (full saturation) are also displayed for comparison purposes.*

3.6.7 Results MGR27

The model predictions for the test MGR27 are shown in Figure 3-106 in terms of axial pressure and in Figure 3-107 in terms of water intake. The time needed to reach equilibrium is remarkably larger than in the other two tests, which is in agreement with the observations made by CEA in the experiments reported in WP4, where heterogeneous samples hydrated from the higher density zone required longer time to reach equilibrium than those samples hydrated from the lower density zone. The swelling pressure predicted is initially significantly higher than the other tests, whereas the final swelling pressure at equilibrium results lower than the test MGR23.

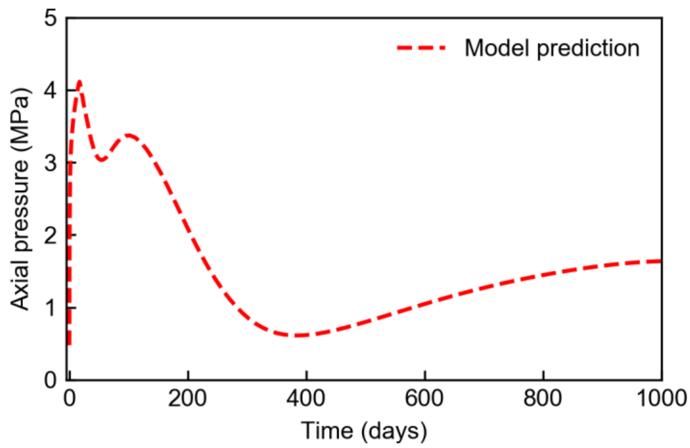

Figure 3-106 *Predicted development of swelling pressure in the test MGR27*

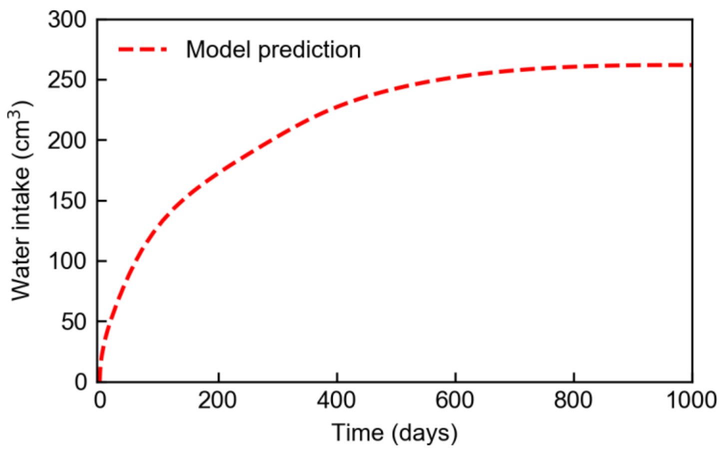

Figure 3-107 *Predicted evolution of water intake in the test MGR27*

The profiles of dry density and water content are displayed in Figure 3-108. As in the previous tests, a quite homogeneous state is predicted after saturation.

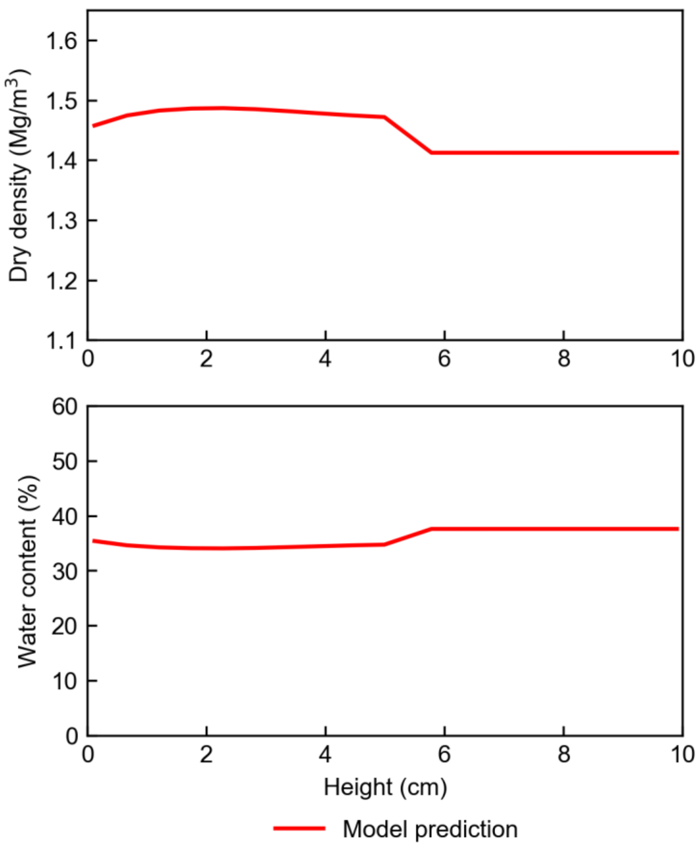

Figure 3-108 *Predicted profiles of dry density and water content after full saturation of the test MGR27*

3.6.8 Discussion

Most of the model parameters, and all the mechanical parameters, have been calibrated against oedometric tests. Only the relative permeability of the pellets has been calibrated on the basis of the results from the MGR tests. This strategy has been chosen in order to have increased confidence in the parameters for each material. The saturated state parameters are set the same between the two materials and only the parameters that are believed to be dependent on the initial compacted state have been set differently, as stated in the section of material calibration. Given that the results in terms of dry density and water content are well predicted for both MGR22 and MGR23 tests using this approach, it has been decided not to modify the mechanical parameters. The state of the bentonite at partial saturation, as observed after dismantling of the tests MGR21 and MGR24 is also well matched by the modelling results when they are compared at equivalent water intake.

The shortcoming of this approach is that the swelling pressure of the MGR tests is underestimated, as the resulting axial pressure is that expected for an equivalent dry density of 1.45 Mg/m^3. This might be because the model presents limitations to reproduce the swelling pressure of bentonite at initially low dry densities ($e > 1$ and dry density < 1.4 Mg/m^3), such as that of the pellets, as observed from Figure 3-98. This also leads to a transient behaviour with high collapse that was not observed in the experiments.

3.7 BGR

3.7.1 Hydro-Mechanical Model

In this section, the mathematical model used for the simulations is described briefly. The first governing equation is the balance of fluid mass. The fluid flow is based on the model of (Richards, 1931) for the two-phase flow equation under isothermal conditions in a deforming porous media (Lewis & Shrefler, 1998). Within this assumption, the change of gas pressure is neglected. The model for the fluid flow is described in more detail in the BEACON deliverable D5.1.2 (J. Talandier, 2019). Therefore, only the deviations to this model are presented here. The relative permeability for Darcy's flow is computed using the model after (Brooks & Corey, 1966):

$$k_{\mathrm{rel,w}} = \left(S_{\mathrm{e}}\right)^{\frac{2+3\lambda_{\mathrm{k}}}{\lambda_{\mathrm{k}}}} \quad . \tag{0.1}$$

Furthermore, the dependency of the permeability to the current porosity is considered to follow a generalised power law as described in (Verma & Pruess, 1988):

$$\mathbf{k} = k \cdot \left(\frac{\phi}{\phi_0}\right)^{\lambda_\phi} \mathbf{1} \quad . \tag{0.2}$$

The second governing equation is the balance of linear momentum for the porous medium. Since the geometrical dimensions are small and the homogenisation process is sufficiently slow the body force contribution and the inertia term are neglected:

$$\nabla \cdot \left(\boldsymbol{\sigma}_{\mathrm{eff}} - \alpha_{\mathrm{Biot}} \chi p^{\mathrm{w}} \mathbf{1} - \boldsymbol{\sigma}_{\mathrm{sw}}\right) = 0 \quad . \tag{0.3}$$

In equation (0.3), the saturation depending Bishop's coefficient $\chi(S^{\mathrm{w}})$ and the Biot factor α_{Biot} reducing the hydro-mechanical coupling. Additionally, the saturation driven swelling stress $\boldsymbol{\sigma}_{\mathrm{sw}}$ is introduced in the balance equation. It is assumed that the swelling stress is proportional to the change of effective saturation via:

$$\boldsymbol{\sigma}_{\mathrm{sw}} = -p_{\mathrm{sw}} (S_{\mathrm{e}}^{\lambda_{\mathrm{sw}}} - S_{0\mathrm{e}}^{\lambda_{\mathrm{sw}}})\, \mathbf{1} \quad . \tag{0.4}$$

The constitutive model for the solid phase is composed of a small-strain isotropic elastoplastic model for the effective stress $\boldsymbol{\sigma}_{\mathrm{eff}}$ and an evolution law for the porosity $\dot{\phi}$.

The effective stresses $\boldsymbol{\sigma}_{\mathrm{eff}}$ are computed according to a modified Cambridge (Cam) Clay elastoplasticity model analogue to (Borja & Lee, 1990). Here only the main characteristics are briefly described. The strains are additively decomposed into an elastic and a plastic part:

$$\boldsymbol{\varepsilon} = \boldsymbol{\varepsilon}_{\mathrm{e}} + \boldsymbol{\varepsilon}_{\mathrm{p}} \quad . \tag{0.5}$$

The stress is computed by linear elasticity:

$$\boldsymbol{\sigma}_{\mathrm{eff}} = K^{\mathrm{skel}} \operatorname{tr}\left(\boldsymbol{\varepsilon}_{\mathrm{e}}\right) \mathbf{1} + \mu\, \boldsymbol{\varepsilon}_{\mathrm{e}}^{\mathrm{dev}} \quad . \tag{0.6}$$

The corresponding Cam Clay yield surface reads:

$$\Phi := q^2 + M^2\, p\left(p - p_c\right) \leq 0 \quad , \tag{0.7}$$

Where q is the von Mises stress and p is the hydrostatic pressure and M is the slope of the critical state line. The pre-consolidation pressure p_c represents the yield stress under pure compression and depends on the volumetric plastic strain and the porosity. The evolution equations for the internal variables are given by:

$$\dot{\boldsymbol{\varepsilon}}_\mathrm{p} = \lambda_\mathrm{p} \frac{\partial \Phi}{\partial \boldsymbol{\sigma}_\mathrm{eff}}$$
$$\dot{p}_\mathrm{c} = -\mathrm{tr}\left(\dot{\boldsymbol{\varepsilon}}_\mathrm{p}\right)\left(\frac{1}{(\lambda_\mathrm{c}-\kappa_\mathrm{c})(1-\phi)}\right) p_\mathrm{c} , \tag{0.8}$$

Where λ_p is the plastic multiplier, λ_c and κ_c are material parameters representing the slope of the virgin consolidation line and the normal swelling line respectively. The set of equations is fulfilled with the classical Karush-Kuhn-Tucker (Luenberger & Ye, 2016) conditions:

$$\lambda_p \geq 0 , \quad \Phi \leq 0 , \quad \lambda_p \Phi = 0 \tag{0.9}$$

and the consistency condition $\lambda_p \dot{\Phi} = 0$.

Together with the internal variables $\{\boldsymbol{\varepsilon}_\mathrm{p}, p_\mathrm{c}\}$ the evolution equation for the porosity ϕ is solved. The evolution of ϕ is directly obtained by the mass balance of the porous solid material assuming incompressible grains:

$$\dot{\phi} + \phi \operatorname{div} \dot{\mathbf{u}} = \mathrm{tr}(\dot{\boldsymbol{\varepsilon}}) \quad \rightarrow \quad \dot{\phi} = (1-\phi)\,\mathrm{tr}(\dot{\boldsymbol{\varepsilon}}) \ . \tag{0.10}$$

In in Table 3-23, all used quantities are summarized.

Table 3-23 Physical quantities and their units used in the model

Symbol	Description	Unit	Symbol	Description	Unit
S_e	Effective saturation	$[-]$	$k_\mathrm{rel,w}$	Relative permeability of the water phase	$[-]$
$\mathbf{k}$	Intrinsic permeability tensor	$[\mathrm{m}^2]$	λ_k	Exponent of relative permeability	$[-]$
k	Intrinsic permeability	$[\mathrm{m}^2]$	$\boldsymbol{\sigma}_\mathrm{eff}$	Effective stress	$[\mathrm{Pa}]$
$\phi,\ \phi_0$	Porosity, Reference porosity	$[-]$	χ	Bishop's coefficient	$[-]$
λ_ϕ	Exponent of porosity dependent permeabilty	$[-]$	p_sw	Swelling pressure parameter	$[\mathrm{Pa}]$
λ_sw	Exponent of swelling law	$[-]$	$\boldsymbol{\sigma}_\mathrm{sw}$	Swelling stress	$[\mathrm{Pa}]$
$\boldsymbol{\varepsilon}$	Linear strain meassure	$[-]$	p	Hydrostatic pressure	$[\mathrm{Pa}]$
$\boldsymbol{\varepsilon}_\mathrm{e}$	Elastic strain	$[-]$	p_c	Pre-consolidation pressure	$[\mathrm{Pa}]$
$\boldsymbol{\varepsilon}_\mathrm{p}$	Plastic strain	$[-]$	M	Slope of the critical state line	$[-]$
μ	Shear modulus	$[\mathrm{Pa}]$	λ_p	Plastic multiplier	$[-]$

λ_c	Slope consolidation line	$[-]$	κ_c	Slope swelling line	$[-]$

3.7.2 Description of the models, Input parameters, Geometry and discretization, Initial and boundary conditions

The governing equations are solved with the finite element analysis software *OpenGeoSys (Bilke et al., 2019)*. Therefore, the geometry of the experimental setup described in the specification document is discretized. This was done using the pre-processing software *Gmsh (Geuzaine & Remacle, 2009)*. Since the test cell and the load of the experiments show rotational symmetry, only an equivalent two dimensional axisymmetric initial boundary value problem is solved. In Table 3-24 and in Table 3 the model parameter common for all three test cases are summarized.

Table 3-24 Model parameter commonly used for bentonite pellets and blocks simulating experiment MGR22, MGR23, MGR 27

Parameter	Value	Unit
Mass densitiy water ρ^{w}	1000	$\left[\frac{\mathrm{kg}}{\mathrm{m}^3}\right]$
Mass densitiy solid ρ^{s}	2135	$\left[\frac{\mathrm{kg}}{\mathrm{m}^3}\right]$
Bulk modulus water K^{w}	2666.7	$[\mathrm{MPa}]$
Biot coefficient α_{Biot}	1	$[-]$
Bishops coefficient χ	$\chi(S)=\begin{cases}1 & \text{if } S=1\\ 0 & \text{else}.\end{cases}$	$[-]$
dynamic viscosity μ	1000	$\left[\frac{\mathrm{kg}}{\mathrm{m\ s}}\right]$
Residual Saturation $S^{\mathrm{w}}_{\mathrm{res}}$	0.0	$[-]$
Maximal Saturation $S^{\mathrm{w}}_{\max}$	1.0	$[-]$

Where most of the parameters related to bentonite can directly be taken from the specification documents, others need to be fit to the experiment or chosen from theoretical observations. First the parameters derived by the specification documents will be described.
The mass density of the solid is computed. With the given dry density $\tilde{\mathrm{n}}_{\mathrm{dry}}$, the volumetric water content w and the saturation S with the relation:

$$\rho_{\mathrm{dry}} = \rho_{\mathrm{S}}(1-\phi) = \rho_{\mathrm{S}}\left(1-\frac{w}{S}\right). \qquad (0.11)$$

In equation (0.11), the identity $\phi = \frac{w}{S}$ is used.

The intrinsic permeability k is chosen according to the given dry density for the different bentonite phases with the aid of Figure 3-109.

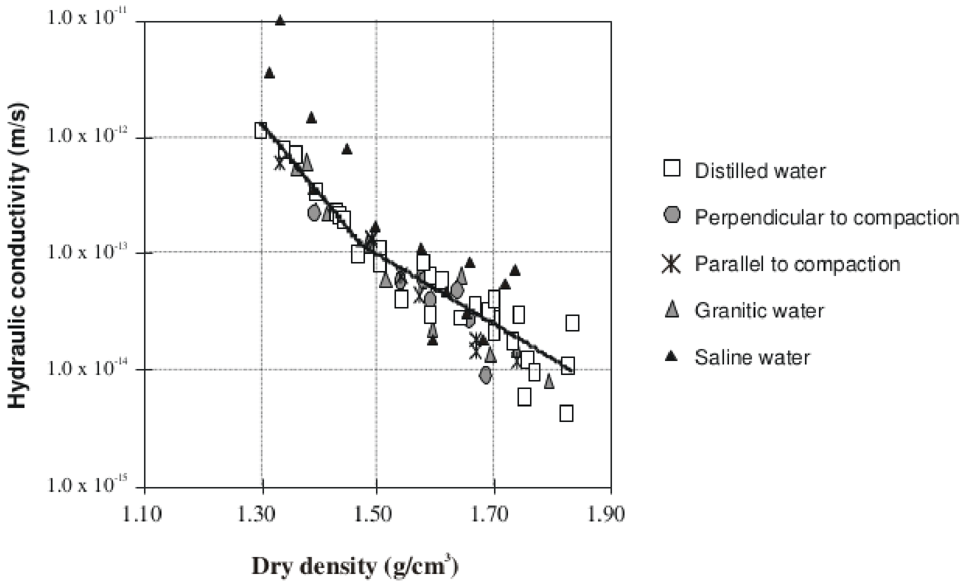

Figure 3-109 Saturated hydraulic conductivity as a function of dry density (Huertas et al., 2000).

The relative permeability follows a potential law depending on the saturation of the specimen with exponents in the range $n \in [1,4]$ as described in the specification document. With the here chosen Brooks Corey law an exponent $\lambda_{\mathrm{k}} = -2$ corresponds to an exponent $n = 2$ which is within the desired range.

For choosing the swelling pressure parameters, the range given in Figure 3-110 was used. Within this range, the parameters were fit to match best to the axial pressure curves given for the considered experiment.

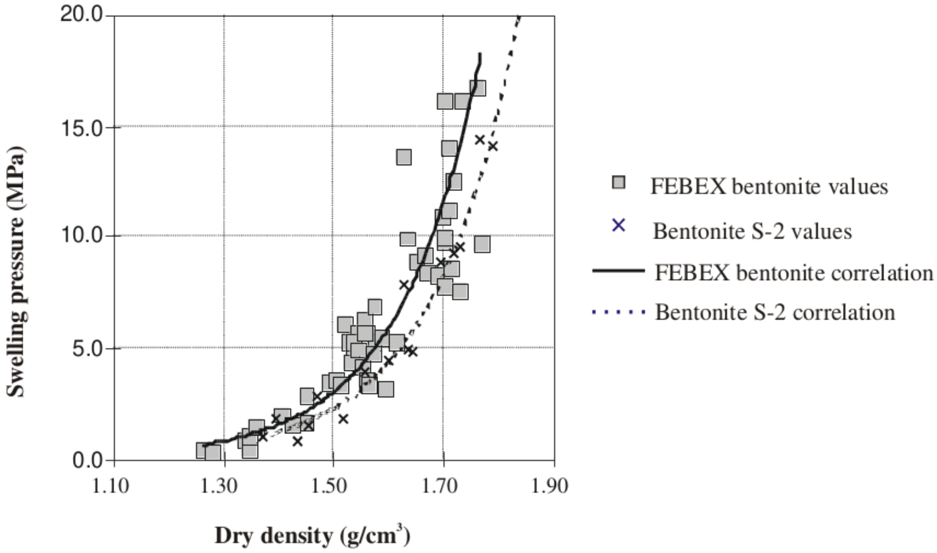

Figure 3-110 Swelling pressure as a function of dry density (Huertas et al., 2000)

The Parameters for the modified Cam Clay model where taken from (Ichikawa et al., 2001).

Table 3.26 Model parameter of the bentonite pellets domain for simulating experiment MGR22, MGR23, MGR 27

Parameter	Value		Unit
	Pellet	Block	
Intrinsic permeability k	$2\cdot10^{-18}$	$1.5\cdot10^{-20}$	$\left[\mathrm{m}^2\right]$
Brooks-Corey Exponent λ_k	-2	-2	$[-]$
Exponent of porosity dependent permeabilty λ_ϕ	10	10	$[-]$
Bulk modulus solid K^{skel}	$1.6667\cdot10^{7}$	$3.33\cdot10^{7}$	$[\mathrm{Pa}]$
Van-Genuchten exponent m	0.22	0.32	$[-]$
Pre-consolidation pressure p_c	1	1	$[\mathrm{MPa}]$
Slope of critical state line M	0.58	0.58	$[-]$
Slope consolidation line λ_c	$9.12\cdot10^{-2}$	$9.12\cdot10^{-2}$	$[-]$
Slope swelling line κ_c	$4.78\cdot10^{-2}$	$4.78\cdot10^{-2}$	$[-]$

Swelling pressure parameter p_{sw}	1.5	5	$[\mathrm{MPa}]$
Exponent of swelling law λ_{sw}	1	1	$[-]$

In the specification document the Van Genuchten parameter for different dry densities of bentonite block were given. For the pellet domain, a lower value for the exponent m was estimated. The gas entry pressure p_{b} for the pellet domain is then chosen to obtain the defined initial saturation of the bentonite pellets with a homogeneous initial pressure in the entire domain.
In order to fit the simulation results to the experimental data the model parameter:

- Young's Modulus of the porous medium
- Poisson ratio of the porous medium
- Exponent of the swelling law λ_{sw}
- Exponent of porosity dependent permeabilty λ_{ϕ}
- Bishops coefficient χ
- Biot's coefficient α_{Biot}

are estimated based on experience.

MGR22

In Figure 3-111 the discretised boundary value problem is shown. It is discretised with 1036 finite elements with biquadratic displacement ansatz and bilinear pressure ansatz (Q2P1). At the inflow surface, the discretization is finer to take high gradients into account. On the entire surface the normal displacement is prescribed as $\mathbf{u}_{\mathrm{n}} = 0$ mm, whereas for the tangential displacement only homogeneous Neumann conditions are used. With this, the bentonite can deform without friction at the boundary. For the hydraulic part of the initial boundary value problem, a constant inflow from the bottom surface of $q = 1.7864 \cdot 10^{-6} \dfrac{\mathrm{kg}}{m^2 s}$ is applied. On the remaining boundary homogeneous Neumann boundary conditions are applied.
The initial pressure is prescribed on the entire domain as $p_0 = -95$ MPa.

With p_0 and with the chosen entry pressure for the pellet water retention function shown in Figure 3-114, no pressure gradient is present at the start of the simulation and with this, no unphysical transfer between block and pellet domain.

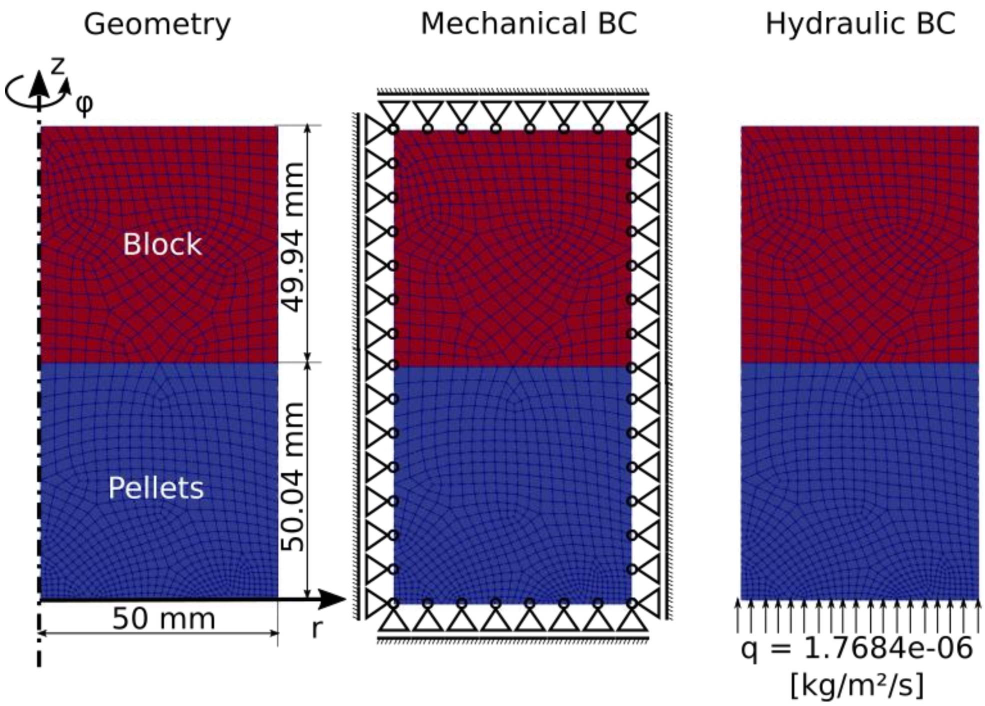

Figure 3-111: *Discretized initial boundary value problem for experiment MGR22. On the left hand side, the geometrical dimensions are shown. In the centre the mechanical boundary conditions and on the right hand side the hydraulic boundary conditions are shown*

Table 3-25 Initial parameters of the pellets domain for simulating experiment MGR22

Parameter	Value: Pellet	Value: Block	Unit
Reference porosity ϕ_0	0.396	0.247	$[-]$
Initial Pressure p_0	-95.4	-95.4	$[\mathrm{MPa}]$
Initial Saturation S_0	0.25	0.55	$[-]$
Entry pressure p_b	0.7	30	$[\mathrm{MPa}]$

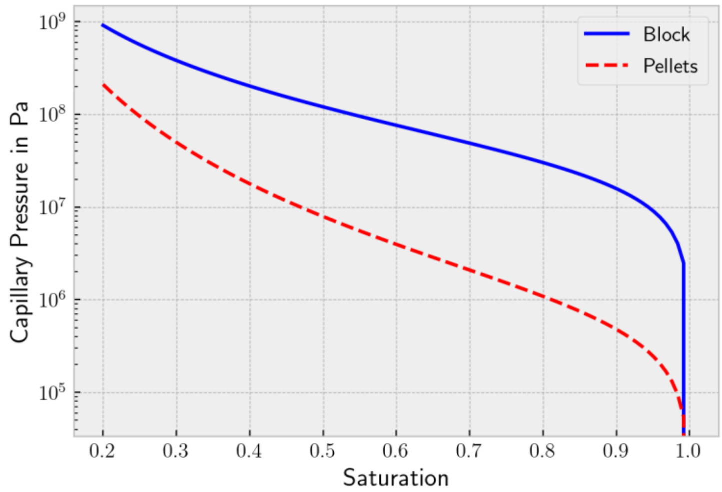

Figure 3-112: Water retention curve for simulation of MGR22. ***MGR23***

In Figure 3-113, the discretised boundary value problem is shown. It is discretized with 1036 Q2P1 elements. On the entire surface the normal displacement is prescribed as $\mathbf{u}_n = 0$ mm, whereas for the tangential displacement only homogeneous Neumann conditions are used. The bentonite can deform without friction at the boundary.

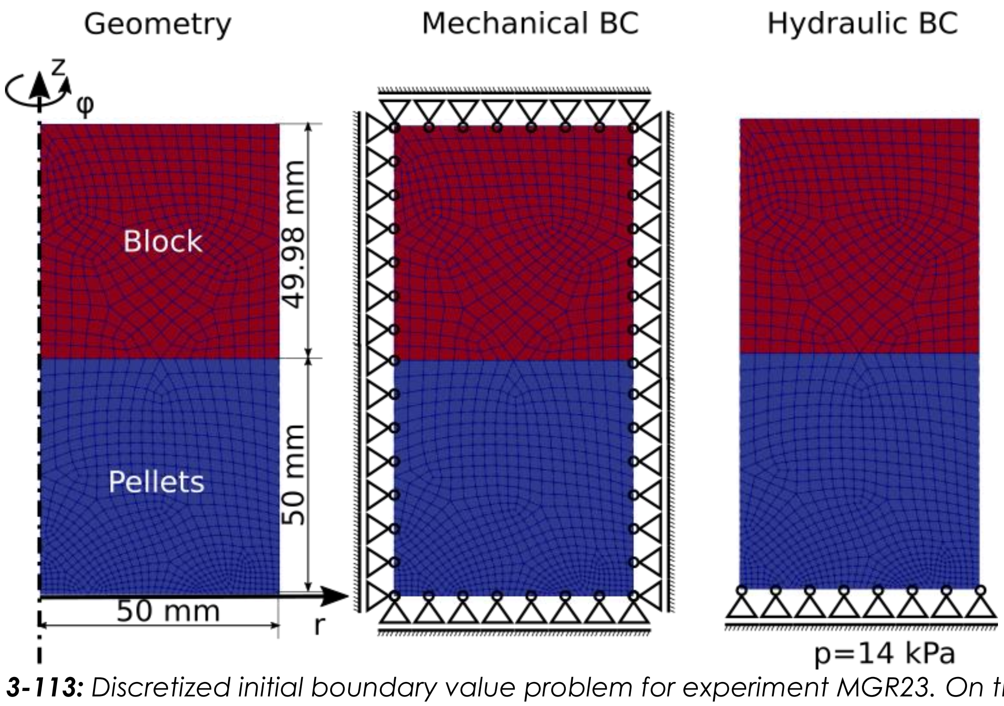

Figure 3-113: *Discretized initial boundary value problem for experiment MGR23. On the left hand side, the geometrical dimensions are shown. In the centre the mechanical boundary conditions and on the right hand side the hydraulic boundary conditions are shown*

For the hydraulic part of the initial boundary value problem a pressure of $p = 14$ kPa is prescribed at the bottom of the domain. The initial pressure is prescribed on the entire domain as $p_0 = -91.1$ MPa. With this and with the chosen entry pressure for the pellet water retention function shown in Figure 3-114 no pressure gradient is present at the start of the simulation.

Table 3-26 Initial parameter the bentonite pellets domain for simulating experiment MGR23 and MGR27

Parameter	Value		Unit
	Pellet	Block	
Reference porosity ϕ_0	0.389	0.254	$[-]$
Initial Pressure p_0	-91.1	-91.1	$[\mathrm{MPa}]$
Initial Saturation S_0	0.09	0.56	$[-]$
Entry pressure p_b	0.018	30	$[\mathrm{MPa}]$

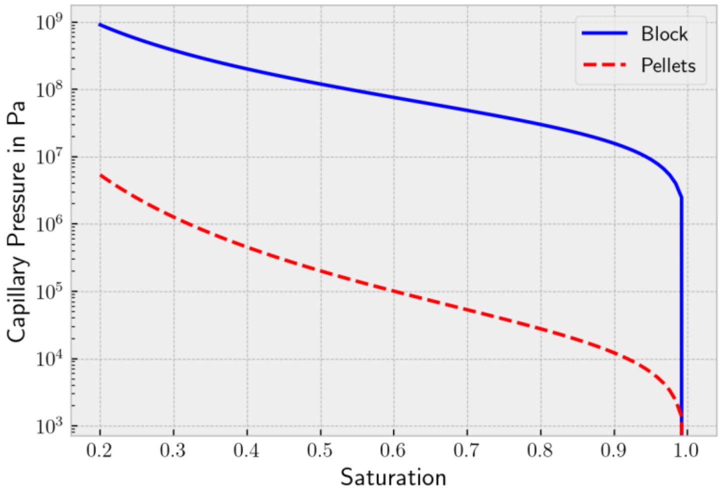

Figure 3-114 *Water retention curve for simulation of experiment MGR23*

MGR27

The initial boundary value problem corresponding to experiment MGR27 has the same parameters and boundary condition as the simulation model of MGR23 described in section 0 and therefore the parameter can be taken from Table 3-25. The only difference between the two models is the arrangement of the pellet and block domains. Whereas for MGR23 the block material is at the top and the pellets are below the domains are interchanged for experiment MGR27.

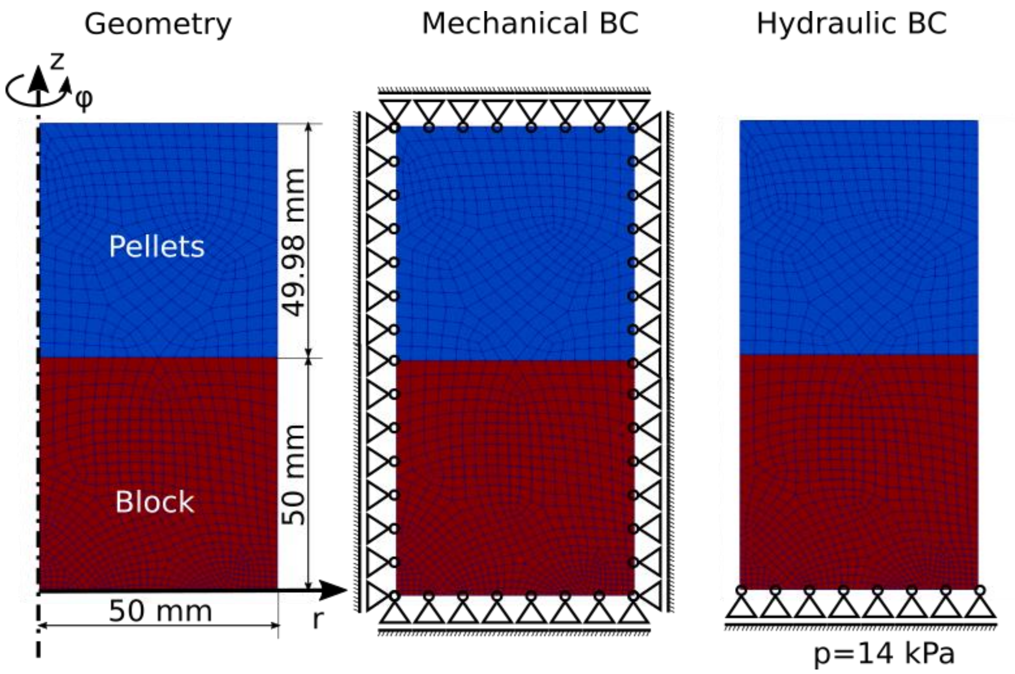

Figure 3-115: *Discretized initial boundary value problem for experiment MGR27. On the left hand side, the geometrical dimensions are shown. In the centre the mechanical boundary conditions and on the right hand side the hydraulic boundary conditions are shown*

3.7.3 Results MGR22

The simulation of MGR22 could not be finished successfully. Local tension dominated stress states introduces a localization where the integration of the material model fails. Therefore, only preliminary results will be shown here.

Stress Plots

Since there is no friction and no inertia considered in the simulation the stress at the top and bottom is nearly equal. This is shown in Figure 3-116. The drop of the stress level at the bottom face reflects the localisation of the problem. For the radial stress a temporally shifted stress curve is obtained for the pellet and for the block domain respectively as depicted in Figure 3-117. The isotropic swelling law is reflected in nearly the same stress level for the radial and axial stresses.

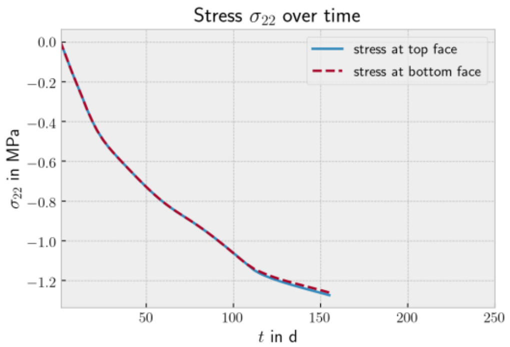

Figure 3-116: *Axial stress over time at the centre point of the bottom and top face*

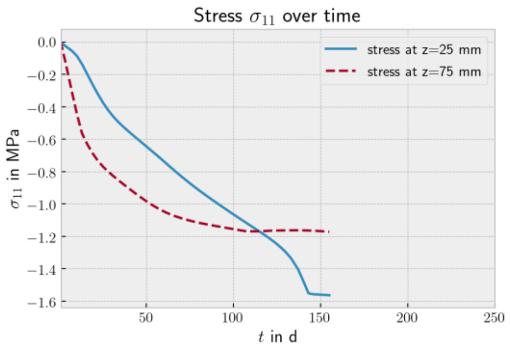

Figure 3-117: *Radial stress of a boundary point over time at z=25 mm and z=75 mm*

Dry Density Plots

The dry density profiles for different z locations are shown in Figure 3-118. In the pellet domain the density increases slightly and the density of the block domain slightly decreases. In Figure 3-119 a)-e), the dry density profiles for different z locations and times are shown. It can be seen that the distribution of the density is nearly constant over the cross section of the specimen. The only exception is at the material interface displayed in Figure 3-119 c). Here, the cross section profile is not homogenous. In Figure 3-119 f), the homogenisation behaviour is shown. A significant density jump is still present at the end of the simulation.

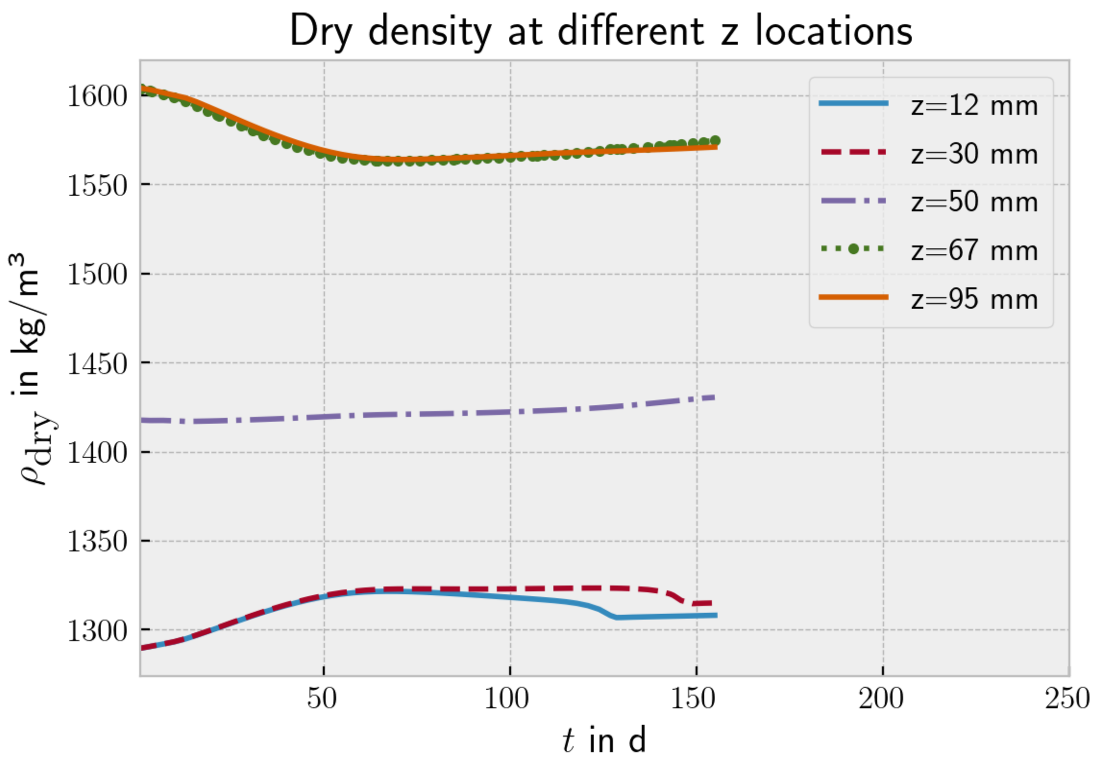

Figure 3-118: *Dry density time history plots for different z locations in the centre of the specimen*

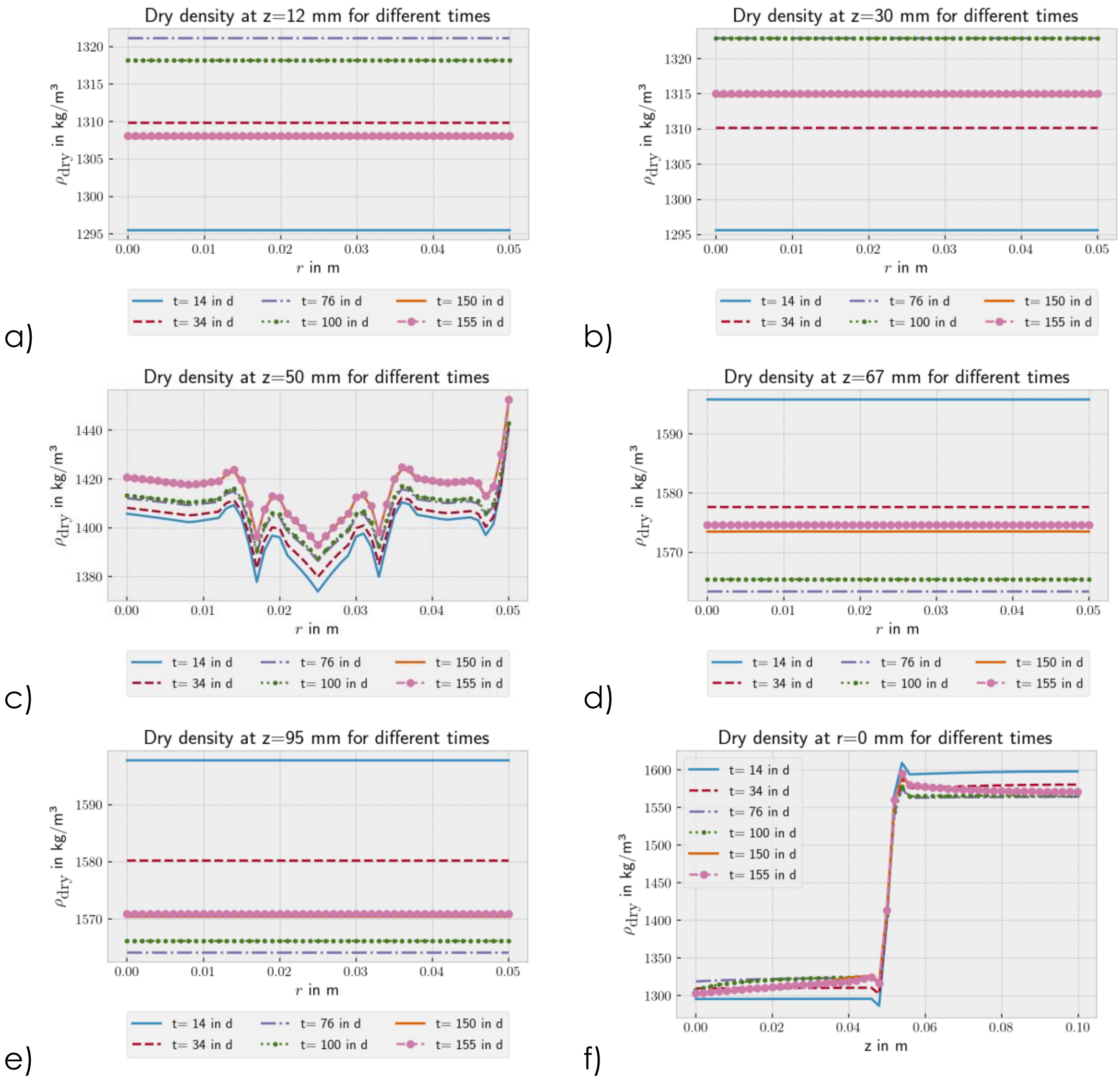

Figure 3-119: *Density profiles at different z profiles for given times (a-e) and density profile along z axis at given times (f)*

Water Content Plots

In Figure 3-120, the time history plots for the volumetric water content at different z locations at r=0 mm is shown.

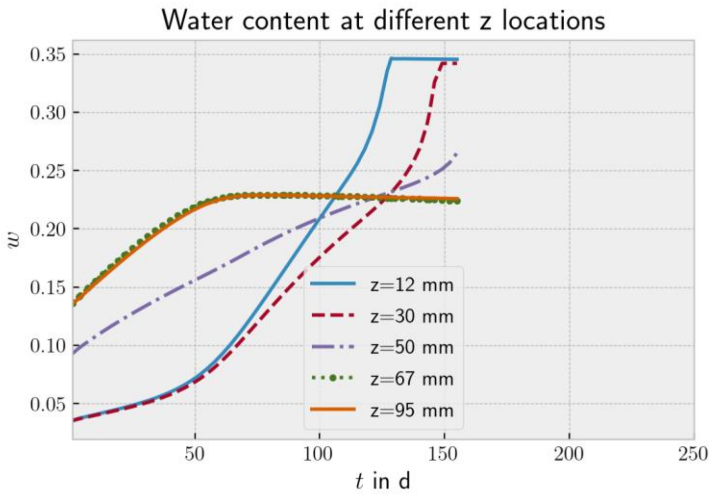

Figure 3-120: *Volumetric water content time history plots for different z locations in the centre of the specimen*

The increase of water content in the pellet domain is significantly higher than its increase in the block domain. In Figure 3-121 a)-e) the profiles of the water content at different z locations for the requested times are plotted.

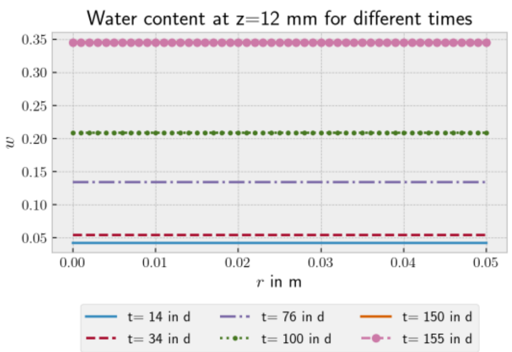

a)

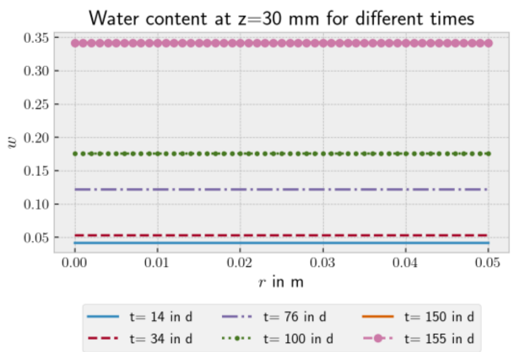

b)

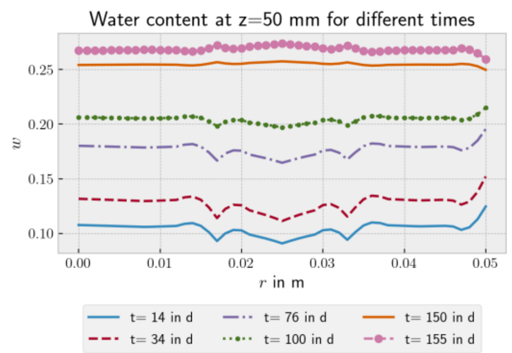

c)

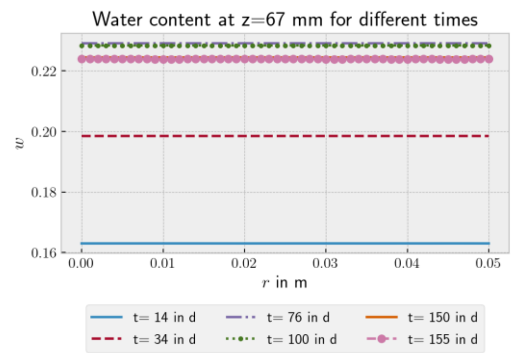

d)

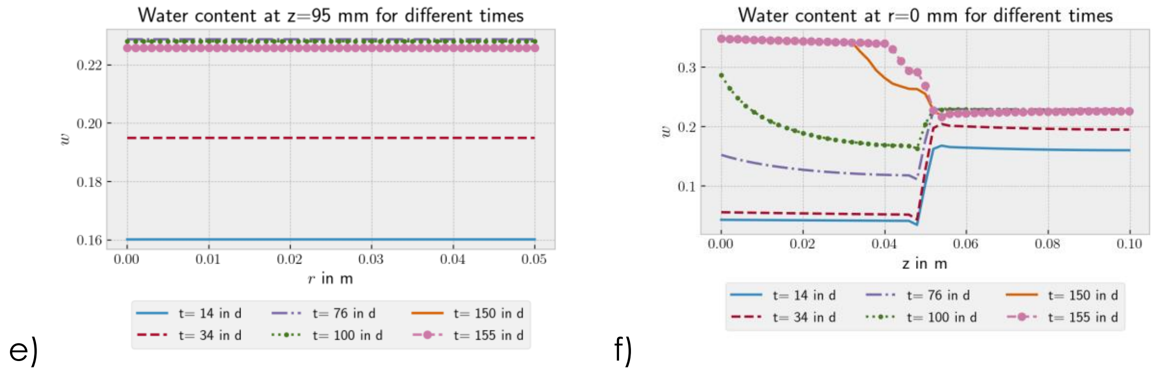

Figure 3-121: Volumetric water content profiles at different z profiles for given times (a-e) and water content profile along z axis at given times (f)

Over the cross section, the profiles are nearly constant as expected due to initial and boundary conditions. An exception is again the profile across the material interface shown in Figure 3-121 c). Figure 3-121 f) displays the profile along the z axis. The jump of the water content successively smears out with increasing time.

Saturation Plots

Figure 3-122 shows the saturation profiles for different times along the z axis. The pellet domain takes much longer to saturate than the block domain. At the end of the simulation nearly the entire domain is saturated.

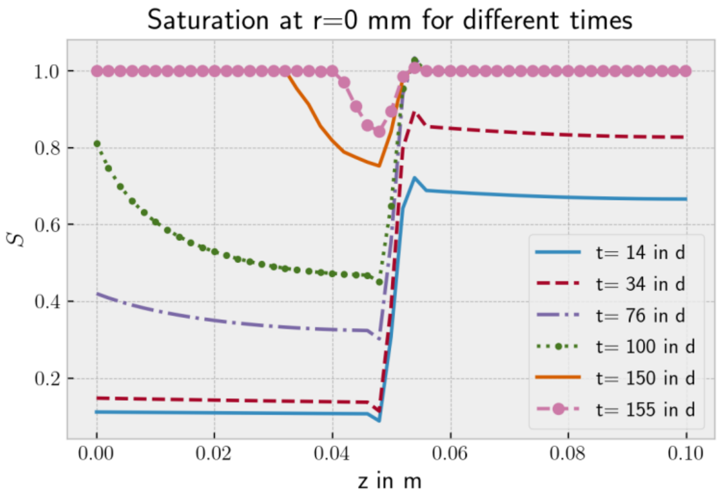

Figure 3-122: Saturation profile along the z axis for given times

3.7.4 Results MGR23

Stress Plots

Since there is no friction and no inertia considered in the simulation the stress at the top and bottom is nearly equals. The slight difference of both curves can be explained by post processing a single point and not the entire surface. This is shown in Figure 3-123. For the radial stress a temporally shifted stress curve is obtained for the pellet and for the block domain respectively as depicted in Figure 3-124. The stress level of radial and axial stresses reflects the isotropic swelling law.

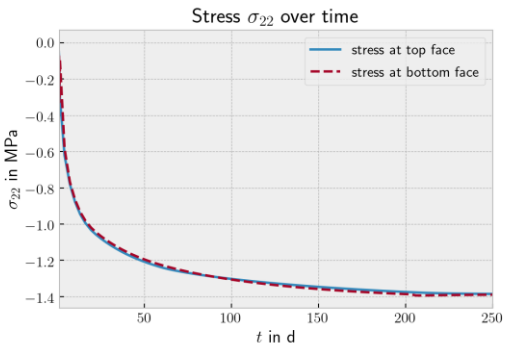

Figure 3-123: *Compressive axial stress over time at bottom and top face*

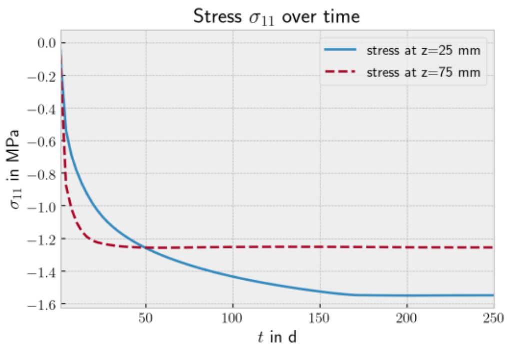

Figure 3-124: *Compressive radial stress over time at z=25 mm and z=75 mm*

Dry Density Plots

The dry density profiles for different z locations are shown in Figure 3-125. In the pellet domain the density increases slightly and the density of the block domain slightly decreases.

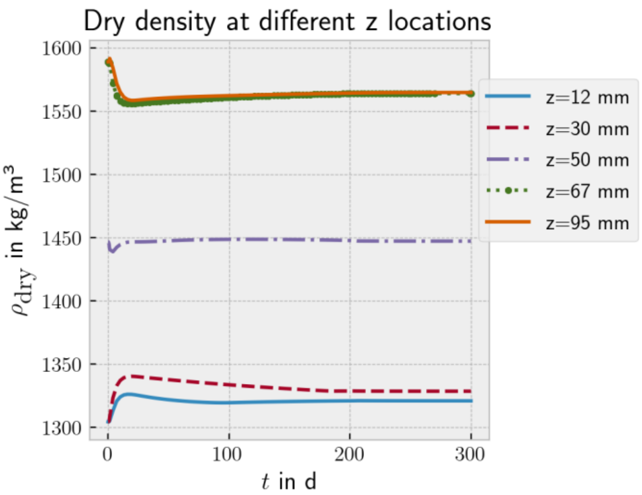

Figure 3-125: *Dry density time history plots for different z locations in the centre of the specimen*

In Figure 3-126 a)-e), the dry density profiles for different z locations and times are shown. It can be seen that the distribution of the density is nearly constant over the cross section of the specimen. In Figure 3-126 f), the homogenisation behaviour is shown. A significant density jump is still present at the end of the simulation.

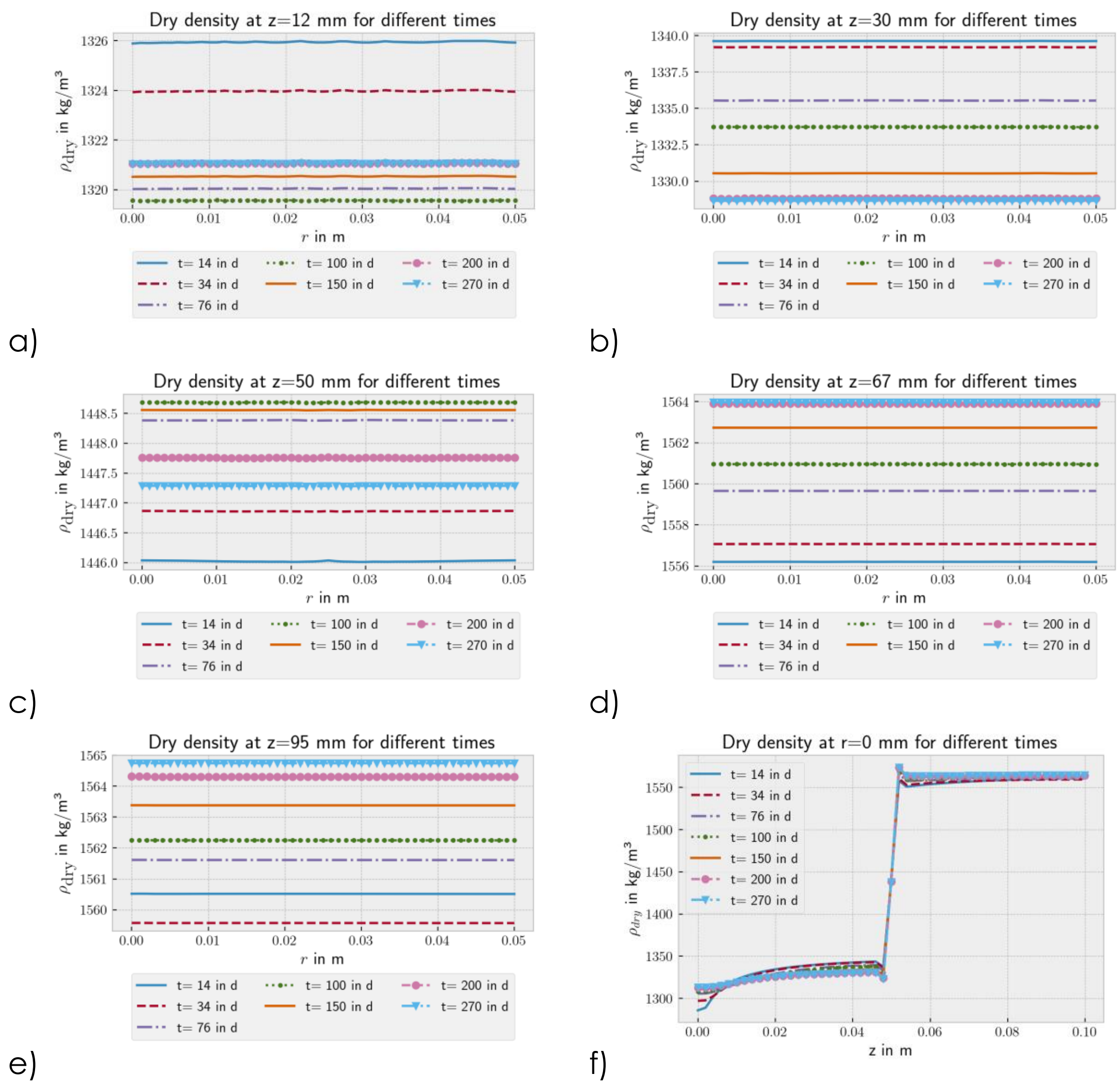

Figure 3-126: Density profiles at different z profiles for given times (a-e) and density profile along z axis at given times (f)

Water Content Plots

In Figure 3-127, the time history plots for the water content at different z locations at r=0 mm is shown. The increase of water content in the pellet domain is significantly higher than its increase in the block domain. In Figure 3-128 a)-e) the profiles of the water content at different z locations for the requested times are plotted. Over the cross section, the profiles are nearly constant. Therefore, Figure 3-128 f) contains all information. The jump of the water content is nearly smeared out at the end of the experiment.

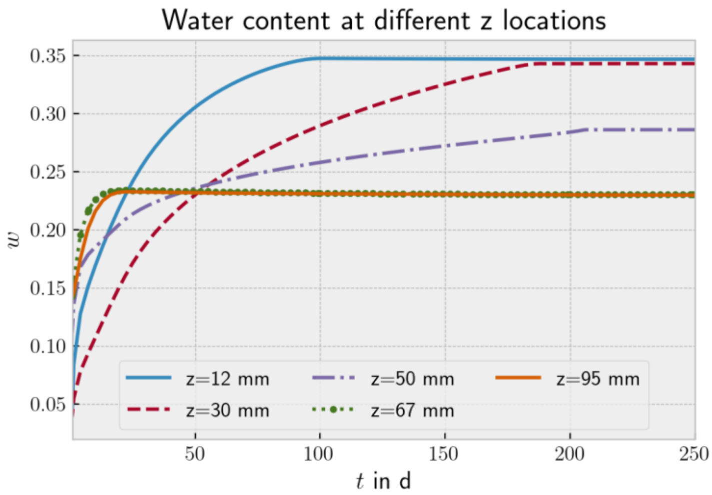

Figure 3-127: Water content time history plots for different z locations in the centre of the specimen

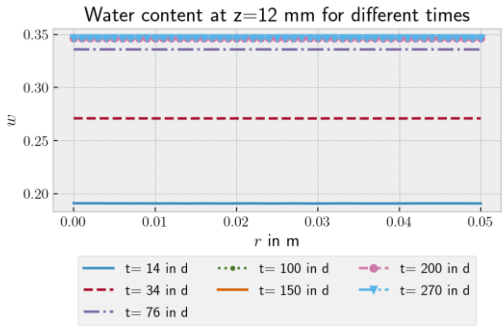

a)

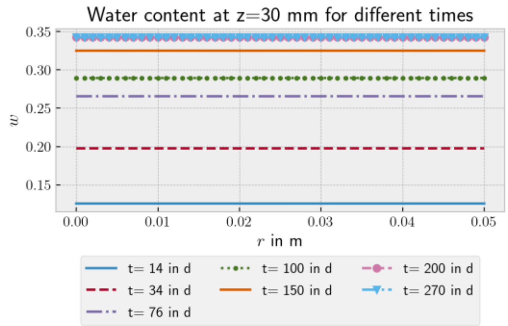

b)

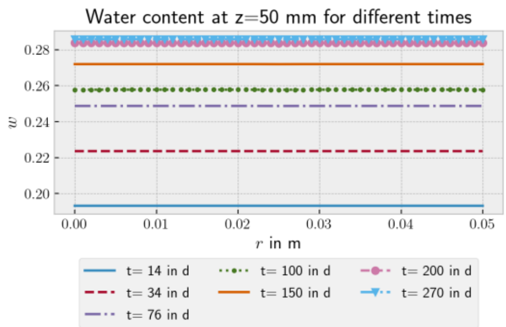

c)

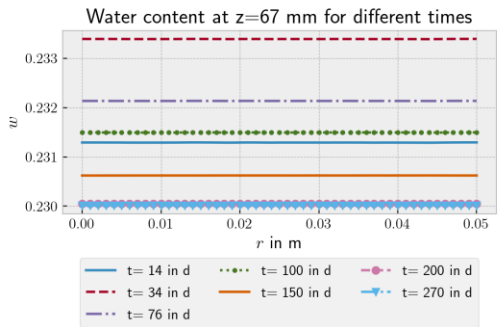

d)

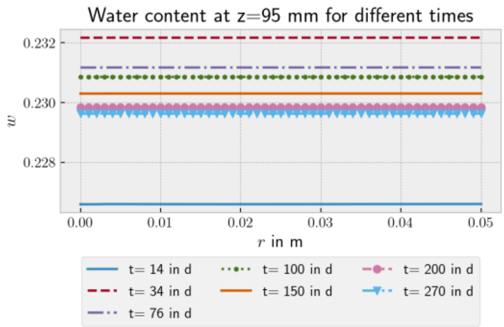

e)

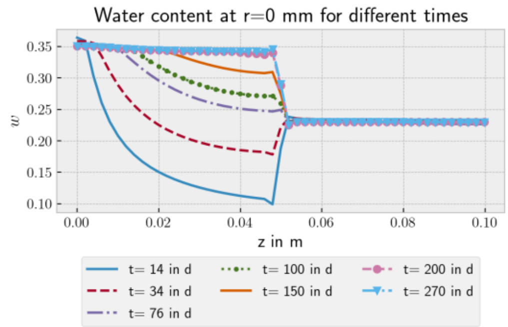

f)

Figure 3-128: *Volumetric water content profiles at different z profiles for given times (a-e) and water content profile along z axis at given times (f)*

Saturation Plots

Figure 3-129 shows the saturation profiles for different times along the z axis. The pellet domain takes much longer to saturate than the block domain. At the end of the experiment the entire domain is saturated.

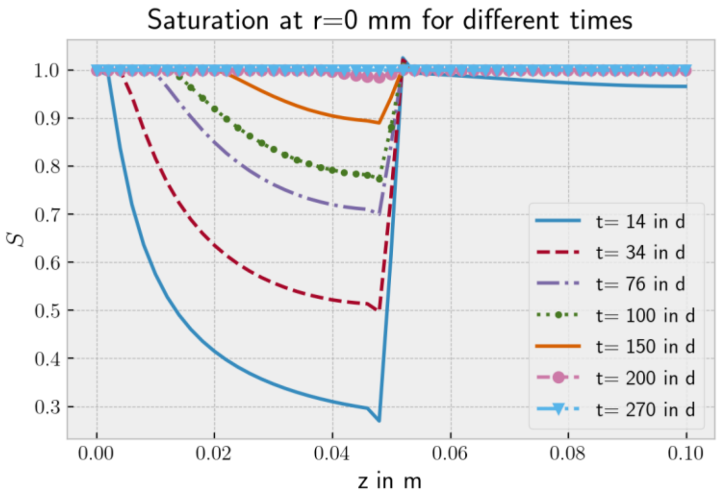

Figure 3-129: Saturation profile along the z axis for given times

3.7.5 Results MGR27

Stress Plots

Figure 3-130 and Figure 3-131 show the curves for the axial and radial compressive stresses over time. Since there is no friction and no inertia considered in the simulation the axial stress at the top and bottom is nearly equals. For the radial stress, a higher stress level is observed in the block domain as depicted in Figure 3-124. Different to experiment MGR23 no temporal difference is present in the evolution of the radial stresses.

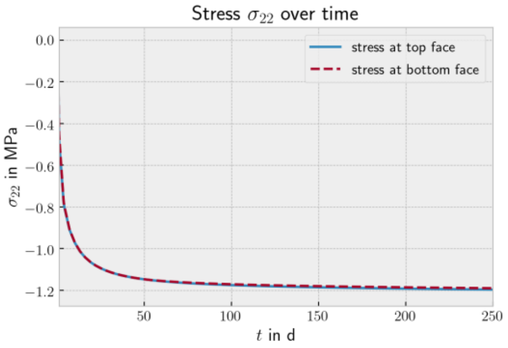

Figure 3-130 Axial stress over time at centre point of bottom and top face

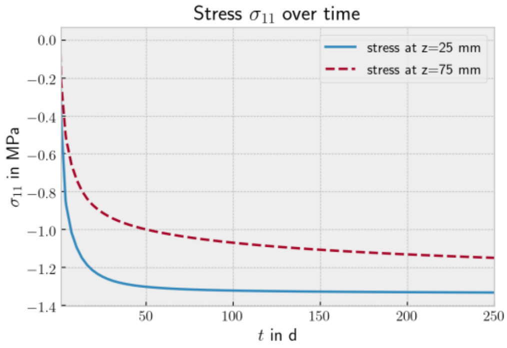

Figure 3-131 Radial stress at boundary point over time at z=25 mm and z=75 mm

Dry Density Plots

In Figure 3-132, the evolution of the dry density for different z locations is shown. The dry density of the pellet domain increases while the dry density of the block domain decreases. As for the previous simulations the distribution over the cross section is nearly constant as could be seen in Figure 3-133 a)-e). In f), a profile along the z axis is shown. The density jump is not homogenised during simulation time.

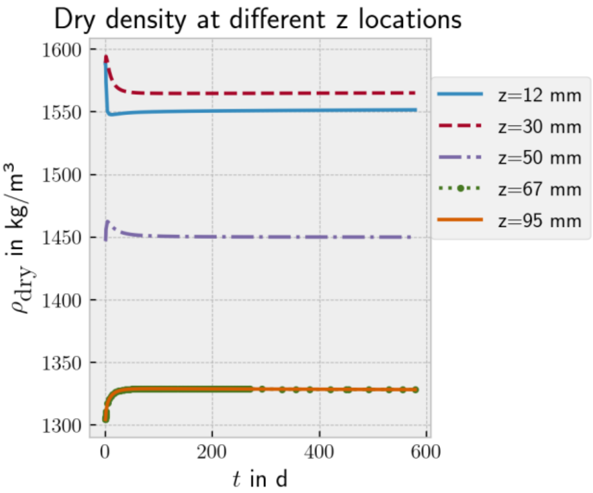

Figure 3-132: Dry density time history plots for different z locations in the centre of the specimen

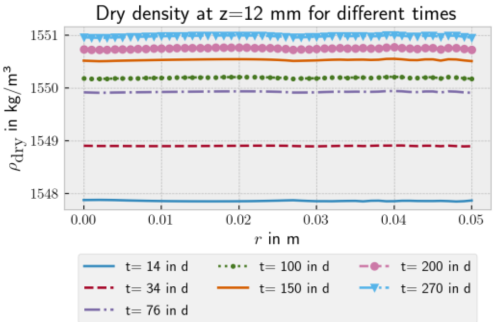

a)

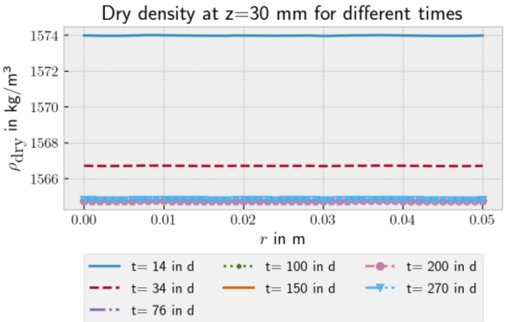

b)

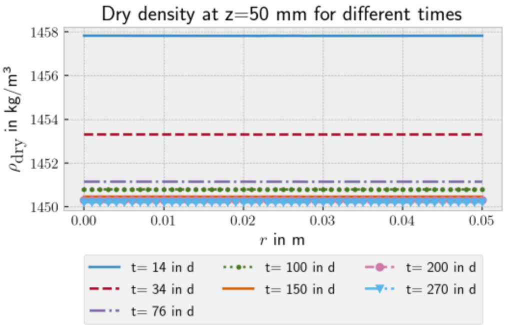

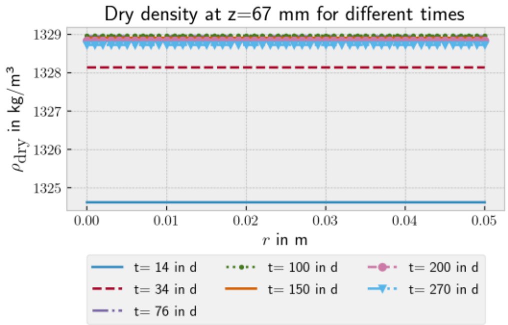

c) d)

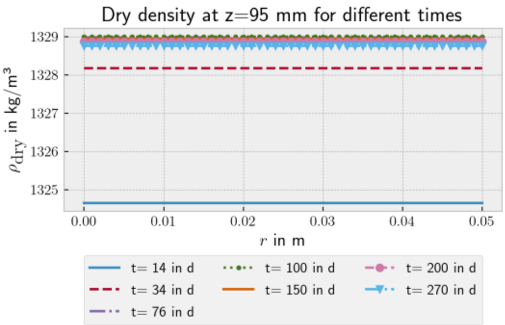

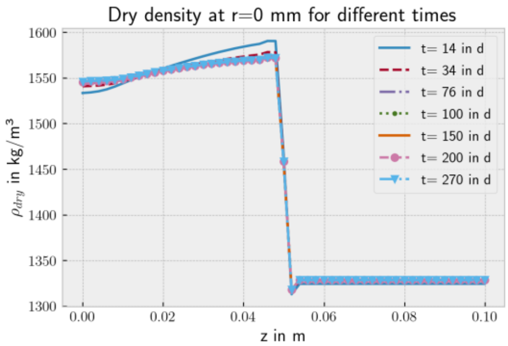

e) f)

Figure 3-133: *Density profiles at different z profiles for given times (a-e) and density profile along z axis at given times (f)*

Water content Plots

In Figure 3-134, the time history for the water content for different z locations is shown. In the block domain, the evolution early runs into a saturation whereas in the pellet domain the steady state is not reached within the time frame of the simulation. In Figure 3-135, the water content profiles along the cross section is shown. Along the profile the water content is constant. In Figure 3-135 f) the profile of the z axis is shown. The jump in water content is not homogenised during simulation time.

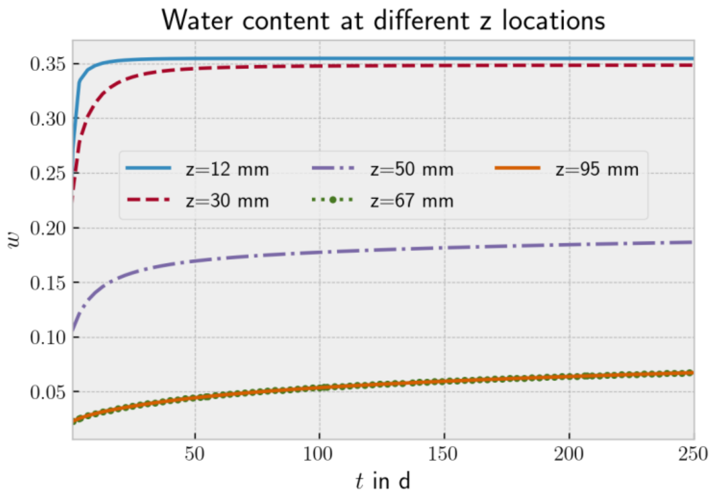

Figure 3-134: *Water content time history plots for different z locations in the centre of the specimen*

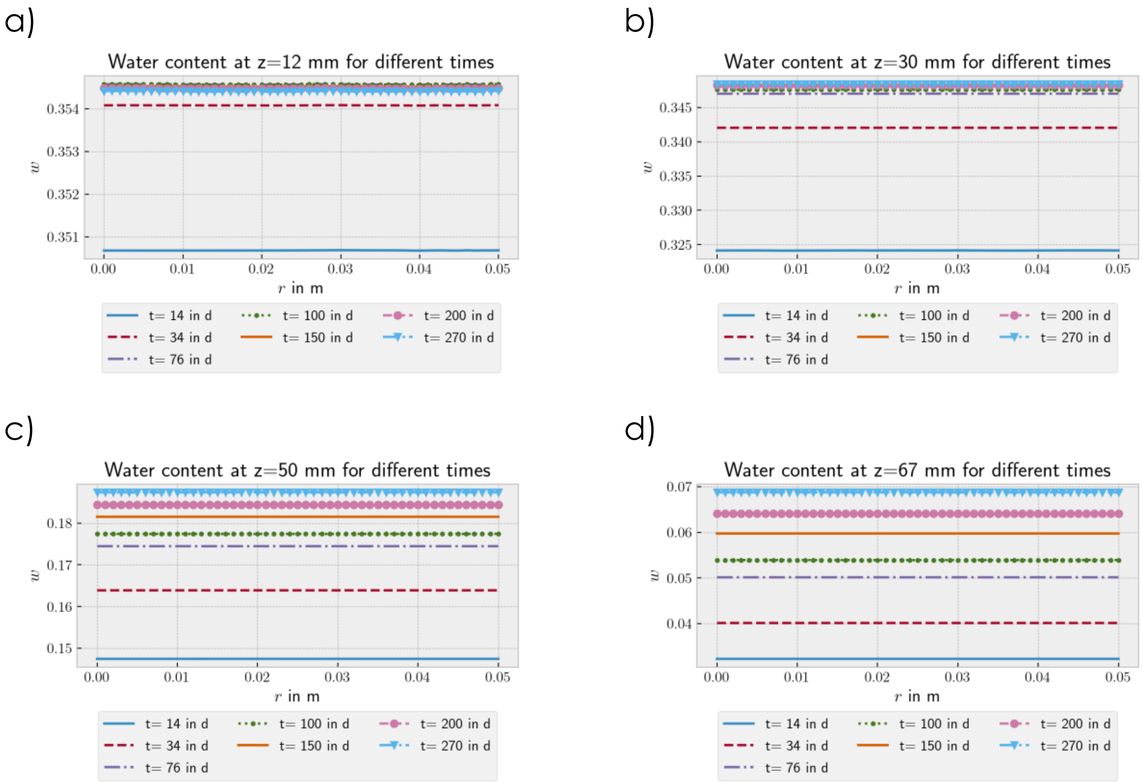

e)

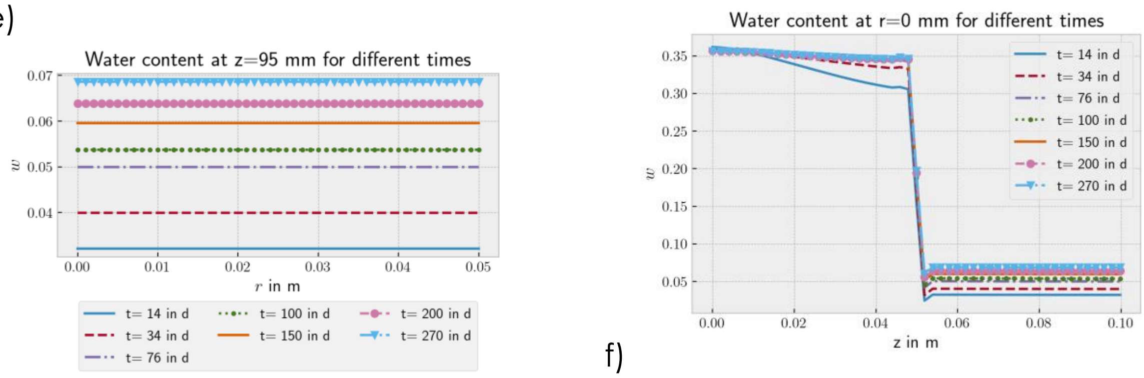

f)

Figure 3-135: *Volumetric Water content profiles at different z profiles for given times (a-e) and water content profile along z axis at given times (f)*

Saturation Plots

In Figure 3-136, the saturation along the z axis is shown for different times. The block domain saturates during the simulation time whereas the saturation in the pellet domain increases but remains unsaturated.

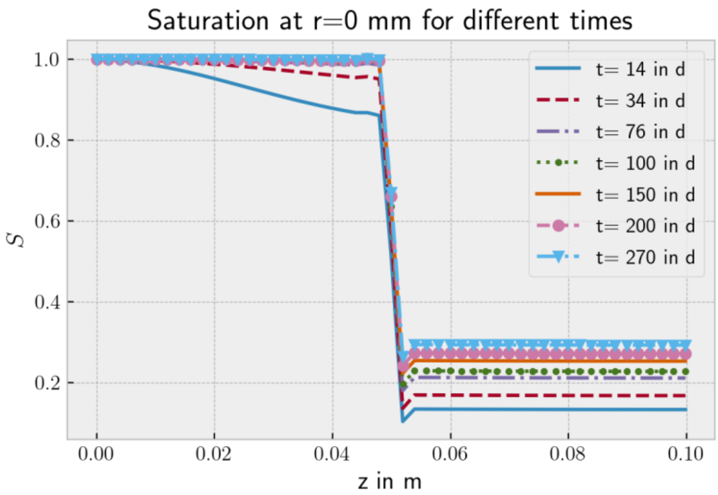

Figure 3-136 *Saturation profile along the z axis for given times*

3.7.1 Comparison with experimental results

For experiment MGR22 and MGR23 experimental data was given. In this chapter these data are compared to the simulation results.

MGR22

In Figure 3-137 Figure 3-140, the computed axial pressure is shown along with the measured one. The model does not predict the slope of axial pressure. This is due to the weak hydro mechanical coupling of the model. This is introduced by the Bishop's function:

$$\chi(S) = \begin{cases} 1 \text{ if } S = 1 \\ 0 \text{ else .} \end{cases} \tag{0.12}$$

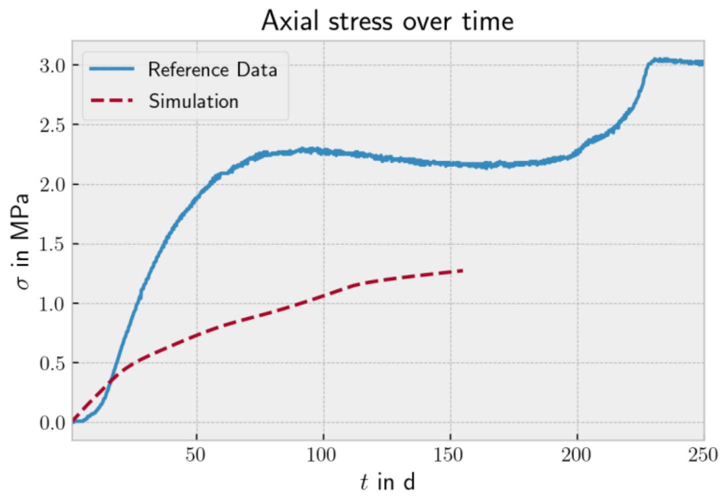

Figure 3-137: *Comparison between measured axial pressure and predicted axial pressure over time*

Therefore, the coupling of the mass balance of water and the balance of linear momentum is only weak. With the chosen model parameters it is not possible to simulate the entire process. At the saturation front a local tension dominated stress state can be observed. This leads to a localisation of the material model and an error in the stress integration algorithm.

In Figure 3-138 and in Figure 3-139 the dry density profile and the water content profile for the end of simulation and the ex situ state respectively are shown. For the dry density the trend of increasing values towards the material interface in the pellet domain is captured only qualitatively. A high jump in the density value is still present in the simulation whereas the material interface is far more homogeised in the experiment. For the water content the same holds true. In the pellet domain the water content decreases towards the material interface. In the simulation a jump in the water content across the interface is present which is smeared out in the experiment.

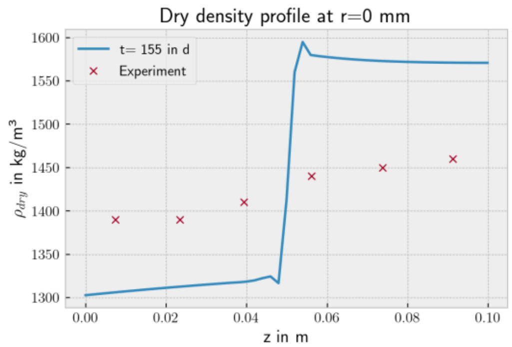

Figure 3-138: *Comparison of the simulated and experimentally observed profile of dry density along the z axis*

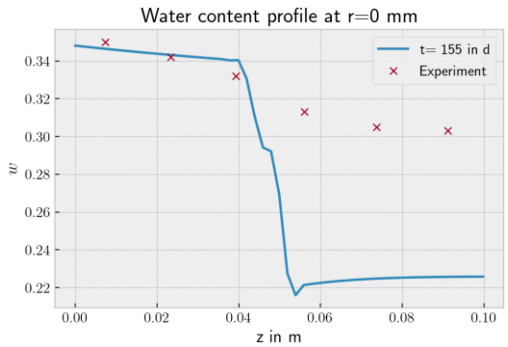

Figure 3-139: *Comparison of the simulated and experimentally observed profile of the volumetric water content along the z axis*

MGR23

In Figure 3-140, the computed axial pressure is shown along with the measured one. The model predicts the first slope of axial pressure reasonably well.

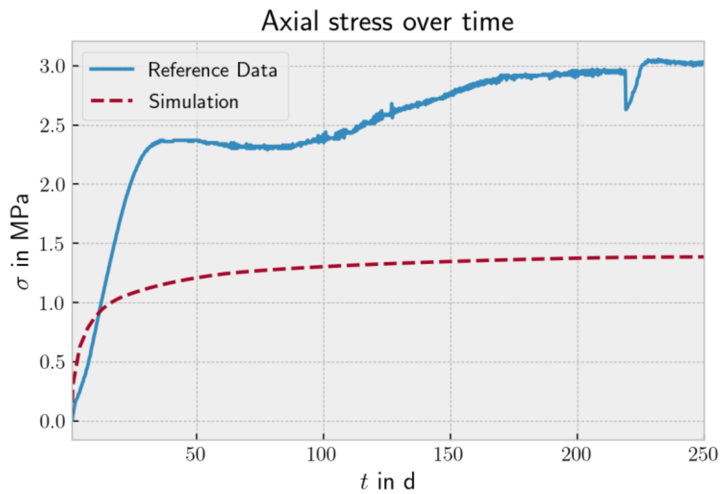

Figure 3-140: *Comparison between measured axial pressure and predicted axial pressure over time*

In addition, the stress plateau is matching well. Nevertheless, the model is not able to reflect the actual stress level. This cannot be explained by the weak hydro mechanical coupling because the pressure boundary condition is of negligible magnitude.
Furthermore, no second increase of axial stress is observed in the simulations. Since the swelling of the bentonite is the only source of stress, the reason for the lack of the second slope is expected to be related to the swelling stress. The swelling is driven by the rate of saturation change in the current implementation. A comparison of the experimental saturation evolution is given in Figure 3-141 and shows a good agreement to the simulated average saturation.

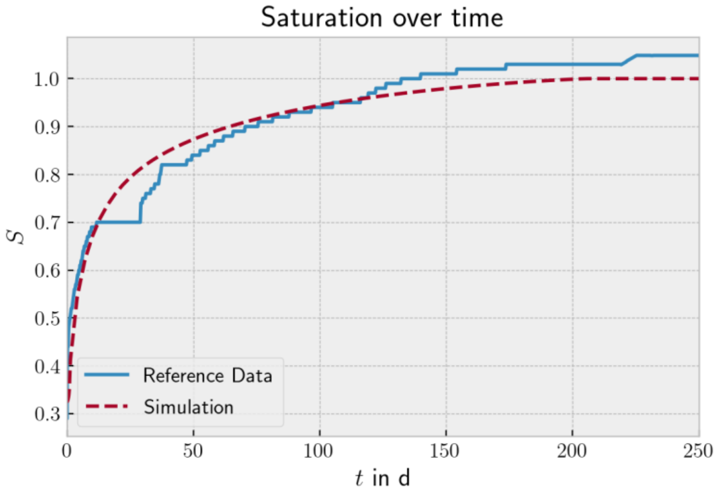

Figure 3-141: *Comparison of mean saturation evolution between simulation and experiment*

A reason for the discrepancy in the axial stresses could be a temporal different development of the saturation in each domain. This is given as shown in Figure 3-129. Since, the saturation of the block domain is at steady state within 50 days, the first increase of the axial stress curve is explained by the combined swelling of bentonite block and pellets. For the further swelling of the bentonite pellets the hardening of the plastic constitutive equation is too weak to significantly increase the stresses further.
In Figure 3-142, the dry density profile and the water content measured after the test is plotted together with the simulation. The trend of homogenising the dry density visible in the experimental data is also existent in the simulation.

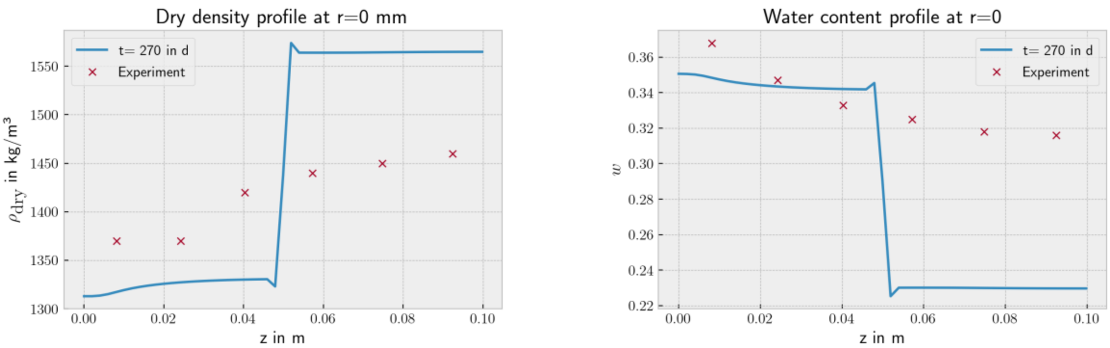

Figure 3-142: *Dry density (left) and water content (right) profile at the center of the specimen at termination of the experiment*

The Water content is highest at the surface of the hydraulic boundary condition. This is true for the experiment as well for the simulation. Furthermore, the content decreases with increasing distance to the hydration surface.

3.7.2 Discussion

Three simulation models for the CIEMAT experiments MGR22, MGR23 and MGR27 are described. After a short description of the governing equations, the constitutive model used for the simulation is outlined. The initial boundary value problem with all boundary conditions, initial conditions and model parameters were listed. The simulation results for all three simulations are shortly described and for experiment MGR22 and MGR23 a short comparison of the simulation results with the experimental data was conducted. The following points were the major outcome of the analysis of the simulations:

- The model currently does not achieve the necessary stress level for the swelling experiment
- The principal trend and timing of a stationary stress field is captured
- A second increase of the stresses due to time shifted saturation process could not be captured
- The average water content evolution is simulated fairly accurately
- For the time evolution of the dry density the correct trend and therefore the trend in porosity change is met as well

To improve the agreement between experimental and simulation results at least two different steps are necessary. First, the chosen parameter can be further tuned to get better results. Unfortunately, the stability of the simulation is quite sensitive to a change of the key parameters (Young's modulus, swelling pressure parameter and plasticity related parameters). Up to now, this can be explained by the numerical properties of the plasticity model and the local tension dominated stress state at the saturation front. Here the second step comes into play. To improve the capabilities of the model the constitutive equations need to be enhanced. This can be done by improving the behaviour in tension dominated stress states. A further improvement would be the reduction of mesh dependent localisations. This is necessary to be more stable for local tension states. Furthermore, the time shifted swelling behaviour needs to be captured. Here additional effort in deriving a suitable model is essential. Therefore, a double structure continuum is under investigation.

3.8 ICL

The results provided by ICL were submitted after the comparison of the results by other modelling teams was completed. They are therefore integrated in the document, but are not included in the comparisons and the final synthesis of task 5.3 given in Section 4.

3.8.1 Description of the models

To simulate the mechanical behaviour of compacted FEBEX bentonite in experiments associated with the Task 5.3, the ICL team has applied the constitutive model presented in the Beacon deliverable D3.1, produced as part of the WP3 of the Beacon project.

The model is an extended and modified version of the Barcelona Basic Modelling (BBM) framework (Alonso et al., 1990; Gens & Alonso, 1992), adopting a double-porosity structure and the formulation with net stress and suction as two independent stress variables (Ghiadistri, 2019; Ghiadistri et al., 2018).

The soil water retention (SWR) model used in the simulations is a form of a non-hysteretic Van Genuchten-type (van Genuchten, 1980) model, formulated in terms of the degree of saturation and matric suction and accounting for the variation of the specific volume (Melgarejo Corredor, 2004).

The adopted hydraulic conductivity (permeability) model (Potts & Zdravkovic, 1999; Nyambayo & Potts, 2010) assumes logarithmic variation of permeability with matric suction.

All models were implemented in the finite element software ICFEP (Potts & Zdravkovic, 1999), which has been applied by the ICL team in all numerical simulations for the Beacon project.

Mechanical model

The constitutive model applied in all analyses to represent the mechanical behaviour of compacted FEBEX bentonite is the Imperial College Double Structure Model (ICDSM), Ghiadistri (2019), Ghiadistri et al. (2018). This is an extension of the previous single structure model (ICSSM, Georgiadis et al., 2005; Tsiampousi et al., 2013) which adopts the Barcelona Basic Modelling (BBM) framework (Alonso et al., 1990).
The ICDSM was introduced in detail in the deliverable D.3.1. Consequently, only the part of the model that enhances the simulation of the behaviour of expansive clays, as appropriate for compacted bentonite, is presented here. Overall, the model is formulated for unsaturated clays, adopting two independent stress variables: suction, $s = u_{air} - u_w$, and net stress, $\bar{\sigma} = \sigma_{tot} - u_{air}$, with u_{air} and u_w being the air and water pressures in the pores, respectively, and σ_{tot} being the total stress. To enable smooth transition from saturated to unsaturated states and vice versa, the model also introduces an equivalent suction, $s_{eq} = s - s_{air}$, and equivalent stress, $\sigma = \bar{\sigma} + s_{air}$, where s_{air} is the air-entry value of suction for a given soil. As such, the model allows realistic values of s_{air} to be prescribed for any soil and full saturation is reached when $s = s_{air}$. The model is further generalised in the (J, p, θ, s_{eq}) space, where J, p and θ are

the invariants of the equivalent stress tensor, representing generalised deviatoric stress, mean equivalent stress and Lode's angle, respectively.

The enhancement of the ICDSM to enable the modelling of unsaturated expansive clays comprises the introduction of a double-porosity structure into the model formulation, in agreement with e.g. Gens & Alonso (1992) and Alonso et al. (1999). This formulation differentiates two levels of structure in the clay: the macro-structure, which is assumed unsaturated and mostly defined by the original ICSSM framework; and the micro-structure, assumed to be elastic, volumetric and fully saturated.

Characteristics of the micro-structure

Assuming the micro-structure to be fully saturated implies that it can be defined in terms of effective stresses, where the mean effective stress is defined as $p' = p + s_{eq}$. The assumptions that it is also volumetric and elastic imply that changes in p' result in elastic volumetric micro-strains, $\Delta\varepsilon^{e}_{v,m}$:

$$\Delta\varepsilon^{e}_{v,m} = \frac{\Delta p'}{K_m} \tag{1}$$

where the micro-structural bulk modulus, K_m, is defined as:

$$K_m = \frac{1 + e_m}{\kappa_m} p' \tag{2}$$

In the above equation, e_m is the micro-structural void ratio and κ_m is the micro-structural elastic compressibility parameter. For consistency, the following must be satisfied:

$$e = e_M + e_m \tag{3}$$

where e_M is the macro-structural void ratio and e is the overall void ratio of the material. The bulk modulus K_m is additional to the two bulk moduli associated with the macro-structure and defined by the ICSSM formulation: $K_{s,M}$, associated with equivalent suction, and $K_{p,M}$, associated with mean equivalent stress, all three defining the overall elastic soil behaviour in the double-structure formulation.

Interaction of the two levels of structure

Although the micro-structural volumetric deformation is elastic, it is assumed to contribute to the macro-structural volumetric plastic strains, $\Delta\varepsilon^{p}_{v,\beta}$, through an additional plastic mechanism:

$$\Delta\varepsilon^{p}_{v,\beta} = f_\beta \cdot \Delta\varepsilon^{e}_{v,m} \tag{4}$$

defined by the interaction function, f_β, between the two levels of structure. The shape of this function is dependent on whether the micro-structure swells or compresses and is defined as:

$$f_\beta = \begin{cases} \begin{cases} c_{c1} + c_{c2}\left(\frac{p_r}{p_0}\right)^{c_{c3}} & if \quad \frac{p_r}{p_0} \geq 0 \\ c_{c1} & if \quad \frac{p_r}{p_0} < 0 \end{cases} & micro-compression \\ \begin{cases} c_{s1} + c_{s2}\left(1 - \frac{p_r}{p_0}\right)^{c_{s3}} & if \quad \frac{p_r}{p_0} \geq 0 \\ c_{s1} + c_{s2} & if \quad \frac{p_r}{p_0} < 0 \end{cases} & micro-swelling \end{cases} \tag{5}$$

in which p_r/p_0 expresses the degree of openness of the structure in terms of the distance between the current stress state (represented by p_r) and yield surface (represented by p_0), while c_{c1}, c_{c2}, c_{c3} and c_{s1}, c_{s2}, c_{s3} are coefficients defining the shape of the interaction function.

Quantification of the micro-structural evolution

Finally, the ICDSM introduces the void factor, $VF = e_m/e$, to enable the quantification of the micro-structural evolution in the clay. This parameter expresses the degree of dominance of each structural level in the overall clay fabric.

All model parameters are summarised in Table 3-27 , together with a list of experiments that enable parameter derivation. A double-structure formulation introduces four additional model parameters, as shown in the table.

Table 3-27 Summary of ICDSM parameters

Parameter		Source
Input parameters for IC SSM	Parameters controlling the shape of the yield surface, M_F, α_F, μ_F	Triaxail compression
	Parameters controlling the shape of the plastic potential surface, α_G, μ_G	Triaxial compression; relationship between dilatancy and J/p ratio
	Generalized stress ratio at critical state, M_J	Triaxial compression, related to the angle of shear resistance at critical state ϕ'_{cs}
	Characteristic pressure, p_c (kPa)	Limiting confining stress at which $p_0 = p_0^* = p_c$
	Specific volume at unit pressure related to the initial equivalent suction, $v_1(s_{eq})$	Isotropic compression test at constant equivalent suction s_{eq}
	Fully saturated plastic compressibility coefficient, $\lambda(0)$	Fully saturated isotropic loading
	Elastic compressibility coefficient, κ	Fully saturated isotropic loading/unloading
	Maximum soil stiffness parameter, r	Isotropic compression tests at different constant values of suction
	Soil stiffness increase parameter, β(1/kPa)	Isotropic compression tests at different constant values of suction
	Elastic compressibility coefficient for changes in suction, κ_s	Drying/wetting test at constant confining stress
	Poisson's ratio, ν	Triaxial compression test
	Plastic compressibility coefficient for changes in suction, λ_s	Drying test at constant confining stress
	Air-entry value of suction, s_{air} (kPa)	From the soil water retention curve
	Yield value of equivalent suction, s_0 (kPa)	Drying test at constant confining stress (usually a high value if it is not to be mobilised)
Additional input parameters for IC DSM	Micro-structural compressibility parameter, κ_m	No direct routine test - potentially from micro-structural investigations (e.g. MIP)
	Void factor, VF	No direct routine test – potentially from micro-structural investigations (e.g. MIP)
	Coefficients for the micro swelling function, c_{s1}, c_{s2}, c_{s3}	No direct routine test – potentially from micro-structural investigations (e.g. MIP)
	Coefficients for the micro compression function, c_{c1}, c_{c2}, c_{c3}	No direct routine test – potentially from micro-structural investigations (e.g. MIP)

Soil water retention (SWR) model

For the analyses presented in this report, a non-hysteretic Van Genuchten-type (van Genuchten, 1980) SWR model was adopted, formulated in terms of the degree of saturation, S_r, and the matric suction (Melgarejo Corredor, 2004):

$$S_r = \left[\frac{1}{1 + \left[\alpha \cdot (v-1)^{\psi} \cdot s_{eq}\right]^n} \right]^m \cdot (1 - S_{r0}) + S_{r0} \tag{6}$$

In the above equation, S_{r0} is the residual degree of saturation, while α, m and n are fitting parameters controlling the shape of the retention curve; ψ is the parameter controlling the effect of the specific volume, v.

Hydraulic conductivity (permeability) model

The variable permeability model (Potts & Zdravkovic, 1999; Nyambayo & Potts, 2010) adopted in all analyses assumes the permeability (hydraulic conductivity) to vary with matric suction according to the expression:

$$\log k = \log k_{sat} - \frac{s - s_1}{s_2 - s_1} \cdot \log \frac{k_{sat}}{k_{min}} \tag{7}$$

where k_{sat} is the saturated value of permeability (m/s), k_{min} its minimum value reached after the prescribed change in matric suction from s_1 to s_2.

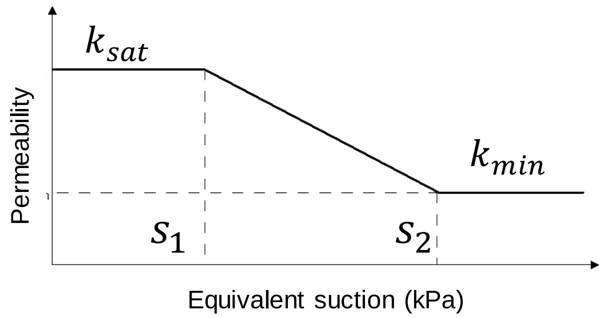

Figure 3-143 *Variable permeability model.*

3.8.2 Geometry and discretization

All the numerical simulations undertaken were hydro-mechanically fully coupled and were carried out with the FE code ICFEP (Potts & Zdravkovic, 1999). Given that the 3 tests analysed were performed under constant volume conditions, no significant displacements were expected, and, therefore, the small displacement formulation was adopted.

Due to the axisymmetric nature of the experiments under investigation (i.e. Tests MGR22, MGR23, MGR27), 3 two-dimensional (2D) axisymmetric finite element (FE) simulations were undertaken. The domains analysed (length of 5cm, height of 10cm) were discretised using 8-noded quadrilateral displacement-based elements, with 4 pore pressure degrees of freedom at the corner nodes. The meshes generated are shown in Figure 3-144, together with the mechanical boundary conditions adopted (see details in Section 3.8.4).

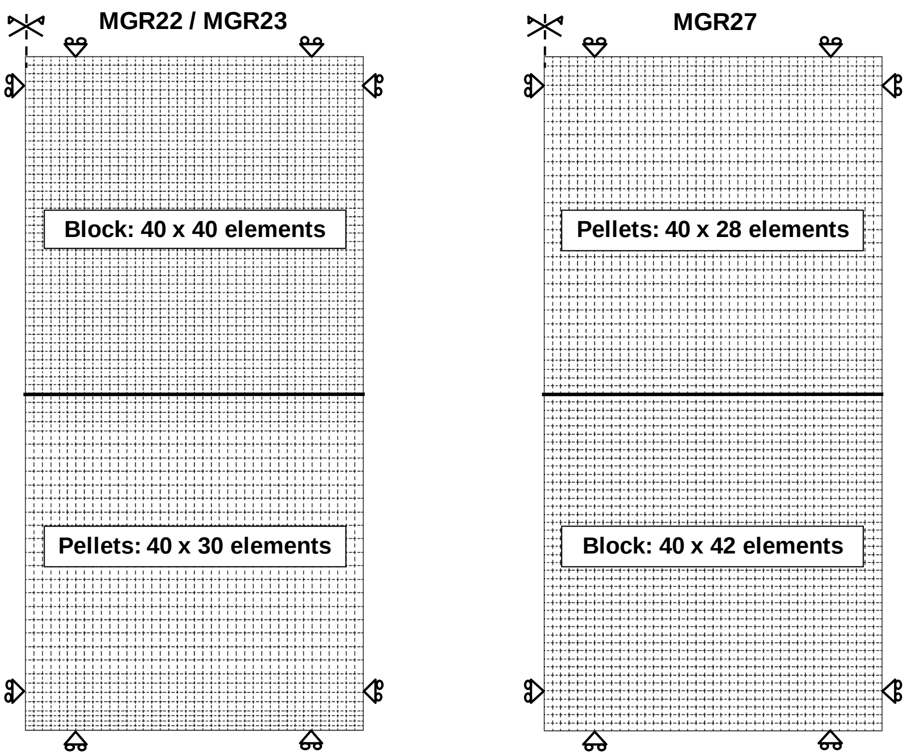

Figure 3-144 *Meshes generated and mechanical boundary conditions adopted*

3.8.3 Input parameters

The model parameters used in the analyses are reported in the following tables, with reference to the Imperial College Double Structure Model (IC DSM), the Soil Water Retention (SWR) model, and the Hydraulic Conductivity Function (HCF), respectively. For the FEBEX bentonite blocks, the parameters were derived from the laboratory data reported in ENRESA (2000), Lloret et al. (2003), Villar & Gomez-Espina (2009), and the BEACON report D5.2.1 (2018). For the FEBEX bentonite pellets, the parameters were derived from the laboratory data reported in Hoffman et al. (2007) and Alonso et al. (2011).

Table 3-28 Input parameters for IC DSM model

Parameter	Value (block)	Value (pellets)
Parameters controlling the shape of the yield surface, M_F, α_F, μ_F	0.53, 0.4, 0.9	0.53, 0.4, 0.9
Parameters controlling the shape of the plastic potential surface, α_G, μ_G	0.4, 0.9	0.4, 0.9
Generalized stress ratio at critical state, M_J	0.53	0.53
Characteristic pressure, p_c (kPa)	10.0	50.0
Specific volume at unit pressure related to the initial equivalent suction, $v_1(s_{ea})$	2.355	3.063
Fully saturated plastic compressibility coefficient, $\lambda(0)$	0.130	0.180
Elastic compressibility coefficient, κ	0.005	0.050
Maximum soil stiffness parameter, r	0.650	0.750
Soil stiffness increase parameter, β(1/kPa)	0.0002	0.000005
Elastic compressibility coefficient for changes in suction, κ_s	0.057	0.083
Poisson's ratio, ν	0.4	0.4
Plastic compressibility coefficient for changes in suction, λ_s	0.229	0.333
Air-entry value of suction, s_{air} (kPa)	0.0	0.0
Yield value of equivalent suction, s_0 (kPa)	10^6	10^6
Micro-structural compressibility parameter, κ_m	0.084	0.100
Void factor, VF	0.665	0.406
Coefficients for the micro swelling function, c_{s1}, c_{s2}, c_{s3}	-0.10, 1.10, 3.00	-0.10, 1.10, 3.00
Coefficients for the micro compression function, c_{c1}, c_{c2}, c_{c3}	-0.10, 1.10, 3.00	-0.10, 1.10, 3.00

Table 3-29 Input parameters for SWR model

Parameter	Value (block)	Value (pellets)
Fitting parameter, $\boldsymbol{\alpha}$ (1/kPa)	0.00018	0.0015
Fitting parameter, $\boldsymbol{m}$	0.33	0.25
Fitting parameter, $\boldsymbol{n}$	1.50	1.05
Fitting parameter, $\boldsymbol{\psi}$	4.5	2.5
Residual degree of saturation, $\boldsymbol{S_{r0}}$	0.01	0.0

Table 3-30 *Input parameters for HCF model*

Parameter	Value (block)	Value (pellets)
Saturated hydraulic conductivity, $\boldsymbol{k_{sat}}$ (m/s)	5×10^{-12}	5×10^{-10}
Minimum hydraulic conductivity, $\boldsymbol{k_{min}}$ (m/s)	5×10^{-13}	5×10^{-10}
Suction $\boldsymbol{s_1}$ (kPa)	0.0	N/A
Suction $\boldsymbol{s_2}$ (kPa)	100000.0	N/A

The predictive capabilities of the models, when adopting the parameters in Table 3-28, Table 3-29, and Table 3-30 can be evaluated from Figure 3-145, where experimental and numerical oedometer test data are shown for both blocks (a) and pellets (b). The SWR curves employed in the analyses, and the corresponding data used for their calibration, are illustrated in Figure 3-146 for both blocks(a) and pellets (b).

The HCF used for the FEBEX blocks is shown in Figure 3-147, in comparison with the hydraulic conductivity variations indicated by Villar & Gomez-Espina (2009). This HCF was adopted in conjunction with a saturated hydraulic conductivity of 5×10^{-12} m/s, which corresponds to the upper bound of the values reported in the literature for FEBEX bentonite blocks.

Regarding the pellets, due to their peculiar structure, Hoffman et al. (2007) show that the hydraulic conductivity tends to decrease with suction reductions, contrarily to what is more generally observed in geo-materials. The HCF available (described in Section 3.8.1) cannot reproduce such a variation, and, therefore, a constant hydraulic conductivity of 5×10^{-10} m/s was selected for the pellets, corresponding to the average value of measurements carried out at different suction levels.

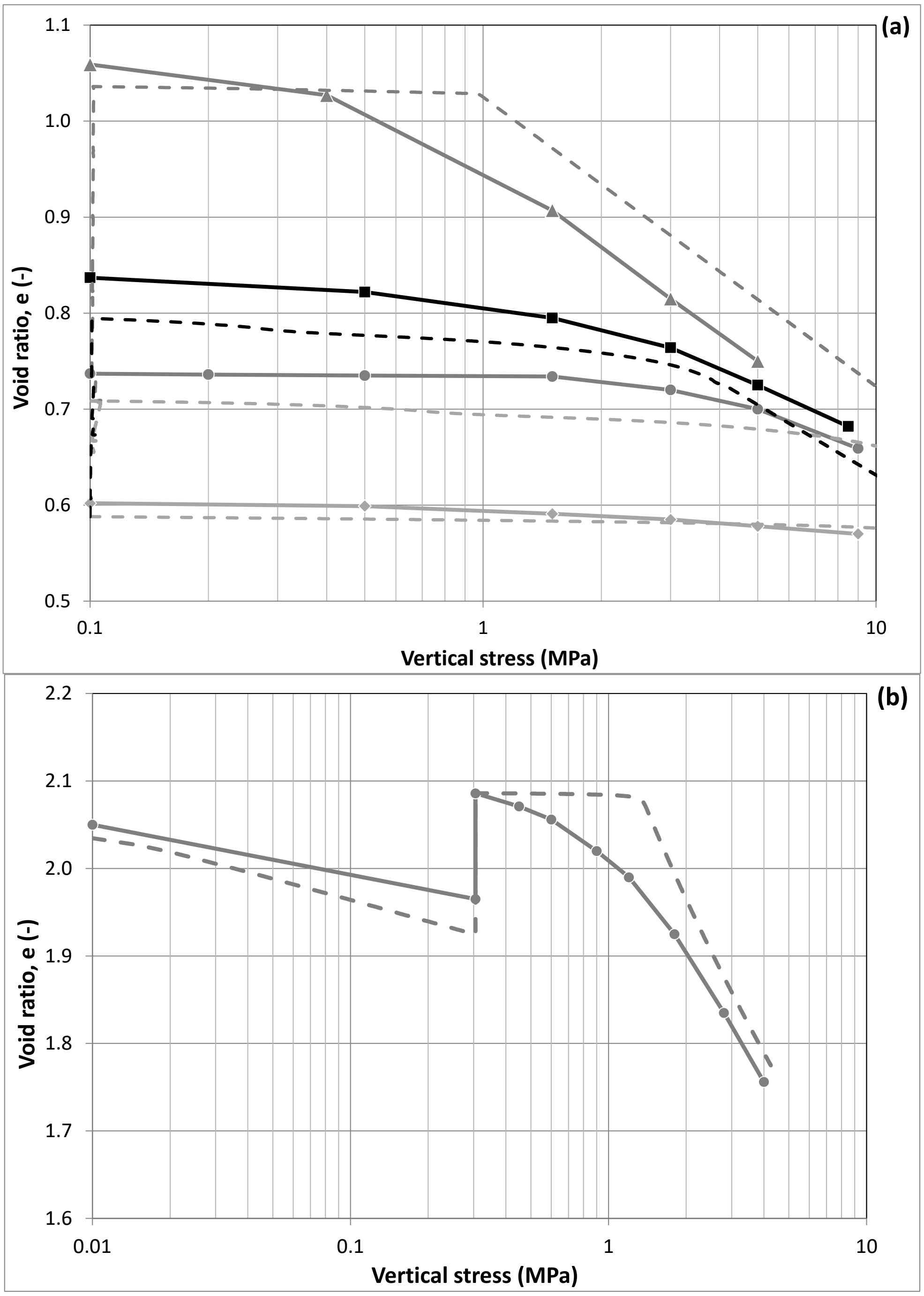

Figure 3-145 *Comparison between experimental (continuous lines) and numerical (dashed lines) oedometer test data for FEBEX bentonite blocks (a) and pellets (b) (laboratory data from Lloret et al., 2003, and Hoffman et al., 2007, respectively)*

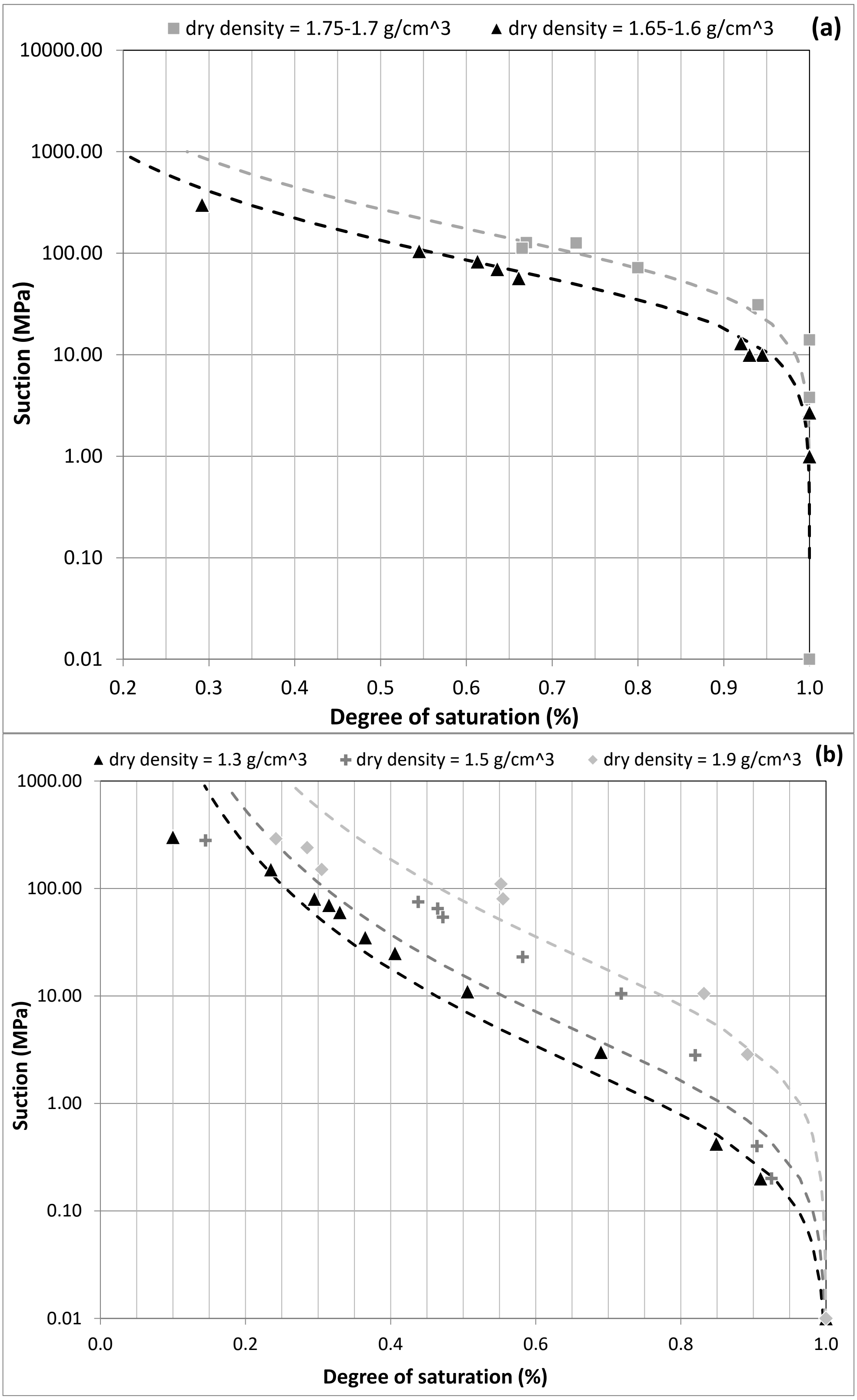

Figure 3-146 *Comparison between adopted soil water retention curves (dashed lines) and laboratory data (symbols) for FEBEX bentonite blocks (a) and pellets (b) (laboratory data from ENRESA, 2000, and Alonso et al., 2011, respectively)*

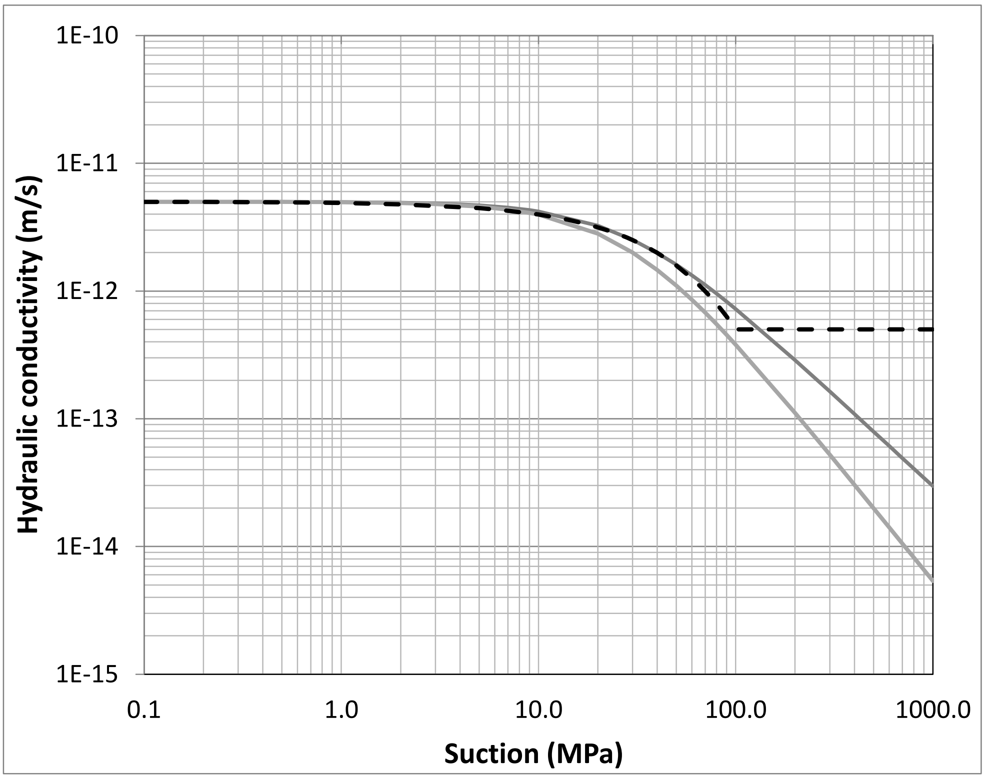

Figure 3-147 *Hydraulic conductivity function adopted for FEBEX bentonite blocks (dashed line) compared with functions (continuous lines) suggested by Villar & Gomez-Espina (2009)*

3.8.4 Initial and boundary conditions

The initial conditions assumed in the analyses are summarised in Table 3-31, Table 3-32 and Table 3-33 for Tests MGR22, MGR23, and MGR27, respectively. For simplicity, the overall height of the samples was assumed to be equal exactly to 10 cm, with the two portions of pellets and blocks having the same height, i.e. 5 cm.

The initial dry densities correspond to the target ones, the latter obtained by changing appropriately the over-consolidation ratio in the model compared to the values used for model calibration. The initial degrees of saturation, instead, are slightly different from those indicated in the test specifications (BEACON D5.5, 2020), and are derived from the initial suctions assigned (based on the SWR curves reported in Figure 3-146). The initial suctions are also indicated in Table 3-31, Table 3-32 and Table 3-33, and correspond to the average suctions of the samples (pellets plus blocks). An initial nominal isotropic total stress of 100 kPa was also assigned to the materials in all tests.

The 3 FE analyses conducted were all divided into two main stages:
- *Stage 1*: during which all model boundaries were assumed impervious and a full hydro-mechanical equilibrium was reached. This stage was divided into 50 increments, with an overall duration variable from test to test.

- *Stage 2*: during which water was allowed to flow into the samples from the bottom boundary (until full saturation) by applying either a constant flow (in case of MGR22) or a constant pore pressure (in case of MGR23 and MGR27).

The constant flow corresponds to the one indicated in the test specifications (i.e. 0.05cm³/h; BEACON D5.5, 2020), while the constant pore pressure corresponds to 10 kPa of suction (imposed by gradually reducing the initial suction values).

The mechanical boundary conditions applied during both *Stages*, i.e. no displacements allowed in the direction orthogonal to the model boundaries, are shown in Figure 3-144.

The results of the analyses presented in the followings sections only refer to the hydration stage, i.e. *Stage 2*, because no significant variations in the hydro-mechanical properties of the materials were detected at the end of *Stage 1*.

Table 3-31 Initial conditions adopted for the MGR22 FE analysis

Material	h (cm)	w (%)	ρ_d (g/cm³)	S_r (%)	s (kPa)
Pellets	5.0	10.1	1.28	24.6	106800.0
Block	5.0	13.3	1.61	52.9	106800.0

Table 3-32 Initial conditions adopted for the MGR23 FE analysis

Material	h (cm)	w (%)	ρ_d (g/cm³)	S_r (%)	s (kPa)
Pellets	5.0	8.6	1.30	21.5	192860.0
Block	5.0	10.1	1.60	39.6	192860.0

Table 3-33 Initial conditions adopted for the MGR27 FE analysis

Material	h (cm)	w (%)	ρ_d (g/cm³)	S_r (%)	s (kPa)
Pellets	5.0	8.6	1.30	21.6	190140.0
Block	5.0	10.2	1.60	39.9	190140.0

3.8.5 Results MGR22

The top axial pressure measured during confined hydration for Test MGR22 is reported in Figure 3-148, together with the top and bottom axial pressure predictions obtained from the FE analysis. Top and bottom axial pressures overlap because the contact between sample and oedometer cell wall was assumed to be frictionless. It is worth observing that hydration was imposed from day 11 onwards in order to simulate a water intake as close as possible to the one imposed in the laboratory (see Figure 3-149).

The swelling pressure tends to increase very rapidly at the beginning of the hydration phase, until a value of around 0.65 MPa is reached (after a few days). Subsequently, the increase in swelling pressure becomes more gradual, following a broadly constant rate until a maximum value of around 2.2 MPa is approached (after circa 125 days). At this point, measured and predicted pressures are essentially identical. The increase in swelling pressure observed up to 125 days occurs at a constant rate probably because the permeability of the pellets was assumed to be constant (i.e. 5×10^{-10} m/s), while, in reality, it is supposed to be larger (around 10^{-7} m/s) at the beginning of the test and lower (around 10^{-12} m/s) after pellets swelling. This is probably the reason why the measured values tend to show a faster increase in the first 50 days and a slower increase afterwards.

After reaching its peak, the predicted swelling pressure tends to reduce until full saturation is attained, i.e. after around 200 days. At this point, the water inflow is stopped (see Figure 3-149) and the swelling pressure remains constant. The pressure reduction predicted at the end of the analysis (indicating a volumetric collapse) is not observed in the laboratory, where a further pressure increase is measured instead. The final value measured in the laboratory is around 3 MPa, compared to a final predicted value of around 1.7 MPa. The analysis, therefore, tends to underestimate the swelling pressure.

The dry density distributions, as predicted at key stages of the analysis, are shown in Figure 3-150, in comparison with *post-mortem* laboratory measurements. The analysis predicts a dry density increase for the pellets and a reduction for the block, until the maximum swelling pressure is attained after circa 125 days. At this point, the dry density distribution becomes very close to the one measured at the end of the test. When the swelling pressure starts to decrease, a decrease in dry density is observed in the pellets, while an increase is observed, instead, in the block. These data would suggest that a volumetric collapse takes place in the block, allowing for a local swelling within the pellets and causing a general swelling pressure reduction. The final dry density distribution is therefore less close to the *post-mortem* measurements compared to the one predicted at the peak of the swelling pressure.

The water content distributions predicted at key stages of the analysis are shown in Figure 3-151, in comparison with the *post-mortem* laboratory measurements. The water content tends to increase in both the pellets and the block, as expected during hydration, resulting in a final distribution which is very similar to the measured one.

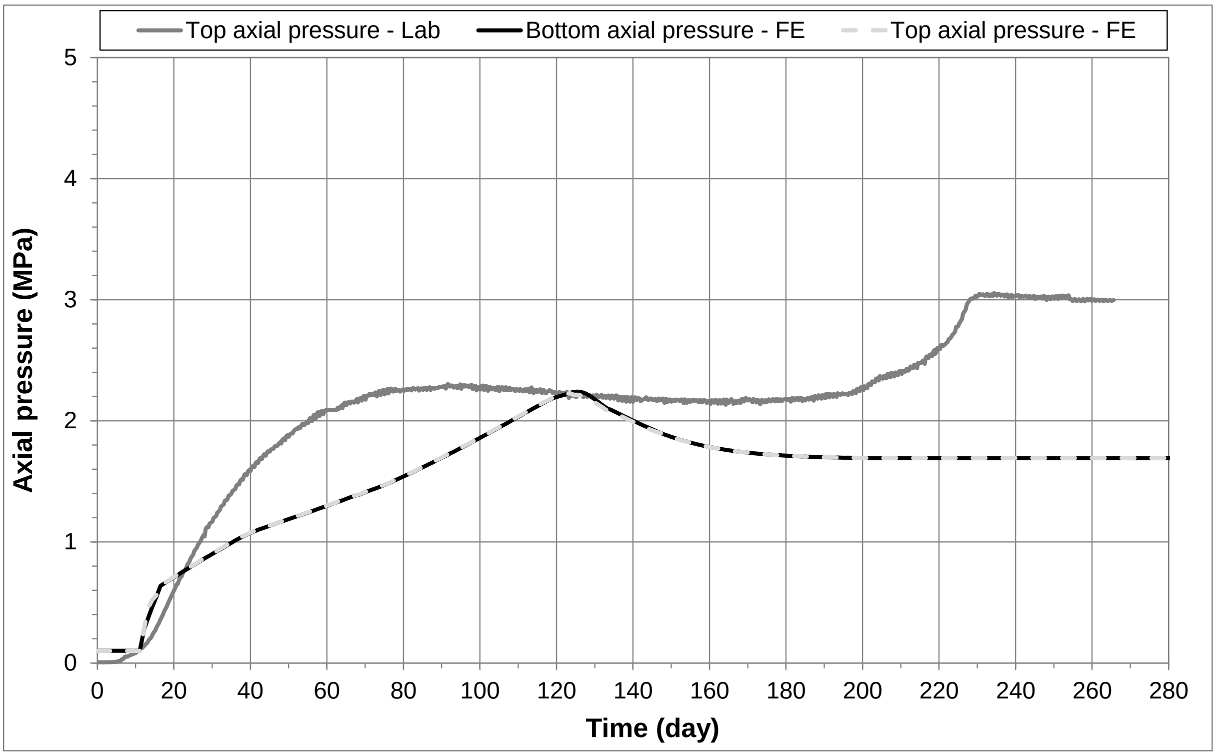

Figure 3-148 *Measured and predicted swelling pressures for Test MGR22*

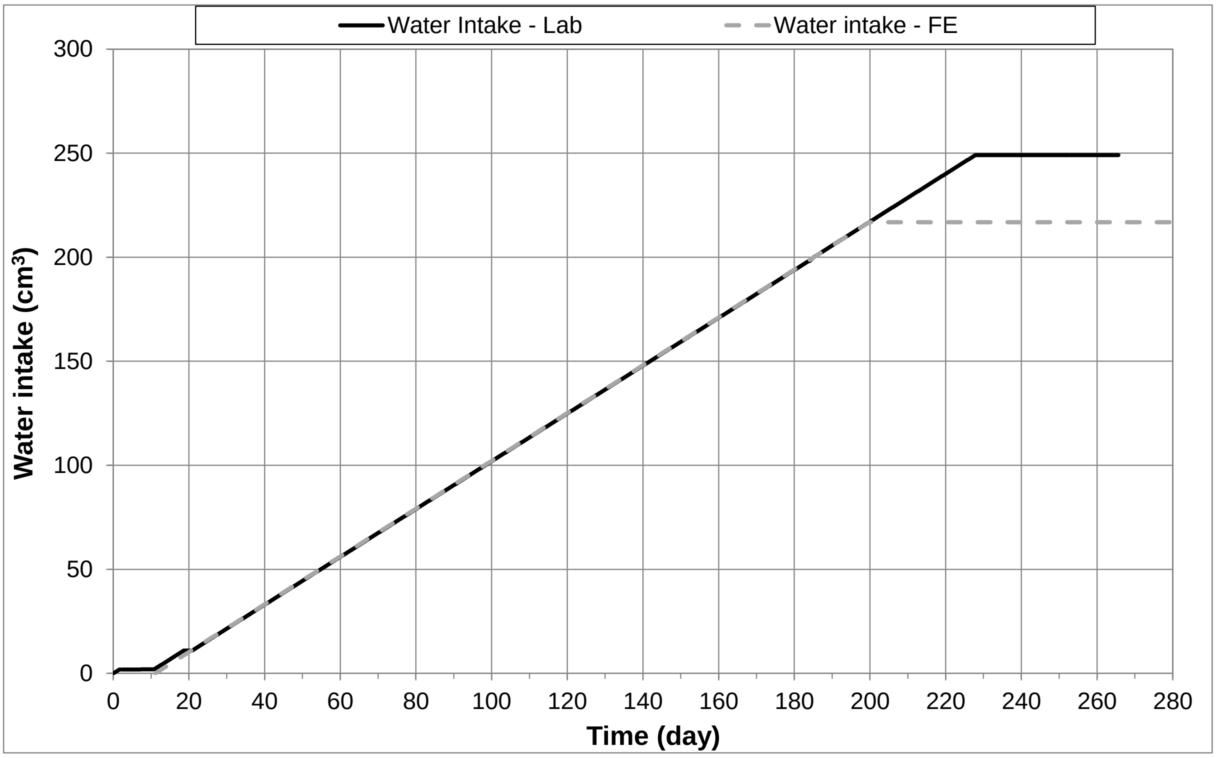

Figure 3-149 *Measured and modelled water intake for Test MGR22*

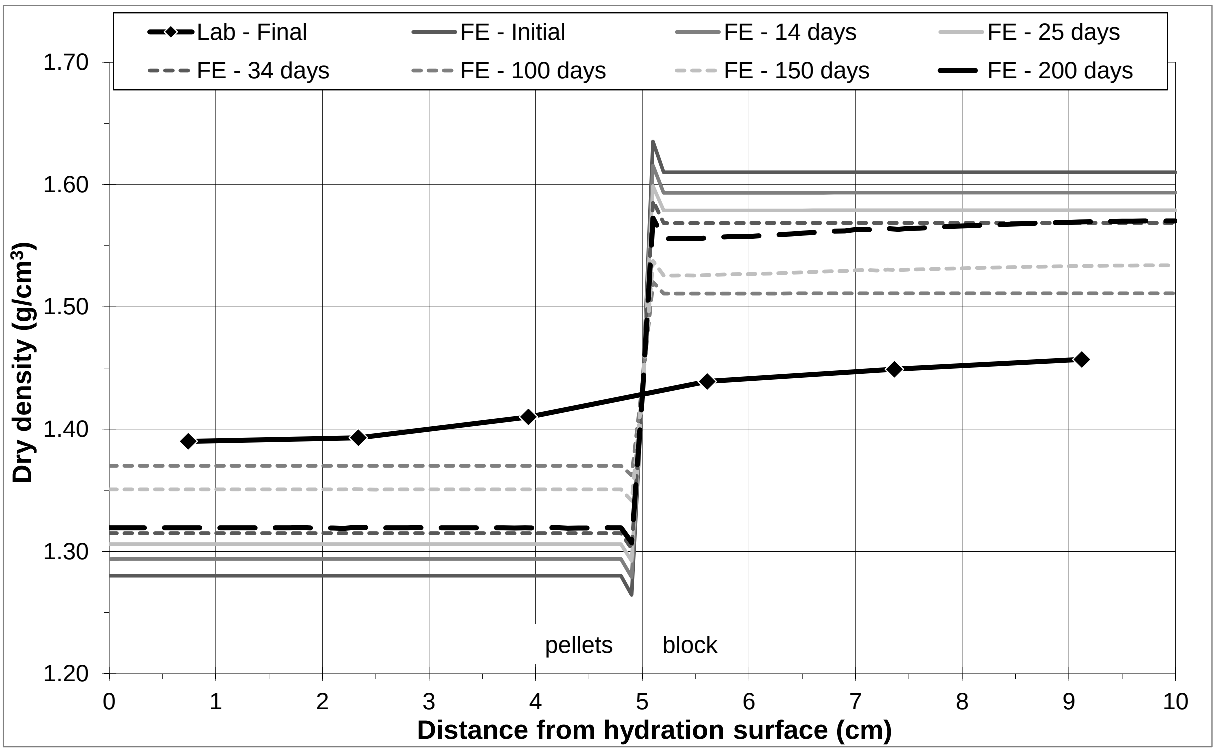

Figure 3-150 *Dry density post-mortem measurements and predicted dry density distributions at key stages of the analysis for Test MGR22*

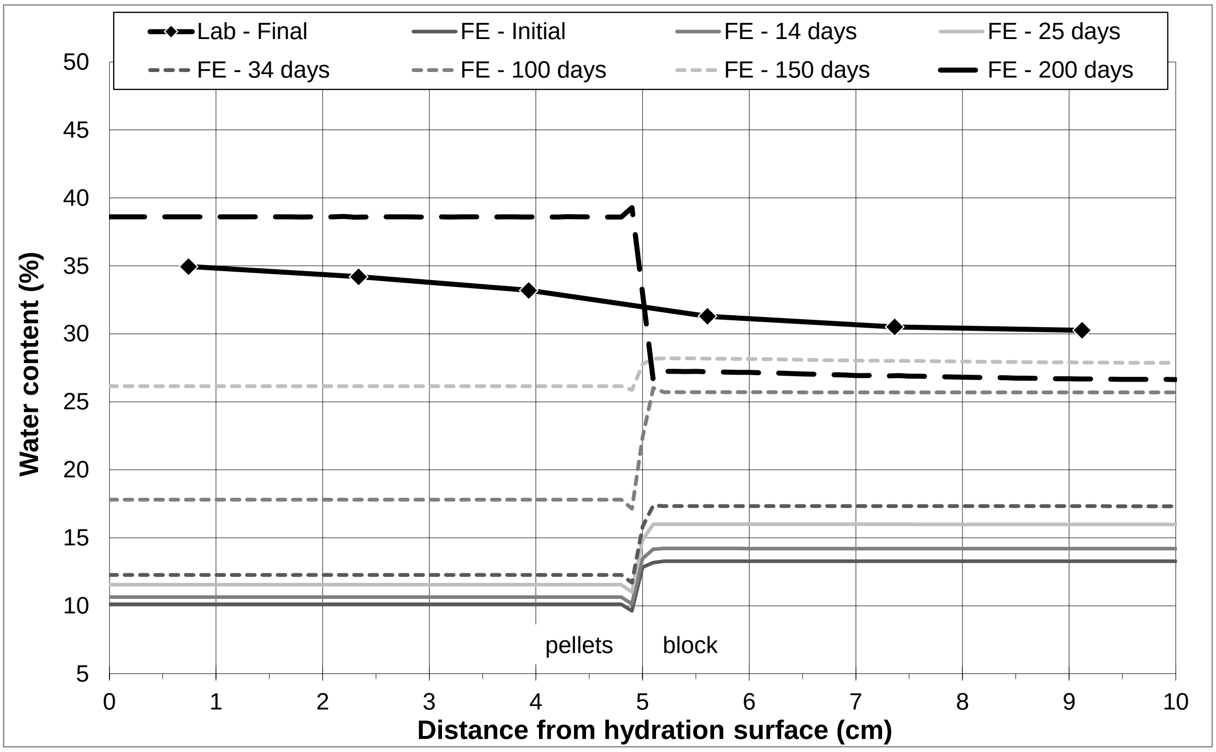

Figure 3-151 *Water content post-mortem measurements and predicted water content distributions at key stages of the analysis for Test MGR22*

3.8.6 Results MGR23

The top axial pressure measured during Test MGR23 is reported in Figure 3-152, together with the top and bottom axial pressure predictions obtained from the FE analysis. Also in this case, top and bottom axial pressures overlap because the contact between sample and oedometer cell wall was assumed to be frictionless.

The initial increase in swelling pressure predicted with the FE analysis is similar to the one observed experimentally. However, in the numerical simulation, after reaching a maximum value of around 2.2 MPa, a slight drop in swelling pressure takes place, while the experimental data show a further pressure increase up to values just below 3 MPa. The predicted swelling pressure reduction stops after around 30 days, when full saturation is approached and the final value of around 1.5 MPa is observed. Therefore, also in this case, the numerical simulation tends to underestimate the swelling pressure.

The dry density and water content distributions, as predicted at key stages of the analysis, are shown in Figure 3-153 and Figure 3-154, respectively, together with the *post-mortem* laboratory measurements. The predicted dry density and water content variations seem to compare reasonably well with the laboratory measurements. It is worth observing that, also in this case, when the swelling pressure starts to decrease, the dry density variation trend changes in both the pellets and the block, as also observed in the MGR22 FE analysis.

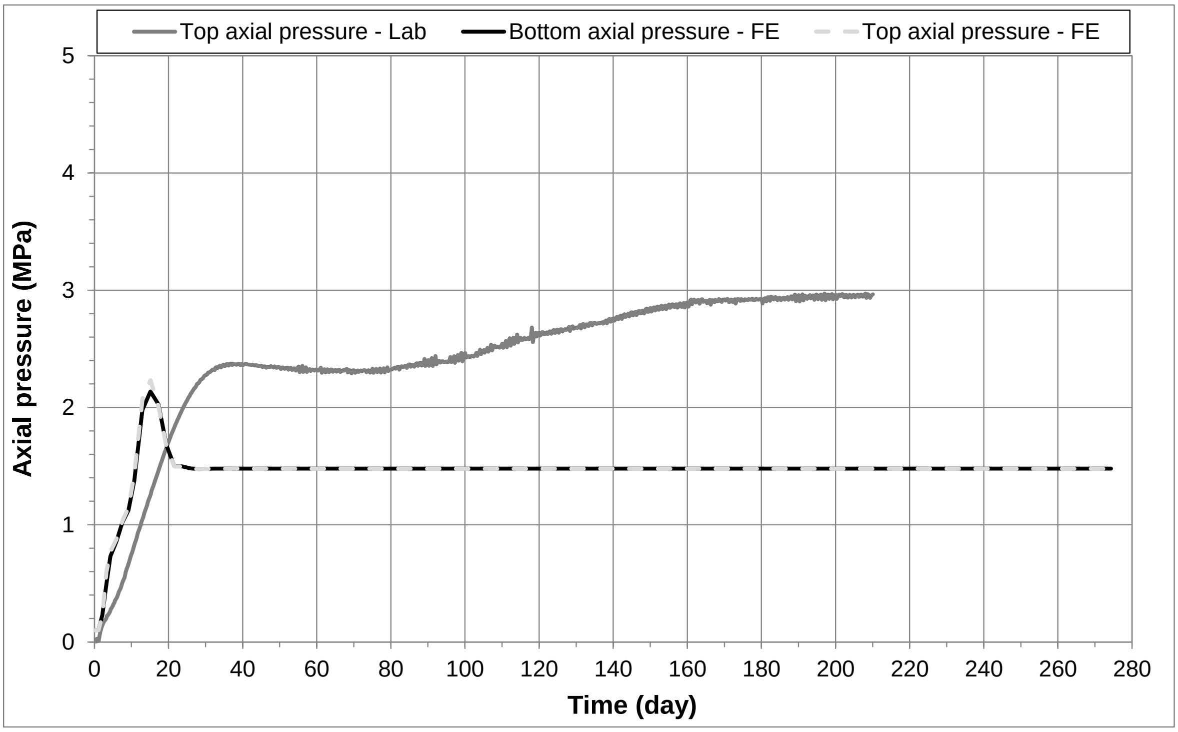

Figure 3-152 *Measured and predicted swelling pressures for Test MGR23*

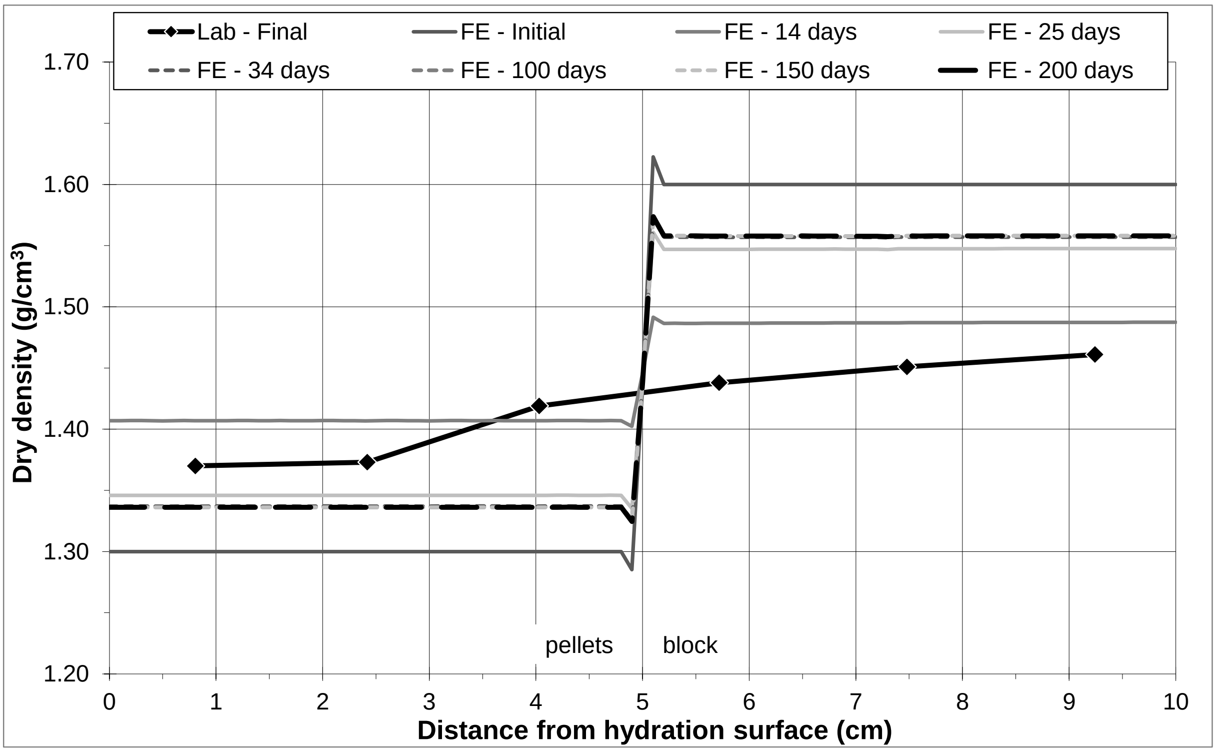

Figure 3-153 *Dry density post-mortem measurements and predicted dry density distributions at key stages of the analysis for Test MGR23*

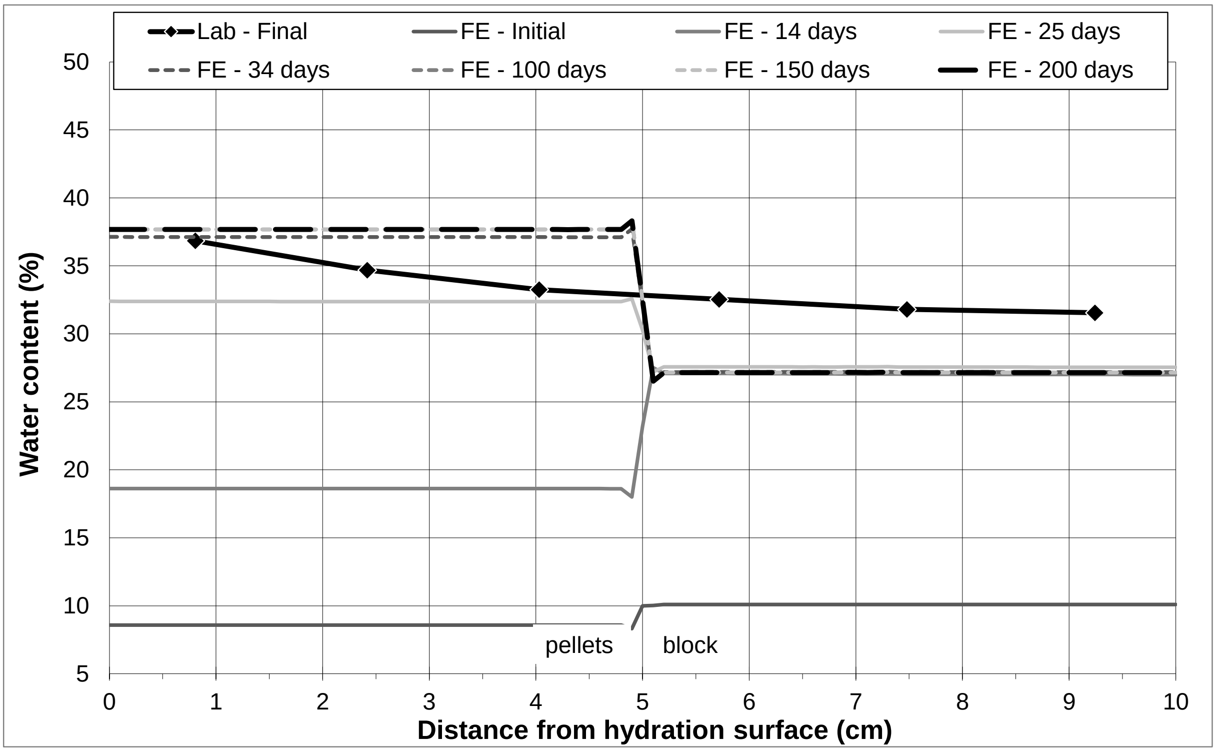

Figure 3-154 *Water content post-mortem measurements and predicted water content distributions at key stages of the analysis for Test MGR23*

3.8.7 Results MGR27

The axial pore pressure variations predicted for Test MGR27, shown in Figure 3-155, are very similar to those predicted for Test MGR23. A rapid swelling pressure increase is predicted, leading to a maximum value of around 2.1 MPa. This pressure increase is followed by a rapid reduction, the latter also ending roughly after 30 days, when a final value of circa 1.5 MPa is reached.

The dry density and water content distributions, as predicted at key stages of the analysis, are shown in Figure 3-156 and Figure 3-157, respectively. As observed for Tests MGR22 and MGR23, before reaching the maximum swelling pressure, the dry density tends to reduce for the block and increase for the pellets. On the other hand, when the swelling pressure starts decreasing, the dry density tends to increase for the block and reduce for the pellets.

The water content, as expected, increases significantly during hydration, similar to what is observed for Tests MGR22 and MGR23. In particular, the water content variation predicted for the pellets is larger than the one observed for the block, and this is also consistent with the results obtained for the other two tests analysed.

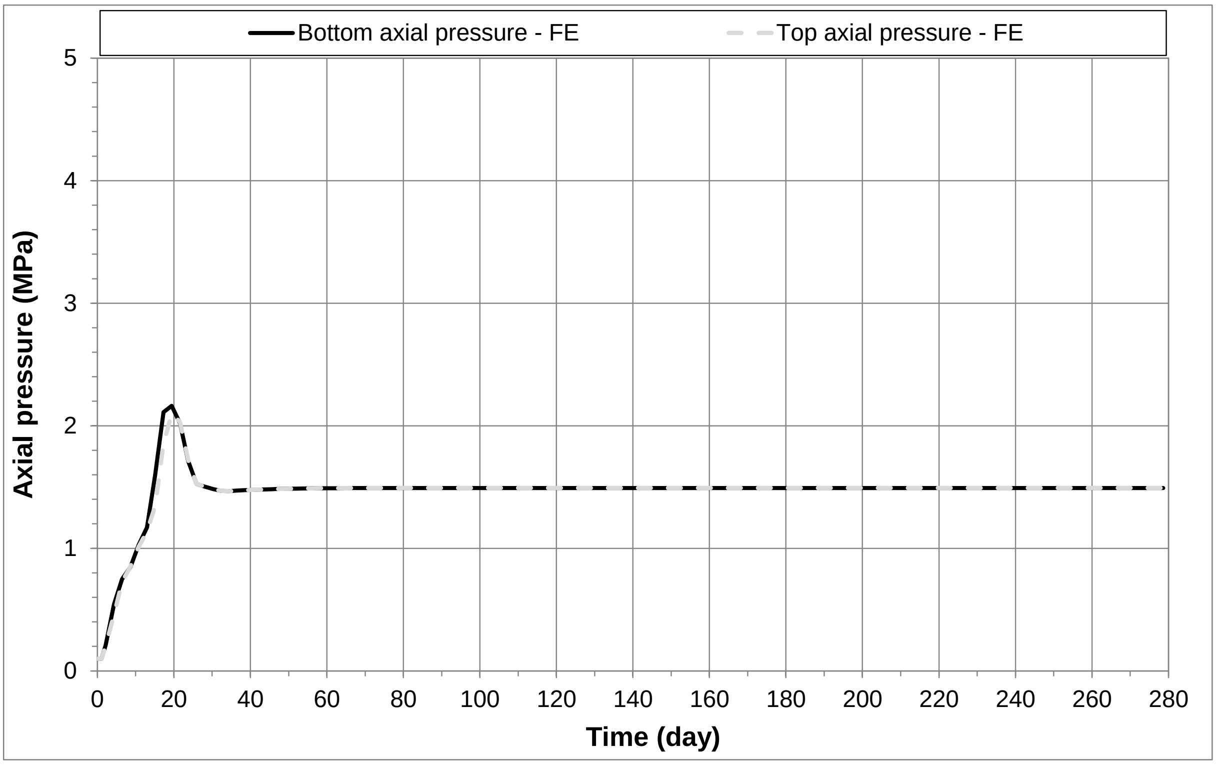

Figure 3-155 *Predicted swelling pressures for Test MGR27*

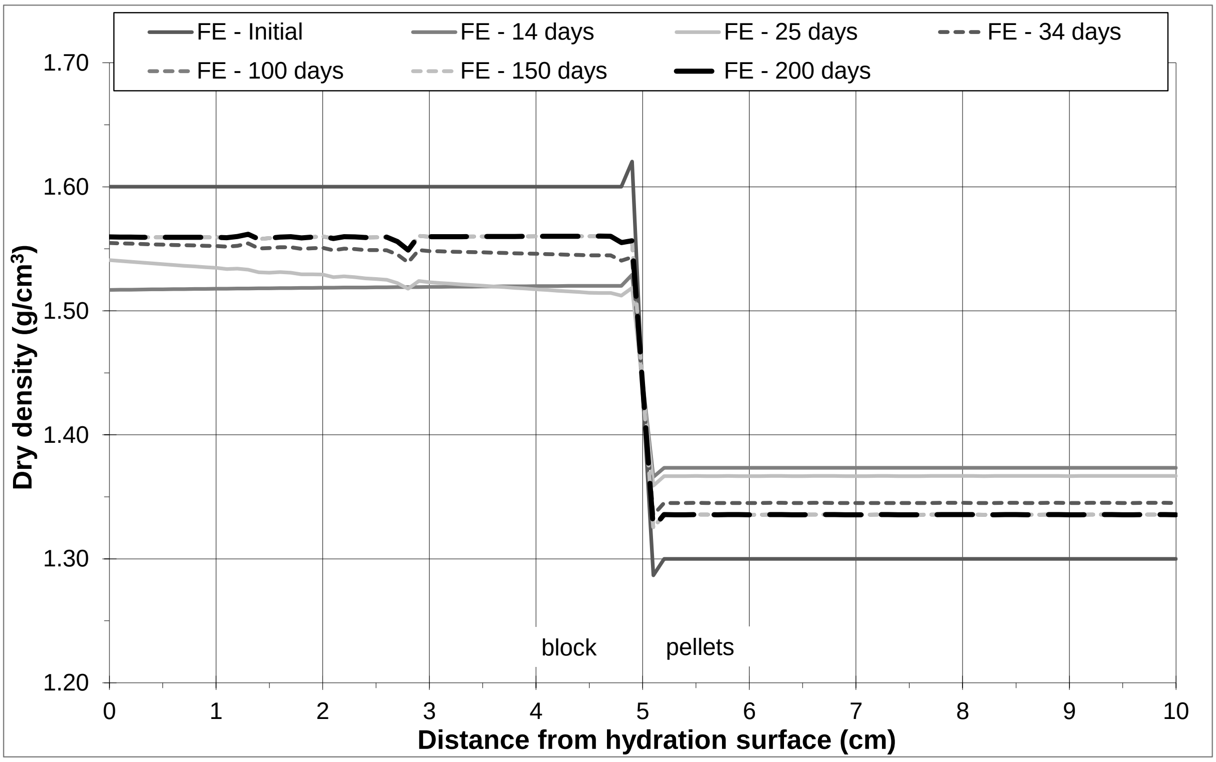

Figure 3-156 *Predicted dry density distributions at key stages of the analysis for Test MGR27*

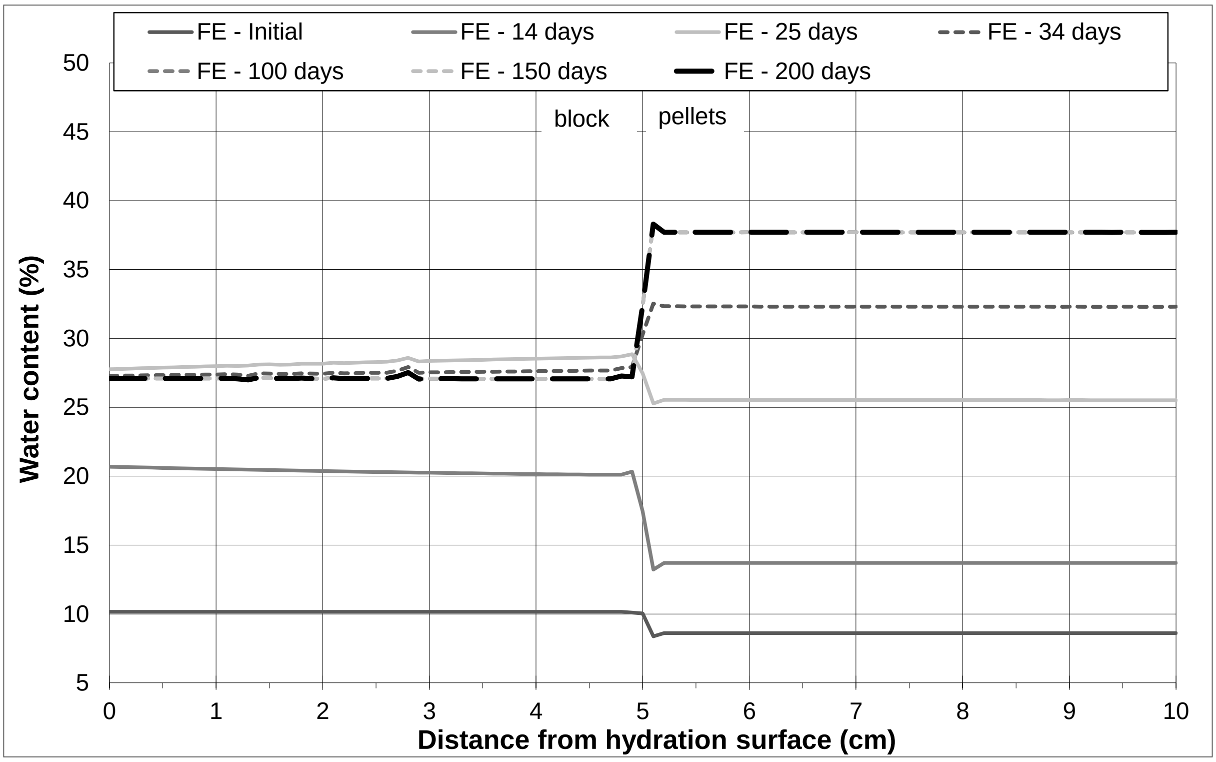

Figure 3-157 *Predicted water content distributions at key stages of the analysis for Test MGR27*

3.8.8 Discussion

This section summarises the key features and the results of the analyses undertaken at ICL in order to simulate Tests MGR22, MGR23, and MGR27.

The order of magnitude of the predicted axial swelling pressures is similar to the one measured in the laboratory, but the analyses tend to underestimate the final swelling pressures attained at the end of the tests. These underestimations are likely to be related to an overestimation of the volumetric collapse of the FEBEX bentonite blocks, the latter associated with swelling pressure reductions observed in the FE analyses. More accurate predictions are likely to be obtained also by adopting more realistic hydraulic conductivity variations for the pellets, which could not be modelled with the HCF introduced in Section 3.8.1.

The variations of the physical properties of both the blocks and the pellets, during hydration, seem to be captured reasonably well by the numerical simulations, irrespective of the hydraulic boundary condition imposed and the location of the block with respect to the pellets. However, the dry density distributions predicted towards the end of the tests are clearly affected by the overestimation of the volumetric collapse of the blocks, and better dry density predictions are likely to be obtained if the volumetric collapse was reduced (i.e. by modifying the Loading Collapse curve of the blocks).

3.9 UPC

The results provided by UPC concerns only tests MGR22 and MGR23.

3.9.1 Description of the model

Basic concepts

The constitutive model used by UPC to represent the behaviour of the FEBEX bentonite is presented in Beacon Deliverables D3.1 and D3.2 corresponding to the WP3 of the BEACON project. For completeness, a brief summary is included here.

The mechanical model developed by UPC is an enhanced version of the Barcelona Expansive Model (BExM), based on elasto-plasticity and a double structure formulation. The coupling between the two structure levels is expressed by means of interaction functions. Thermal effects are being incorporated but, as they are not used in Beacon, they have not been included in this description.

In the formulation, the expansive clay is defined as a double-structure material composed by the arrangement of clay aggregates and micro- and macro-pores (Figure 3-158). The porous medium under study consists of three phases [solid (s), liquid (l) and gas (g)] and three main components [solid (s), water (w) and air (a)]. Each structural level contains air and water in gas and liquid state. Additionally, the possibility to have unsaturated states in the microstructural level is a new feature respect to the formulation of Sánchez, (2004). This feature is required because strong drying paths or some compaction procedures (e.g. bentonite pellets) can produce this state in the micropores.

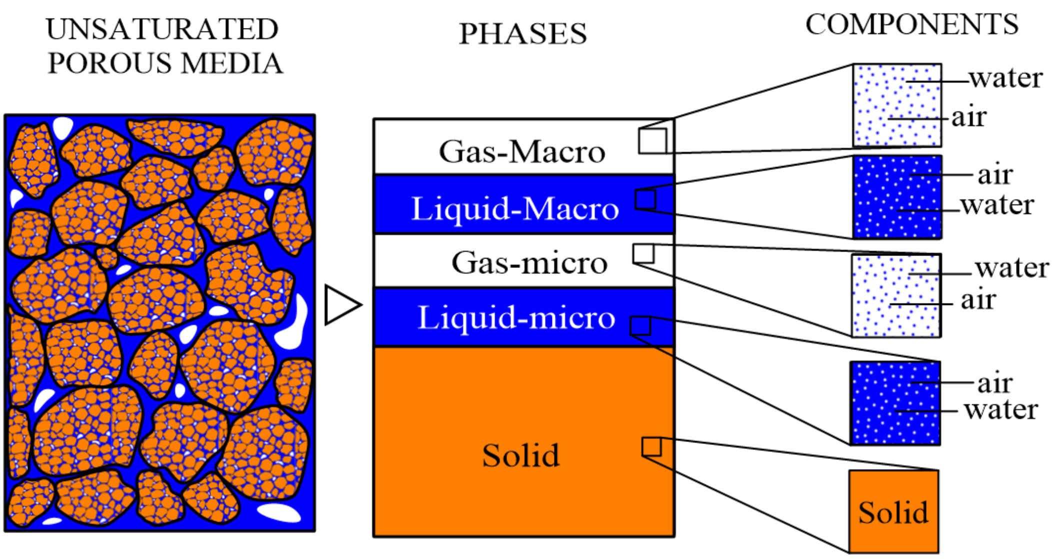

Figure 3-158 *Continuum approximation of unsaturated double-structure porous media. Phases and components at each structural level.*

One of the main requirements in the formulation is the reference of the quantities respect to the whole representative elementary volume (REV). In this respect, the *volume fraction concept* plays a key role. Volume fractions are given by the ratio of the volume of the constituents to the total volume of the REV.

Figure 3-159 shows the phase volumes distribution in a double-structure porous media. The *micro pore volume fraction* [1-1], the *macro pore volume fraction* [1-2] and the *solid volume fraction* [1-3] are defines as,

$$\bar{\phi}_{\text{micro}} = \frac{(V_{\text{Pores}})_{\text{micro}}}{V} \tag{1-1}$$

$$\bar{\phi}_{\text{Macro}} = \frac{(V_{\text{Pores}})_{\text{Macro}}}{V} \tag{1-2}$$

$$\bar{\phi}_{\text{Solid}} = \frac{(V_{\text{Solid}})_{\text{micro}}}{V} \tag{1-3}$$

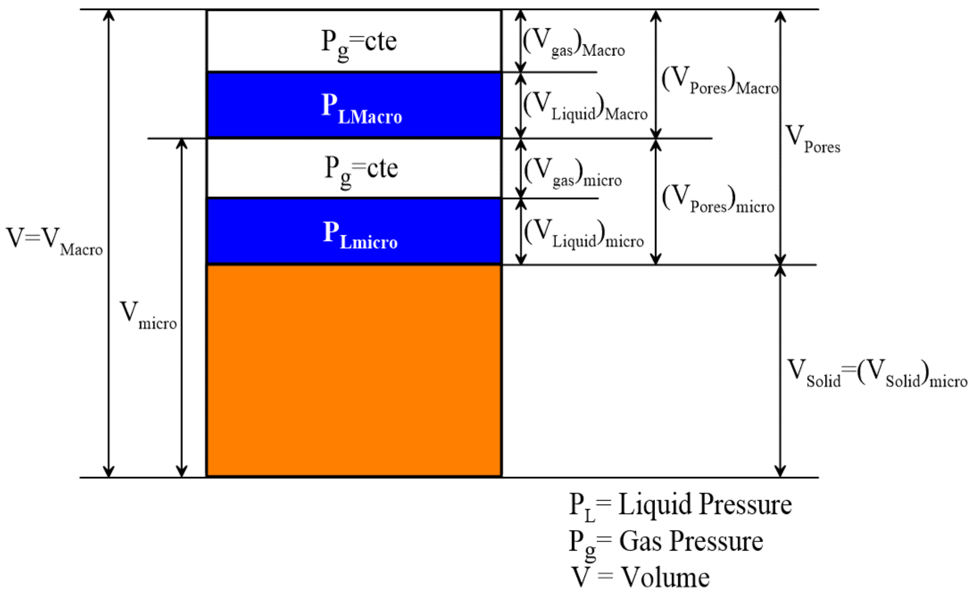

Figure 3-159 *Phase diagram of an unsaturated double-structure soil*

Obviously, the sum of the volume fractions has to be equal to one [1-4]

$$\sum \bar{\phi} = \bar{\phi}_{\text{micro}} + \bar{\phi}_{\text{Macro}} + \bar{\phi}_{\text{Solid}} = 1 \tag{1-4}$$

Also, the *total porosity* of the double-structure soil results from the sum of the two pore volume fractions [1-5]

$$\phi = \bar{\phi}_{\text{micro}} + \bar{\phi}_{\text{Macro}} \tag{1-5}$$

From a conceptual point of view, it is useful to define the *micro porosity* ϕ_{micro} as the ratio of the volume of micro pores and the volume of the microstructural level. It would correspond to the porosity of the aggregates.

Mechanical constitutive model

The phenomenological response of the expansive soils is obtained by the consideration of several plastic mechanisms that can act jointly or not at different stages of the analysis. It is postulated that the microstructure is the seat of the basic physical-chemical phenomena occurring at clay particle level, which is the main responsible of the expansive soil behaviour (Gens & Alonso, 1992). On the other hand, deformations due to loading and collapse will affect the macrostructural level and they can be described by conventional models for unsaturated soils, such as the elasto-plastic Barcelona Basic Model (BBM) (Alonso et al. 1990). A fundamental assumption is that the microstructural behaviour is not affected by the macrostructure state but it only responds to changes of the driving variables (i.e. stresses and suction) at local microstructural level. In contrast, microstructural deformation may give rise to plastic macrostructural strains.

At least two constitutive variables are generally required to represent adequately the full range of unsaturated soil behaviour, i.e. including strength and deformation. They can be called the first and second constitutive variables, FCV and SCV (Gens 2010). Usually, the FCV tries to account for the overall stress state of the soil, whereas the SCV tends to address the effect of suction changes. Table 3-34 shows the constitutive variables used for this constitutive model. Note that the subscripts 1 and 2 correspond to the microstructure and macrostructure, respectively.

Table 3-34 *Constitutive variables used in the double-structure model*

	First constitutive variables, FCV	Second constitutive variables, SCV
microstructural level	Bishop's effective stress $\boldsymbol{\sigma}_1' = \boldsymbol{\sigma}_1 - \mathrm{P_{g1}}\mathbf{I} + \mathrm{Sl_1 s_1}\mathbf{I}$	micro suction $\mathrm{s_1} = \max(\mathrm{P_{g1}} - \mathrm{P_{L1}}, 0)$
macrostructural level	Net stress $\boldsymbol{\sigma}_2'' = \boldsymbol{\sigma}_2 - \mathrm{P_{g2}}\mathbf{I}$	macro suction $\mathrm{s_2} = \max(\mathrm{P_{g2}} - \mathrm{P_{L1}}, 0)$

Microstructural strains (referred, of course, to the overall volume) are considered fully reversible and defined by means of a non-linear elastic model:

$$\mathrm{d}\bar{\boldsymbol{\varepsilon}}_1 = \bar{\mathbf{D}}_1^{-1}\mathrm{d}\boldsymbol{\sigma}_1' \qquad \textbf{[1-6]}$$

$$\bar{\mathrm{K}}_1 = \frac{1+\mathrm{e}}{1+\mathrm{e}_1}\mathrm{K}_1 \qquad \textbf{[1-7]}$$

$$\mathrm{K}_1 = \frac{\mathrm{p}_1'}{(1+\phi_1)\kappa_1} \qquad \textbf{[1-8]}$$

where
- $\boldsymbol{e}$ is the void ratio of the expansive clay;
- e_1 is the void ratio at macrostructural level;
- $\bar{\mathrm{K}}_1$ and $\bar{\mathrm{G}}_1$ are the bulk and shear moduli;
- $\boldsymbol{p}_1'$ is the mean Bishop's effective stress at microstructure.

As indicated above, the macrostructural behaviour is defined by the BBM elastoplastic model. Thus,

$$\boldsymbol{\sigma}_2'' = \mathbf{D}_2\left(\mathrm{d}\boldsymbol{\varepsilon}_2 - \mathrm{d}\boldsymbol{\varepsilon}_{s_2}^{r} - \mathrm{d}\boldsymbol{\varepsilon}_{LC}^{p}\right) \qquad [1\text{-}9]$$

where

- $\varepsilon_{s_2}^{r}$ is the reversible strain tensor due to suction changes;
- $\boldsymbol{\varepsilon}_{LC}^{p}$ is the plastic strain at macrostructural level;
- $\boldsymbol{\varepsilon}_2$ is the strains at macrostructural level;
- $\mathbf{D}_2$ is the constitutive tensor. Equivalent to $\overline{\mathbf{D}}_1$ at this level.

The constitutive expressions for defining the LC yield surface and plastic potential are:

$$F_{LC} = C_F g_F^2(\theta) J^2 - (p + p_s)(p_o - p) \qquad [1\text{-}10]$$

$$C_F = \frac{3}{M_F^2\, g_F^2\left(-\frac{\pi}{6}\right)} \qquad [1\text{-}11]$$

$$M_F = \frac{6\sin\varphi}{3 - \sin\varphi} \qquad [1\text{-}12]$$

$$p_o = p_c\left(\frac{p_o^*}{p_c}\right)^{\frac{\lambda_{sat}-\bar{\kappa}_2}{\lambda_{(s_2)}-\bar{\kappa}_2}} \qquad [1\text{-}13]$$

$$G = G_1 = \bar{\phi}_2 \bar{G}_2 \qquad [1\text{-}14]$$

$$p_s = (p_s)_o + k_s s_2 \qquad [1\text{-}15]$$

$$\lambda(s_2) = \lambda_{sat}\left[r + (1 - r)e^{-\beta s_2}\right] \qquad [1\text{-}16]$$

$$G_{LC} = \alpha_{BBM} \frac{3}{M_F^2} \frac{g_G^2(\theta)}{g_G^2\left(-\frac{\pi}{6}\right)} J^2 - (p + p_s)(p_o - p) \qquad [1\text{-}17]$$

The plastic macrostructural strain induced by microstructural effects are controlled by interaction functions, f_β (Figure 3-160):

$$\mathrm{d}\boldsymbol{\varepsilon}_\beta = f_\beta \mathrm{d}\bar{\boldsymbol{\varepsilon}}_1 \qquad [1\text{-}18]$$

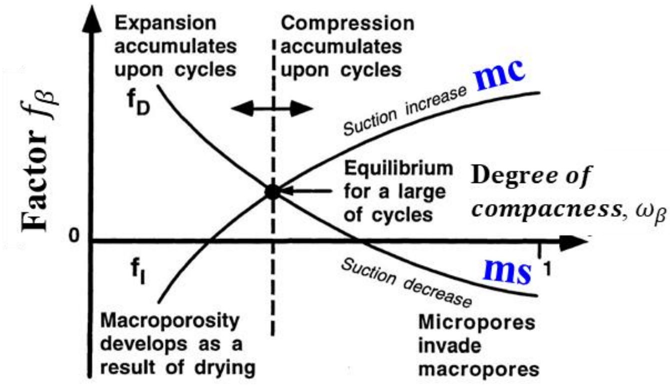

Figure 3-160 *Interaction functions*

Two interaction functions are defined: **mc** for microstructural contraction paths and **ms** for microstructural swelling paths. In the case of generalized load, the interaction function depends on a measure of the degree of openness of the macrostructure defined by the normalised distance of the current (generalised) stress point of the LC yield surface.

In this case, the selected interaction functions are:

$$f_\beta = \begin{Bmatrix} f_{MC}^{(1)} + (f_{MC}^{(0)} - f_{MC}^{(1)}) - (1-\mu_\beta)^{\eta_{MC}} \text{ if } \omega_\beta = +1 \\ f_{MS}^{(1)} + (f_{MS}^{(0)} - f_{MS}^{(1)}) - (1-\mu_\beta)^{\eta_{MS}} \text{ if } \omega_\beta = -1 \end{Bmatrix} \qquad \textbf{\textit{[1-19]}}$$

Finally, the hardening of the double-structure medium is given by the evolution of the isotropic yield stress (hardening parameter) due to the variation of plastic volumetric strains:

$$\mathrm{dp}_\mathrm{o}^* = \frac{(1+\bar{\mathrm{e}}_2)\mathrm{p}_\mathrm{o}^*}{\lambda_{\mathrm{sat}} - \kappa_2}\mathrm{d}\varepsilon_\mathrm{v}^\mathrm{p} = \frac{(1+\bar{\mathrm{e}}_2)\mathrm{p}_\mathrm{o}^*}{\lambda_{\mathrm{sat}} - \kappa_2}(\mathrm{d}\varepsilon_{\mathrm{LC}}^\mathrm{p} + \mathrm{d}\varepsilon_\beta) \qquad \textbf{\textit{[1-20]}}$$

The parameters of the mechanical constitutive model are listed in Table 3-35.

Table 3-35 Parameters of the mechanical constitutive model

Effective stress for microstructural level	χ	Bishop's effective stress parameter for microstructure
Non-linear elasticity	$\bar{\kappa}_2$	Slope of the unloading/reloading related to the macrostructure
	κ_s	Slope of the drying/wetting related to expansive clay
	$(\bar{K}_2)_{min}$	Minimum value of volumetric elastic modulus related to the macrostructure.
	$(K_s)_{min}$	Minimum value of volumetric elastic modulus related to the suction at macro-structure.
	ν	Poisson's ratio
Mechanical interaction Macro-micro Interaction functions	f_{ms0}	Parameters for the case of micro-structure swelling
	f_{ms1}	
	n_{ms}	
	f_{mc0}	Parameters for the case of micro-structure contraction
	f_{mc1}	
	n_{mc}	
Plastic mechanism Macrostructural level (BBM)	φ	Friction angle
	p_c	Parameter in LC curve (MPa)
	λ_{sat}	Slope of the virgin loading at saturated state
	r	Parameter in LC curve
	β	Parameter in LC curve
	k_s	Coefficient setting the increase of tensile strength with suction
	α	Coefficient of non-associativity

Hydraulic constitutive model

The volumetric advective fluxes used in the balance equations are defined by the mass fraction of the component times the mass flow with respect to the solid phase.

$$\mathbf{j}_\alpha^i = \theta_\alpha^i \mathbf{q}_\alpha \qquad [1\text{-}21]$$

where:
- i indicates the component (w=water and a=air);
- α refers to the phase (l=liquid and g=gas).

The generalized Darcy's law governs liquid and gas flow. It is only formulated for the macrostructural level, advective fluxes in the microstructure are neglected.

$$\mathbf{q}_{\alpha 2} = -\frac{\mathbf{k}_2 k_{r\alpha 2}}{\mu_\alpha}(\nabla P_{\alpha 2} - \rho_{\alpha 2}\,\mathbf{g}) \qquad [1\text{-}22]$$

where:
- $\mathbf{k}_2$ is the intrinsic permeability tensor of the macrostructure;
- $k_{r\alpha 2}$ is the relative permeability of gas and liquid;

- μ_α is the fluid viscosity which is function of temperature;
- $P_{\alpha 2}$ is the gas or liquid pressure at macrostructure;
- $\rho_{\alpha 2}$ is the fluid density;
- $\mathbf{g}$ is the gravity body force.

A power law defines the intrinsic permeability, which expresses the effect of degree of saturation (or suction) on permeability [1-22]. The intrinsic permeability depends on many factors such as pore size distribution, pore shape, tortuosity and porosity. Here a simple dependence of intrinsic permeability on macrostructural porosity is adopted:

$$(\mathrm{k_r})_\alpha = [(\mathrm{S_e})_\alpha]^c \qquad \textbf{[1-23]}$$

$$\mathbf{k}_2 = \mathbf{k}_{o2} exp[b(\overline{\phi}_2 - (\overline{\phi}_o)_2)] \qquad \textbf{[1-24]}$$

where:

- c is the power for relative permeability law;
- S_e is the effective degree of saturation;
- $\mathbf{k}_{o2}$ is the initial intrinsic permeability tensor.

Finally, the retention curve relates suction (or potential) with degree of saturation for both structural levels. The Van Genuchten expression has been adopted:

$$\mathrm{S_e} = \left[1 + \left(\frac{\mathrm{s}}{\mathrm{P_o}}\right)^{1/(1-\lambda_o)}\right]^{-\lambda_o} \left(1 - \frac{\mathrm{s}}{\mathrm{P_d}}\right)^{\lambda_d} \qquad \textbf{[1-25]}$$

where P_o, P_d, λ_o and λ_d are model parameters.

Hydraulic equilibrium between two structural levels is not assumed; i.e., at each point of the domain the water potentials (ψ) in the macro- and microstructure may be different, leading to an exchange of water mass that is assumed to be governed by a linear relationship. Gas pressure is assumed to be the same in both structural levels, so the mass transfer mechanism refers to water exchange only.

$$\Gamma^w = \gamma(\psi_1 - \psi_2) \qquad \textbf{[1-26]}$$

where:

- ψ is the total water potential for micro(1)- and macro-structure (2);
- γ is a parameter that control the rate of water transfer (often called the leakage parameter).

It is assumed that only matric and gravitational potential contribute to the total potential of the macrostructure but an additional osmotic component may also contribute to the microstructural potential. Here, potential is defined in pressure units. As the water exchange is local in space, the gravitational potential will be the same for the two pore levels. Therefore, water exchange will only be driven by suction differences:

$$\Gamma^w = \gamma(s_1 - s_2) \qquad \textbf{[1-27]}$$

where suction is defined as

$$s = \max(P_g - P_L, 0) \quad \textbf{[1-28]}$$

The parameters of the hydraulic constitutive model are collected in Table 3-36.

Table 3-36 *Parameters of the hydraulic constitutive model*

Hydraulic interaction Macro-micro	γ	Leakage parameter (kg/s.m^3)
Water retention curve for micro-structural level	$(P_{To})_1$	Measured air entry pressure (MPa)
	σ_{To}	Surface tension at temperature in which $(P_{To})_1$ was measured (Usually 0.072 N/m at 20°C)
	$(\lambda_o)_1$	Shape function
	$(S_r)_{L1}$	Residual saturation
	$(S_m)_{L1}$	Maximum saturation
	$(P_d)_1$	Pressure related with suction at zero degree of saturation
	$(\lambda_d)_1$	Model parameter
Water retention curve for Macro-structural level	$(P_{To})_2$	Measured air entry pressure (MPa)
	σ_{To}	Surface tension at temperature in which $(P_{To})_2$ was measured (Usually 0.072 N/m at 20°C)
	$(\lambda_o)_2$	Shape function
	$(S_r)_{L2}$	Residual saturation
	$(S_m)_{L2}$	Maximum saturation
	$(P_d)_2$	Pressure related with suction at zero degree of saturation
	$(\lambda_d)_2$	Model parameter
Intrinsic permeability for the double-structure medium	$(k_o)_{11}$	Intrinsic permeability, 1st principal direction (m^2)
	$(k_o)_{22}$	Intrinsic permeability, 2nd principal direction (m^2)
	$(k_o)_{33}$	Intrinsic permeability, 3rd principal direction (m^2)
	$(\phi_o)_2$	Reference porosity for read intrinsic permeability
	$(\phi_{min})_2$	Minimum porosity
Relative permeability for the double-structure medium	A	Constant
	b	Power

3.9.2 Geometry and discretization

For the numerical simulations, the solution of the governing coupled hydromechanical equations has been carried out using the Code_Bright software.

All the tests to be analysed have the same geometry, a cylinder of diameter 5 cm and 10 cm high. One half of the cylinder is occupied by granular bentonite (pellets) and the other half by a compacted block. Consequently, an axisymmetric domain has been used discretised by 400 linear quadrilaterals with a total of 451nodes. A selective integration technique has been used to avoid locking of the linear finite elements. The mesh employed is shown in Figure 3-161. It can be observed that the finite element mesh is finer near the hydration surface and in the vicinity of the block/pellets contact surface. It should be noted, however, that, in the absence of friction, the problem is in fact purely-one dimensional, so that a one-dimensional mesh would be sufficient to solve it.

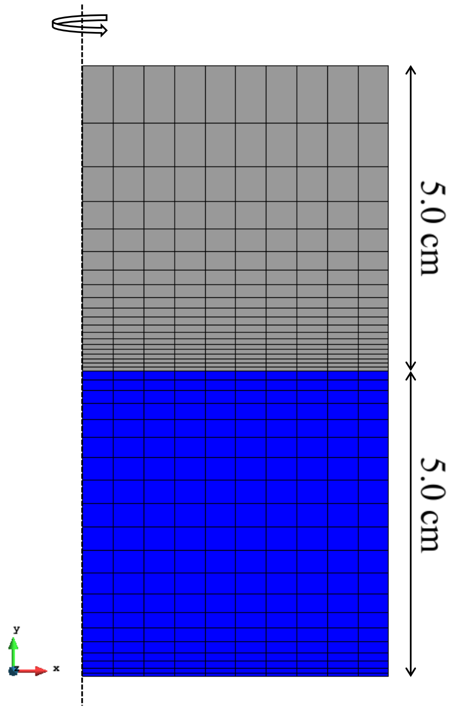

Figure 3-161 *Analysis domain and discretization*

3.9.3 Input parameters

Parameters were derived from available information on the Febex bentonite both as compacted blocks and as pellets (Alonso et al. (2011), ENRESA (2000), Hoffman et al. (2007) , Lloret et al. (2003), Villar & Gomez-Espina (2009) and the BEACON report D5.2.1 (2018)). Because of the conditions of the tests to be simulated, particular attention has been paid to the swelling pressure tests of Lloret et al (2003) for the compacted block and of Hoffman et al. (2007) for the pellets.

The same input parameters have of course used in the simulations reported here. The parameters for the mechanical and hydraulic models are listed in Table 3-37 and Table 3-38, respectively.

Table 3-37 *Parameters of the mechanical constitutive model used in the simulations*

Material	**Parameter (units)**	**Pellets**	**Block**
Bishop Parameter Microstructural level	p_{χ} (-) q_{χ} (-)	0.7 100	0.7 100
Non-linear elasticity	$\bar{\kappa}$ (-) $\bar{\kappa}_s$ (-) υ (-)	1.0e-4 4.0e-2 0.3	9.0e-4 9.0e-3 0.3
Macro-micro mechanical interaction function	f_{ms0} (-) f_{ms1} (-) n_{ms} (-) f_{mc0} (-) f_{mc1} (-) n_{mc} (-)	1 0 2 0 1 2	2 0 7 0 2 5
Macrostructural level: Plastic mechanism (BBM)	φ (°) p_c (MPa) λ_{sat} (-) r (-) β (MPa^{-1}) k_s (-) p_{s0} (MPa) α	27 0.100 0.25 0.6 0.03 0.01 0.1 1	25 0.5 0.23 0.80 0.05 0.01 0.1 1

Table 3-38 Parameters of the hydraulic constitutive model used in the simulations

Material	Parameter (units)	Pellets	Block
Leakage Parameter	γ (kg/s/m^3/MPa)	4e-6	4e-6
Water retention curve for microstructural level	P_0 (MPa)	180	180
	σ_0	0.072	0.072
	λ (-)	0.7	0.65
	S_r (-)	0.2	0.3
	S_m (-)	1	1
	P_d (MPa)	700	700
	λ_d (-)	3	1.5
Water retention curve for macrostructural level	P_0 (MPa)	0.4	12
	σ_0	0.072	0.072
	λ (-)	0.45	0.27
	S_r (-)	0.01	0
	S_m (-)	1	1
	P_d (MPa)	2000	2000
	λ_d (-)	1.5	2
Intrinsic permeability	k_0 (m^2)	6e-19	1e-20
	b (-)	6	12
	ϕ_0 (-)	0.205	0.188

An important component of the simulations is the retention curve, often a key feature in the prediction of hydration processes. With the double structure model, it is necessary to specify a retention curve of the microstructure and a retention curve for the macrostructure. The measured retention curve would be an average of the two, taking into account the respective volume fractions. Figure 3-162 shows the retention curves (micro, macro and average) for pellets and blocks. It can be noted that there is a significant difference in the macrostructure retention curves for pellets and blocks reflecting the different sizes and arrangements of the macropores.

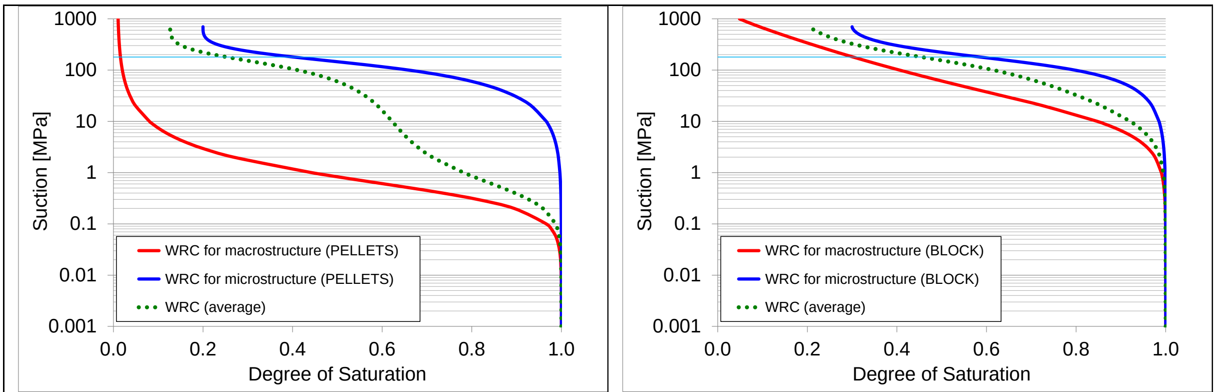

a)	b)

Figure 3-162 *Retention curves, a) pellets, b) block*

3.9.4 Initial and boundary conditions

In all tests the initial state of the pellets and block are set the same. The initial porosity of the block is 0.404 (split in volume fractions of 0.216 for the micro-level and 0.188 for the macro-level) whereas the initial porosity of the pellets is 0.528 (divided in volume fractions of 0.323 for the micro-level and 0.205 for the macro-level). The porosity partition between microstructure and macrostructure has been based on the porosimetry (MIP) data provided by CIEMAT. The initial degree of saturation is 0.46 for the block and 0.25 for the pellets. The initial suction of 180 MPa has been derived from the value of water content and retention curves. Hydraulic equilibrium between microstructure and macrostructure has been assumed at the start of the test.

The mechanical boundary conditions are illustrated in Figure 3-163. They are the same in all the cases. The measurement of axial load is carried out at the top where zero vertical displacements are prescribed. Hydration is performed through the bottom boundary. In MGR 22 a constant flow rate has been applied whereas in MGR 23, a constant water pressure is prescribed.

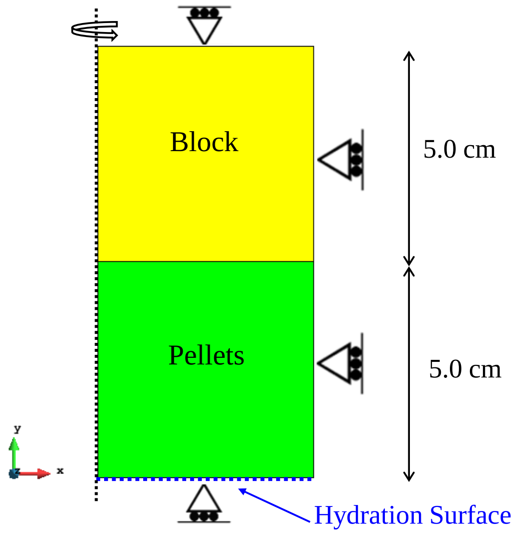

Figure 3-163 *Mechanical boundary conditions.*

3.9.5 Results MGR22

Test MGR22 was hydrated using a constant flow condition at the bottom surface. The modelling attempts to reproduce the experimental history including an initial period of about 10 days without water entry followed by a water injection of 0.047 cm^3/h instead of the specified value of 0.05 cm^3/h (Figure 3-164a). In Figure 3-164b the evolution of the axial pressure with time is plotted and compared with the experimental results. It can be observed that the final swelling pressure is correctly anticipated. The evolution is also adequately reproduced but the initial rate of axial pressure increase is faster than observed. The result indicates that, probably, the leakage parameter should be smaller to slow down the initial water transfer from the macrostructure to the microstructure. The wobble visible in the axial pressure evolution curve is a numerical artefact due to the change of boundary conditions.

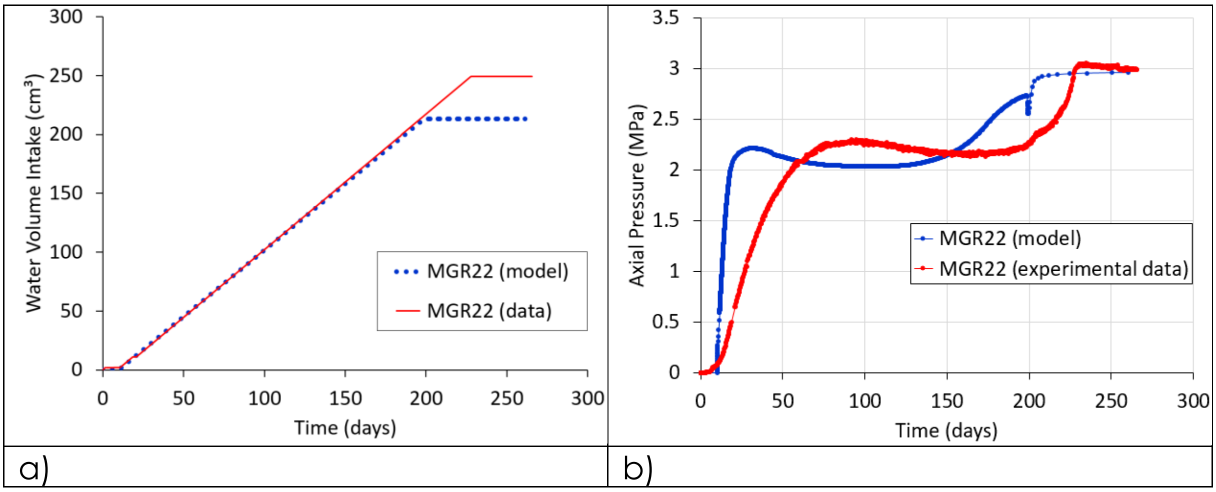

Figure 3-164 *Test MGR22, experimental and modelling results. a) Water volume intake, b) Axial pressure evolution*

The progress of homogenization can be readily followed plotting the evolution with time of the overall porosity at three different points (Figure 3-165). Point at y=2.5 cm is located in the centre of the pellets section whereas points at y=7.5 cm and y=10 cm correspond to the centre of the block section and to the top of the column, respectively. It can be noted that the porosity of the pellets (y= 2.5 cm) reduce while the porosity of the block (y = 7.5 cm, y=10 cm) increases so that the difference of the two porosities has reduced significantly at the end of the test. It is also worth noticing that the reduction of porosity is very similar throughout the block section.

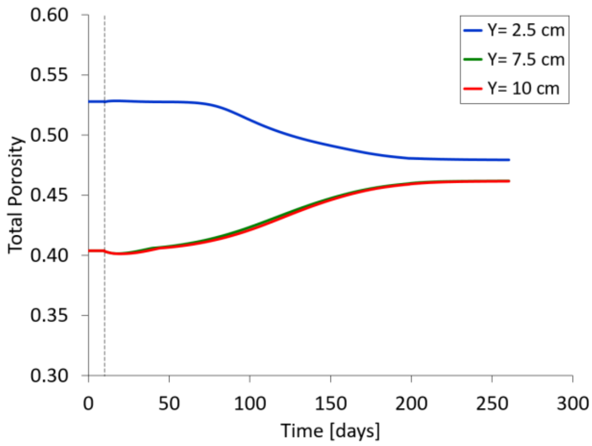

Figure 3-165 *Test MGR22. Evolution of porosity with time at three points at different distances from the hydration surface*

Further information on the variation of porosity can be obtained by plotting the evolution with time of the micro and macro volume fractions (Figure 3-166). It can be seen that the change of micro volume fraction is similar at all points corresponding to the hydration of the microstructure. However, the reduction of the macro volume fraction is much larger in the pellets because the available volume for compression is significantly larger.

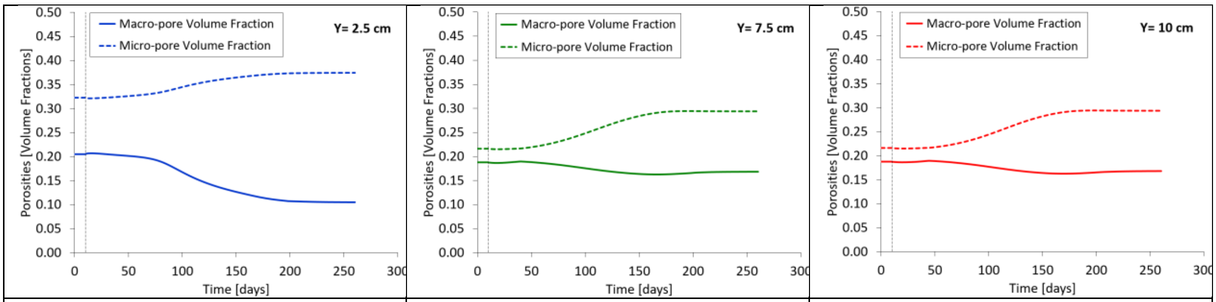

a) b) c)

Figure 3-166 *Test MGR22. Evolution of micro and macro volume fractions at three points at different distances from the hydration surface, y. a) y = 2.5 cm, b) y = 7.5 cm, c) y = 10 cm.*

The progress of hydration is illustrated by tracking the changes of degree of saturation with time for the same three points as before (Figure 3-167). Total, micro and macro degrees of saturation are shown. The plots show that the column is fully saturated after about 200 days. During the test, the macro degree of saturation is always lower than the micro one until reaching saturation because its initial value is lower, especially in the pellets section.

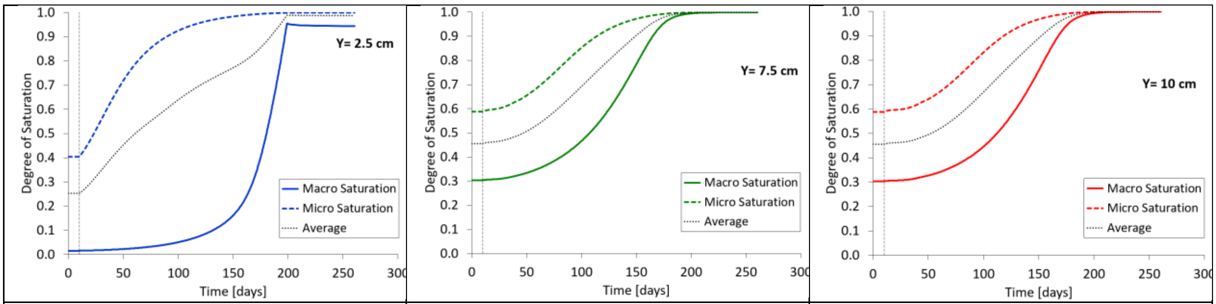

a) b) c)

Figure 3-167 *Test MGR22. Evolution of micro, macro and total degree of saturation at three points at different distances from the hydration surface, y. a) y = 2.5 cm, b) y = 7.5 cm, c) y = 10 cm.*

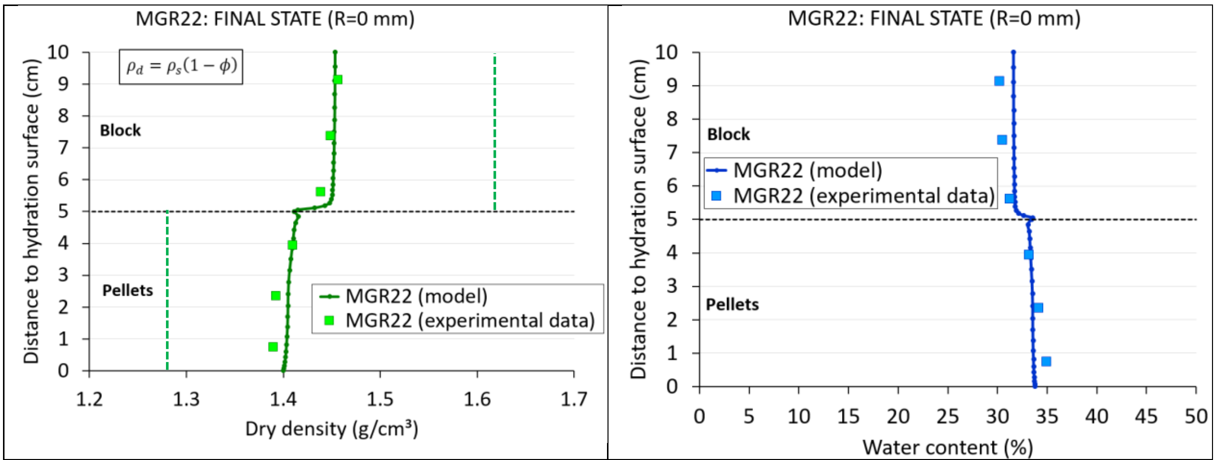

a) b)

Figure 3-168 *Test MGR22, experimental and modelling results. a) Distribution of dry density at the end of the test (vertical dashed lines indicate initial values), b) Distribution of water content at the end of the test.*

Finally, Figure 3-168a presents the distribution of computed dry density throughout the column at the end of the test compared with experimental results. It is apparent that a good agreement has been obtained. A large degree of homogenization has taken place with respect to the initial distribution of dry densities that is represented as vertical dashed lines in the Figure. As the material is basically saturated at the end of the test, the water content distribution follows the pattern of the dry density one (Figure 3-168b).

Results MGR23

Test MGR23 was hydrated prescribing a constant water pressure of 15 kPa at the bottom surface. To avoid numerical convergence issues, the boundary water pressure is not applied instantaneously bit over a period of 1 day. In spite of this, the solution at the start of the test is still somewhat unstable but it becomes reliable a few days after.

Figure 3-169a shows the computed and experimental time evolution of water intake. It can be noted that the observed trend is reproduced adequately although the early hydration rate is underestimated. In contrast, the rate of axial pressure increase is overestimated although the observed swelling pressure is obtained in the simulation (Figure 3-169b). The disparity in the initial evolution rates may indicate that a lower value of the leakage parameter might be more appropriate.

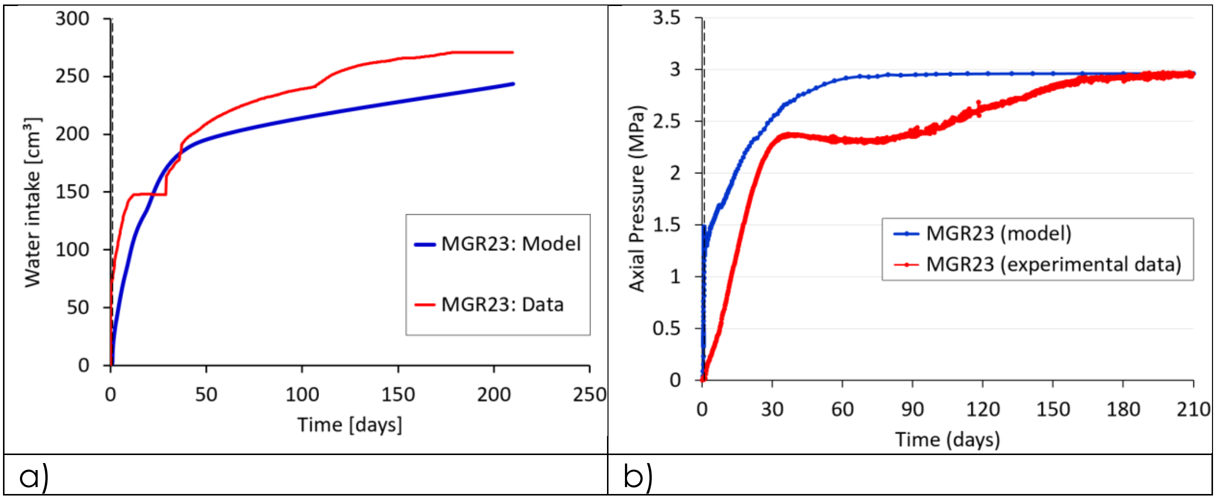

Figure 3-169 *Test MGR23, experimental and modelling results. a) Water volume intake, b) Axial pressure*

The variation of porosity with time at three different points (Figure 3-170) shows a similar degree of homogenisation as in test MGR22 in spite of the different hydration conditions. Again, the evolution of total porosity is very uniform in the block section. Tests MGR22 and MGR 23 are also very similar concerning the evolution of micro and macro volume fractions (Figure 3-171).

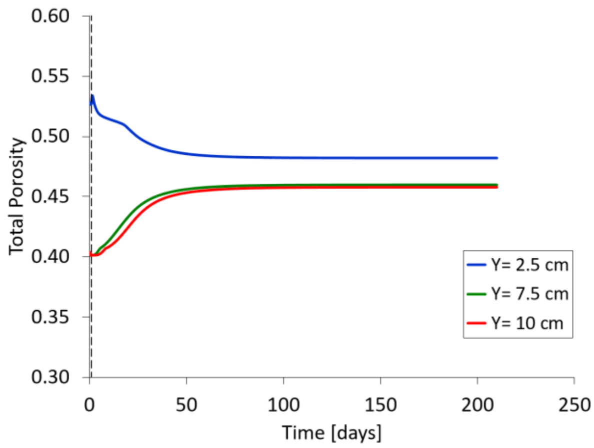

Figure 3-170 *Test MGR23. Evolution of porosity with time at three points at different distances from the hydration surface*

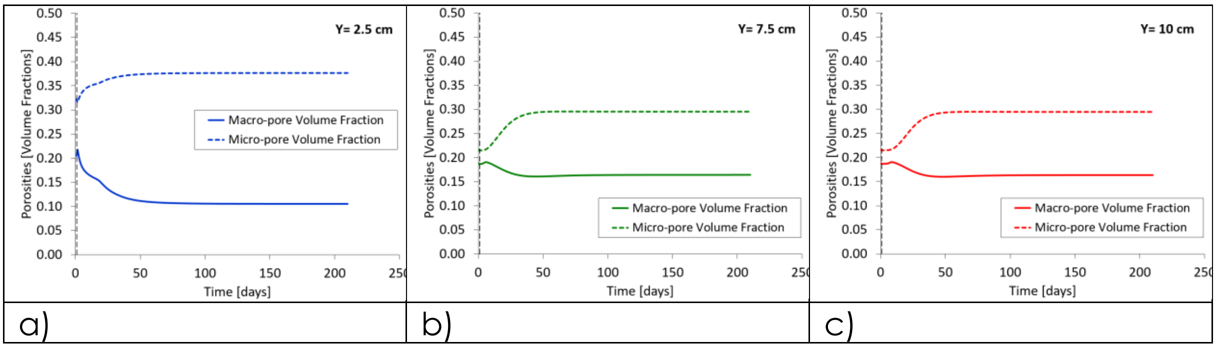

Figure 3-171 *Test MGR23. Evolution of micro and macro volume fractions at three points at different distances from the hydration surface, y. a) y = 2.5 cm, b) y = 7.5 cm, c) y = 10 cm.*

The column ha reached saturation at the end of the test practically throughout (Figure 3-172). The not quite saturated state in the pellets macrostructure is due to the retention curve used where a very small suction close to zero results still in some unsaturation. This is the consequence of not considering the effect of void ratio changes on the retention curve. However, as the macrostructural porosity is in fact quite small upon hydration, the pellets are still practically saturated overall.

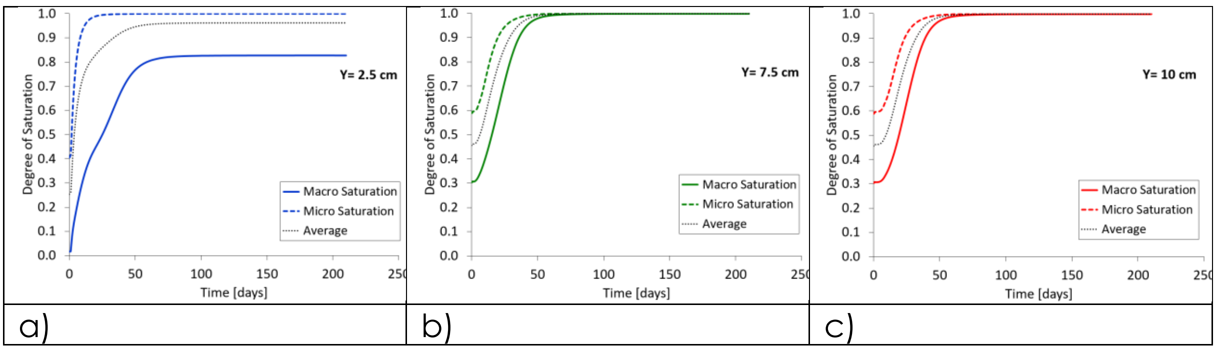

Figure 3-172 *Test MGR23. Evolution of micro, macro and total degree of saturation at three points at different distances from the hydration surface, y. a) y = 2.5 cm, b) y = 7.5 cm, c) y = 10 cm.*

The computed distribution of dry density at the end of the test (Figure 3-173a) shows that the observed homogenization of the column has been well represented by the analysis in spite of starting from very different values in pellets and blocks. Again, the water content distribution follows the same trend as the bentonite is practically saturated all along the column (Figure 3-173b).

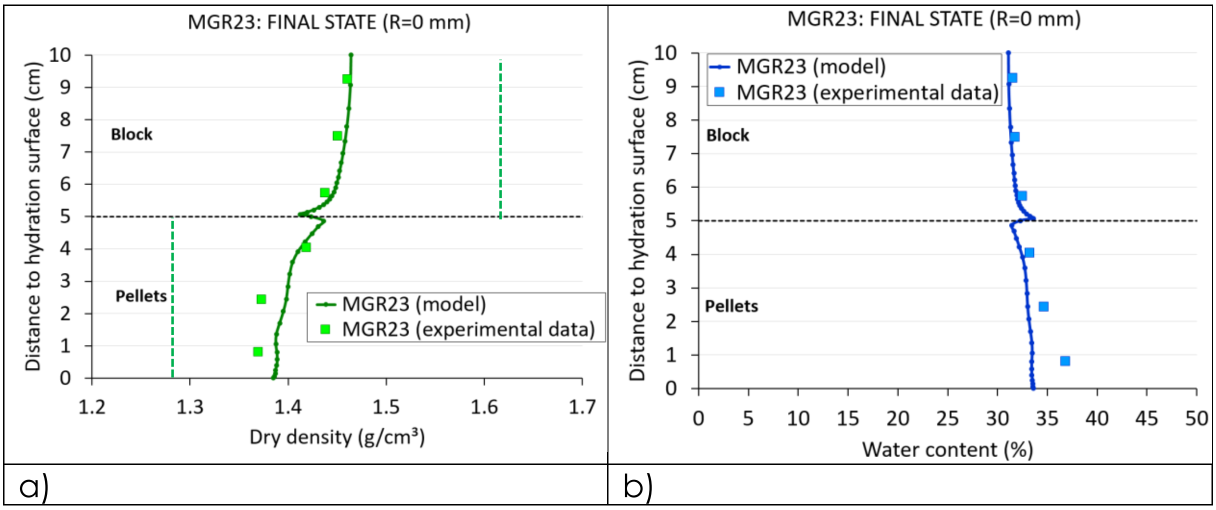

Figure 3-173 *Test MGR23, experimental and modelling results. a) Distribution of dry density at the end of the test (vertical dashed lines indicate initial values), b) Distribution of water content at the end of the test.*

3.9.6 Discussion

Overall, the results of the analyses of tests MGR22 and MGR 23 can be regarded as globally satisfactory. The final swelling pressure has been correctly predicted in both cases although there are some departures from the observed time evolution of water intake and swelling pressure, especially in the early part of the test when the rate of variation proves difficult to capture in every detail.

The final state of the saturation of the column at the end of the test is also correctly reproduced in the two cases. More importantly, the computed final state of the bentonite in terms of distribution of dry density agrees well with the experimental data, showing a large measure of homogenization from a very heterogeneous initial state. The results of the analyses suggest that most of the homogenization occurs relatively early in the performance of the test.

The mechanical behaviour of the bentonite has been modelled by a double structure constitutive law with separate (but coupled) consideration of the microstructure and the macrostructure. The double structure model appears to have performed well and provides additional information to examine the process of hydration and homogenization from a wider perspective. It also allows, for instance, to ascribe the changes in permeability to variation of the macrostructure porosity alone which is probably more realistic. However, the dependence of permeability on porosity has an obvious limitation because it does not take into account the key role that the size of the pores plays in this respect. This is particularly important when the change of pore size is large as it is the case of the pellets section during hydration.

4 Synthesis of task 5.3 – key lessons

The benchmark exercise was done knowing only the experimental results of tests MGR21, MGR22, MGR23, MGR24. The simulations performed for the MGR27 test were done in blind.
Experimental results for MGR 27 test were presented only after receiving numerical simulation results, during the meeting on 5 February 2021 (online WP3/WP5 meeting). 9 teams participated to the exercise proposed for task 5.3 of WP5 but only 7 performed the blind prediction on time. This explains why in the comparison graphs for MGR27, only results from 7 partners are presented.

In the following analysis, the MGR27 experimental results are presented as the other ones, without any distinction.

Numerical results are presented anonymously, however the colour code per team is constant in this synthesis.

4.1 Models comparison and parameters calibration

Comparing the mechanical behaviour is not an easy task. Each team has a different model, and few parameters are comparable. Moreover 2 teams (E & F) consider also friction between bentonite and cell wall.

A short synthesis of the mechanical constitutive models used by the different teams is presented in Table 4-1.

Table 4-1 Mechanical constitutive models used in the benchmark

Team	Model
A	Bishop effective stress; modified CamClay
B	Hysteresis Based Material (HBM) model
C	double-structure hypoplastic model for expansive clays
D	ACMEG – TS elastoplastic model
E	ILM
F	Modified BBM elastoplastic model
G	Elastic with modulus depending on water saturation
H	Modified BBM with double structure ICDSM
I	Modified Barcelona Expensive Model BExM

Few mechanical parameters can be compared.

Table 4-2 presents parameters related to the saturated volumetric behaviour (stiffness parameters κ and λ), and the deviatoric behaviour (Poisson ratio ν and friction angle Φ(°)). These comparisons should be considered with care!

Table 4-2 Mechanical parameters used by the partners

Team	Φ(°)	ν	κ	λ
A	15-16 [1]		0.0478	0.0912
B	-	-	-	-
C	25	0.25	0.025	0.14
D	16	0.35	0.060	0.088
E	-	0.27	-	-
F	20 & 26	0.25 & 0.35	0.012 & 0.074	0.12 & 0.20
G	-	0.30 & 0.41	-	-
H		0.4	0.005 & 0.050	0.13 & 0.18
I	27 & 25	0.3	1.E-4 & 9.E-4	0.25 & 0.23

[1]: from the slope of critical state line, M = 0.58

The friction between bentonite and steel is considered by 2 teams (E & F); friction coefficients are 0,3 and 0,36.

Most teams consider that permeability depends on the void volume (porosity, void ratio or density). Table 4-3 presents the strategy of the different teams regarding permeability.

Table 4-3 Models for permeability used by the teams

Team	Model
A	Permeability depends on porosity
B	Permeability depends on void ratio
C	Constant permeability
D	Permeability depends on void ratio
E	Permeability depends on density
F	Permeability depends on macro void ratio
G	Permeability depends on density
H	Permeability doesn't depend on porosity but on suction
I	Permeability depends on porosity

Water content and suction are related through the water retention curve. Most teams follow the experimental water content and derive the suction from the water retention curve. Few teams do the opposite and start from the experimental suction. The strategy of each team is presented in Table 4-4.

Table 4-4 Strategy to represent water content/suction evolution

Team	
A	Uniform suction, water content follows from the retention curve
B	Water content from experiment, suction is deduced from the retention curve
C	Suction from experiment, water content follows and is overestimated, need a smaller water intake.
D	Water content from experiment, suction is deduced from the retention curve. Water density can vary.
E	Water content from experiment, suction is deduced from the retention curve
F	Water content from experiment, suction is deduced from the retention curve
G	Water content from experiment, suction is deduced from the retention curve
H	Uniform suction, water content follows from the retention curve
I	Water content from experiment, suction is deduced from the retention curve

Initial and final values of intrinsic permeability (m²) and hydraulic conductivity (m/s) for pellets and blocks are presented in Table 4-5 and Table 4-6.

Table 4-5 Initial and final hydraulic conductivity and water permeability for pellets

Team	Pellets	Initial (m2)	Initial (m/s)	Final min (m2)	Final max (m2)	Final min (m/s)	Final max (m/s)
A	all	1.00E-19	1.00E-12	2.60E-20	3.48E-19	2.6E-13	3.48E-12
	MGR22	3.30E-19	4.52E-14	1.01E-19	1.07E-19	9.65E-13	1.05E-12
	MGR23	2.77E-19	1.92E-15	9.84E-20	1.16E-19	9.65E-13	1.13E-12
B	MGR27	2.77E-19	1.92E-15	7.09E-20	7.49E-20	6.01E-13	6.39E-13
C	all	5.00E-21	5.00E-14	5.00E-21	5.00E-21	5.00E-14	5.00E-14
D	all	2.00E-19	3.00E-13	8.19E-20	8.59E-20	8.19E-13	8.59E-13
	MGR22	2.42E-21	2.38E-14	2.84E-20	3.68E-20	2.79E-13	3.61E-13
	MGR23	8.14E-23	7.98E-16	2.42E-20	4.53E-20	2.37E-13	4.44E-13
E	MGR27	8.14E-23	7.98E-16	1.51E-20	6.92E-20	1.48E-13	6.78E-13
F	all	8.64E-20	8.48E-13	2.89E-20	3.21E-20	2.8351E-13	3.149E-13
G	all	4.72E-21	4.64E-14	2.57E-20	4.57E-20	2.52E-13	4.47E-13
H	all	5.102E-17	5.00E-10	5.102E-17	5.102E-17	5E-10	5E-10
I	MGR23	6.00E-19	2.29E-15	2.91E-19	3.44E-19	2.04E-12	2.40E-12

min	8.1E-23	8.0E-16	5.0E-21		5.0E-14	
max	5.1E-17	5.0E-10		5.1E-17		5.0E-10

For pellets, 3 orders of magnitude can be observed in initial hydraulic conductivity between the different teams' choices. Permeability evolves during saturation, this is induced partly by strains and pore volume evolution partly by saturation. In the final state, the range of teams' intrinsic permeability is reduced to about 1 order of magnitude, while there are still 2 orders of magnitude in the hydraulic conductivity.

For blocks, the initial range is lower (2 orders of magnitude), indicating a better knowledge of the property. Permeability evolves also in the blocks, with an increase of 2 order of magnitude for most teams, but for some other teams there is no significant evolution. The final values remain highly different from one team to another.

Table 4-6 Initial and final hydraulic conductivity and water permeability for blocks

Team	Blocks	Initial (m2)	Initial (m/s)	Final min (m2)	Final max (m2)	Final min (m/s)	Final max (m/s)
A	all	4.65E-21	4.65E-14	5.50E-21	5.50E-21	5.5E-14	5.5E-14
B	MGR 22	4.45E-21	6.72E-15	1.66E-20	1.96E-20	1.53E-13	1.85E-13
	MGR23	4.87E-21	7.99E-15	1.35E-20	2.24E-20	1.30E-13	2.17E-13
	MGR 27	4.87E-21	7.99E-15	1.91E-20	3.10E-20	1.78E-13	3.04E-13
C	all	2.00E-20	2.00E-13	2.00E-20	2.00E-20	2.00E-13	2.00E-13
D	all	3.00E-21	3.00E-15	6.76E-21	8.20E-21	6.41E-14	8.13E-14
E	MGR22	7.51E-22	7.37E-15	1.57E-20	2.49E-20	1.54E-13	2.44E-13
	MGR23	8.74E-22	8.75E-15	1.40E-20	2.09E-20	1.37E-13	2.05E-13
	MGR27	9.50E-22	9.32E-15	8.61E-21	1.13E-20	8.44E-14	1.11E-13
F	all	3.21E-20	3.15E-13	2.85E-20	3.22E-20	2.80E-13	3.16E-13
G	all	8.70E-22	8.51E-15	1.03E-20	1.18E-20	1.01E-13	1.16E-13
H	all	5.10E-20	5.00E-13	5.10E-19	5.10E-19	5.00E-12	5.00E-12
I	MGR23	1.00E-20	2.80E-15	7.43E-21	8.51E-21	7.42E-14	8.50E-14

min	7.5E-22	2.8E-15	5.5E-21		5.5E-14	
max	5.1E-20	5.0E-13		5.1E-19		5.0E-12

4.2 Water intake

The water intake observed experimentally in MGR21, MGR22, MGR23, MGR24 and MGR27 tests are presented in Figure 4-1. The total volume is about the same for tests MGR22, MGR23 and MGR27. This is normal as the available pore space is more or less identical. However, the time scale is different, as the hydration proceeds differently: hydration is driven at constant pressure through the pellets part for MGR23 (higher initial permeability and quicker wetting), at constant pressure through the block part for MGR27 (lower initial permeability and slow wetting), and at constant flow rate through the pellets part for MGR22.

Test MGR23 has been repeated two times with early stops at 14 days and 34 days, allowing a comparison at early times.

The water flow is imposed in MGR22, so most teams follow exactly the experimental water intake. However, two teams were not able to impose such boundary condition with the FE code used, or to model until the full saturation.

MGR23 experimental results were known before modelling. 5 teams follow accurately the experimental results, but don't represent the plateau at 150 cm3 water intake (this was not required). This shows that the permeability models and calibration are efficient, when results are known. However, this good result is surprising compared to the large range of permeability values considered by the different teams. Two teams predict low water intake; surprisingly, they predict full saturation at the test end, which indicates possibly an underestimation of the pore volume available for hydration.

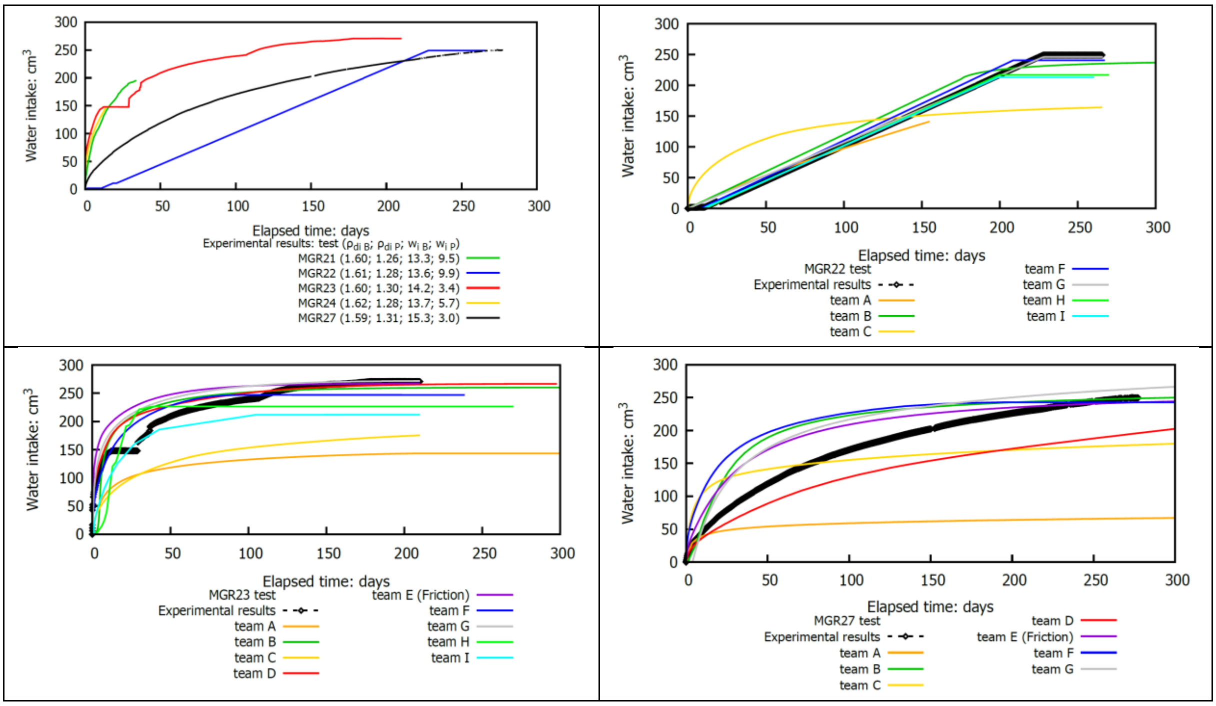

Figure 4-1 *Water intake, comparison between numerical and experimental results (a. all experimental results, b. MGR22, c. MGR23, d. MGR27)*

MGR27 was a blind test and invert the pellets and block part. 4 teams give similar results and obtain the good final saturation at the good time (200 – 300 days), but the hydration beginning is much faster: 150 cm3 enter in 20 to 30 days, while experimentally it needs about 75 days. One observes a factor 2 to 3 in the initial flow between model and test. The initial block hydraulic conductivity (3.E-15 to 3.E-13 m/s) is probably overestimated in the numerical models.

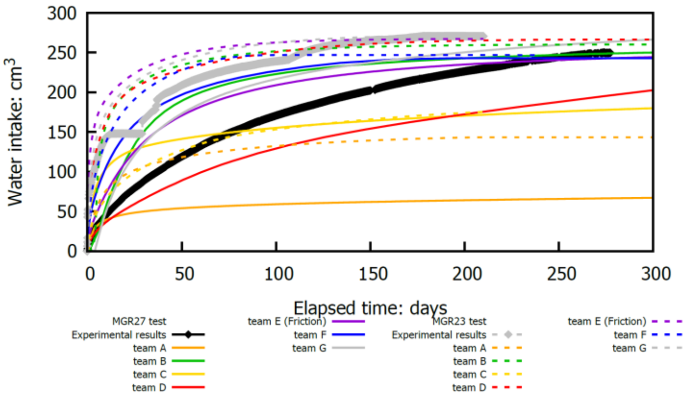

Figure 4-2 *Comparison of water intake between MGR23 and MGR27 test, numerical and experimental results*

The Figure 4-2 compares numerical results for MGR23 and MGR27. It appears clearly that for both tests the initial hydraulic conductivity value (3.E-15 to 3.E-13 m/s for blocs; 8.E-16 to 8.E-13 m/s for pellets) could be overestimated.

Early results for MGR23 are available thanks to tests MGR21 and MGR24 (Figure 4-3). It shows differences between simulations, and highlights differences in the initial permeability values for pellets material.

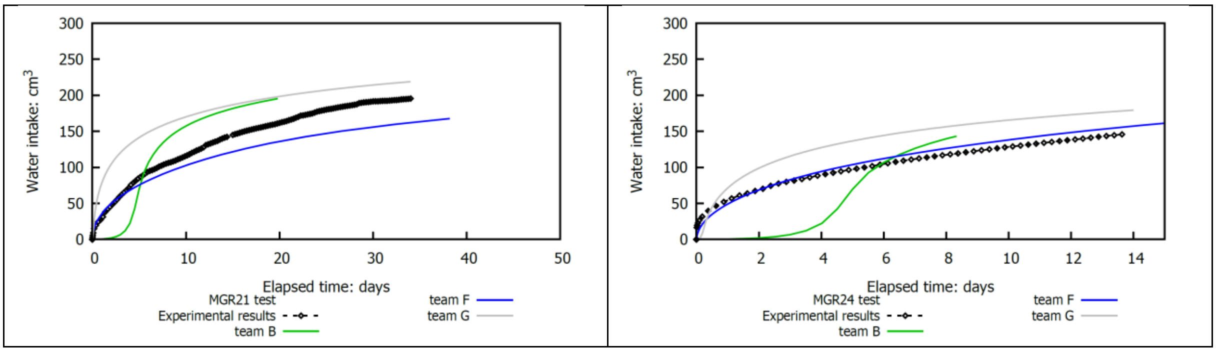

Figure 4-3 *Water intake at early time, a. MGR21 – 34 days, b. MGR24 – 14 days*

Water intake as predicted in block and in pellets by simulation are compared on Figure 4-4. Time evolution in block is similarly predicted by all teams. Large variations can be observed for pellets, which hydrated more quickly than block when they are directly in contact with water.

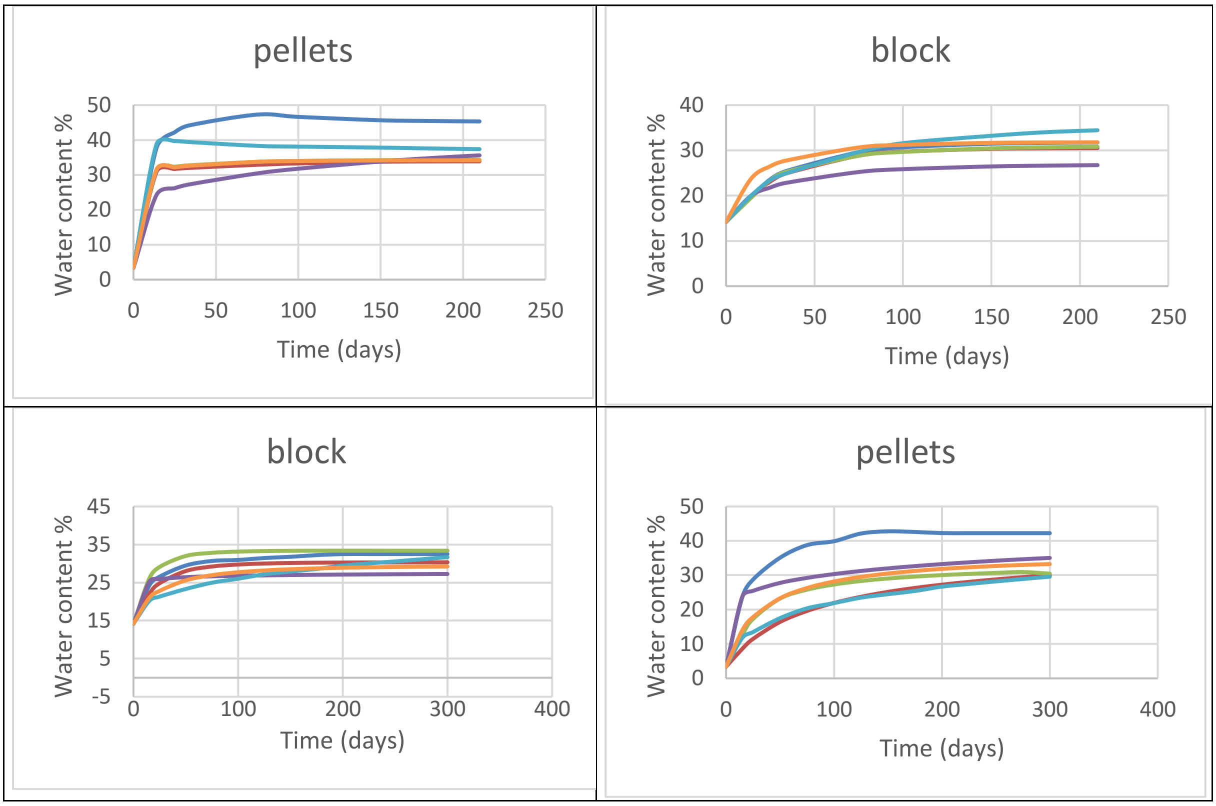

Figure 4-4 *Water intake respectively in pellets and in block (1st line MGR23; 2nd line MGR27*

4.3 Dry densities

MGR22 and MGR23 experimental results are very similar, which means that the different velocity of water intake has a small influence on the final dry density field. Bloc and pellets materials have different final dry densities. MGR27 final dry density is more homogeneous.

Numerical results for MGR22 and MGR23 are close to experimental ones. Three teams give results far from the experimental ones, but the same teams underestimate the water intake, and probably, due to that, the swelling strains. Same conclusions may be drawn for MGR27 blind simulation, while results are a little more dispersed between teams.

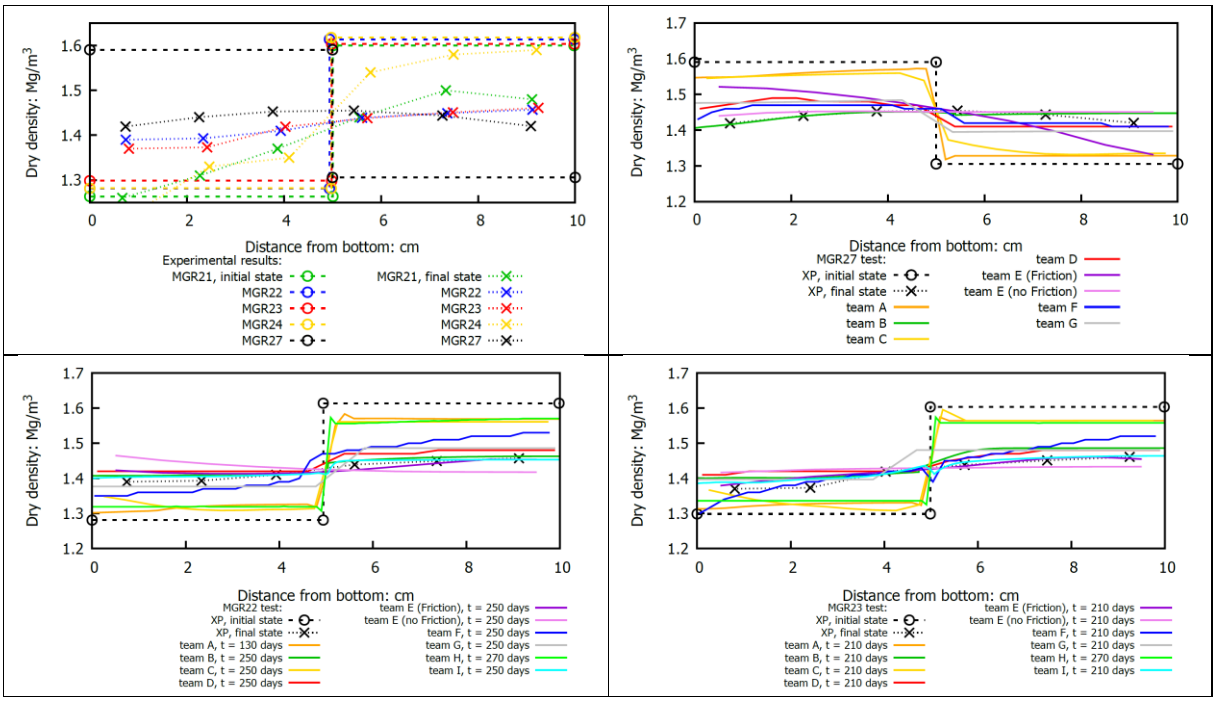

Figure 4-5 *Dry densities at saturation; a. comparison of all experimental results; b. results for MGR27; c. results for MGR22; d. results for MGR23*

Considering densities at early stage, MGR21 & MGR24 tests were early dismantled in partial-saturation state. Numerical models give good results. Team F, which takes into account friction between bentonite and cell walls, shows a higher density gradient.

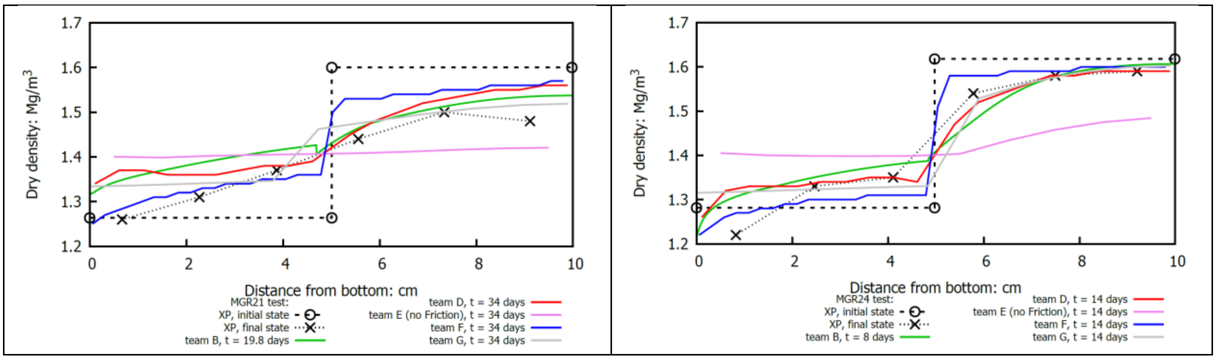

Figure 4-6 Dry densities at early time, a. MGR21 – 34 days, b. MGR24 – 14 days

4.4 Gravimetric water content

Similar analysis may be drawn for gravimetric water content as for dry densities at saturated / final state, as pores are full of water. No real difference in conclusion may be expected.

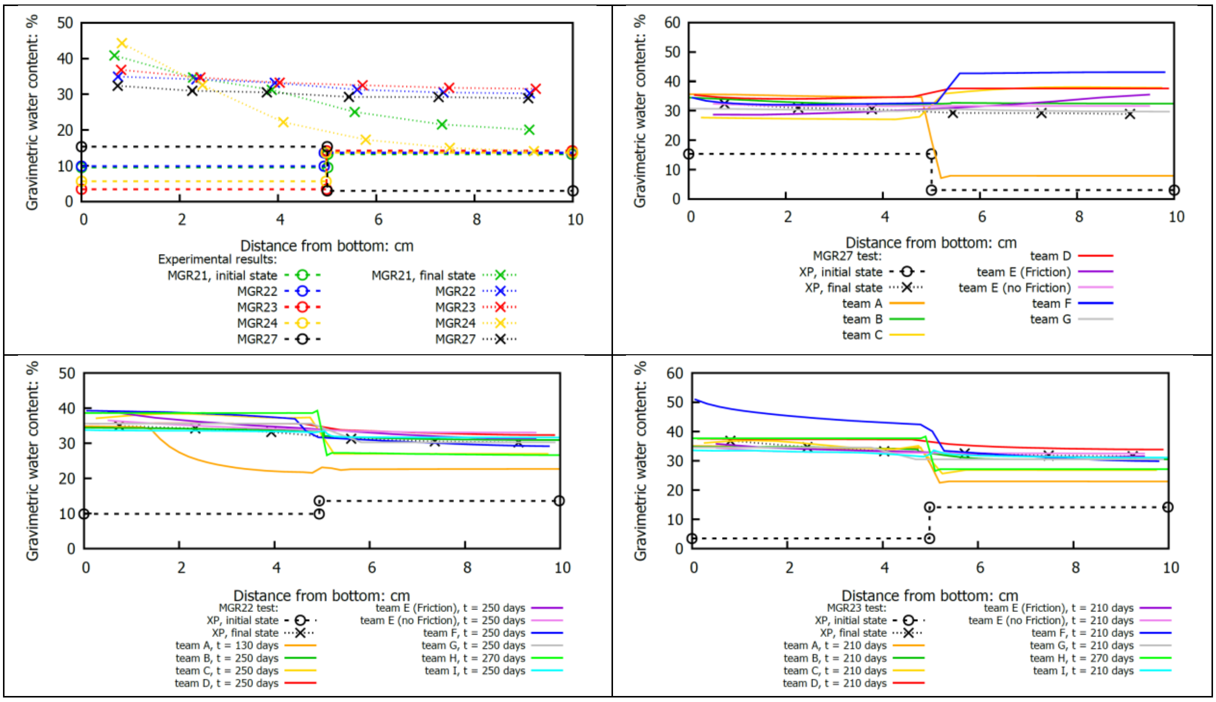

Figure 4-7 *Gravimetric water content at saturation; a. comparison of all experimental results; b. results for MGR27; c. results for MGR22; d. results for MGR23*

While dry density has not evolved much after 14 days, water content has significantly changed (Figure 4-8). The average saturation degree is about 70%. The global trend is well reproduced by most numerical models, but the difference between bloc and pellets seems overestimated by the numerical models. After 34 days, the saturation degree is around 90%. The water content has homogenised and differences between models are reduced.

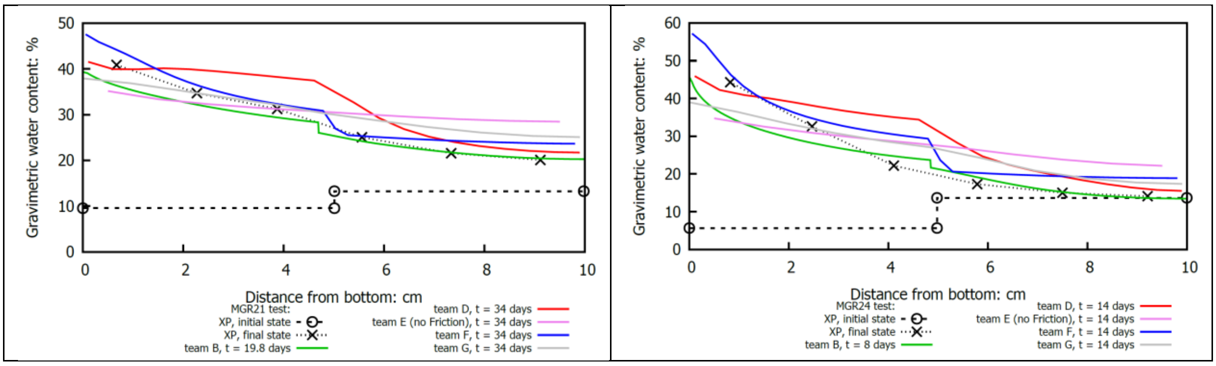

Figure 4-8 *Gravimetric water content at early time, a. MGR21 – 34 days, b. MGR24 – 14 days – tests similar to MGR23.*

For test MGR27, as hydration occurs through the block, water content evolves much slowly (Figure 4-9), which illustrates clearly the permeability difference between block and pellets.

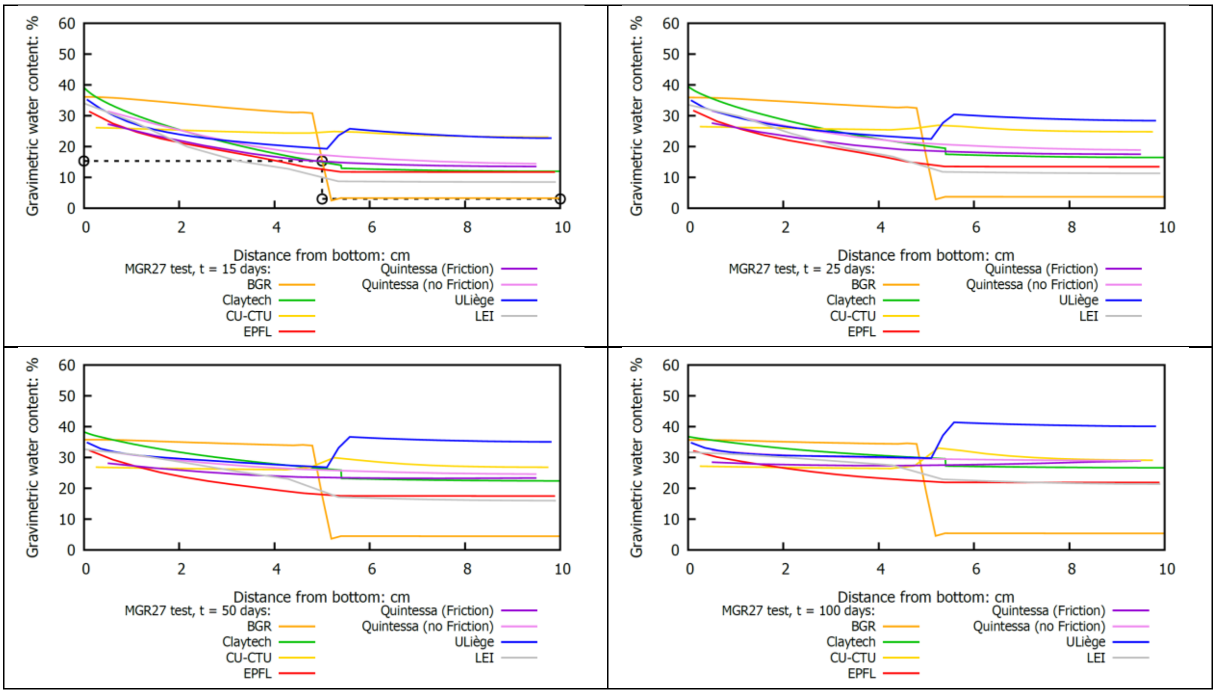

Figure 4-9 *MGR27 Gravimetric water content at early time, a.15 days, b. 25 days, c.50 days, d. 100 days.*

4.5 Stresses

Comparing experimental results (Figure 4-10) shows on the one hand that the hydration strategy has a clear influence on the stress evolution but not on the final value (MGR22 vs MGR23). Stresses in the pellets and in the block are highly different in the final state (MGR23 vs MGR27), with a factor >2.

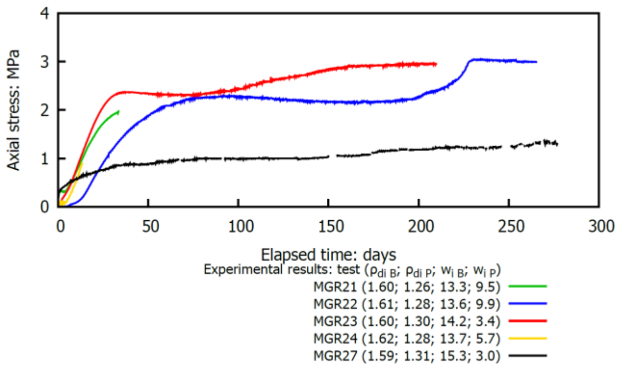

Figure 4-10 *Comparison of axial stresses in experimental results*

Experimental results are limited to one sensor measuring the axial force at the cell top, the base opposite to the hydration one. While experimental results were known for MGR22 and MGR23, numerical predictions present a large dispersion, including the final swelling pressure, the range of which is larger than the measured value. The time evolution is more or less similar to the experimental one for MGR23. This is not the case for MGR22, which is driven by a constant flux hydration. This boundary condition seems critical for a number of codes / models.

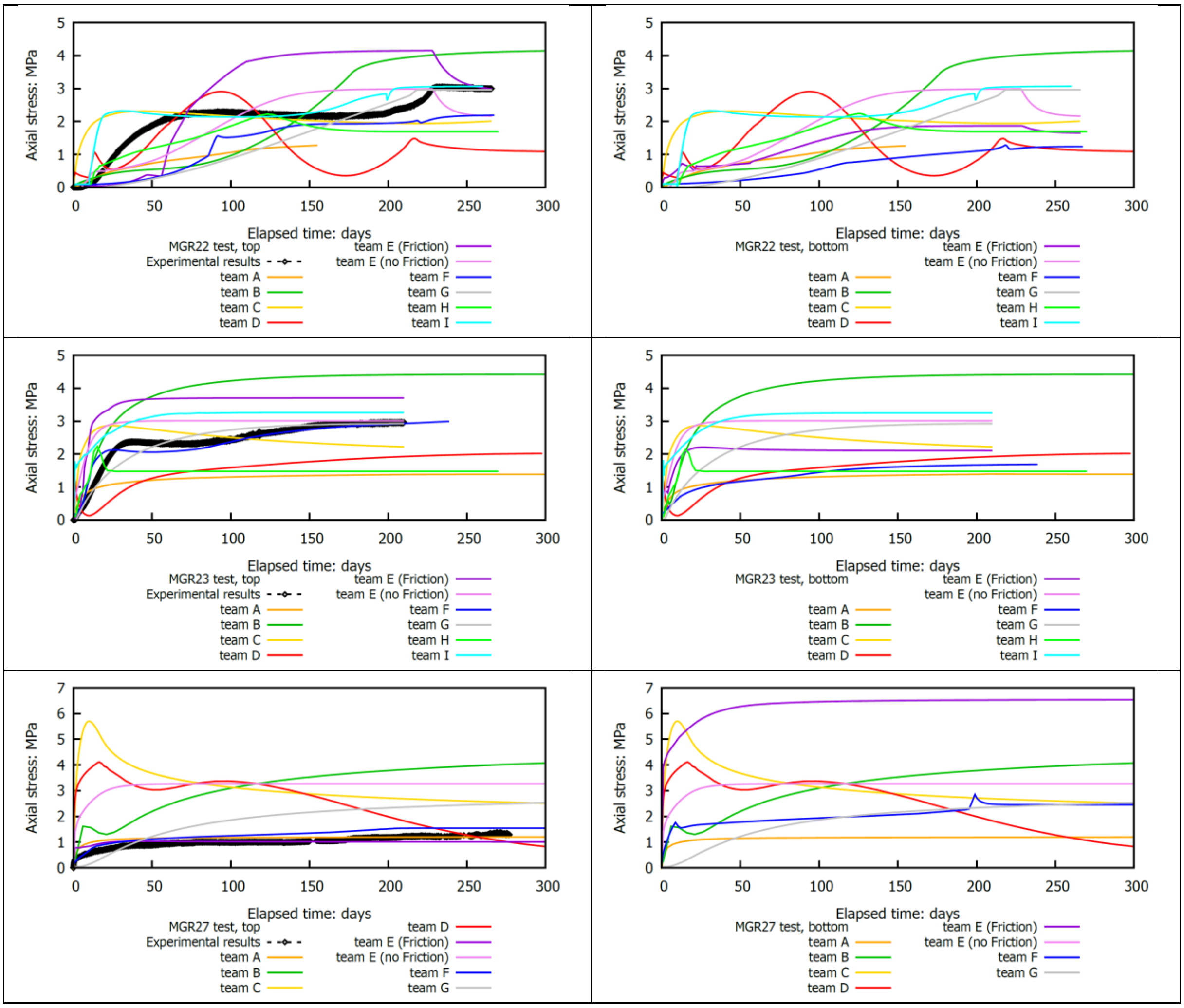

Figure 4-11 *Axial stress, left top, right bottom, line 1 MGR22, line 2 MGR23, line 3 MGR27*

Only two teams model a friction between bentonite and cell wall; consequently, the top and bottom stresses differ. They also predict much better the axial stresses for the MGR27 (blind prediction). The other teams predict identical stresses at top and bottom and largely over predict the axial stress for MGR27.

Radial stresses were not measured, so there is no reference for the numerical simulations. Radial stresses are lower in pellets compared to stresses in block. The radial stress evolution is dispersed as for the axial one. The hydration at constant pressure and through the pellet powder seems easier for the constitutive models compared to the hydration through the block or at constant rate, which give much oscillation for a number of models.

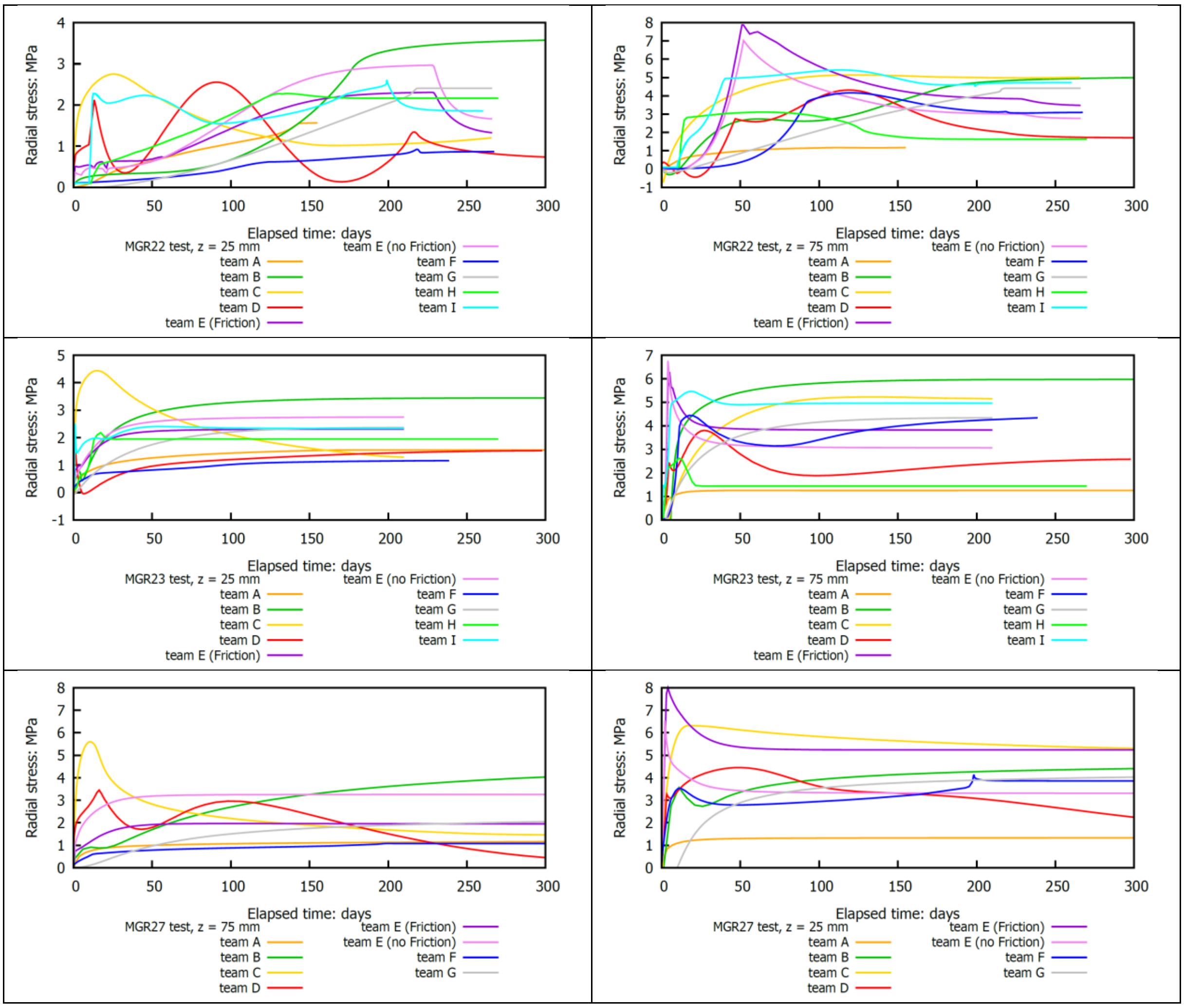

Figure 4-12 *Radial stress, left powder pellets, right block, line 1 MGR22, line 2 MGR23, line 3 MGR27*

4.6 Conclusions

The water intake with time seems well modelled by most teams. However, one may observe a number of variations or divergences. Moreover, prediction is less easy for early times of hydration. These globally good results may be surprising considering the very large range of permeability used in the simulations by the different teams.

The idealisation of the initial state, especially of the initial water content affects significantly the final results and the evolution curves. The water retention curve, the water content and the suction must be consistent, which requires a choice.
Interestingly, some teams used as hydraulic initial value the suction and overestimated the initial water content, while other teams started from the actual water content and deduced the suction from the retention curve. The option with an over estimation of the initial water content appear to strongly degrade the prediction of the water intake and of the final water content. This approach should probably be avoided. The initial value of the water content plays an important role in the water intake curve.

Accuracy: the full water intake in the experimental reporting may be higher than the initial void space (about 10 cm^3 compared to 260 cm^3).

The tests imply 2 materials with very different properties and initial states. The initial permeability of pellets powder material is not easy to evaluate; it remains a challenge. The initial permeability of blocs is overestimated (MGR27 water intake). A very nice analysis by ClayTech (fig. 4.57 & 4.58) compares the water content at early stages and shows its evolution with time, comparing the different ways water enters.

The boundary conditions with constant water flux remain difficult to assess for few numerical codes.

The final (at saturated state) dry densities are well reproduced. They do not depend significantly on the mechanical models (including law and friction aspects). Accuracy: the measured final densities may be lower than what should be obtained based on a constant volume assumption, which could imply an error around 0.03 g/cm3 for an average density of 1.45 g/cm3.

It is very difficult to predict the stresses final value and time evolution. Stresses evolution shows much variation between teams. These values are the most difficult to model! The influence of friction is suggested by the difference in the time evolution and final value of axial stress in experimental tests MGR23 and MGR27. Two teams have modelled friction at the cell wall – bentonite interface. These teams satisfactorily blind-predicted the evolution of axial stress in MGR27.

References

Alonso E. E., Gens A. and Josa A. A constitutive model for partially saturated soils [Journal] // Géotechnique 40. - 1990. - pp. No. 3, 405–430.

Alonso E.E., Romero, E. and Hoffman, C. Hydromechanical behaviour of compacted granular expansive mixtures: experimental and constitutive study. Geotechnique 6(4), pp. 329-344 [Report]. - 2011.

BEACON D5.2.1 BEACON project. Specifications for BEACON WP5: testing, verification and validation of models - Step 2 - Large scale experiments [Report]. - 2018.

BEACON D5.5 BEACON project. Specifications for BEACON WP5: testing, verification and validation of models - Step 3 [Report]. - 2020.

BEACON deliverable report D32 Description of improved constitutive models and their implementation and verification. BEACON deliverable report D32 [Report]. - 2019.

BEACON deliverable report D33 (under preparation) Description of the constitutive models developed in the project. Conceptual bases, mathematical description and model capabilities. Assessment of predictive power [Report].

BEACON deliverable report D4.1/2 Bentonite mechanical evolution – experimental work for the support of model development and validation. BEACON deliverable report D4.1/2 [Report]. - 2019.

Bilke L., Flemisch, B., Kalbacher, T., Kolditz, O., Helmig, R., and Nagel, T. Development of Open-Source Porous Media Simulators: Principles and Experiences. Transport in Porous Media, 130(1), 337–361 [Report]. - 2019.

Borja R. I., and Lee, S. R. Cam-Clay plasticity, Part 1: Implicit integration of elasto-plastic constitutive relations. Computer Methods in Applied Mechanics and Engineering, 78(1), 49–72 [Report]. - 1990.

Brooks R. H., and Corey, A. T. Properties of porous media affecting fluid flow. Journal of the Irrigation and Drainage Division, 92(2), 61–90 [Report]. - 1966.

Cerfontaine B. [et al.] 3D zero-thickness coupled interface finite element: Formulation and application [Journal]. - [s.l.] : Computers and Geotechnics, 2015.

Charlier R. Approche unifiée de quelques problèmes non linéaires de mécanique des milieux continus par la méthode des éléments finis. PhD Thesis, Université de Liège in Department ArGEnCo. - Liège, Belgium : [s.n.], 1987.

Collin F., Li, X.L., Radu, J.P. and Charlier, R. Thermo-hydro-mechanical coupling in clay barriers. Engineering Geology, 64(2-3):179-193 [Report]. - 2002.

Dieudonne A. C. Hydromechanical behaviour of compacted bentonite: from micro-scale analysis to macro-scale modelling [Report]. - Liege : Universite' de Liege, 2016.

Dueck A. and Nilsson U. Thermo-Hydro-Mechanical properties of MX-80 [Report]. - [s.l.] : SKB, 2010.

Dueck A., Börgesson, L., Kristensson, O., Malmberg, D. and Åkesson, M. Bentonite homogenization. Laboratory study, model development and modelling of homogenisation processes. Svensk Kärnbränslehantering AB. In progress [Report]. - 2018.

ENRESA FEBEX project. Full-scale engineered barriers experiment for a deep geological repository for high level radioactive waste in crystalline host rock. Final report. ENRESA, Madrid [Report]. - 2000.

François B. and Laloui, L. ACMEG-TS: A constitutive model for unsaturated soils under non-isothermal conditions. International Journal for Numerical and Analytical Methods in Geomechanics 32, 1955–1988. doi:10.1002/nag.712. - 2008.

Gens A. and Alonso, E.E A framework for the behaviour of unsaturated expansive clays. Canadian Geotechnical Journal 29 (6), pp. 1013-1032 [Report]. - 1992.

Geuzaine C., and Remacle, J.-F. Gmsh: A 3-D finite element mesh generator with built-in pre- and post-processing facilities. International Journal for Numerical Methods in Engineering, 79(11), 1309–1331 [Report]. - 2009.

Ghiadistri G. M., Potts, D. M., Zdravkovic, L. and Tsiampousi, A. A new double structure model for expansive clays. 7th Int. Conf. on Unsaturated Soils, UNSAT 2018, 3-5 August, 2018, Hong Kong [Report]. - 2018.

Ghiadistri G.M. Constitutive modelling of compacted clays for applications in nuclear waste disposal. PhD Thesis, Imperial College London, UK [Report]. - 2019.

Hoffman C., Alonso E. E. and Romero E. Hydro-mechanical behaviour of bentonite pellet mixtures [Journal]. - [s.l.] : Physics and Chemistry of the Earth, 2007. - Vol. 32.

Huerta F., Fuentes-Cantillana, J. L., Jullien, F., Rivas, P., Linares, J., Fariña, P., Ghoreychi, M., Jockwer, N., Kickmaier, W. and Martínez, M. A. Full-scale engineered barriers experiment for a deep geological repository for high-level radioactive waste in crystalline host rock(FEBEX project). EUR(Luxembourg) [Report]. - 2000.

Ichikawa Y., Kawamura, K., Nakano, M., Kitayama, K., Seiki, T., and Theramast, N. Seepage and consolidation of bentonite saturated with pure- or salt-water by the method of unified molecular dynamics and homogenization analysis. Engineering Geology, 60(1-4), 127–138 [Report]. - 2001.

Lewis R. W., and Shrefler, B. A. The finite element method in the static and dynamic deformation and consolidation of porous media. John Wiley [Report]. - 1998.

Lloret A., Romoero, E. and Villar, M. V. FEBEX II Project Final report on thermo-hydro-mechanical laboratory tests, ENRESA [Report]. - 2005.

Lloret A., Villar M. V. and Pintado X. Ensayos THM: Informe de síntesis. Internal report [Report]. - [s.l.] : CIEMAT, 2002.

Lloret A., Villar, M. V., Sanchez, M., Gens, A., Pintado, X. and Alonso, E. E. Mechanical behaviour of heavily compacted bentonite under high suction changes. Geotechnique 53 (1), pp. 27-40 [Report]. - 2003.

Luenberger D. G. and Ye Y. Linear and Nonlinear Programming (Vol. 228). Springer International Publishing [Report]. - 2016.

Melgarejo Corredor M. L. Laboratory and numerical investigations of soil retention curves. PhD Thesis, Imperial College, University of London, UK [Report]. - 2004.

Nyambayo V. P. and Potts, D. M. Numerical simulation of evapotranspiration using root water uptake model. Computers & Geotechnics 37, pp. 175-186 [Report]. - 2010.

Potts D. M. and Zdravkovic, L. Finite element analysis in geotechnical engineering: theory. Thomas Telford Publishing, London, UK [Report]. - 1999.

Richards L. A. CAPILLARY CONDUCTION OF LIQUIDS THROUGH POROUS MEDIUMS. Physics, 1(5), 318–333 [Report]. - 1931.

Romero E. A microstructural insight into compacted clayey soils and their hydraulic properties [Journal] // Engineering geology. - 2013. - 165. - pp. 3-19.

Talandier J. Specifications for BEACON WP5: testing, verification and validation of models. Step 1- verification cases. BEACON deliverable report D5.1.1 [Report]. - 2018.

Talandier J. Specifications for BEACON WP5: testing, verification and validation of models. Step 2- large scale experiments. BEACON deliverable report D5.2.1 [Report]. - 2018.

Van Genuchten M. T. A closed-form equation for predicting the hydraulic conductivity of unsaturated soils. Soil Science Society of America Journal, 44, pp. 892-898 [Report]. - 1980.

Verma A., and Pruess, K. Thermohydrological conditions and silica redistribution near high-level nuclear wastes emplaced in saturated geological formations. Journal of Geophysical Research, 93(B2), 1159 [Report]. - 1988.

Villar M. V. and Talandier, J. Specifications for BEACON WP5: testing, verification and validation of models. Step 3 – predictive test cases. BEACON deliverable report D5.5 [Report]. - 2020.

Villar M. V. Thermo-hydro-mechanical characterisation of a bentonite from Cabo de Gata: A study applied to the use of bentonite as sealing material in high-level radioactive waste repositories, Technical Publication 01/2002. Madrid: Enresa [Report]. - 2002.

Villar M. V., Fernández, A. M., Romero, E., Dueck, A., Cuevas, J., Plötze, M., Kaufhold, S., Dohrmann, R., Iglesias, R., Sakaki, T., Voltolini, M., Zheng, L., Kawamoto, K. and Kober, F. FEBEX-DP Post-mortem THM/THG Analysis Report, NAB 16-17 Rev.1, Nagra [Report]. - 2018.

Villar M.V. and Gómez-Espina R Report on Thermo-Hydro-Mechanical Laboratory Tests Performed by CIEMAT on Febex Bentonite 2004-2008. CIEMAT report 1178, Madrid [Report]. - 2009.

Villar M.V., Iglesias, R.J., Gutiérrez-Álvarez, C., Carbonell, B. Pellets/block bentonite barriers: laboratory study of their evolution upon hydration. [Journal]. - [s.l.] : Engineering Geology, 2021. - Vol. in press.

Åkesson M., Börgesson, L. and Kristensson, O. SR-Site Data report – THM modelling of buffer, backfill and other system component. SKB TR-10-44, Svensk Kärnbränslehantering AB [Report]. - 2010.

Åkesson M., Kristensson, O. and Malmberg, D. The Hysteresis Based Material model. Deliverable (D3.1) Beacon Report. February 2018 [Report]. - 2018.